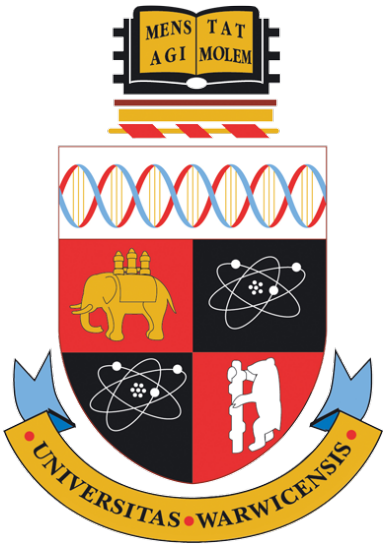

Fluorescence, phosphorescence, thermoluminescence and charge transfer in synthetic diamond

by

Jiahui (Gloria) Zhao

Thesis

Submitted to the University of Warwick

for the degree of

Doctor of Philosophy

Department of Physics

April 2022

Contents

List of Tables

List of Figures

Acknowledgments

First and foremost, I am indebted to Prof. Mark Newton for his excellent supervision and guidance, for contributing constructive ideas to this thesis, for motivating me with his research enthusiasm and for always reaching out when I needed it. I would like to thank Dr. Ben Green for all the thoughts he contributed and for impressing me with his intelligence and diligence. Equally, I would like to thank Dr. Ben Breeze for his tremendous and meticulous help in building up the experimental setups in my research and for his sense of humour and friendliness.

I am grateful to the De Beers Group for funding such an exciting topic. I am thankful to Dr. Simon Lawson for his encouragement to me and early research on phosphorescence in diamonds, to Dr. Philip Martineau for his questions guiding my research orientation, to Dr. David Fisher for his willing to support and interest in my research. I would like to particularly thank Dr. Phil Diggle for always being helpful and reliable and for proofreading this thesis. Without interesting diamond samples, this study is impossible to be achieved. Therefore, I will thank the late Dr. Tom Anthony of the General Electric Research & Development Centre, Hunter Yuan of the Sino-crystal Diamond Co., Ltd., and the Gemmological Institute of America (GIA) for the loan of samples.

I feel honoured to be a part of the Diamond Science and Technology Centre for Doctoral Training (DST CDT). I am grateful to Dr. Jon Goss, Prof. Paul May, Dr. Gavin Morley, Prof. Julie Macpherson, Prof. Jason Smith, Prof. Alan Kemp and all the researchers from academia and industry who delivered inspiring and informative lectures. This provided support in understanding diamonds and a broad perspective for my research. Also, a thank you to all my classmates in Cohort 3 for the enjoyable learning atmosphere. I want to thank Dr. Claire Hurley for her warm regards and care in helping me cope with the new environment. I am also grateful to all the members of the Warwick diamond group students, past and present, Luke, Raj, Lawrence, Chloe, Imogen, Helen, Lewis, Collins, Enrik, Angelo, Jenny, etc., for what you have taught me and providing support.

I owe thanks to Dr. Wuyi Wang for his kindness and favour and for providing me an opportunity to intern at GIA, the lab and New York city were both remarkable.

In addition, I would like to thank Dr. Ulrika D'Haenens-Johansson, Dr. Sally Magaña, Dr. Hiroshi Takahashi, Dr. Chloe Peaker, Dr. Tsung-Han Tsai, Dr. Karen Smit, Dr. Chunhui Zhou, Mr. Troy Ardon for being supportive and making me feel so welcome. I also would like to thank Prof. Alan Collins, Prof. Jim Butler, Dr. Daniel Twitchen, Dr. Andy Edmonds for the illuminating discussions; Mr. Zhaoda Sun and Dr. Taijin Lu for generous support during my trip in China.

My sincere thank you to my husband Weiqing, without his intimate companionship and generous solicitude, I would not be able to have so many unforgettable happy times. I must acknowledge my mum and dad; throughout my upbringing, they helped me build self-confidence and the ability to connect and trust others.

Finally, I have to thank Mr. Zhiqiang Pu, who has deeply inspired me with his efforts to fight for freedom of speech and his courage to persist in uncovering the truth. A realistic attitude and freedom of thought are not only the foundation of scientific research, but also the guarantee of human well-being. I am grateful to all those who stand up for honesty and conscience: it is to them that I dedicate this thesis.

Declaration and published work

I declare that the work presented in this thesis is my own except where stated otherwise, and was carried out entirely at the University of Warwick, during the period of November 2017 to December 2021, under the supervision of Prof. Mark Newton and Dr. Ben Green. The research reported here has not been submitted, either wholly or in part, in this or any other academic institution for admission to a higher degree.

Some parts of the work reported and other work not reported in this thesis have been published, as listed below. It is anticipated that further parts of this work will be submitted for publication in due course.

Published papers

1. J. Zhao, B. G. Breeze, B. L. Green and M. E. Newton, *Phosphorescence and thermoluminescence in HPHT synthetic type II diamonds*, Proceedings of China International Gems & Jewelry Academic Conference (2019)

Papers in preparation

1. G. Zhao, B. G. Breeze, B. L. Green and M. E. Newton, *Phosphorescence and donor-acceptor pair recombination in laboratory-grown diamonds*
2. G. Zhao, B. G. Breeze, B. L. Green and M. E. Newton, *Delayed luminescence in laboratory-grown diamonds*
3. G. Zhao, B. G. Breeze, B. L. Green and M. E. Newton, *Phosphorescence in diamond revisited*

Conference presentations and seminar

1. G. Zhao, B. G. Breeze, B. L. Green and M. E. Newton, *Phosphorescence in type II High Pressure High Temperature synthetic diamond*, International Gems & Jewelry Academic Conference, Beijing, China, oral presentation (2021)

2. G. Zhao, B. G. Breeze, B. L. Green and M. E. Newton, *Phosphorescence in type II High-Pressure High-Temperature synthetic diamond*, 71st De Beers Conference, University of Warwick, poster presentation (2021)

3. G. Zhao, B. G. Breeze, B. L. Green and M. E. Newton, *Fluorescence, phosphorescence and thermoluminescence in type II HPHT synthetic diamonds*, China International Gems & Jewelry Academic Conference, Beijing, China, oral presentation (2019)

4. G. Zhao, B. G. Breeze, B. L. Green and M. E. Newton, *Fluorescence, phosphorescence and thermoluminescence studies of synthetic diamond*, 70th De Beers Conference, University of Warwick, oral presentation and poster presentation (2019)

5. G. Zhao, B. G. Breeze, B. L. Green, P. L. Diggle and M. E. Newton, *Fluorescence, phosphorescence and charge transfer in synthetic diamonds*, The GIA Symposium, Carlsbad LA, United States of America, oral presentation (2018)

6. G. Zhao, B. G. Breeze, B. L. Green and M. E. Newton, *Phosphorescence and thermoluminescence studies of synthetic diamonds*, 69th De Beers Conference, University of Warwick, poster presentation (2018)

Abstract

This thesis reports the investigation of the physics of long-lived phosphorescence in lab-grown High-Pressure High-Temperature (HPHT) diamond. To understand of luminescence and related charge transfer processes, a combination of techniques have been employed including cathodoluminescence (CL), photoluminescence (PL), the phosphorescence lifetime and spectroscopic studies, thermoluminescence (TL); as well as temperature-variable time-resolved Fourier Transform Infrared (FTIR) absorption spectroscopy and Electron Paramagnetic Resonance (EPR) measurements used to monitor the dynamics in concentrations of neutral boron acceptors and deep nitrogen donors during phosphorescence emission.

The "blue-green" phosphorescence spectrum, lifetime, and intensity in different growth sectors have been studied. Variations between growth sectors is due to differences in the concentration of substitutional boron (B_S) and substitutional nitrogen (N_S) defects. Substitutional boron can exist in neutral and negative charge states. B_S^0 is a relatively shallow acceptor. In this work it is conclusively shown that substitutional nitrogen can exist in positive, neutral and importantly negative charge states. Time-resolved EPR studies of the recovery of N_S^0 after optical excitation have enabled identification of N_S^- as a shallow trap with an acceptor level lying ~ 0.2 eV below the conduction band minimum. N_S^- plays an important role in "blue-green" phosphorescence. A model for the mechanism of "blue-green" phosphorescence in type II HPHT synthetic diamonds has been proposed. Substitutional boron-nitrogen donor-acceptor pairs (DAPs) (N_S^0...B_S^0) are shown to be responsible for the "blue-green" luminescence/phosphorescence commonly observed in near-colourless lab-grown HPHT diamonds.

The change in the lifetime and emission spectra of the "blue-green" phosphorescence at different temperatures is due to a change in mechanism. At low temperatures (< 173 K), the phosphorescence spectrum and lifetime are temperature independent. The emission (centred at 2.25 eV) is dominated by distant N_S^0...B_S^0 pairs and the charge tunneling between defects can reset emission centres.

A significant population of isolated B_S^0, N_S^- and N_S^0 defects persist. Above ~ 273 K, thermal excitation of carriers to conduction and valence bands and subsequent capture by ionized N_S...B_S pairs facilitates close pairs to emit many times. The phosphorescence peak shifts to 2.5 eV and is dominated by emission from close donor-acceptor pairs. The shift in energy is consistent with the size of the Coulomb correction to the DAP emission energies. At intermediate temperatures, both tunneling and thermal carrier excitation contribute and the phosphorescence peak shifts to higher energy at longer times after optical excitation is removed. The large configurational change between N_S^0 and N_S^+ explains why the N_S...B_S DAP emission energy is shifted to lower energy than predicted by the simple model widely used for shallow DAPs.

"Orange" and "red" emission bands observed in some HPHT lab-grown diamonds are associated with as yet unidentified colour centres where the delay emission originates from charge capture into an excited state followed by emission of the new charge state of the defect.

Abbreviations

[X]	Concentration of X
BDD	Boron-doped diamond
BE	Bound exciton
CB	Conduction band
CL	Cathodoluminescence
CPL	Complex power law
ct	Carat
CVD	Chemical vapour deposition
CW	Continuous wave
CW-EPR	Continuous wave electron paramagnetic resonance
DAP	Donor-acceptor pair
DC	Direct-current
E_F	Fermi level
E_g	Bandgap energy
EPR	Electron paramagnetic resonance
FCC	Face centred cubic
FE	Free exciton
FTPS	Fourier-transform photocurrent spectroscopy
FTIR	Fourier transform infrared
FWHM	Full width at half maximum
GE	General Electric
$\hbar\Omega$	Energy of a phonon
$\hbar\omega$	Energy of a photon
HFCVD	Hot-filament CVD
HPHT	High pressure high temperature

I_0	Initial intensity
IR	Infrared
λ	Wavelength of light
LA	Longitudinal acoustic
LO	Longitudinal optical
LVM	Local vibrational mode
MPCVD	Microwave plasma CVD
MSE	Modified stretched exponential
MW	Microwave
PL	Photoluminescence
ppb	Parts per billion atomic density
ppm	Parts per million atomic density
PSB	Phonon side-band
Q	Resonator quality factor
RMS	Root-mean-square deviation
RP-EPR	Rapid passage electron paramagnetic resonance
RT	Room temperature
SEM	Scanning electron microscope
SIMS	Secondary ion mass spectrometry
SNR	Signal to noise ratio
SP-EPR	Slow passage electron paramagnetic resonance
T	Temperature
TA	Transverse acoustic
τ	Characteristic lifetime of a process
TL	Thermoluminescence
TO	Transverse optical
TTL	Transistor-Transistor Logic
UV	Ultraviolet
UV-Vis	Ultraviolet-visible
VB	Valence band
ZPL	Zero-phonon line

Chapter 1

Introduction

As a well-known and valuable gemstone, diamonds have attracted people with their characteristic sparkling "fire", clarity, durability, and natural rarity for hundreds of years. Diamond plays a key role in the gem trade as the symbol of love, wealth and power. Famous diamonds such as the biggest diamond, the Cullinan weighing 3106 ct[1], the blue Hope Diamond and the unnamed 1174 ct high gem-quality diamond recently discovered in Botswana attract considerable popular interest. [1]

The synthesis of diamonds has always attracted great interest. Before the first report in the 1950s, many attempts had been made. [2] With the advancement of diamond synthesis technology, identifying gem-grade man-made diamonds from natural diamonds has become more challenging. Characteristic features such as fluorescence and phosphorescence have become important for identifying the origin of diamonds. However, after decades of research and development, laboratory-grown diamonds are not only used in jewellery but are widely used in various applications due to their outstanding physical properties. It is of no doubt that, in the future, lab-grown diamonds will have both high commercial and industrial value.

[1] 1 ct = 0.2 grams

1.1 Diamond synopsis

1.1.1 Diamond structure

Carbon is the only element in the periodic table with four isomers ranging from 0 to 3 dimensions. [3] Carbon, with an atomic number of 6 and has six electrons, two of them in the innermost shell and four valence electrons in the outer shell with the ground state configuration $1s^2 2s^2 2p^2$. [2] Graphite with sp^2 hybridised orbitals and diamond with sp^3 hybridised orbitals are well-known examples of carbon allotropes. [3] When one of the $2s^2$ electrons is excited to occupy an empty $2p$ orbital, the $2s$ and three $2p$ orbitals can hybridise into four sp^3 orbitals. The four equivalent bonds formed lead to the tetrahedral coordination of the atoms in the diamond lattice. [3, 4]

The carbon atoms in the diamond lattice are arranged in a face-centred cubic (FCC) crystal structure with a two-atom basis (0,0,0) and $(\frac{1}{4}, \frac{1}{4}, \frac{1}{4})$, with each carbon atom covalently bonded with four other surrounding carbon atoms. Atoms on the FCC sites are often referred to as occupying sub-lattice I, where as the other atoms are on sub-lattice II. The conventional unit cell of diamond consists of 8 carbon atoms is shown in figure 1.1, with the C-C bonds having a length of 0.154 nm and an included angle of 109.5 °. [4]

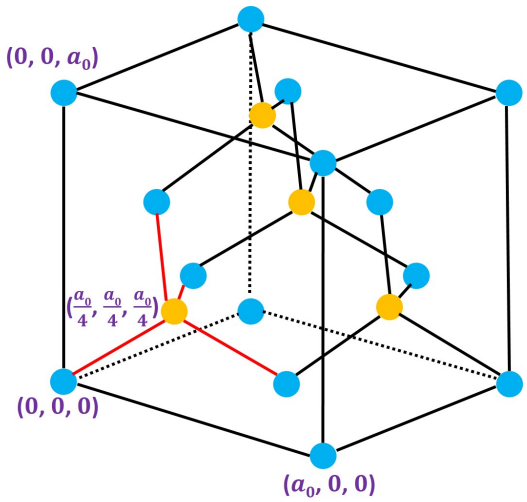

Figure 1.1: The unit cell of diamond with cell length $a_0 = 0.357$ nm, and the C-C bond length is 0.154 nm at room temperature. [5] The tetrahedral symmetry of the diamond lattice is highlighted by the red line. The blue circles represent lattice sites of the face-centred cubic (FCC) in type I geometry. The yellow circles represent internal tetrahedral sites of the FCC in type II geometry. [6]

Due to the close packing arrangement of the diamond lattice, the density of diamond is 3.52 $g\,cm^{-3}$ giving the highest atomic density of all solids as $1.76 \times 10^{23}\,cm^{-3}$. [7] Therefore, a point defect concentration of 1 part per billion carbon atoms (ppb) is equivalent to 1.76×10^{14} point defects per cm^3.

1.1.2 The properties and applications of diamond

Due to its unique atomic structure combining high atomic density and high C-C bond energy (347 kJ mol^{-1}), diamond has outstanding physical properties listed in table 1.1, that enables exploitation in many demanding applications. [7] For a long time, diamonds have been widely used in machining, grinding, cutting, milling, sawing and polishing because of their high hardness and good thermal conductivity. [8] The high transparency from approximately 220 nm to the far IR region makes pure diamond ideal for optical windows and lenses. [8] In addition, the large Raman gain shift and thermo-mechanical properties enable the fabrication of high-performance diamond Raman lasers. [9, 10] As a result of the high acoustic wave velocity in diamonds, the break-up frequency of diamond tweeters are improved by a factor of two compared to high-quality aluminium tweeters. [10]

The doping of diamond and colour-centre engineering techniques enable more advanced applications of diamonds. Electrically conducting boron-doped diamond (BDD) works as a superior electrode for electrochemistry application due to its wide solvent window, low background currents, reduced fouling and stability in the challenging environment. [11] The introduction and control of colour centres: the most studied are the negatively charged nitrogen-vacancy (NV) and silicon-vacancy (SiV) centres in diamonds, which makes world leading quantum technology platforms for applications such as high sensitivity magnetic field sensing, quantum computing and quantum communication. [12] Furthermore, multiple medical applications of diamond have been developed, including prostheses, sensing, imaging, and drug delivery because of its chemical inertness and bio-compatibility. [7]

Table 1.1: A summary of extreme properties associated with diamond.

Properties of diamond		Ref
Electronic		
Wide bandgap (indirect)	5.47 eV	[13]
Wide bandgap (direct)	7.30 eV	[13]
High breakdown field	20 $MV\,cm^{-1}$	[14]
High electron mobility	4500 $cm^2\,V^{-1}\,s^{-1}$	[15]
High hole mobility	3800 $cm^2\,V^{-1}\,s^{-1}$	[15]
Good insulator (resistivity at RT)	$10^{16}\,\Omega\,cm$	[16]
Thermal		
High thermal conductivity	2230 $W\,m^{-1}\,K^{-1}$ (natural)	
	3320 $W\,m^{-1}\,K^{-1}$ (^{13}C enriched)	[17, 18]
Low linear thermal expansion	0.8×10^{-6} K	[5]
Mechanical		
High hardness	80-120 GPa	[19]
Highest Mohs hardness	10	[5]
Bulk modulus	445 GPa	[19]
Shear modulus	530 GPa	[19]
Largest Young's modulus	1223 GPa	[20]
Low coefficient of friction	0.1	[5]
Optical		
Board optical transparency	Deep UV to the far IR region	[16]
Raman gain	15 $cm\,GW^{-1}$	[10]
Acoustic		
Highest acoustic wave velocity	18 $km\,s^{-1}$	[21]
Others		
Chemically inert		[16]
Biologically compatible		[16]

1.1.3 Classification of diamond

The type I and type II diamond classification based on the IR absorption (figure 1.2) was proposed by Robertson *et al.* in 1934. [22] Approximately 98 % of natural diamonds are classified as type I diamonds, typically containing much more than 1 ppm nitrogen, detectable by infrared absorption measurements. [23–25] Type I diamonds can be classified into various subtypes based on the different forms of nitrogen impurities within the diamond lattice. For instance, type IaA comprises predominately of A-centres (a nearest-neighbour nitrogen pair) whilst type IaB comprises predominately B-centres (four nitrogen atoms surrounding a vacancy).

Type Ib is predominated by C-centres (single substitutional nitrogen). [23, 26, 27]

Type II diamonds, which are rare among natural diamonds, are typically more chemically pure and contain very low levels of nitrogen impurities (< 1 ppm). Type IIa diamonds are transparent throughout the visible and ultraviolet spectral regions down to approximately 230 nm in wavelength, therefore, they have a colourless appearance and can be of great commercial value. [23] Type IIb diamonds are generally light blue due to the significant presence of substitutional boron impurities in the diamond lattice. The substitutional boron acceptor is responsible for the semiconducting behaviour of type IIb diamonds. [24]

<table>
<tr><th colspan="3">Classification of diamond</th></tr>
<tr><td rowspan="4">Type I
Nitrogen concentration >1ppm detectable by IR absorption measurement</td><td rowspan="3">Type Ia
Aggregated nitrogen</td><td>Type IaA
contains A-centre (N_2)</td></tr>
<tr><td>Type IaB
contains B-centre (N_4V)</td></tr>
<tr><td>Type IaAB
contains A- and B-centres</td></tr>
<tr><td colspan="2">Type Ib
Single substitutional nitrogen C-centre (N_S)</td></tr>
<tr><td rowspan="2">Type II
Nitrogen concentration <1ppm undetectable by IR absorption measurement</td><td colspan="2">Type IIa
Boron undetectable by IR</td></tr>
<tr><td colspan="2">Type IIb
Boron detectable by IR</td></tr>
</table>

Figure 1.2: Diamond type classification of diamonds is based on spectral features detected by infrared absorption measurements.

1.2 Synthesis of diamond

The synthesis of diamond has been of great interest because the supply, quality, size, and dopants of synthetic diamonds can be well-controlled compared with natural diamonds. The high-pressure high-temperature (HPHT) synthesis and chemical vapour deposition (CVD) synthesis are the most widely used methods for man-made diamond growth, not only for polycrystalline diamonds but also single-crystal diamonds. As shown in figure 1.3, HPHT and CVD synthetic diamonds are grown under different pressure and temperature conditions. The Berman-Simon line, namely the graphite-diamond equilibrium line, divides the diamond thermodynamic stability region (HPHT diamond growth) and the graphite stable region where

CVD diamond is grown. [28, 29]

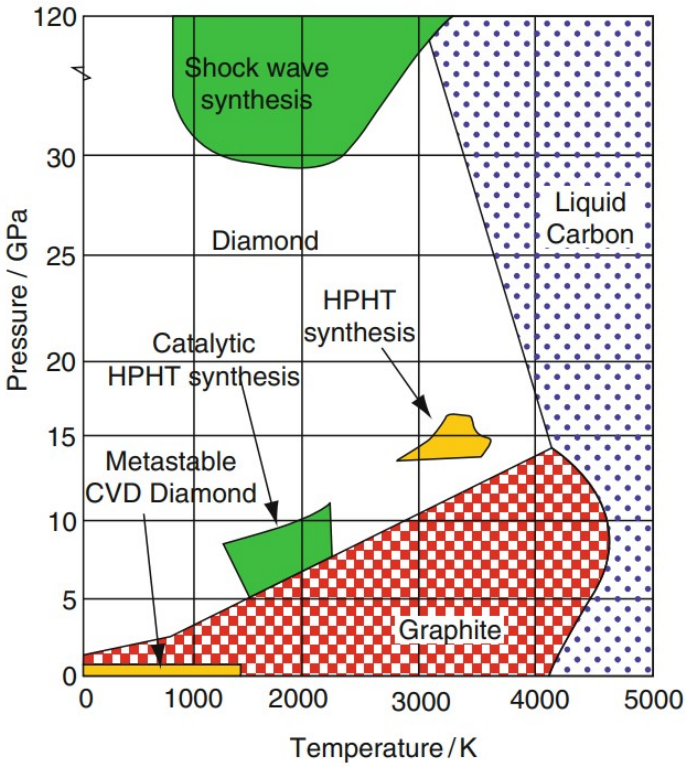

Figure 1.3: Phase diagram for graphite and diamond. Adapted from [3].

1.2.1 High-Pressure High-Temperature (HPHT) synthesis

HPHT synthetic diamonds are grown in similar pressure and temperature conditions to natural diamonds. However, high-clarity (very few/no inclusions) are difficult to obtain, so they are often used in applications that exploit their hardness where clarity is of little concern. Increasing control over colour, clarity, and size has opened up jewellery and other applications that exploit the optical properties. [3, 30] In addition, the research on HPHT synthesis of diamonds is helpful for better understanding of the natural diamond growth environment. [31]

The attempt to synthesis diamonds based on the research and understanding of natural diamonds began in the 19th century. [2] For tens of years, scientists tried different approaches, failed but still contributed by developing principles and ideas of diamond synthesis and creating the high-pressure environment for diamond growth. [2] General Electric researchers announced the first success to convert graphite into tiny diamonds in a belt press in 1954, later published

in 1955. [32] Although these diamonds "grown" was subsequently found to be natural type Ia diamonds, the same system were used to successfully synthesis diamonds at higher pressures. [33] By optimising the recipe and P-T conditions, the high-pressure and high-temperature synthetic diamond technology has been significantly improved, enabling the commercially grow high-quality colourless and large-size HPHT diamonds (> 10 mm). [34]

1.2.1.1 Mechanisms and methods

The first large single-crystal diamond was grown under HPHT conditions using the temperature gradient method (TGM) in 1971, which is still one of the most effective methods to grow gem-quality diamonds. [35, 36] As shown in figure 1.4, carbon sources, catalysts, seed crystals are placed inside the reaction cell of the press which provides the high-pressure and high-temperature environment. Nitrogen getters are added when colourless diamonds are targeted, detailed discussed later in this section. Under P-T conditions of thermodynamic stability of diamond, carbon sources are dissolved in the molten catalysts. [37–39] The temperature gradient leads to the difference in solubility of carbon on the top and bottom of the capsule, therefore, growth occurs on the colder seed. [38, 40, 41] Besides seeded growth described above, spontaneous crystallization is also applied for HPHT growth of diamond "grit", which is of a similar mechanism and generally at a higher temperature. [29, 42] The morphology of HPHT synthetic diamonds are usually cubic, cubo-octahedral or octahedral with {100} and {111} surfaces dominant. [38, 43] Minor surfaces such as {113}, {110}, {115}, and {117}, etc. also present under different growth conditions. [2, 38]

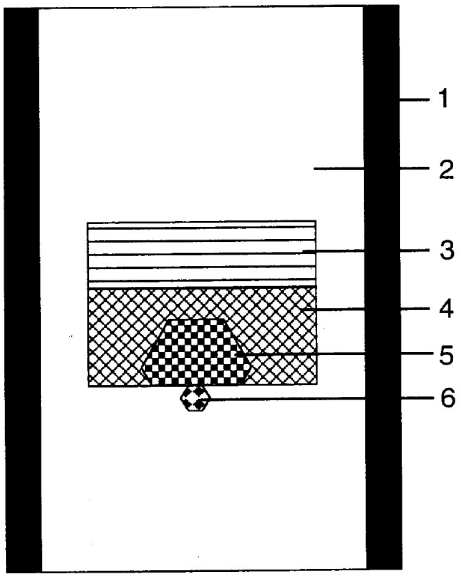

Figure 1.4: Schematic for a reaction cell for diamond growth by the temperature gradient method. 1. Graphite heater 2. NaCl pressure medium 3. Carbon source 4. Catalyst solvent 5. Grown diamond 6. Seed crystal. Adapted from [38].

The growth rate, morphology, and quality of HPHT synthetic diamond depend on factors like the purity of carbon source, seed crystals, P-T conditions, and selection of catalyst and nitrogen getters. [2, 44]

Graphite disks or powder are usually used as carbon sources for HPHT temperature gradient diamond growth. [38] The impurities in the graphite can be incorporated into the diamond lattice and form various defects. Moreover, the initial structure of the graphite material significantly affects the quality of the diamond. For example, the percentage of hexagonal perfection should be above 50 % in order to achieve diamond growth. [45]

The size, quality, morphology and position of diamond seeds all influence the growth rate and quality of the grown diamond. [36, 38, 46] The large seed method has been reported in the literature, which mentions that the {100} seed is not suitable for type IIa diamond growth, and large inclusions can be trapped due to the sudden start of crystal growth on the large seed surface. [47] In addition, the effects of the carbon convection field around on the growing diamond under HPHT conditions has been studied. [36] Extended dislocations and structural defects (e.g. twin planes) in the seed crystal can extend into the synthetic diamond during HPHT diamond growth. [38] The influence of the seed on the diamond produced has been discussed in detail by Sumiya *et al.*. [46]

Various presses, such as the belt press, the tetrahedral press, the BARS press, and the cubic press, are utilised to achieve a high-pressure and high-temperature environment for diamond growth. [2, 37, 42] The pressure for HPHT diamond growth is generally between 5 GPa to 7 GPa. [38, 48] The pressure applied depends on the variety of catalysts; for example, relatively high pressure up to 8.5 GPa is required when growing diamonds with non-metallic catalysts or metallic catalysts in which the solubility of carbon is low. [49, 50] The temperature range for HPHT diamond growth is around 1200 °C to 2000 °C, which should be precisely controlled. Also the temperature gradient must be precisely controlled. Normally the higher the temperature, the higher the diamond growth rate. [38] The morphology of diamond changes from cubic to octahedral as temperature increases. [48] The temperature for diamond growth depends on the catalyst. It has been reported that HPHT diamond can be grown below 1000 °C in Ni-Ge catalyst, and when using Cu, Zn, or non-metallic catalysts, a temperature above 2000 °C is required. [51, 52] Generally speaking, too low-temperature results in the formation of skeletal crystals, and too high P-T parameters leads to too many inclusions trapped in diamond or even chaotic growth. [42, 53]

Catalysts play important roles for diamond synthesis under high-pressure, high-temperature conditions: firstly, the solvent catalyst should efficiently break the hexagonal bonds of the graphite material and dissolve the carbon source; secondly, conducting heat and delivering carbon atoms to the seed crystal for re-crystallization as diamond; thirdly, lowering the kinetic barrier for transformation from graphite to diamond, therefore, enabling diamond growth with lower P-T parameters (Figure 1.3). [2, 41, 42, 48, 54] The conventional metal catalysts, such as Fe [55–58], Co [53], Ni [36, 39, 51], Mn [59] and their alloys, have relatively high melting temperatures. The diamonds begin to grow immediately when these catalysts melt. [56, 60] To improve HPHT diamond synthesis, more metallic catalysts have been evaluated, including Cu [60, 61], Mg [37, 62–65], Sn [66], Zn, Sb [67], etc. The melting temperature of those catalysts is relatively low; the temperature for diamond growth is required to exceed the melting point of catalysts and temperatures that enable diamond growth. [60] In terms of the Mg-based system, the solubility of carbon is lower than conventional metallic

catalysts, but the diamond growth rate is increased by a factor of 8 -10. [37, 62] In addition, the nitrogen content in diamonds grown in Fe-Mg catalyst is far less than those in Fe-C system. Therefore, solvents like Fe-Mg enable very good quality diamond synthesis. [29] Without nitrogen doping, diamonds grown in Ni-based and Fe-based catalyst normally have lower nitrogen contents than in Cu, Ge, Sb catalysts. [56, 66] The synthesis of diamonds in non-metallic catalysts, including S [50, 68], P [69–72], and Ge (metalloid) [37, 73], requires higher pressures (6 - 8 GPa) and higher temperatures (1500 - 2200 °C). Although those diamonds are usually small in size and have poor quality, there is potential for them to be used as diamond material containing germanium-vacancy or P-related defects. [37, 40] The colour, morphology, and quality of HPHT diamonds are determined by the types of catalysts, the capsule geometry, which influences the growth process by changing the temperature distribution. [40, 44, 49]

Nitrogen getters, such as Al, Ti, Zr, and Mg, are added into the solvent catalyst to minimise the nitrogen incorporation in the HPHT synthetic diamond in order to obtain a colourless appearance. [30, 38] These elements combine with nitrogen atoms to form insoluble nitrates or nitrides, reducing the nitrogen available for incorporating into the diamond lattice during growth. [30] By adding a nitrogen getter, the nitrogen concentration in HPHT diamond can be reduced to below 0.1 ppm. [53] Inclusions are more readily trapped into a diamond when the nitrogen getters content is increased. Therefore, aiming for better crystal clarity, the growth temperature should be reduced to slow down the growth rate of diamonds. [38, 53, 74] In addition, nitrogen getters are less effective as temperature increases. [38] The common nitrogen getters and their effects on diamond morphology and growth rate are listed in table 1.2. As a nitrogen getter, Ti is more effective than Al for the removal of nitrogen in diamonds. [74] Adding Cu when using Ti can reduce the formation of TiC and leave more Ti to act as the nitrogen getter, thereby further improving the nitrogen removal efficiency. [53, 75] The Ti or Ti-Cu nitrogen getters also enable nitrogen and boron co-doping. [76] Other elements V, Cr, Mn, are in the same group of Ti, which also work as nitrogen getters but are less effective than Ti. [38] The amount of nitrogen getters should be adjusted depending on the catalyst. For example, more nitrogen getters are required at

higher Co content in the Co-Fe system. [53] Moreover, no diamonds grow when additive Zr is more than 6.wt% in the Fe-Co solvent. [77]

1.2.1.2 Impurities in HPHT-grown diamond

The metallic catalysts can be trapped in the diamond lattice and form large inclusions in HPHT synthetic diamonds, especially when the growth rate is high. [38] The inclusions in diamonds are usually studied by X-ray diffraction, X-ray micro-tomography, and X-ray fluorescence. In order to improve the clarity of diamonds, the growth rate should be well-controlled. [38]

Dislocations in the seed crystals extend to the grown diamonds, hence high-quality diamonds can be obtained by using seed crystals with a low density of dislocations. [38] In addition, high nitrogen contents in the metal melts lead to a high density of dislocations in HPHT grown diamonds. [83]

It is common for natural diamonds to contain more than 1,000 ppm nitrogen. For HPHT synthesis, the nitrogen impurities in the carbon sources, catalysts, and the growth environment lead to the incorporation of nitrogen atoms into diamonds during growth. [53] The efficiency of nitrogen incorporation depends on the type of catalyst. Compared with non-metallic catalysts, HPHT diamonds are grown in conventional metal solvents and usually contain less nitrogen, up to 800 ppm. [38] To grow diamond containing very high nitrogen concentration, nitrogen dopants, like FeN, or NaN_3, can be added, by which the nitrogen concentration can reach 3300 ppm. [58] There is a limitation for nitrogen dopants: when the nitrogen concentrations in the solvent are more than 0.4 atom % (4000 ppm), the nucleation and growth of diamonds are terminated. [83]

The nitrogen concentration in the {111} growth sectors is usually the highest, but the nitrogen incorporation efficiency in the {100} growth sector is more sensitive to the temperature. Therefore, in some diamonds grown at relatively low temperature, the nitrogen in {100} growth sector is greater than that in {111}. [38, 83] Nitrogen atoms prefer to exist as single substitutional nitrogen in the diamond lattice when the growth temperature is relatively low. At temperatures above $\sim$ 1500 °C, nitrogen begins to aggregate into A centres, with B centres being formed at temperature approaching 2500 °C. [38] The nitrogen-related defects in

Table 1.2: Summary of nitrogen getters used in the high-temperature, high-pressure synthesis of diamond.

Nitrogen getter	Content wt.%	Pressure (GPa)	Temperature (°C)	Catalyst	Morphology	Growth rate	Reference
Al	0-20	4.9 - 5.5	1240-1500	Fe Ni	suppresses {100} develops {113},{119}	reduce	[52]
		5.6 - 5.8	1330-1530	Fe Mn	{111} dominates	reduce	[78]
	4	5.5	1290	Ni Mn Co		reduce	[74]
Ti	10	7	1700	Fe			[79]
	1 - 2	6	1350 -1500	Fe Co	increases {100} {110} {113} present		[76]
	1.8 - 5.4	5.5 - 6.1	1380 - 1680	Fe Co	-	almost no change	[80]
Ti/Cu		5.3 - 5.9	1230 -1380	Fe Ni	develops {111},{113}		[81]
		5.6	1270	Fe Ni			[75]
	1.5/1.8	5.5	1290	Ni Mn Co		reduce	[74]
	0.5 - 2	5.6	1280	Fe Ni Co			[82]
	0.5 - 2	5.6	1280	Mn Ni Co			[82]
Zr	0.64 - 6.3	5.5 - 6.1	1380 - 1680	Fe Co	-	almost no change	[80]
	0.64 - 5	6 - 6.5	1400 -1700	Fe Co	{111},{100} {110},{113},{115} present	< 2.54 % no change	[77]
Mg	1 - 2	4.5	1250 ± 50	Ni Mn	increases {100}	> 2 % reduce	[30]
	0-9.2 mol %	6	1335 - 1435	Fe	increases {100}		[49]

HPHT synthetic diamonds have been reviewed in the literature. [23] The single substitutional nitrogen defect is discussed in detail in Chapter 5.

Boron impurities in carbon sources, solvent catalysts, and capsule materials can give rise to boron defects in HPHT grown diamonds, making them p-type semiconductors and resulting in blue, dark blue to black colour appearance. [38, 53] The efficiency of boron-doping depends on the catalyst. For example, less boron incorporates into a diamond lattice when Fe content is higher in an Fe alloy solvent. [44] The distribution of boron in HPHT synthetic diamonds is growth sector dependent: the concentration of boron defect is usually highest in the {111} growth sector. [53] In the {111} growth sector of nitrogen and boron co-doped diamonds, the concentration of nitrogen is greater when little boron is added; conversely, boron defects are dominant when large amount of boron is added. [38] In addition, adding boron inhibits the growth of {100} growth sector, when it reaches 0.4 .wt% (4000 ppm), {100} surfaces disappear. [84, 85] More about boron defects in diamonds are introduced in Chapter 4.

Nickel and cobalt atoms are easily incorporated into the diamond lattice in {111} growth sectors. [38, 53] The photoluminescence peaks at 884 nm, 484 nm are assigned to Ni-related defects. [86] Those defects are characteristic of HPHT grown diamonds. In comparison, iron in the molten catalyst is rarely incorporated into the diamond lattice and no Fe related point defects have been conclusively identified. [87]

1.2.2 Chemical Vapour Deposition (CVD) synthesis

Diamonds produced by the chemical vapour deposition (CVD) method grow at low pressures and moderate temperatures where graphite is the stable form of carbon (Figure 1.3). [3, 88] At present, single-crystal diamond and polycrystalline diamond synthesised by the CVD process are commercially available for various optical, thermal, electronic, mechanical, and quantum-technology applications. These include high-power laser windows, electrochemical sensors, high-power electronics, magnetometer, medical diagnostics, etc. [89, 90] More details for CVD diamonds properties and applications are introduced in the literature. [10, 91] For high-performance applications, natural diamond is usually limited by size, supply,

perfection and purity. For diamonds grown by HPHT synthesis, high purity is very difficult to achieve. [92, 93] CVD growth can achieve a high growth rate and high purity. Control of dislocation densities and distributions is still challenging, but this material is enabling for many applications. [10, 94]

In 1958, the first CVD diamond was successfully grown on natural diamond crystal using a carbon-containing gas at low pressure (0.1 Torr) and low temperature (900 °C) by William Eversole; the process was patented in 1962. [95, 96] However, the crystal growth rate was very low, and lots of graphite was deposited simultaneously with the diamond film. [97] In 1968, Augus *et al.* contributed to higher diamond quality by discovering that atomic hydrogen etches graphite rather than diamond during CVD growth. [98, 99] In the 1980s, further improvements in the CVD synthesis of diamond materials worldwide were accomplished, which established a good understanding of the CVD diamond synthesis process and enabled industrialised CVD diamond growth by different methods. [90, 92] Specifically, Russian scientists developed techniques to grow diamonds on diamond (homoepitaxial) and non-diamond (heteroepitaxial) substrates in 1981, suitable for single-crystal diamond growth and polycrystalline diamond growth, respectively. [100, 101] In the next two years, a Japanese research group at the National Institute for Research in Inorganic Materials (NIRIM) successively designed and built up the hot-filament CVD reactor (HFCVD) and microwave plasma CVD reactor (MP-CVD) platforms, which could achieve a diamond crystal growth rate over 1 μmh^{-1}. [102, 103] Since the early 2000s, CVD diamond synthesis techniques have been advanced dramatically, and the technology is relatively mature and commercially available. Studies are still targeting larger size, higher quality, faster growth rate and better control of impurities and defects in CVD diamond. [89, 90, 104]

1.2.2.1 Mechanisms and methods

The mechanisms of the CVD process for diamond growth is described in figure 1.5. The precursor gas phase mixture typically includes the carbon-containing gas methane (or other hydrocarbon molecules), and hydrogen. Oxygen, and other gases are often added. The gas mixture is thermally dissociated into active species, such as C, H, CH, CH_2, CH_3, by hot filament, microwave plasma, DC plasma,

or an oxy-acetylene flame, in order to achieve an appreciable growth rate. [101] The free radicals, mainly CH_3, then chemically react and nucleate or deposit on the substrate. [3, 99, 105] Atomic H is essential for diamond growth: firstly, it abstracts surface-H atoms leaving behind a surface radical site; secondly, it keeps the surface sp^3 bonded; thirdly, it etches away non-diamond carbon like graphite deposits simultaneously from the surface. [99, 101, 106] The standard growth model for CVD diamonds is described in [107]. The morphology of CVD diamonds most commonly presents cubo-octahedral habits with cubic {001}, octahedral {111} facets or both, which can be well-controlled by varying conditions like temperature or gas phase in the reactor. [91] The other facets grows significantly faster, therefore, rapidly disappear during growth. [92, 101]

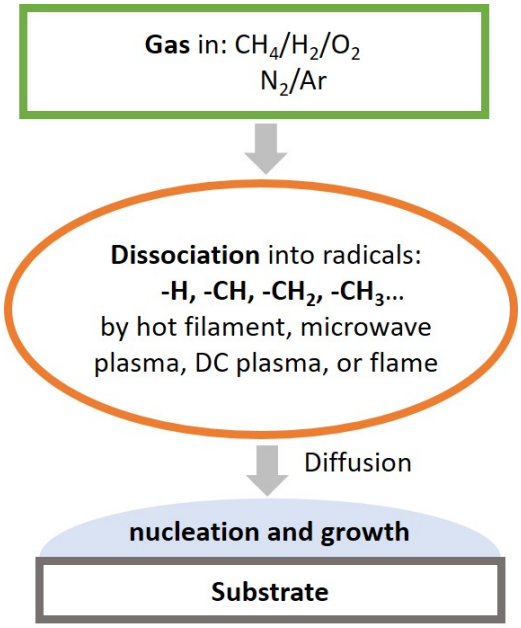

Figure 1.5: Schematic diagram of diamond growth mechanism from CVD processes.

Several CVD methods based on the different reactors have been utilised for diamond growth, which are reviewed in the literature. [88, 101, 106] Among them, hot filament (HF) reactors and microwave plasma reactors are the most widely used in CVD growth: HF reactors have lower cost, but the diamond growth rate is slower and typically lower quality, not suitable for oxygen-containing precursors (limited by high temperature, and requires frequent replacement of the filament); the microwave plasma CVD approach is expensive in terms of energy input required but beneficial for the highest purity and large (or thick) diamond growth without

any limitation on precursors. [88, 99, 108] Specific MPCVD reactor and methods can be seen in [3, 104, 105].

Generally speaking, there are several key issues to be considered for the CVD process: the gas source, the selection of substrate, and the temperature and pressure conditions. [2, 99]

The carbon source and hydrogen are the most critical in the gas mixture, and sometimes oxygen is also added. [105] The form of hydrocarbon molecules added is dissociated in the reactor, typically can be methane (CH_4), acetylene (C_2H_2), ethane (C_2H_6), propane (C_3H_3), etc.. [2, 10, 94] As mentioned above, atomic hydrogen maintains the tetrahedral arrangement, etches away non-diamond carbon, and removes the hydrogen atoms on the top of the diamond lattice, leaving a dangling bond to receive another carbon-containing radical. [3, 101] The addition of oxygen-containing such as O_2, CO, or CO_2 is not necessary but enables diamond growth at lower substrate temperatures and can enhance the quality of the diamond produced. [10, 94, 101] It is noticeable that being too oxygen-rich in the gas phase leads to no diamond growth. (or etching of the substrate) [88, 99] The C-H-O phase diagram shown in figure 1.6 published in 1991 by Bachmann *et al.* is a good description and summary of the relation between CVD diamond growth and the ratio of carbon, hydrogen and oxygen. [88] Only a small region above the C-O tie-line on this phase diagram allows diamond growth. Within this region, maximising the hydrogen concentration improves diamond quality with fewer defects incorporated; maximising the carbon concentration leads to a higher growth rate. [99, 104]

Other gases can also be involved in precursors for various purposes. For example, argon having a thermal conductivity lower than that of H_2, can be added up to 40 % of the gas mixture to increase the growth rate without any modification on the morphology of diamond grown. [104] The addition of halogenated gases can achieve diamond "deposition" at lower temperatures (250 °C to 750 °C). [101] When the concentration of nitrogen addition in the gas phase is a few ppm, the {100} plane growth rate is obviously increased with the nitrogen concentration. However, more nitrogen addition in the gas phase results in lower quality diamond growth. [104]

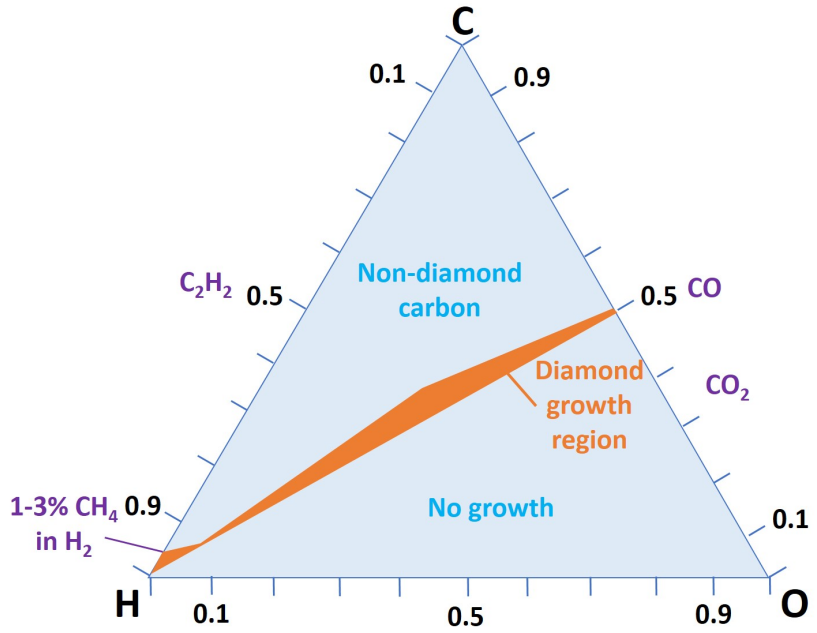

Figure 1.6: Simplified Bachmann triangle C-H-O phase diagram. Adapted from [99].

The substrate materials should be selected based on the properties, such as the crystalline structure, thermal expansion coefficient, thermal conductivity, etc. [94] Obviously, diamond is a suitable substrate for CVD diamond synthesis, especially for growing single-crystal diamonds. [3] Diamond grown on a {100} single-crystal substrate surface keeps the same crystalline orientation. [97] Non-diamond materials, including metals like molybdenum, tungsten and titanium, and silicon, can be used as substrates for polycrystalline growth. [3] Heteroepitaxy has several problems: firstly, the lattice mismatch, for example, the lattice constant of the diamond is approximately 52 % less than silicon; secondly, diamond thermal expansion coefficient is almost the smallest; therefore, a substrate made of other materials might bend or crack when cooling down back to room temperature; thirdly, the nucleation on a non-diamond substrate is difficult. [3, 99] This has been overcame to a large extent by using ion bombardment induced buried lateral growth method on iridium surface, which enables synthesis of laterally large pseudo single crystal. [109] The pre-treatment of substrate improves the CVD growth of diamonds. For example, a single-crystal diamond substrate polished with an off-angle of 2° to 20° enhances the growth rate by a higher density of growth steps. [104] Roughening the non-diamond substrate with diamond powders assists

nucleation by creating more nucleate sites and embedding seed crystals on the surface. [94, 101] Moreover, preparing substrates with low surface damage and low densities of extended defects, dislocations in the grown diamonds can be efficiently reduced. [110]

The substrate temperature is normally in between 500 °C to 1200 °C. [94, 97, 99] Generally, higher substrate temperature in this range increases the surface active sites, drives faster species mobility and chemical reactions, leading to a faster diamond crystal growth rate. [104] For substrate temperature below 500 °C or above 1200 °C, non-diamond deposition or no film growth is observed. [99, 101] Power density of the plasma differs depending on the CVD reactor; the growth rate and quality of diamond are usually higher for higher temperatures (high dissociation fraction for H_2). In addition, the size of the heated area, the distribution of temperature should be carefully optimised. [99, 105] The pressure in the CVD reactor is usually between 10 Torr to 300 Torr. [97, 99] Pressure in this range helps prevent dissociated atomic hydrogen recombing into H_2. [99] Lower pressure results in a low diamond growth rate and poor crystal quality. When the pressure is higher in the chamber, the growth rate can significantly improve, but the active species might react before reaching the substrate. [99]

Other factors also affect the quality of CVD growth, such as the shape of plasma, the purity of gas source, the gas flow, etc.. [104]

1.2.2.2 Impurities in CVD synthetic diamond

Dislocations and stacking faults are usually highest in {111} planes and at the interface with the substrate of CVD synthesis diamond, especially when the growth rate is fast. [93, 111] Dislocations and other extended defects in the substrate propagate into the CVD diamonds during growth. [110] The distribution of dislocations in diamonds is studied by X-ray topography. [97] The concentration of dislocations in CVD diamond is normally between $10^4\,\mathrm{cm}^{-2}$ to $10^6\,\mathrm{cm}^{-2}$, which is lower than its concentration in natural diamond and higher than that in HPHT lab-grown diamonds. [104] These will result in lower crystal quality and can be prohibitive in some high-performance applications. [112] By improving substrate preparation technology, surface damage and extended defects in the substrate are

minimised, the growth of large CVD diamond with low dislocation density has been achieved. [104, 110, 110, 113]

During CVD growth, nitrogen in source gases can be incorporated into diamond. The source can be a contaminant through unintentional leaking of air into the chamber, or as a dopant deliberately added via e.g. N_2/NH_3. [97, 104] The doping efficiencies of nitrogen depends on the morphology and nitrogen-carbon ratio in the gas phase, which varies between approximately 7.5×10^{-5} to 10^{-4}. [114] Temperature also affects nitrogen doping efficiency. [114] Unless targeting high-performance diamonds by using ultra-high purity gases and a low leak rate vacuum system, CVD grown diamonds typically contain 0.1 to a few ppm nitrogen impurities. [104, 114] The nitrogen in CVD synthetic diamond commonly exists as substitutional nitrogen, NV centre or NVH defect. [97, 104]

By adding diborane or trimethyl borane to the plasma, the electronic conductivity of diamond is dramatically increased. Depending on the boron doping concentration, diamonds can behave as a semiconductor, metal, or superconducting material (at low temperature). [101, 115] The incorporation coefficient of boron in CVD growth diamond is between 10^{-1} to 10^{-2}, and is higher in {111}-oriented film than in {100}-oriented film. [116] It is worth noting that all diamond grown in the chamber that has been used for boron doping will contain boron impurities unless chamber and gas pipelines etc. are thoroughly cleaned.

Some defects found in CVD synthetic diamonds are rare or not seen at all in natural diamond and HPHT synthetic diamonds. The silicon substrate is frequently used for polycrystalline diamond growth; silicon is also contained in the reactor's quartz walls and windows. Therefore, silicon atoms etched by the CVD plasma can be incorporated into the grown diamond as substitutional Si, and silicon-vacancy (SiV) centres. [104, 117–119] Hydrogen atoms can also be easily incorporated into the diamond lattice, forming defects such as the vacancy-hydrogen complex, the nitrogen-vacancy-hydrogen complex or the SiVH complex. [120] These hydrogen-related defects have been well-studied both theoretically and experimentally. [114, 121] The spectral characteristics of those unique defects in CVD-grown diamonds are usually used to identify the diamond as "CVD-grown". [97]

1.3 Motivation for study

Phosphorescence, or delayed luminescence is routinely observed in the majority of high-pressure high-temperature (HPHT) grown diamond that are near colourless following bandgap excitation. The phosphorescence, which typically lasts for a few milliseconds up to several hours after the excitation has been removed, is of considerable scientific and industrial interest. [122, 123] In the gem diamond trade, the combination of phosphorescence characteristics and other identification techniques are utilised to distinguish lab-grown diamonds from natural diamonds.

In previous work this phosphorescence has been explained as a temperature-dependent process by a model based on donor-acceptor pair recombination where the substitutional boron defect plays a key role as the acceptor. [122] However, the detailed mechanism of this phosphorescence in diamonds has not been well-understood to date and the following areas are required further investigation:

- The distribution of defects is growth sector dependent in HPHT synthetic diamonds, while the sector differences in phosphorescence behaviour have not been fully investigated.
- The nature of donors is not conclusively identified, and the involvement of other defects or luminescence centres needs to be investigated.
- The luminescence centre responsible for the characteristic "blue-green" phosphorescence has not been conclusively identified and the shift of the phosphorescence band with temperature and time is not explained.
- Phosphorescence observed at very low temperatures, such as liquid nitrogen temperature, cannot be explained by the thermal excitation mechanism proposed in the literature.
- It is surprising that the low concentration of defects in type II HPHT diamond is sufficient to give rise to the high intensity of phosphorescence usually observed.

In order to investigate the phosphorescence physics in type II diamond and help address the limitations of previous work as outlined above, several different experimental techniques have been employed in this thesis, including:

- Phosphorescence lifetime and spectroscopic studies at temperatures between 83 K and 473 K.
- Thermoluminescence intensity and spectroscopic measurements at temperatures between 83 K and 473 K.
- Time-resolved Electron Paramagnetic Resonance measurements on the neutral substitutional nitrogen defect following the removal of the optical excitation.
- Time-resolved Fourier Transform Infrared absorption measurements on the neutral substitutional boron acceptor at and above room temperature following the removal of the optical excitation.

plus standard spectroscopic characterisation including cathodoluminescence, photoluminescence, electron paramagnetic resonance, and optical absorption. A phosphorescence model consistent with all the findings will be proposed in this thesis, answering the outstanding questions that arose from the previously proposed models: in addition to the substitutional boron proposed in the literature [122], substitutional nitrogen defects have also been conclusively shown to play an important role in the "blue-green" phosphorescence observed in type II diamond. $N_S^0...B_S^0$ donor-acceptor pairs give rise to the "blue-green" emission and N_S^- can act as a shallow trap. $N_S^0...B_S^0$ luminescence centres can be reset multiple times by capture of electrons (from N_S^-) and holes (from B_S^0). The mechanisms of phosphorescence switch at different temperatures: tunneling process dominates at low temperatures, thermal activation dominates at high temperature, at intermediate temperatures both tunneling and thermal activation contribute.

1.4 Thesis outline

An outline of the remainder of this thesis is as follows:

- Chapter 2 introduces the theory explaining electronic and optical properties of diamond including charge transfer and various luminescence mechanisms, as well as the theoretical basis for the electron paramagnetic resonance technique utilised in this research.

- Chapter 3 provides information regarding diamond samples and experimental setups, including a self-built experimental system for time-resolved luminescence investigations, EPR, FTIR, and other experiments for characterisation of diamond samples.

- Chapter 4 analyses the change in uncompensated boron concentration after optical excitation over a range of temperatures.

- Chapter 5 employs time-resolved EPR measurement to investigate substitutional nitrogen related charge transfer over a range of temperatures and using different optical excitation energies.

- Chapter 6 explores phosphorescence behaviour using optical excitation conditions and temperatures in various diamonds, to help construct a new comprehensive understanding of luminescence and charge transfer mechanisms.

- Chapter 7 investigates thermoluminescence in various diamonds to construct an understanding of the thermal-related luminescence process.

- Chapter 8 proposes models for the observed phosphorescence and thermoluminescence in different diamonds.

Bibliography

[1] A. Butler, Karowe sets world record with 1174 carat diamond discovery (2021).

[2] A. S. Barnard, *The Diamond Formula: Diamond synthesis - a gemmological perspective* (Butterworth Heinemann, Oxford, 2000).

[3] R. M. Nor, S. A. Bakar, T. M. Thandavan, and M. Rusop, Carbon and Oxide Nanostructures , 195 (2010).

[4] M. W. Dale, *Colour centres on demand in diamond*, Ph.D. thesis, University of Warwick (2015).

[5] J. E. Field, *Properties of Natural and Synthetic Diamond* (Academic Press, London, 1992).

[6] D. G. Thomas, M. Gershenzon, and F. A. Trumbore, Physical Review **133**, A269 (1964).

[7] R. J. Narayan, R. D. Boehm, and A. V. Sumant, Materials Today **14**, 154 (2011).

[8] J. E. Field, Reports on Progress in Physics **75**, 126505 (2012).

[9] S. Reilly, V. G. Savitski, H. Liu, E. Gu, M. D. Dawson, and A. J. Kemp, Optics Letters **40**, 930 (2015).

[10] R. S. Balmer, J. R. Brandon, S. L. Clewes, H. K. Dhillon, J. M. Dodson, I. Friel, P. N. Inglis, T. D. Madgwick, M. L. Markham, T. P. Mollart, *et al.*, Journal of Physics: Condensed Matter **21**, 364221 (2009).

[11] J. V. Macpherson, Physical Chemistry Chemical Physics **17**, 2935 (2015).

[12] A. M. Edmonds, C. A. Hart, M. J. Turner, P. O. Colard, J. M. Schloss, K. Olsson, R. Trubko, M. L. Markham, A. Rathmill, B. Horne-Smith, *et al.*, arXiv:2004.01746 (2020).

[13] W. Saslow, T. K. Bergstresser, and M. L. Cohen, Physical Review Letters **16**, 354 (1966).

[14] S. Hadlington, IEE Review **51**, 30 (2005).

[15] J. Isberg, J. Hammersberg, E. Johansson, T. Wikström, D. J. Twitchen, A. J. Whitehead, S. E. Coe, and G. A. Scarsbrook, Science **297**, 1670 (2002).

[16] P. W. May, Endeavour **19**, 101 (1995).

[17] T. R. Anthony, W. F. Banholzer, J. F. Fleischer, L. Wei, P. K. Kuo, R. L. Thomas, and R. W. Pryor, Physical Review B **42**, 1104 (1990).

[18] D. J. Twitchen, C. S. J. Pickles, S. E. Coe, R. S. Sussmann, and C. E. Hall, Diamond and Related Materials **10**, 731 (2001).

[19] V. V. Brazhkin and V. L. Solozhenko, Journal of Applied Physics **125**, 130901 (2019).

[20] S. F. Wang, Y. F. Hsu, J. C. Pu, J. C. Sung, and L. G. Hwa, Materials Chemistry and Physics **85**, 432 (2004).

[21] C. M. Flannery, M. D. Whitfield, and R. B. Jackman, Semiconductor Science and Technology **18**, S86 (2003).

[22] R. Robertson, J. J. Fox, and A. E. Martin, Philosophical Transactions of the Royal Society A **232**, 463 (1933).

[23] M. N. R. Ashfold, J. P. Goss, B. L. Green, P. W. May, M. E. Newton, and C. V. Peaker, Chemical Reviews **120**, 5745 (2020).

[24] A. T. Collins, Physica B: Condensed Matter **185**, 284 (1993).

[25] G. B. B. M. Sutherland, D. E. Blackwell, and W. G. Simeral, Nature **174**, 901 (1954).

[26] G. Davies, Journal of Physics C: Solid State Physics **9**, L537 (1976).

[27] R. Jones, P. R. Briddon, and S. Öberg, Philosophical Magazine Letters **66**, 67 (1992).

[28] R. Berman and S. F. Simon, Zeitschrift für Elektrochemie, Berichte der Bunsengesellschaft für physikalische Chemie **59**, 333 (1955).

[29] V. V. Lysakovskyi, N. V. Novikov, S. A. Ivakhnenko, O. A. Zanevskyy, and T. V. Kovalenko, Journal of Superhard Materials **40**, 315 (2018).

[30] L. T. S. Soffner, A. A. A. dos Santos, D. W. Trindade, M. Filgueira, and M. G. Azevedo, Journal of Crystal Growth **550**, 125888 (2020).

[31] L. Guo, H. Ma, L. Chen, N. Chen, X. Miao, Y. Wang, Z. Wang, Z. Yang, C. Fang, and X. Jia, International Journal of Refractory Metals and Hard Materials **79**, 47 (2019).

[32] F. P. Bundy, H. T. Hall, H. M. Strong, and R. H. Wentorfjun, Nature **176**, 51 (1955).

[33] H. P. Bovenkerk, F. P. Bundy, R. M. Chrenko, P. J. Codella, H. M. Strong, and R. H. Wentorf Jr, Nature **365**, 19 (1993).

[34] U. F. S. D'Haenens-Johansson, A. Katrusha, K. S. Moe, P. Johnson, and W. Wang, Gems & Gemology **51**, 260 (2015).

[35] R. H. Wentorf Jr, The Journal of Physical Chemistry **75**, 1833 (1971).

[36] M. H. Hu, S. S. Li, H. A. Ma, T. C. Su, X. L. Li, Q. Hu, and X. P. Jia, Chinese Physics B **21**, 098101 (2012).

[37] Y. N. Palyanov, I. N. Kupriyanov, A. F. Khokhryakov, and Y. M. Borzdov, CrystEngComm **19**, 4459 (2017).

[38] H. Kanda, Brazilian Journal of Physics **30**, 482 (2000).

[39] J. W. Yang, J. H. Park, M. G. Byun, J. Park, B. D. Yu, and N. M. Hwang, Diamond and Related Materials **107**, 107875 (2020).

[40] Y. D. Li, X. P. Jia, B. M. Yan, N. Chen, C. Fang, Y. Li, and H. A. Ma, Chinese Physics B **25**, 048103 (2016).

[41] Y. A. Sorb, F. P. Bundy, and R. C. DeVries, Reference Module in Materials Science and Materials Engineering , 1 (2016).

[42] D. Choudhary and J. Bellare, Ceramics International **26**, 73 (2000).

[43] I. Sunagawa, Journal of Crystal Growth **99**, 1156 (1990).

[44] L. Chen, X. Miao, X. He, L. Guo, S. Fang, Y. Wang, Z. Wang, C. Fang, H. Ma, and X. Jia, Journal of Crystal Growth **498**, 67 (2018).

[45] A. L. D. Skury, G. S. Bobrovnitchii, and S. N. Monteiro, Diamond and Related Materials **13**, 1725 (2004).

[46] H. Sumiya and K. Tamasaku, Japanese Journal of Applied Physics **51**, 090102 (2012).

[47] H. Sumiya, N. Toda, and S. Satoh, Journal of Crystal Growth **237**, 1281 (2002).

[48] I. Sunagawa, Journal of Gemmology **24**, 485 (1995).

[49] G. F. Huang, Y. J. Zheng, Z. C. Li, Q. Gao, Z. Ma, S. M. Shi, B. G. Jiang, and H. Zhao, Chinese Physics B **25**, 088104 (2016).

[50] K. Sato and T. Katsura, Journal of Crystal Growth **223**, 189 (2001).

[51] X. Yan, H. Kanda, T. Ohsawa, S. Yamaoka, and O. Fukunaga, Journal of Materials Science **25**, 1585 (1990).

[52] Z. F. Zhang, X. P. Jia, X. B. Liu, M. H. Hu, Y. Li, B. M. Yan, and H. A. Ma, Science China Physics, Mechanics and Astronomy **55**, 781 (2012).

[53] H. Sumiya and S. Satoh, Diamond and Related Materials **5**, 1359 (1996).

[54] H. M. Strong, The Journal of Chemical Physics **39**, 2057 (1963).

[55] S. S. Sun, Z. H. Xu, W. Cui, X. P. Jia, and H. A. Ma, Chinese Physics B **26**, 098101 (2017).

[56] Z. Wang, H. Ma, S. Fang, Z. Yang, X. Miao, L. Chen, and X. Jia, Journal of Crystal Growth **531**, 125371 (2020).

[57] L. Chen, X. Miao, X. He, L. Guo, S. Fang, Y. Wang, Z. Wang, C. Fang, H. Ma, and X. Jia, Journal of Crystal Growth **498**, 67 (2018).

[58] Y. Borzdov, Y. Pal'Yanov, I. Kupriyanov, V. Gusev, A. Khokhryakov, A. Sokol, and A. Efremov, Diamond and Related Materials **11**, 1863 (2002).

[59] N. D. Zhigadlo, Journal of Crystal Growth **395**, 1 (2014).

[60] S. K. Singhal and H. Kanda, Journal of Crystal Growth **154**, 297 (1995).

[61] I. N. Kupriyanov, A. F. Khokhryakov, Y. M. Borzdov, and Y. N. Palyanov, Diamond and Related Materials **69**, 198 (2016).

[62] T. V. Kovalenko and S. A. Ivakhnenko, Journal of Superhard Materials **35**, 131 (2013).

[63] A. F. Khokhryakov, A. G. Sokol, Y. M. Borzdov, and Y. N. Palyanov, Journal of Crystal Growth **426**, 276 (2015).

[64] Y. N. Palyanov, I. N. Kupriyanov, Y. M. Borzdov, and D. V. Nechaev, Diamond and Related Materials **89**, 1 (2018).

[65] A. J. Sideris Jr, G. S. Bobrovnitchii, and A. L. D. Skury, High Pressure Research **29**, 618 (2009).

[66] Y. N. Palyanov, Y. M. Borzdov, I. N. Kupriyanov, Y. V. Bataleva, and A. F. Khohkhryakov, Diamond and Related Materials **58**, 40 (2015).

[67] Y. N. Palyanov, Y. M. Borzdov, I. N. Kupriyanov, Y. V. Bataleva, A. F. Khokhryakov, and A. G. Sokol, Crystal Growth & Design **15**, 2539 (2015).

[68] Y. N. Palyanov, I. N. Kupriyanov, Y. M. Borzdov, A. G. Sokol, and A. F. Khokhryakov, Crystal Growth and Design **9**, 2922 (2009).

[69] M. Akaishi, Diamond and Related Materials **2**, 183 (1993).

[70] D. Michau, H. Knada, and S. Yamaoka, Diamond and Related Materials **8**, 1125 (1999).

[71] L. Sun, Q. Wu, D. Dai, J. Zhang, Z. Qin, and W. Wang, Science in China Series A: Mathematics **42**, 834 (1999).

[72] Y. N. Palyanov, I. N. Kupriyanov, A. G. Sokol, A. F. Khokhryakov, and Y. M. Borzdov, Crystal Growth & Design **11**, 2599 (2011).

[73] Y. N. Palyanov, I. N. Kupriyanov, Y. M. Borzdov, and N. V. Surovtsev, Scientific Reports **5**, 1 (2015).

[74] S. S. Li, X. P. Jia, C. Y. Zang, T. Yu, Y. F. Zhang, H. Y. Xiao, G. F. Huang, L. Q. Ma, L. Yong, X. L. Li, *et al.*, Chinese Physics Letters **25**, 3801 (2008).

[75] M. M. Guo, S. S. Li, F. Lu, M. H. Hu, T. C. Su, G. J. Gao, J. Z. Wang, Y. You, and Y. Nie, New Carbon Materials **35**, 559 (2020).

[76] V. V. Lysakovskii, S. A. Ivakhnenko, and A. N. Katrusha, Journal of Superhard Materials **29**, 353 (2007).

[77] V. V. Lysakovskii, Journal of Superhard Materials **36**, 303 (2014).

[78] W. Q. Liu, H. A. Ma, X. L. Li, Z. Z. Liang, R. Li, and X. Jia, Diamond and Related Materials **16**, 1486 (2007).

[79] S. Naka, H. Itoh, and T. Tsutsui, Journal of Materials Science **22**, 1753 (1987).

[80] V. V. Lysakovskii and S. A. Ivakhnenko, Journal of Superhard Materials **31**, 7 (2009).

[81] M. M. Guo, S. S. Li, M. H. Hu, T. C. Su, J. Z. Wang, G. J. Gao, Y. You, and Y. Nie, Chinese Physics B **29**, 018101 (2020).

[82] S. S. Li, H. Zhang, T. C. Su, Q. Hu, M. H. Hu, C. S. Gong, H. A. Ma, X. P. Jia, Y. Li, and H. Y. Xiao, Chinese Physics B **26**, 068102 (2017).

[83] Y. N. Palyanov, Y. M. Borzdov, A. F. Khokhryakov, I. N. Kupriyanov, and A. G. Sokol, Crystal Growth & Design **10**, 3169 (2010).

[84] J. Q. Zhang, H. A. Ma, Y. P. Jiang, Z. Z. Liang, Y. Tian, and X. Jia, Diamond and Related Materials **16**, 283 (2007).

[85] K. Thonke, Semiconductor Science and Technology **18**, S20 (2003).

[86] A. M. Zaitsev, *Optical Properties of Diamond: A Data Handbook* (Springer Science & Business Media, New York, 2001).

[87] N. Chen, G. Zhang, R. Li, G. Xu, F. Wang, H. Ma, and X. Jia, Crystal Growth & Design **20**, 3358 (2020).

[88] P. K. Bachmann, D. Leers, and D. U. Wiechert, Journal de Physique IV **2**, C2 (1991).

[89] S. E. Coe and R. S. Sussmann, Diamond and Related Materials **9**, 1726 (2000).

[90] R. J. Nemanich, J. A. Carlisle, A. Hirata, and K. Haenen, MRS Bulletin **39**, 490 (2014).

[91] A. Gicquel, K. Hassouni, F. Silva, and J. Achard, Current Applied Physics **1**, 479 (2001).

[92] J. E. Butler and H. Windischmann, MRS Bulletin **23**, 22 (1998).

[93] P. M. Martineau, M. P. Gaukroger, K. B. Guy, S. C. Lawson, D. J. Twitchen, I. Friel, J. O. Hansen, G. C. Summerton, T. P. G. Addison, and R. Burns, Journal of Physics: Condensed Matter **21**, 364205 (2009).

[94] F. Faili, N. Palmer, S. Oh, and D. Twitchen, 2017 16th IEEE Intersociety Conference on Thermal and Thermomechanical Phenomena in Electronic Systems (ITherm) , 1 (2017).

[95] W. G. Eversole and N. Y. Kenmore, Synthesis of diamond (1962), US Patent 3030187.

[96] W. G. Eversole and N. Y. Kenmore, Synthesis of diamond (1962), US Patent 3030188.

[97] P. M. Martineau, S. C. Lawson, A. J. Taylor, S. J. Quinn, D. J. F. Evans, and M. J. Crowder, Gems & Gemology **40**, 2 (2004).

[98] J. C. Angus, H. A. Will, and W. S. Stanko, Journal of Applied Physics **39**, 2915 (1968).

[99] P. W. May, Philosophical Transactions of the Royal Society A **358**, 473 (2000).

[100] B. V. Spitsyn, L. L. Bouilov, and B. V. Derjaguin, Journal of Crystal Growth **52**, 219 (1981).

[101] J. J. Gracio, Q. H. Fan, and J. C. Madaleno, Journal of Physics D: Applied Physics **43**, 374017 (2010).

[102] S. Matsumoto, Y. Sato, M. Tsutsumi, and N. Setaka, Journal of Materials Science **17**, 3106 (1982).

[103] M. Kamo, Y. Sato, S. Matsumoto, and N. Setaka, Journal of crystal growth **62**, 642 (1983).

[104] A. Tallaire, J. Achard, F. Silva, O. Brinza, and A. Gicquel, Comptes Rendus Physique **14**, 169 (2013).

[105] M. Schwander and K. Partes, Diamond and Related Materials **20**, 1287 (2011).

[106] N. Tokuda, Novel Aspects of Diamond **121**, 1 (2019).

[107] P. May, Modelling CVD diamond growth (2021), `http://www.chm.bris.ac.uk/pt/diamond/growthmodel.htm`. Accessed September 2021.

[108] J. Achard, F. Silva, A. Tallaire, X. Bonnin, G. Lombardi, K. Hassouni, and A. Gicquel, Journal of Physics D: Applied Physics **40**, 6175 (2007).

[109] M. Schreck, S. Gsell, R. Brescia, and M. Fischer, Scientific reports **7**, 1 (2017).

[110] I. Friel, S. L. Clewes, H. K. Dhillon, N. Perkins, D. J. Twitchen, and G. A. Scarsbrook, Diamond and Related Materials **18**, 808 (2009).

[111] P. Martineau, M. Gaukroger, R. Khan, and D. Evans, Physica Status Solidi (c) **6**, 1953 (2009).

[112] P. L. Diggle, *Single point defect imaging studies in diamond*, Ph.D. thesis, University of Warwick (2019).

[113] A. Boussadi, A. Tallaire, M. Kasu, J. Barjon, and J. Achard, Diamond and Related Materials **83**, 162 (2018).

[114] A. Tallaire, A. T. Collins, D. Charles, J. Achard, R. Sussmann, A. Gicquel, M. E. Newton, A. M. Edmonds, and R. J. Cruddace, Diamond and Related Materials **15**, 1700 (2006).

[115] T. Yokoya, T. Nakamura, T. Matsushita, T. Muro, Y. Takano, M. Nagao, T. Takenouchi, H. Kawarada, and T. Oguchi, Nature **438**, 647 (2005).

[116] R. Samlenski, C. Haug, R. Brenn, C. Wild, R. Locher, and P. Koidl, Diamond and Related Materials **5**, 947 (1996).

[117] J. Barjon, E. Rzepka, F. Jomard, J. M. Laroche, D. Ballutaud, T. Kociniewski, and J. Chevallier, Physica Status Solidi (a) **202**, 2177 (2005).

[118] B. L. Green, M. W. Doherty, E. Nako, N. B. Manson, U. F. S. D'Haenens-Johansson, S. D. Williams, D. J. Twitchen, and M. E. Newton, Physical Review B **99**, 161112 (2019).

[119] B. G. Breeze, C. J. Meara, X. X. Wu, C. P. Michaels, R. Gupta, P. L. Diggle, M. W. Dale, B. L. Cann, T. Ardon, U. F. S. D'Haenens-Johansson, *et al.*, Physical Review B **101**, 184115 (2020).

[120] C. Glover, M. E. Newton, P. M. Martineau, S. Quinn, and D. J. Twitchen, Physical Review Letters **92**, 135502 (2004).

[121] T. Van Regemorter and K. Larsson, Diamond and Related Materials **17**, 1076 (2008).

[122] K. Watanabe, S. C. Lawson, J. Isoya, H. Kanda, and Y. Sato, Diamond and Related Materials **6**, 99 (1997).

[123] S. Eaton-Magaña and C. M. Breeding, Gems & Gemology **52**, 2 (2016).

Chapter 2

Theory

2.1 Electronic properties of diamond

2.1.1 Intrinsic

Intrinsic diamond is considered to be a non-degenerate semiconductor (Fermi level $\geq 3k_BT$ from either band edge) with an indirect bandgap of 5.47 eV at 300 K. [1] The electronic proprieties of diamond are determined by the band structure, phonons, and extrinsic defects for doped diamond. [2] The band structure of diamond is shown in figure 2.1.

In thermodynamic equilibrium for a semiconductor, the probability that a level at energy E is occupied $P_e(E)$ is given by the Fermi-Dirac distribution $f_e(E)$ (figure 2.2):

$$P_e(E) = f_e(E) = \frac{1}{\exp\left(\frac{E-E_F}{k_BT}\right)+1}, \tag{2.1}$$

where E_F is the Fermi level, k_B is the Boltzmann constant, T is the temperature in Kelvin.

If $(E - E_F) \gg k_BT$,

$$P_e(E) \approx \exp\left(\frac{E_F - E}{k_BT}\right), \tag{2.2}$$

the system is said to be **non-degenerate**. The density of states in the conduction

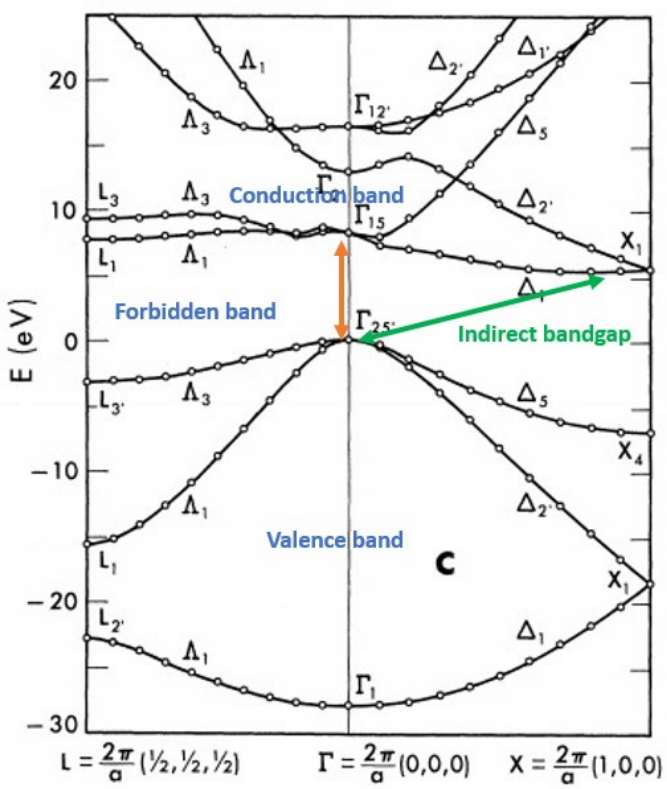

Figure 2.1: The electronic band structure of diamond. The conduction and valence band, forbidden band, and indirect bandgap are labelled. The top of the valence band is not directly below the bottom of the conduction band; their wave-vectors are different. [3]

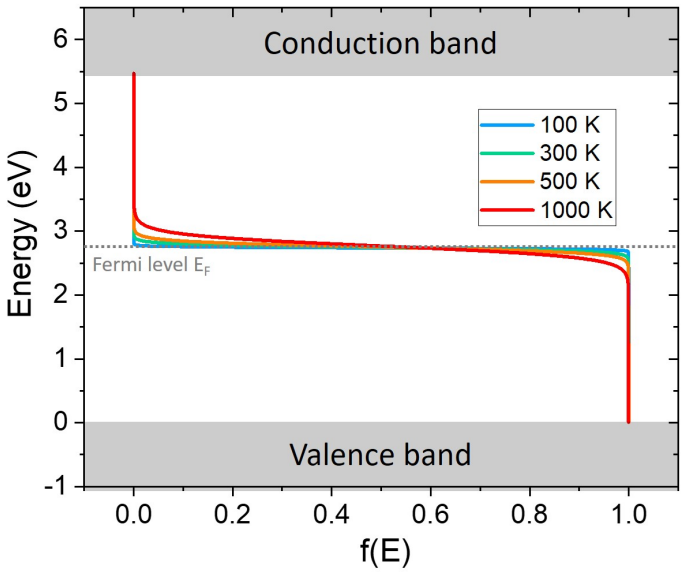

Figure 2.2: Fermi-Dirac distribution at different temperatures 100 K, 300 K, 500 K, 1000 K.

band can be approximated by

$$D_C(E) = \frac{1}{2\pi^2} \left(\frac{2m_e}{\hbar^2}\right)^{(3/2)} \sqrt{E - E_g}, \tag{2.3}$$

where m_e is the electron effective mass, $\hbar$ is the reduced Planck's constant ($\frac{h}{2\pi}$), E_g is the bandgap energy. The number of electrons in the conduction band is

$$n = \int_{E_g}^{\infty} D_C(E)\, P_e(E)\, \mathrm{d}E, \tag{2.4}$$

$$n = N_C \exp\left(\frac{E_F - E_g}{k_B T}\right), \tag{2.5}$$

where N_C is the effective density of states in the conduction band and equals to $2(\frac{2\pi m_e k_B T}{\hbar^2})^{(3/2)}$.

The distribution for holes is $f_h = 1 - f_e$. Thus

$$P_h(E) = f_h(E) = \frac{1}{\exp\left(\frac{E_F - E}{k_B T}\right) + 1}. \tag{2.6}$$

The density of hole states in the valence band is approximated by

$$D_V(E) = \frac{1}{2\pi^2} \left(\frac{2m_h}{\hbar^2}\right)^{(3/2)} \sqrt{-E}, \tag{2.7}$$

where m_h is the hole effective mass. The density of holes in the valence band is

$$p = \int_{-\infty}^{0} D_V(E)\, P_h(E)\, \mathrm{d}E, \tag{2.8}$$

$$p = N_V \exp\left(\frac{-E_F}{k_B T}\right), \tag{2.9}$$

where N_V is the effective density of states in the valence band and equals to $2(\frac{2\pi m_h k_B T}{\hbar^2})^{(3/2)}$. Hence the product of the electron and hole density is

$$np = 4 \left(\frac{2\pi k_B T}{\hbar^2}\right)^3 (m_e m_h)^{(3/2)} \exp\left(-\frac{E_g}{k_B T}\right), \tag{2.10}$$

with the assumption that the distance of Fermi energy from the edge of the conduction band, or the edge of the valence band, must be large compared to $k_B T$.

The **law of mass action** holds for extrinsic and intrinsic semiconductors. Namely the concentrations of free electrons and holes under thermal equilibrium are equal, meaning equations 2.5 and 2.9 are equal. For an intrinsic semiconductor which is ideally pure,

$$n_i = p_i = \sqrt{N_C N_V}\, \exp\left(\frac{-E_g}{2k_B T}\right), \tag{2.11}$$

where n_i and p_i is the electron concentration and the hole concentration in the intrinsic semiconductor, respectively. The intrinsic carrier concentration is exponentially dependent on the bandgap. The intrinsic Fermi energy of diamond E_i is close to halfway between the conduction band and valence band edge and can be expressed by [4]

$$E_i = \frac{E_g}{2} + \frac{3}{4} k_B T\, \ln\left(\frac{m_h}{m_e}\right) \tag{2.12}$$

and

$$E_i = \frac{E_g}{2} + \frac{1}{2} k_B T \left(\frac{N_V}{N_C}\right). \tag{2.13}$$

In terms of electronic properties, diamond is an excellent material having high electron and hole mobilities, which the Hall effect technique can measure. [1, 2, 5] The electron and hole mobilities in intrinsic high purity diamond produced by CVD at RT are as high as 4500 $\mathrm{cm^2\,V^{-1}\,s^{-1}}$ and 3800 $\mathrm{cm^2\,V^{-1}\,s^{-1}}$. [6] Ultimately the carrier mobilities are limited by thermal phonon scattering; therefore, the larger mobilities are reached at low temperatures. Impurities can dramatically reduce electron and hole mobilities.

2.1.2 Extrinsic

Defects incorporated in diamond lattice during growth leads to the change of electronic properties of the diamond by varying the carrier density. If electrons in the conduction band (CB) or holes in the valence band (VB) are non-degenerate, that is the Fermi-level $\geq 2k_B T$ below CB or $\geq 2k_B T$ above VB, equation 2.5 and equation 2.9 still hold. But the Fermi level E_F is no longer given by equation 2.13.

Atomic impurities (point defects) in diamonds whose valence electron are easily ionised and thus donate electrons to the conduction band are called donors, making diamond a **n-type** semiconductor. Likewise, those with unfilled energy levels

which are easily ionised and give rise to holes in the valence band, which are called acceptors, making diamond a **p-type** semiconductor.

2.1.2.1 Donor or acceptor doping

Note that even when donor and acceptor ionization energies are comparable to k_BT, all are ionized because of the effective density of states in the CB and VB, N_C and N_V, are very much larger than impurity concentrations. The usual approach considers either a donor or an acceptor and assumes that these are ionised at a temperature of interest.

For **n-type**,

$$n - p = {N_D}^+ = N_D, \tag{2.14}$$

where N_D is the concentration of neutral donors, ${N_D}^+$ is the concentration of ionized donors. The law of mass action is applied under thermal equilibrium $np = {n_i}^2$, hence

$$n^2 - N_D n - {n_i}^2 = 0 \tag{2.15}$$

$$n = \frac{N_D}{2}\left[1 + \sqrt{1 + \frac{4{n_i}^2}{{N_D}^2}}\right]. \tag{2.16}$$

If $N_C > N_D \gg n_i$,

$$n \simeq N_D + \frac{{n_i}^2}{N_D}, \tag{2.17}$$

$$p \simeq \frac{{n_i}^2}{N_D}; \tag{2.18}$$

if very light doping $N_D \ll n_i$,

$$n \simeq n_i + \frac{1}{2}N_D, \tag{2.19}$$

$$p \simeq n_i - \frac{1}{2}N_D. \tag{2.20}$$

For **p-type**,

$$n - p = {N_A}^- = N_A, \tag{2.21}$$

where N_A is the concentration of neutral acceptors, ${N_A}^-$ is the concentration of ionized acceptors. The law of mass action is applied under thermal equilibrium

$np = {n_i}^2$, hence

$$p^2 - N_A p - {n_i}^2 = 0 \tag{2.22}$$

$$p = \frac{N_A}{2}\left[1 + \sqrt{1 + \frac{4{n_i}^2}{{N_A}^2}}\right]. \tag{2.23}$$

If $N_V > N_A \gg n_i$,

$$n \simeq \frac{{n_i}^2}{N_A}, \tag{2.24}$$

$$p \simeq N_A + \frac{{n_i}^2}{N_A}; \tag{2.25}$$

if very light doping $N_A \ll n_i$,

$$n \simeq n_i - \frac{1}{2}N_A, \tag{2.26}$$

$$p \simeq n_i + \frac{1}{2}N_A. \tag{2.27}$$

2.1.2.2 Donor and acceptor co-doping

A. Complete ionization

Considering the case when both donors and acceptors are present and at least one thermally ionized. Suppose $(N_D - N_A) \gg n_i$. When $N_A = 0$, the Fermi-level will be pinned close to donor level if donor energy $E_D \gg k_B T$. (See Figure 2.3)

If the donor is shallow such that ${N_D}^+ \simeq N_D$ then

$$n = N_D = N_C \exp\left(\frac{E_F - E_g}{k_B T}\right), \tag{2.28}$$

and

$$E_F = E_g + k_B T \ln\left(\frac{N_D}{N_C}\right), \tag{2.29}$$

In either case, the Fermi-level will be close to the middle of the gap. As acceptors are added, they will have a high probability of being ionized as they are well below the Fermi level. Electrons filling acceptors will have dropped from donors or the conduction band. The number of free holes p will be very small since the

Fermi-level is still high. The number of effective donors $(N_D - N_A)$ is

$$n = N_D - N_A = N_C \exp\left(\frac{E_F - E_g}{k_B T}\right), \tag{2.30}$$

as N_A approaches N_D, acceptors will neutralize donors, and the Fermi-level will move towards the intrinsic position as shown in figure 2.3. When $N_A > N_D$, we have $N_A - N_D$ effective acceptors, all the electrons from the donors filling acceptors and the Fermi-level will move towards the valence band.

$$p = N_A - N_D = N_V \exp\left(\frac{-E_g}{k_B T}\right), \tag{2.31}$$

$$E_F = k_B T \ln\left(\frac{N_V}{N_A - N_D}\right), \tag{2.32}$$

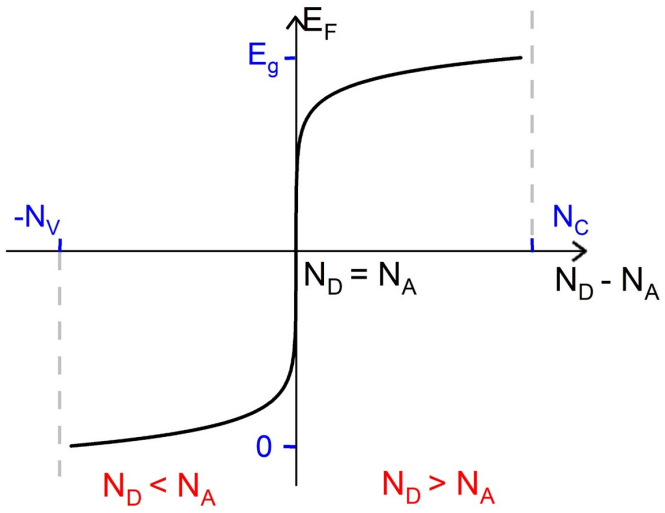

Figure 2.3: A schematic of how the Fermi level varies with the difference between the donor concentration N_D and the acceptor concentration N_A.

B. Incomplete ionization

If donor and acceptors are not fully ionized $(E_A, E_D \gg k_B T)$, due to the condition for electrical neutrality, we always have

$$n + {N_A}^- = p + {N_D}^+. \tag{2.33}$$

[7, 8] The concentration of ionized donors is

$$N_D{}^+ = \frac{N_D}{1 + 2\exp\left[\frac{E_F - (E_g - E_D)}{k_B T}\right]}, \tag{2.34}$$

$N_D{}^0$ can be occupied by spin up and spin down; when ionized no electrons (assuming only one electron can be bound at each donor). [9] The concentration of ionized acceptors is

$$N_A{}^- = \frac{N_A}{1 + 2\exp\left(\frac{E_A - E_F}{k_B T}\right)} \tag{2.35}$$

Therefore, it is possible to use the four expression equations 2.5, 2.9, 2.34 and 2.35 into the condition for charge neutrality and with the law of mass action $np = {n_i}^2$ to determine E_F, n and p.

C. An example for a diamond containing N_S and B_S

Isolated single substitutional nitrogen ($N_S{}^0$) is a deep-donor with ionization energy of 1.7 eV. [10] Boron is the most common shallow acceptor in diamond with an activation energy of 0.37 eV. [2] Donors and acceptors can be co-doped into diamond, in which case, the carrier densities are determined by the relative concentration of donors and acceptors and the density of states in CB (N_C) and VB (N_V). Shallow donors and acceptors, or donors and acceptors that are physically close in the lattice, compensate each other without generating free carriers. An example of how the concentration of intrinsic carriers and the concentration of free carriers for different circumstances varies with temperature is shown in figure 2.4. When the donor or acceptor dominates, the other is considered to be fully ionized. When $N_A > N_D$, the Fermi-level is in the lower half of the bandgap, hence n can be ignored, equation 2.33 can be written as

$$p \simeq N_A{}^- - N_D. \tag{2.36}$$

Substituting equation 2.35 and equation 2.9, we then set

$$N_V{}' = \frac{N_V}{2}\exp\left(-\frac{E_A}{k_B T}\right). \tag{2.37}$$

Hence

$$p = -\frac{1}{2}\left[-(N_V{}' + N_D) + \sqrt{(N_V{}' + N_D)^2 + 4N_V{}'(N_A - N_D)}\right], \tag{2.38}$$

which can be rewritten as Equation 1 in the Collins's paper [11]

$$\frac{p\,(N_D + p)}{N_A - N_D - p} = N_V{}' = \left(\frac{2\pi m_e k_B T}{\hbar^2}\right)^{(3/2)} \exp\left(-\frac{E_A}{k_B T}\right). \tag{2.39}$$

For $\lim_{p\to 0}$,

$$p \simeq \frac{N_V(N_A - N_D)}{2N_D} \exp\left(-\frac{E_A}{k_B T}\right), \tag{2.40}$$

$$E_F = E_A - k_B T \ln\left(\frac{N_A - N_D}{2N_D}\right); \tag{2.41}$$

for $N_A \gg N_V{}' \gg N_D$,

$$p \simeq \frac{1}{\sqrt{2}} (N_V N_A)^{(1/2)} \exp\left(-\frac{E_A}{2k_B T}\right), \tag{2.42}$$

$$E_F = \frac{E_A}{2} - k_B T \ln\left(\frac{N_A}{N_V}\right). \tag{2.43}$$

When $N_D > N_A$, follows similar calculation:

$$n = -\frac{1}{2}\left[-(N_C{}' + N_A) + \sqrt{(N_C{}' + N_A)^2 + 4N_C{}'(N_D - N_A)}\right], \tag{2.44}$$

for $\lim_{n\to 0}$,

$$E_F = (E_g - E_D) - k_B T \ln\left(\frac{N_D - N_A}{2N_A}\right). \tag{2.45}$$

Consider a diamond containing only substitution nitrogen and boron. Substitutional nitrogen is hardly ionised at room temperature due to the large activation energy compared to the thermal energy $k_B T$. Hence when calculating the position of the Fermi level, the equation 2.41 and equation 2.45 for the carrier freeze-out region should be applied [12]. The position of the Fermi level as a function of nitrogen donor concentration for a diamond containing a certain concentration of boron acceptor was discussed by Collins. [12] The impurity distribution functions and equation 2.33 should be applied to generate a more general solution of the Fermi energy level calculation, which is described in the literature. [8] An example

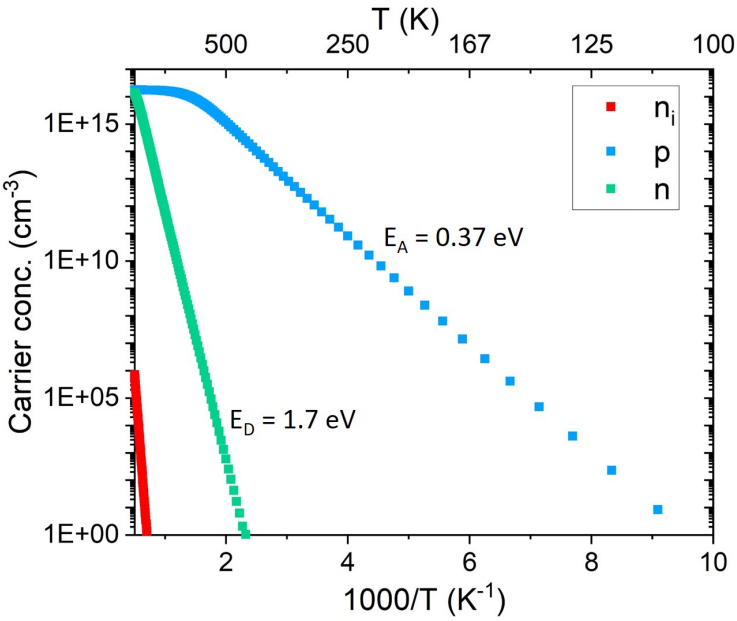

Figure 2.4: The carriers concentration versus 1000/T. n_i is the concentration of intrinsic charge carriers calculated by equation 2.11. p is the concentration of free holes in diamond calculated by equation 2.38 when [B_S]= 500 ppb, [N_S] = 400 ppb ($N_A > N_D$). n is the concentration of free electrons in diamond 2.44 when [B_S]= 100 ppb, [N_S] = 400 ppb ($N_D \gg N_A$).

is provided as shown in figure 2.5. When the nitrogen concentration is less than boron concentration, the Fermi energy level is close to the boron acceptor level and rises significantly as the temperature increases. When the nitrogen concentration is greater than boron concentration, the Fermi energy level is close to the nitrogen donor level and varies slightly with temperature.

2.2 Intrinsic optical properties of diamond

2.2.1 Refractive index

The refractive index n describes the speed of light passing through a material. For light incident at normal to air to material interface, the reflectance R_{refl} and transmittance T_{tran} can be given by

$$R_{refl} = \left(\frac{n-1}{n+1}\right)^2 \tag{2.46}$$

$$T_{tran} = \frac{4n}{(n+1)^2}. \tag{2.47}$$

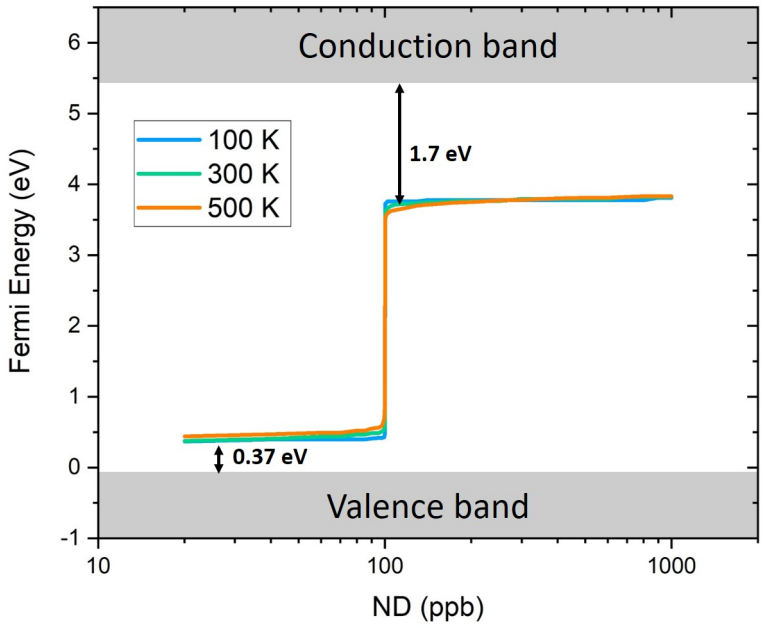

Figure 2.5: Position of the Fermi level as a function of nitrogen donor concentration for a diamond containing 100 ppb boron acceptors in a range of temperature from 100 K to 1000 K, calculated using the methods introduced in [8].

The temperature dependence of the refractive index is described as

$$n(T) = n_0 + K\left[n_{BE}(\hbar\Omega_{eff}, T) + \frac{1}{2}\right] \tag{2.48}$$

where $n_{BE}(\hbar\Omega_{eff}, T)$ is the Bose-Einstein factor for an effective phonon frequency, and K is 0.019 $\pm$ 0.007. [13] The temperature dependence of refractive index measured on various type IIa diamond is summarised in the literature and shown in figure 2.6, which corresponds to equation 2.48. The refractive index is constant below 200 K and climbs linearly above 600 K.

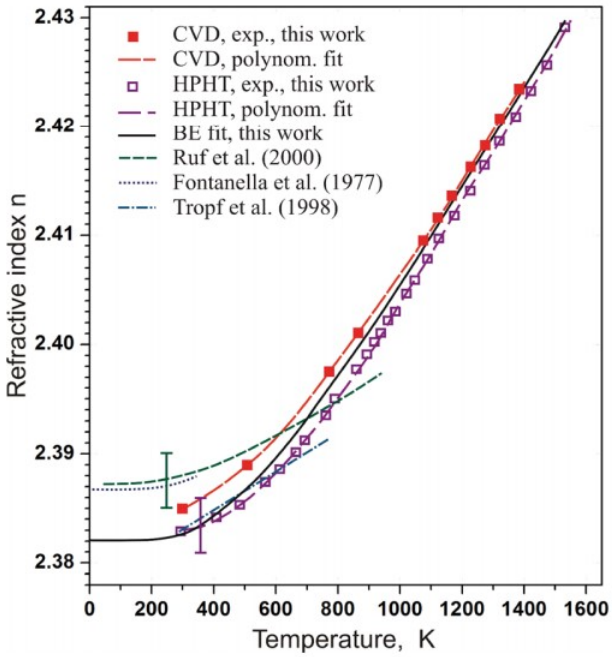

Figure 2.6: The temperature dependence of refractive index $n(T)$ for a diamond at different wavelengths. Adapted from [14]

The refractive index is wavelength-dependent. [13] As shown in figure 2.7, the value of the refractive index drops from approximately 2.7 to 2.4 when the light varying from UV to infra-red region.

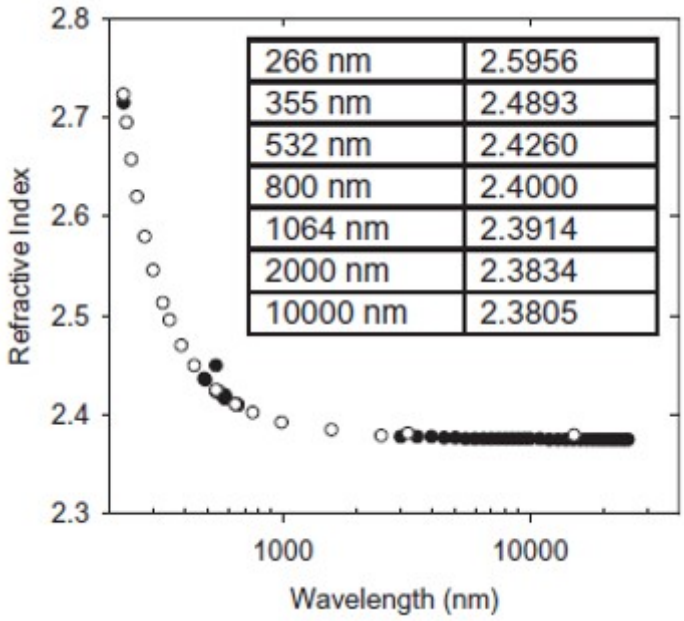

Figure 2.7: The refractive index is a function of the wavelength of the incident light. (hollow - [15], filled - [16]) Adapted from [13]

Hence considering equation 2.51, the absorption of incident light in diamond

depends on both the wavelength and temperature. The UV light can only propagate into a thin layer of diamond, while the electrons and holes created by the UV excitation can transport for long distances inside the crystal. For example, the absorption coefficient at 5.535 eV (224 nm) varies from approximately 50 cm^{-1} at 100 K to much more than 200 cm^{-1} at 350 K (and higher at higher temperatures), corresponding to 10 % intensity penetration depths of 0.46 mm to less than 0.11 mm, depending on the sample temperature. [17]

2.2.2 Absorption coefficient

The incident light of a specific frequency can be absorbed by the medium during propagation. The absorption in a semiconductor can be classified as intrinsic depending on the fundamental band gap and vibrational properties of the material and extrinsic absorption, which is induced by impurities and defects. [18, 19]

The absorption coefficient $\alpha(\omega)$ is defined as the fraction of an electromagnetic wave of angular frequency ω absorbed in a unit length in a specific direction of the medium. The optical attenuation of material follows the Beer-Lambert Law, which is expressed as

$$I(z,\omega) = I_{(0,\omega)}\, e^{-\alpha(\omega)z} \tag{2.49}$$

where $I(z,\omega)$ is the light intensity at position z, $I_{(0,\omega)}$ is the initial intensity. The absorbance A at a frequency ω, which is also known as optical density, is defined by the thickness l and absorption coefficient as [18]:

$$A(\omega) = -\log_{10}\left(\frac{I(l,\omega)}{I_{(0,\omega)}}\right) = \frac{\alpha(\omega)\, l}{\log_e(10)} = 0.434\,\alpha(\omega)\, l. \tag{2.50}$$

The transmission through a parallel-sided plate of material thickness l refractive index n at normal incidence, can be calculated by

$$T(\omega) = \frac{[1-R(\omega)]^2\, \exp[-\alpha(\omega)l]}{1-R(\omega)^2\, \exp[-2\alpha(\omega)l]} \tag{2.51}$$

where R is reflectivity, equals to $(n-1)^2/(n+1)^2$ varying with wavelength. [20] In terms of 100 μm thick intrinsic diamond at room temperature, the transmission of infra-red and UV light ($>$ 230 nm) is above 60 %, and for visible light (400 nm -

700 nm), it reaches approximately 71 %. [20]

2.2.3 Lattice absorption

Interband electronic absorption occurs when the energy of optical excitation is greater than the bandgap of material ($\hbar\omega > E_g$), leading to electronic transitions between the valence band and conduction band and the creation of electron-hole pairs. The intrinsic band structure determines the fundamental absorption band edge of semiconductors. [18]

The transition from the valence band to the conduction band can be achieved by: either absorbing an optical photon with enough energy to cross the indirect bandgap and creating or destroying a phonon to conserve momentum; or absorbing an optical photon with sufficient energy to cross the bigger direct bandgap E_D. (Figure 2.8) Therefore, the transition probability of such a second-order process is lower than that of direct bandgap semiconductors. [18, 21]

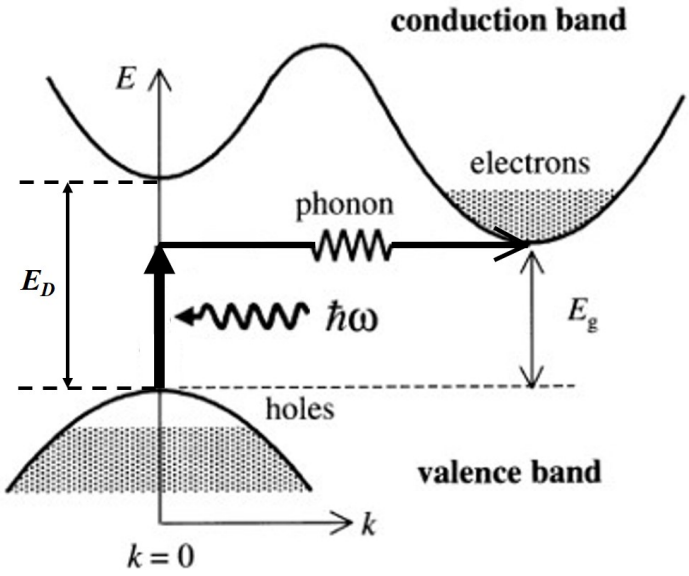

Figure 2.8: Schematic of electronic band of diamond explaining the absorption mechanism. E_D is the direct bandgap (E_D = 7.3 eV) and indirect bandgap (E_g = 5.47 eV at RT). [13, 18]

The conservation of energy for indirect transition can be described as

$$E_f = E_i + \hbar\omega \pm \hbar\Omega \tag{2.52}$$

where E_f is the final state of an electron in the conduction band, E_i is the initial state in the valence band, $\hbar\omega$ is absorbed photon energy, and $\hbar\Omega$ is the energy of absorbed or emitted phonon.

The absorption spectrum of the intrinsic diamond (Figure 2.9) is a result of the vibrational properties of the diamond lattice. The intrinsic diamond (pure type IIa diamond), with a large indirect bandgap of 5.49 eV (225.8 nm) at 77 K, is transparent in the one-phonon region due to the symmetry of the homonuclear tetrahedrally-bonded lattice. The maximum frequency of a single phonon propagating through the diamond lattice is 1331.7 ± 0.2 cm^{-1} (approximately 165 meV), which is achieved at the Brillouin zone centre, also known as the Raman frequency of diamond. [19, 20, 22] Diamond also exhibits intrinsic absorption between approximately 1500 to 4000 cm^{-1} (186 to 496 meV) due to multi-photon interactions and will be shown in the next section. [19, 20]

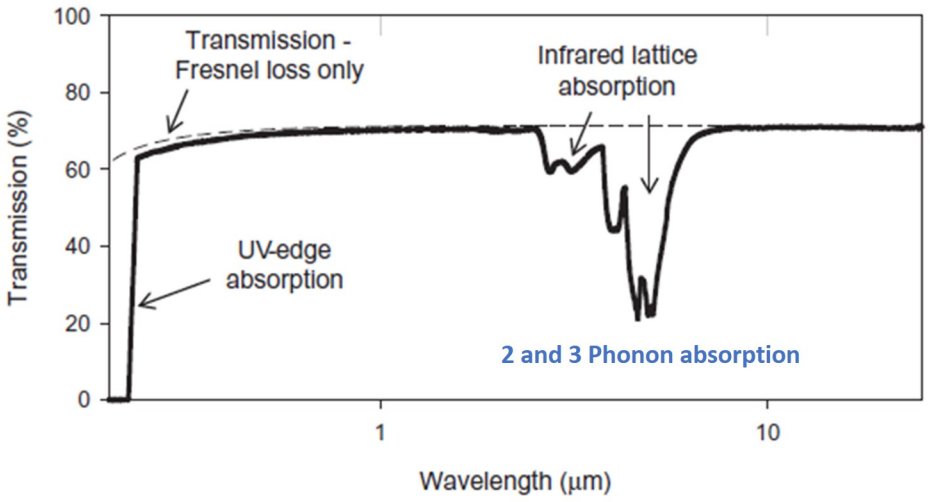

Figure 2.9: The transmission spectrum for a type IIa diamond of 1 mm thickness. Adapted from [13]

The thermal population of phonons and phonon mode frequency are temperature dependent. Hence the diamond absorption spectrum alters with temperature (Figure 2.10). The intrinsic infrared absorption increases as the temperature is increased due to the increased phonon excitation. [13]

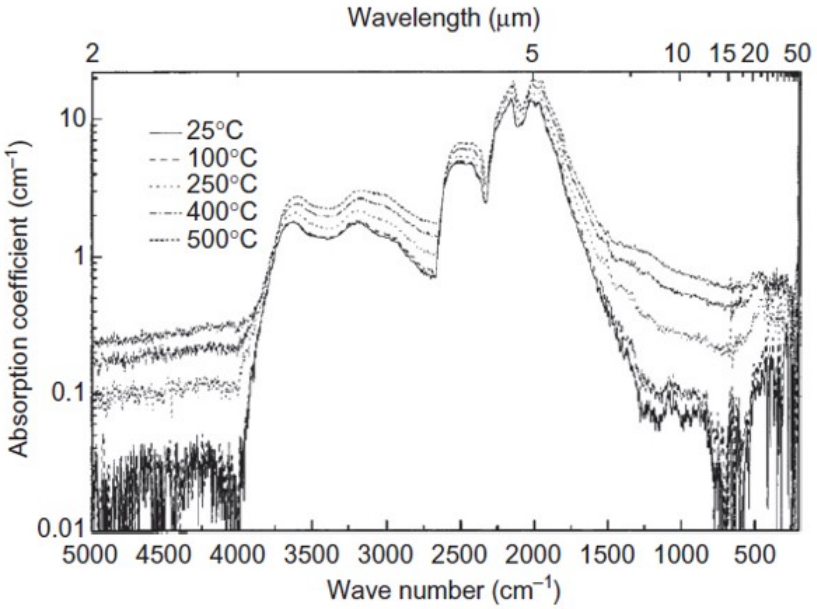

Figure 2.10: Temperature dependence of intrinsic diamond absorption. Adapted from [13]

2.2.4 UV absorption edge

The threshold of absorption is approximately but not equal to E_g for indirect bandgap semiconductors. The phonon absorption is temperature-dependent, and the Bose-Einstein formula gives the probability of a phonon state of energy E been occupied [18]:

$$f_{BE}(E) = \frac{1}{\exp\left(\frac{E}{k_B T}\right) - 1}. \tag{2.53}$$

As shown in figure 2.11, the UV absorption edge changes with temperature. At low temperatures, the absorption edge is only determined by the transverse acoustic (TA) phonon emission rather than any phonon absorption. [18]

At room temperature, three thresholds of the UV edge absorption can be seen. [13, 20, 23] Firstly, the absorption occurs at 236 nm, which corresponds to the excitation of an electron from the top of the valence band to the excitonic state just below the conduction band, assisted by the highest energy phonon; secondly, the thresholds at 235.5 nm and 233.5 nm, are related to the contributions from the low-energy TO (transverse optical) and TA (transverse acoustic) phonon modes, respectively; thirdly, thresholds at 226 nm and 224 nm, when the photon exceeds the thresholds for TA and TO phonon emission.

At higher temperatures, the absorption increases for the wavelength longer than 236 nm due to the increased density of thermal phonons and reduction in phonon energy due to lattice expansion. [13]

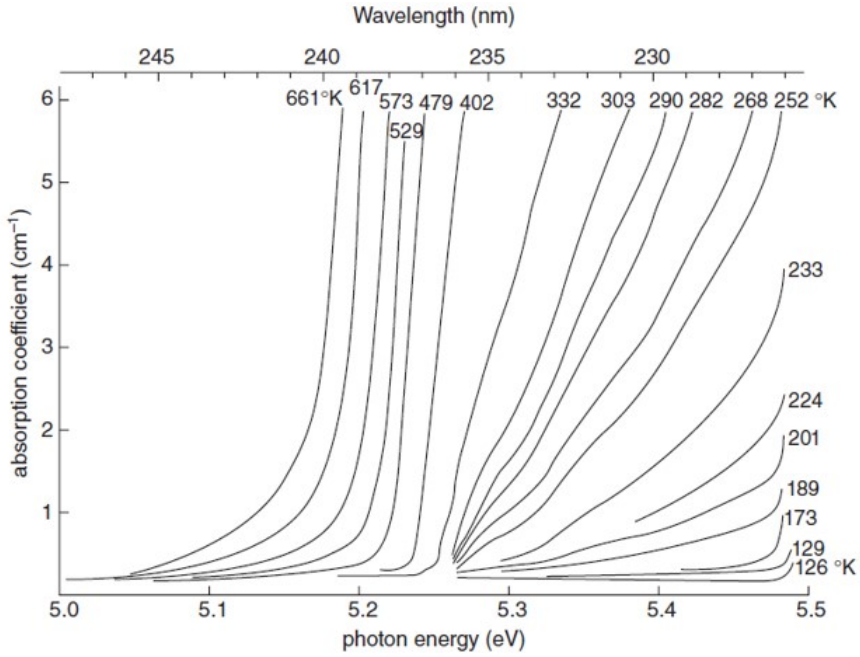

Figure 2.11: UV absorption edge as a function of temperature. Adapted from [13]

2.2.5 Two-photon absorption

The transitions between different energy states achieved by absorbing one photon are described by Beer-Lambert law (equation 2.49) above. There are also probabilities that two or more lower energy photons of equal or different energies are absorbed simultaneously and enable excitation from the ground state to an excited state. The probability of two-photon absorption is proportional to the square root of the incident light intensity. The two-photon absorption, therefore, is a non-linear optical process. The light intensity decay in the diamond crystal for two-photon absorption is given by

$$I(x) = \frac{I_0}{1 + \beta x I_0} \tag{2.54}$$

where $I(x)$ is the light intensity at the path length of x, β is the absorption coefficient for two-photon absorption (2PA), I_0 is the initial intensity of incident light. The investigation on two photon-absorption and three-photon absorption in diamonds and the corresponding absorption coefficients calculation were reported

[21].

In terms of the cross bandgap transitions in diamond, it can be a phonon-assisted one-photon absorption with photon energy exceeding the diamond indirect bandgap ($E_g = 5.47$ eV), a two-photon absorption with photon energies smaller than E_g and greater than half of E_D, or a three-photon absorption with smaller photon energies and lower probability [21].

2.2.6 Exciton

When an electron in the conduction band and a hole in the valence band are created at the same point in space by absorbing photons or electrons, they attract each other due to the Coulomb interaction and form a bound electron-hole pair, called an exciton. There are two types of excitons (Figure 2.12): the free excitons have a large radius that encompasses many atoms, and they are delocalized states that can move freely throughout the crystal; the tightly bound excitons are bounded to shallow acceptor/donor states in the bandgap, which may also give rise to radiative recombination with the assistance of phonons with a relatively low probability.

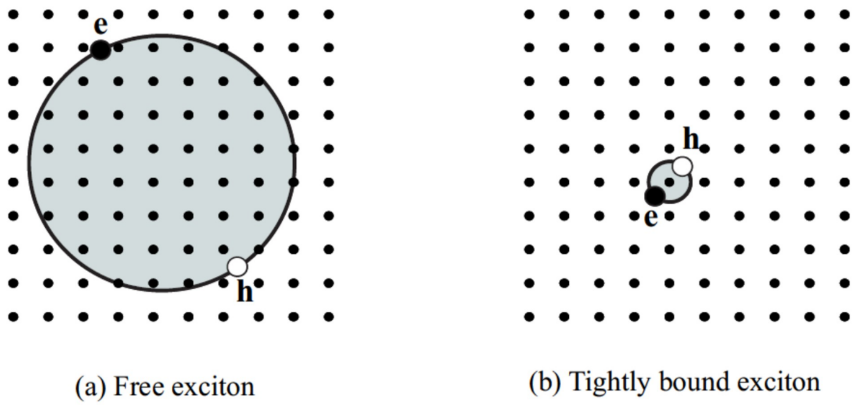

Figure 2.12: Schematic of (a) a free exciton (Wannier-Mott exciton) (b) a tightly bound exciton (Frenkel exciton). Adapted from [18]

In intrinsic diamond, the luminescence from free exciton (FE) recombination assisted with a transverse optical (TO) phonon occurs in the ultraviolet range and produces luminescence line with maxima at 235.2 nm (5.272 eV), luminescence lines are also observed with other phonon modes TA(transverse acoustic), LO (longitudinal optical), LA (longitudinal acoustic) with less intensity. [24, 25]

2.3 Extrinsic optical properties of diamond

2.3.1 Trap and recombination centre

In semiconductor and insulator materials like diamond, energy levels localized in the bandgap are categorized as traps or recombination centres. Shallow levels are traps for which the capture cross-section of one type of carrier is larger than that of the opposite type. Recombination centres are located close to the middle of the bandgap and have a large capture cross-section for both electrons and holes. [26, 27]

The probability of thermal excitation of trapped electrons (or holes) is given by

$$P_t = s \exp(-E/k_B T) \tag{2.55}$$

where s is constant, E is the depth of energy level. The probability of trapping or recombination is

$$P_r = n_r A_r \tag{2.56}$$

where n_r is the densities of trapped charge, and A_r is the recombination transition coefficient. [27]

2.3.1.1 Recombination process

As shown in figure 2.13, recombination processes include direct recombination (band-to-band transition), which must be radiative, as well as indirection recombination (band-to-centre or centre-to-centre transition), which can be radiative or non-radiative. [27] Excitation of direct transitions with quantum energy greater or equal to the energy gap can easily be self-absorbed. [28] For a diamond with various defects, multiple types of electronic transitions may occur after excitation. The relative probability of radiative transitions and non-radiative transitions determines whether the system is luminescent or not.[27] Generally, indirect recombination dominates because the probability of direct recombination is small. [26]

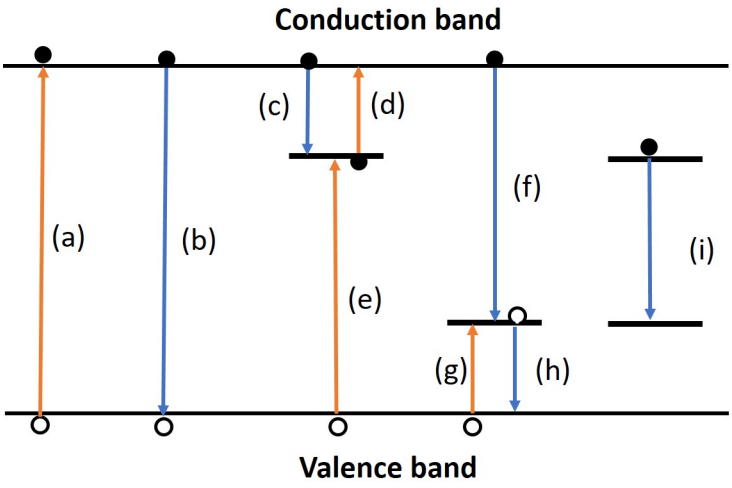

Figure 2.13: Common electronic transitions in semiconductors:(a) band gap absorption (b) direct recombination; (c) and (g) electron and hole trapping respectively; (d) and (h) electron and hole release; (e) and (f) indirect recombination;(i) centre to centre recombination. Electrons, solid circles; holes, open circles. [27]

The lifetime τ_r of a free carrier for direct recombination is given by

$$\tau_r = \frac{n_i}{2R} \tag{2.57}$$

where n_i is the intrinsic free carrier density, and R is the temperature-dependent rate of direct recombination.[27] When both radiative and non-radiative recombination exists, the observable lifetime is

$$\tau = \frac{\tau_{rr}\tau_{nr}}{\tau_{rr} + \tau_{nr}} \tag{2.58}$$

where τ_{rr} and τ_{nr} are the radiative and non-radiative recombination lifetimes respectively.[26, 29] The luminescence efficiency η of a phosphor has strong temperature dependency and is defined as

$$\eta = \frac{R_{rr}}{R} = \frac{P_{rr}}{P_{rr} + P_{nr}} \tag{2.59}$$

where R is the total recombination rate. P_{rr} and P_{nr} are the radiative and non-radiative transitions probabilities respectively. For indirect bandgap semiconductors, diamond, for example, the band-band luminescence efficiency is relatively small comparing to direct bandgap materials, because phonon emission or absorp-

tion must be involved, which leads to smaller transition probabilities and longer radiative lifetime. [18, 29] P_{rr} is temperature independent, whereas P_{nr} is affected by temperature and proportional to a Boltzmann factor, hence η can be written as

$$\eta = \frac{1}{1 + c\ \exp(-\Delta E/k_B T)} \tag{2.60}$$

where c is a constant.[26, 27]

2.3.1.2 Shallow donor-acceptor pair recombination

Donor-acceptor pair (DAP) recombination can lead to luminescence by recombining an electron captured by a donor and a hole captured by an acceptor. The energy of the DAP recombination transition is given by

$$\hbar\omega = E_g - (E_D + E_A) + \Delta E_C \tag{2.61}$$

where E_g, E_D, E_A and ΔE_C are the energy gap, the binding energy of donor and acceptor, and the correction term for the electronic static potential energy of the Coulomb interaction between donor and acceptor, respectively. ΔE_C for an isolated pair consisting of one donor and one acceptor is given by

$$\Delta E_C = \frac{e^2}{4\pi\epsilon_0\epsilon_r r} \tag{2.62}$$

Where ϵ_0 and ϵ_r are the electric constant and the relative static permittivity, respectively. r is the distance between donor and acceptor. [26, 30, 31]

The distribution of the distances between the donor and acceptor r is discrete, which can give rise to the sharp lines on spectra. [32] In fact, the broadband from DAP recombination is normally seen instead. This is because of different broad mechanisms, such as Coulomb interaction between close-pair and near neighbour charged impurities, phonon coupling, and strain [32, 33].

To understand the line shape of DAP recombination transitions in more detail, the standard DAP model developed by Thomas *et al.* [31, 32, 34, 35] is introduced

as follows. The intensity of DAP recombination transitions is given by

$$I_k(r)\mathrm{d}r \propto N_r\, G(r)\mathrm{d}r\, W(r)\, f_e(r)\, \sigma_k \tag{2.63}$$

Where $I_k(r)$ represents the lineshape of the DAP recombination transitions. N_r is the number of DAPs. $G(r)\mathrm{d}r$ is the DAP pair distribution function. $W(r)$ is the recombination probability of a donor-acceptor pair at a separation r. $f_e(r)$ is the occupation probability of the DAP levels. σ_k is the probability for the creation of k phonons.

A. The number of DAPs with a certain separation - N_r

The number of equivalent sites for donor-acceptor pairs with different separations in diamond lattice is calculated on the assumption that the donor and acceptor are substitutional impurities as shown in figure 2.14 (a). The distances r between atoms is given by

neighbour on sub-lattice I

$$r = (\frac{m}{2})^{1/2}\, a_0 \tag{2.64}$$

neighbour on sub-lattice II

$$r = (\frac{m}{2} - \frac{5}{16})^{1/2}\, a_0 \tag{2.65}$$

where m is the shell number, and a_0 is the lattice constant of a diamond. For type II geometry, the shell number m is a continuous integer m = 1,2,3.... However, there are no atoms for shells with m equal to 14, 30, 46, 56, 62... for type I geometry. [32, 34] The diamond shell number and distances between carbon atoms are listed in Appendix A. The spectral lines shift in energy by the Coulomb interaction between donor and acceptor is given by equation 2.62. As shown in figure 2.14 (b), the DAP recombination results in a set of resolved lines on the spectrum when the donor-acceptor separation r is small compared to the diamond lattice constant. As the separation r increases, the spectral lines gradually merge into broadband. [32]

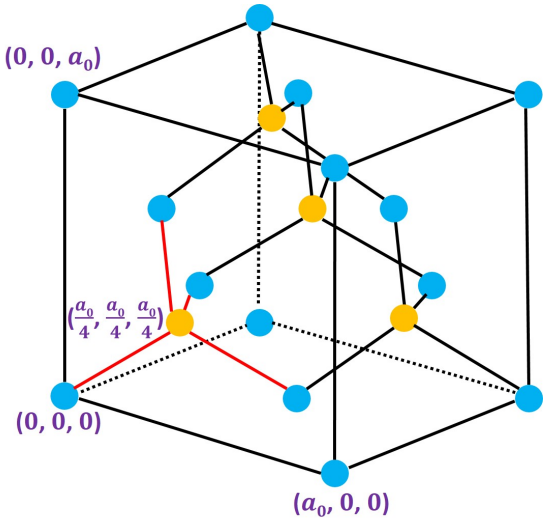

(a)

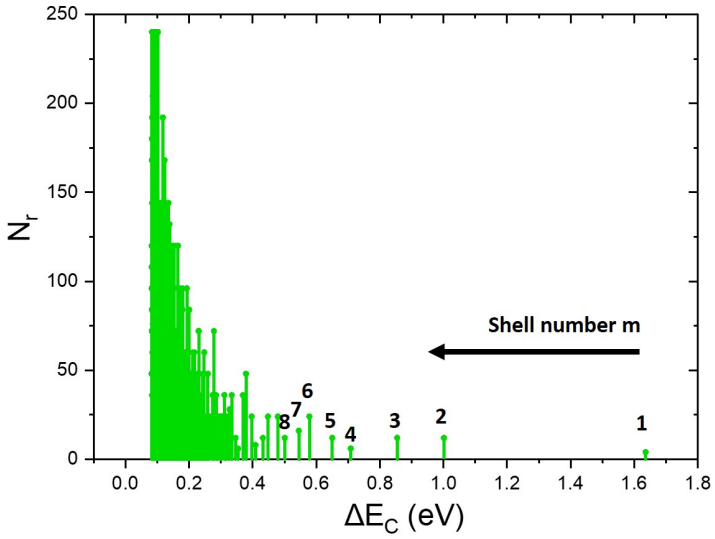

(b)

Figure 2.14: (a) Diamond lattice unit cell with the first, second, to eighth nearest neighbours labelled. (The third nearest neighbour is in the adjacent unit cell.) Blue atoms are face-centred cubic lattice atoms (type I geometry), yellow atoms belong to type II geometry. (b) The number of equivalent sites of DAPs in diamond lattice versus shifts in photon energy of the spectral lines. The calculation of shell numbers up to 150, including type I and type II geometry.

B. The random distribution - G(r)

A random distribution of impurities can be described by

$$G(r) = 4\pi r^2 N \exp\left(-\frac{4\pi r^3}{3}\right) \tag{2.66}$$

Where r is the distance between impurities, N is the concentration of donor-acceptor pairs in m^{-3}. [36] It is noticeable that the distribution of impurities is usually not homogeneous during diamond growth. For different growth sectors and boundaries, the incorporation efficiency of various impurities into a diamond lattice (such as boron and substitutional nitrogen) is different [24].

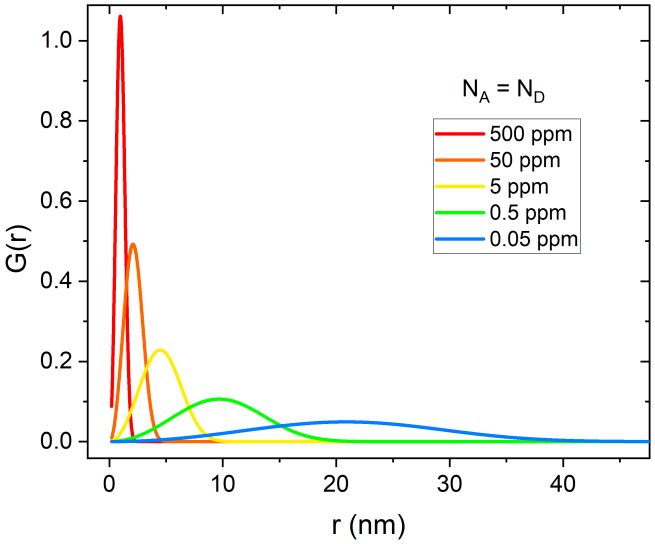

Figure 2.15: Random distribution of different concentrations of donors and acceptors on the assumption that $N_D = N_A$.

C. The recombination probability - W(r)

The recombination probability of a donor-acceptor pair with a separation r is

$$W(r) = W_0 \exp\left(-\frac{2r}{a_{d,a}}\right) \tag{2.67}$$

Where W_0 is a constant, a_{da} is a Bohr radius of donor or acceptor with the larger radius, smaller binding energy. [37] As shown in figure 2.16, in terms of the same DAPs distribution, the bigger the Bohr radius, the higher intensity of the DAP recombination transitions. The symmetry of the spectral band shape is a function of the Bohr radius of the electron and hole.

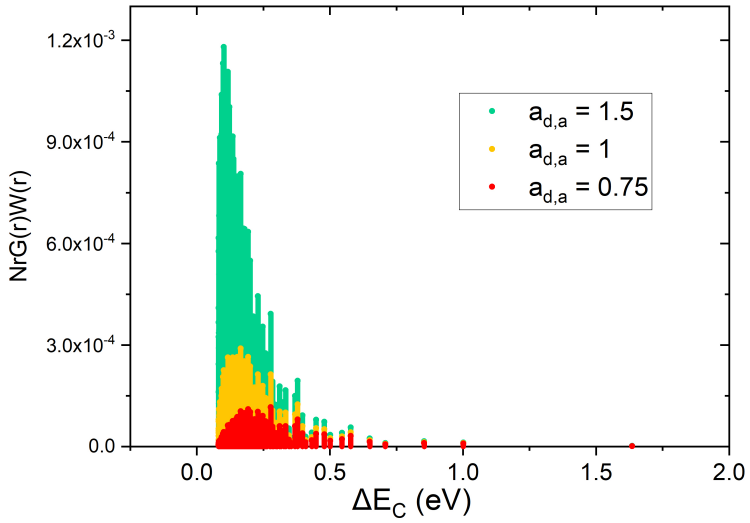

Figure 2.16: Simulation of line shape of DAP recombination transition (DAPs with shell number up to 150) considering N_r, $G(r)$ and $W(r)$, when the number of random distributed donors and acceptors both equal to 0.5 ppm. $a_{d,a}$ equals to 0.75 nm, 1 nm and 1.5 nm, respectively.

For the distant DAPs (large r), the overlap of the wave functions of the trapped holes and electrons is small and results in a longer lifetime. [32] When the excitation intensity is low, the broad emission band arise from distant DAPs (large r) are observed as the re-pump rate is low and there is a much higher population of centers with distant separation. Alternatively, under high intensity excitation, the rapid recombination rate of close pairs enables them to emit multiple times during the long lifetime of distant pairs, so they dominate the spectrum.[26, 32] Hence, as the excitation intensity increases, the probability of close-pair recombination rises, leading to an increase in intensity and a peak shift to higher energies. In terms of phosphorescence emission after the excitation, the close DAPs recombine within a short delay time. Then the phosphorescence emission band is shifted to lower energy at longer times due to the longer-lived distant DAP recombination. [26, 38]

D. Phonon-coupling

The shape of the DAP recombination transition band is also determined by the electron-phonon interaction, which is explained by the Franck-Condon principle shown in figure 2.17 (1D configuration coordinate diagram). [31, 36, 39, 40] The optical transition band's full width at half maximum (FWHM) will increase as the

temperature increases. [40] The spectral lineshape based on the 1D vibrational broadening model in the literature [40, 41] can be calculated by summing up all possible transitions between the vibrational levels, which is given by

$$I(E) = \sum_n e^{-S} \frac{S^n}{n!} g_\Gamma \left(E_{ZPL} - nE_{ph} - E\right) \tag{2.68}$$

Where S is the Huang-Rhys factor that quantifies the number of phonons generated during optical transitions. n = 1,2,3... are the phonon replicas. E_{ph} is the average phonon energy. g_Γ is a Gaussian function with a parameter Γ defining the width of the Gaussian peak. Hence equation 2.68 can be written as

$$I(E) = \sum_n e^{-S} \frac{S^n}{n!} \left[\frac{1}{\Gamma\sqrt{2\pi}} \exp\left(-\frac{1}{2}\frac{(E_{ZPL} - nE_{ph} - E)^2}{\Gamma^2}\right)\right] \tag{2.69}$$

The DAP recombination lineshape is, therefore, determined by three variables, including the Huang-Rhys factor S, the Gaussian peak line width parameter Γ, and the average phonon energy E_{ph}.

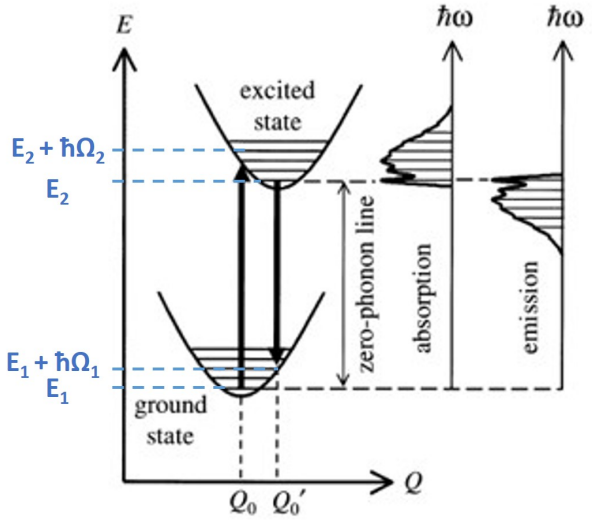

Figure 2.17: Configuration diagram for the ground state and one of the excited electronic states. Q_0 and Q_0' are the equilibrium position of the minimum value of the configuration coordinate for those two states, respectively. The optical transitions are labelled as vertical arrows. The right-hand side of the figure shows the general shape of the absorption and emission spectra that would be expected. [18]

Comparing (a) and (b) in figure 2.18, the vibrational features of the optical

transition band are more obvious when the average phonon energy E_{ph} is higher. The Huang-Rhys factor S indicates the extent of the electron-phonon coupling: the symmetry and width of the lineshape changed significantly as the variation of S. In addition, the band centre position can be shifted by a few eV (redshift for emission and blue shift for absorption) when the electron-phonon interaction is strong.

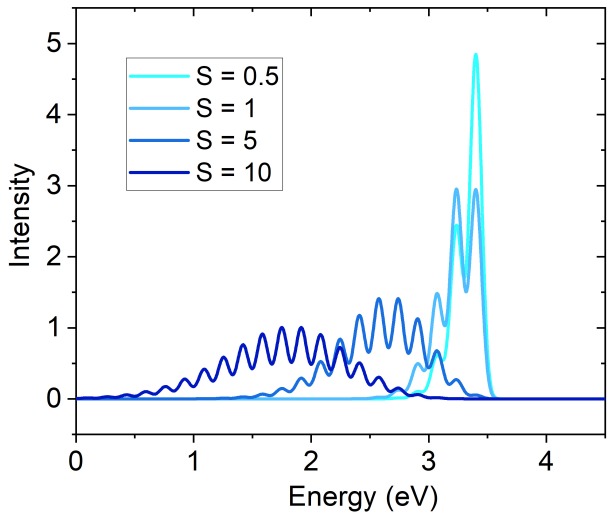

(a)

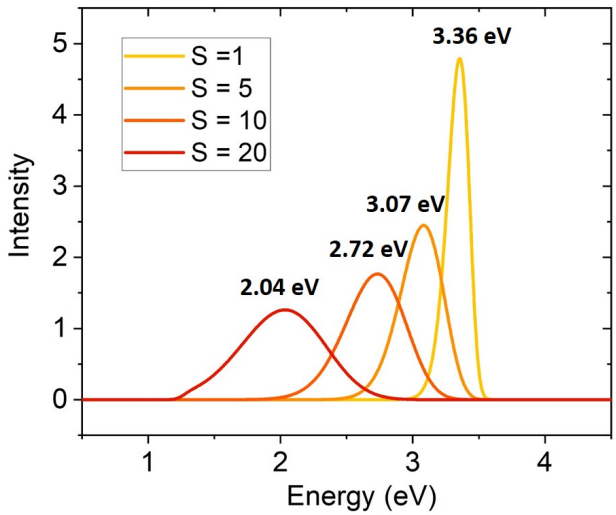

(b)

Figure 2.18: Simulation of DAP recombination luminescence lineshape considering phonon-coupling using equation 2.69 with the parameters $E_{ZPL} = 3.4$ eV, $\Gamma = 0.05$ eV (a) $E_{ph} = 0.165$ eV (b) $E_{ph} = 0.07$ eV. (n up to 30)

E. Effect of Coulomb correlations

The Coulomb interaction (ΔE_C) of an isolated pair consisting of one donor and one acceptor (1-complex) is described by equation 2.62. However, there is a probability that luminescence centres consisting of multiple donors or acceptors, such as complex shown in figure 2.19. The nearby charged donor (or acceptor) alters the DAP recombination energy, for example. [33, 38]

$$\Delta E_C = \frac{e^2}{4\pi\epsilon_0\epsilon_r r_1} + \frac{e^2}{4\pi\epsilon_0\epsilon_r r_2} - \frac{e^2}{4\pi\epsilon_0\epsilon_r r_{12}}. \tag{2.70}$$

For the different configurations shown in figure 2.19, the Coulomb correction of the DAP recombination energy is the same, while the lifetime of DAP recombination is different due to the difference in distance between donor and acceptor of the initial neutral pair.

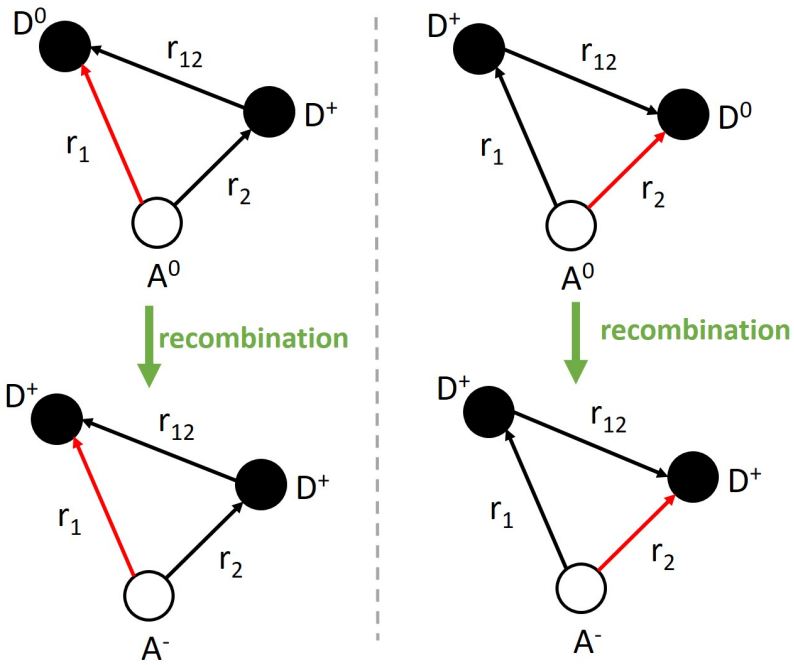

Figure 2.19: The schematic of 2-complex. The recombination occurs between donor-acceptor with different distance r_1 or r_2 (labelled as red) in between. Donor, solid circles; acceptor, open circles.

2.3.2 Optical absorption

Defects in the crystal disrupt the symmetry of the crystal lattice and can produce weak dipole moments, thereby introducing extrinsic absorption features, which are

spectral fingerprints of specific defect varieties. For diamond, some of those defect-induced absorption features may occur in the one-phonon mid-infrared region, such as single nitrogen (also absorption in visible) and nitrogen aggregates (also absorption in UV). [19, 20] The absorption coefficient is proportional to the density of absorbing defects. Hence, absorption spectroscopy, i.e. UV-Vis absorption (Ultraviolet-visible absorption) or FTIR (Fourier Transform Infra-red Absorption), is a robust tool for investigating the characteristics of various absorbing impurities and for quantitative measurement of its concentration. [19]

Generally speaking, a transition between a defect-induced in-gap state and the delocalized band (CB or VB) give rise to a broad, largely featureless continuous band in absorption or emission spectra. However, from a transition between two localised states, the spectral feature consists of a zero-phonon line (ZPL) and a phonon side-band (PSB). [18, 19, 42]

As shown in figure 2.17, this system is formed by electronic-vibrational interaction between the electronic states of impurities and the vibrational modes of the defect/diamond lattice. The absorption transitions in the vibronic system are described as

$$\hbar\omega_a = (E_2 + \hbar\Omega_2) - E_1 = (E_2 - E_1) + \hbar\Omega_2. \tag{2.71}$$

After the absorption, the electron non-radiatively relaxes to the bottom of the excited state. The emission transition afterwards is described as

$$\hbar\omega_e = E_2 - (E_1 + \hbar\Omega_1) = (E_2 - E_1) - \hbar\Omega_1. \tag{2.72}$$

where the ground electronic state and excited electronic state are at energy E_1 and E_2, Ω_1 and Ω_2 are the frequency of the phonon created in the ground state band and excited state band, respectively.

The emission energy is lower than that of the absorption, and such red-shift is named Stokes shift. [18] The pure electronic transitions $(E_2 - E_1)$ between the lowest vibrational level of the ground state and the lowest vibrational level of the excited state is observed as a sharp line with the same frequency in absorption, and emission spectrum, namely the ZPL (as narrow as about 1 meV in diamond). [19] The side-band corresponding to the electron-phonon coupling transitions may

form continuous bands instead of discrete lines that is because the electronic state can couple to many different phonon modes with a whole range of frequencies. [18] From equations 2.71 and 2.72, the PSB is at higher energies than the ZPL in the absorption spectrum. Conversely, the PSB is at lower energies in the luminescence spectrum. In addition, the ratio of ZPL and PSB varies with temperature because the number of phonons in the lattice is T-dependent. Experimentally, the spectrum is usually acquired at low temperatures (77 K) to maximise emission into the ZPL. [42]

When the impurity atoms are lighter than carbon atoms or at high-strained sites, the atoms vibrate at a frequency that is higher than the allowed frequencies for the fundamental vibrations ($>$ 165 meV in diamond). Thus the vibration can not propagate in the lattice, resulting in a local vibrational mode (LVM), which appears as a sharp line in the spectrum. [19, 20, 43] Moreover, some vibronic bands exhibit a sharp one-phonon cut-off at an energy of 165 meV from the ZPL due to this limitation on the fundamental vibration in the lattice. [20]

2.3.3 Photoluminescence (PL)

The energy emitted as photons from a solid after absorbing incident energy is called luminescence. The variety of luminescence depends on forms of incident energy, such as photoluminescence by optical excitation, cathodoluminescence excited by electron beams, and thermoluminescence by thermal excitation. [26, 27]

Photoluminescence is the emission of photons generated from optical stimulation, which can be categorized as fluorescence and phosphorescence according to the emission lifetime. The fluorescence lifetime is typically less than 50 nanoseconds. Phosphorescence may last for tens of nanoseconds to hours after removing the excitation light source. [27]

2.3.4 Phosphorescence

The delay between the absorption and light emission can occur through multiple processes, including the following two types of processes, which also determine the temperature dependency of phosphorescence (Figure 2.20). Firstly, electrons trapped at defects are thermally excited into the conduction band (trapped holes

are thermally released into valence band) and induce radiative recombination at remote luminescence centres, which is a strongly temperature-dependent process. Secondly, athermal tunnelling between traps and luminescence centres, which is temperature-independent. Thermal-assisted tunnelling is possible to occur when the trap includes multiple energy levels. The electrons can be thermally excited from the lower energy level to an excited energy level locating close to the luminescence centre. The thermal-assisted tunnelling process is slightly affected by the temperature. [27, 44, 45] Various impurities in diamonds, such as donor-acceptor pairs, could serve as a luminescence centre. [30]

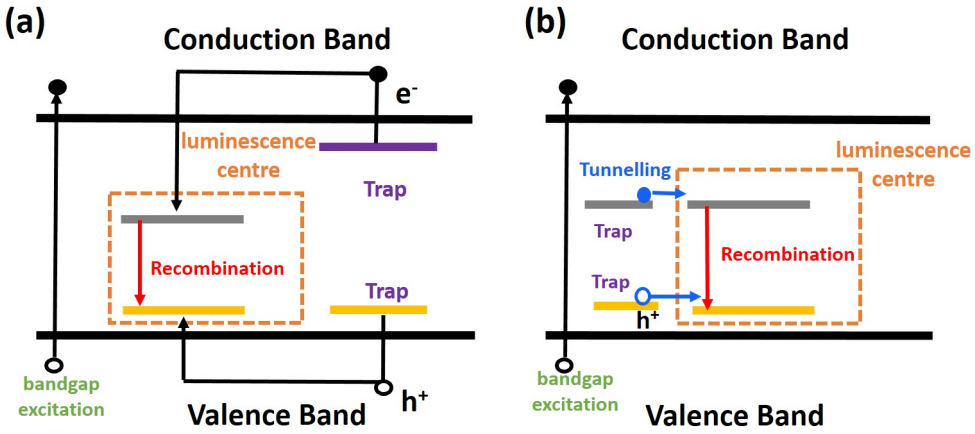

Figure 2.20: Schematic of different processes leading to phosphorescence: (a) thermal process (b) athermal tunnelling process.

2.3.4.1 Thermal process

As shown in figure 2.20(a), during optical excitation, electrons or holes are trapped at localized energy levels. After excitation, those trapped charge carriers are thermally released into the conduction band or the valence band and then re-trapped at an isolated trap or radiative recombine at a centre, at which light may be subsequently emitted. The relative number of traps and luminescence centres determine whether retrapping or radiative recombination process dominates. [27, 44]

To start with, only one type of trap and luminescence centre is considered. The probability of an electron escaping from a trap of a depth E_{Trap} at temperature T

is

$$p = s\ \exp\left(-\frac{E_{Trap}}{k_B T}\right), \tag{2.73}$$

where s is a constant, which may, however, vary slowly with temperature. When the concentration of luminescence centres is much higher than that of traps, recombination dominates, and the phosphorescence process follows **first-order kinetics**. In this case, if an electron is liberated from a trap, it always goes straight to a luminescence centre and does not on its way fall into another trap.

$$\frac{\mathrm{d}N}{\mathrm{d}t} = -pN = -N\,s\ \exp\left(-\frac{E_{Trap}}{k_B T}\right), \tag{2.74}$$

where the number of trapped carriers N at a delay time t is given by

$$N(t) = N_0\ \exp(-\alpha t). \tag{2.75}$$

$$\alpha = s\ \exp\left(-\frac{E_{Trap}}{k_B T}\right). \tag{2.76}$$

The intensity of phosphorescence emission is proportional to the rate of supply of electrons to the luminescence centres.

$$I(t) = -\frac{\mathrm{d}N(t)}{\mathrm{d}t}, \tag{2.77}$$

$$I(t) = N_0\,s\ \exp\left(-\frac{E_{Trap}}{k_B T}\right)\ \exp\left[-s\ \exp\left(-\frac{E_{Trap}}{k_B T}\right)t\right], \tag{2.78}$$

Hence

$$I(t) = I_0\ \exp(-\alpha\, t), \tag{2.79}$$

where I_0 is the initial intensity, at very high temperature I_0 decreases. t is a delay time, τ is the lifetime of traps:

$$\frac{1}{\tau} = \frac{1}{s}\ \exp\left(-\frac{E_{Trap}}{k_B T}\right), \tag{2.80}$$

Therefore, for a constant T, the decay follows a simple exponential decay. [27, 44, 45]

When traps are more abundant, both retrapping and recombination are considered; the phosphorescence process follows **second-order kinetics**. The phosphorescence intensity is proportional to both the number of trapped carriers and

the number of luminescence centres available for recombination (assumed both equal to n).

$$I(t) \propto -dn/dt = \alpha n^2, \tag{2.81}$$

where α is a constant. Integration gives

$$I(t) = \frac{I_0}{(n_0\,\alpha t + 1)^2}. \tag{2.82}$$

The constant α describes the relative possibilities of the retrapping and the recombination processes. In this case, the phosphorescence decay follows a power-law decay with the power of two, namely a hyperbolic decay. [27, 45]

Mean lifetime and half-life time are both commonly used scaling times for the discussion of phosphorescence decay. Mean lifetime is the time when the intensity reduces to $1/e$ times the initial intensity. Half-life time indicates when the intensity of the phosphorescence is half of the initial intensity.

2.3.4.2 Tunnelling process

2.3.4.2.1 Athermal tunnelling process The athermal tunnelling process, as shown in figure 2.20(b), does not involve the conduction band or the valence band but occurs between traps (donors or acceptors) and nearby luminescence centres with aligned energy levels in the bandgap. [44, 46] The probability of tunnelling is determined by the overlap of the trap/luminescence centre wave functions. Generally speaking, a high concentration of related defects enables the formation of close trap-centre pairs for tunnelling. [44] The tunnelling process is also achievable between far distance trap and luminescence centre by a chain-like path which consists of several traps delivering carriers to the luminescence centre when the concentration of traps is high. [44]

Only considering pairs containing one variety of trap and luminescence centre separated by a distance r (ignoring the chain-like path tunnelling), the tunnelling rate is time-independent and given by

$$W(r) = W_0\, e^{-2r/a}, \tag{2.83}$$

where W_0 in unit s^{-1} is a coefficient proportional to the fraction of (paired) trapping centres in their tunnelling states, a is the effective radius for overlap of the wave function. [46] The density of trap-centre pairs at a different time is written as

$$p(r) = p_0(r)\ \exp[-W(r)t], \tag{2.84}$$

where $p_0(r)$ is the initial density of pairs after excitation. Hence the distribution of pairs at any time is determined by the mode of excitation (wavelength and intensity) and the total number of pairs that have subsequently recombined. [44, 46] The phosphorescence intensity (photons emitted per second) is

$$I(t) = \int_0^\infty p_0(r)\, W(r)\ \exp[-W(r)t]\, \mathrm{d}r \tag{2.85}$$

depending on the experimental conditions (illumination energy, illumination intensity), approximate solutions of equation 2.85 can take the form

$$I(t) \propto 1/t \tag{2.86}$$

or

$$I(t) = \frac{I_0}{(1 + t/\tau)} \tag{2.87}$$

where τ depends on the intensity of excitation [47].

2.3.4.2.2 Thermally-assisted tunnelling process For the circumstances that the energy level of the luminescence centre is close to the excited state of the trap, electrons can be thermally excited from the ground state to a higher vibrational level, giving rise to tunnelling between the trap and luminescence centre. The phosphorescence decay depends on both thermal excitation at traps and tunnelling between trap-centre pairs. [44]

2.3.4.3 Decay curve fitting methods

2.3.4.3.1 Power law decay function A power-law decay function effectively describes different phosphorescence decay species, such as those arising from second-order thermal processes of various traps in materials (equation 2.82) or tunnelling

processes occurring between the random distribution of trap-centre pairs (equation 2.87), with the power varying from 1 - 2. [46, 48]

A complex power-law function (compressed hyperbola) was devised by Becquerel to provide a more general solution for phosphorescence decay fitting as a supplement to the exponential function and to accommodate more possible factors, such as the distribution of traps with different depth and the interaction of different luminescence centres. The equation is written as

$$I(t) = \frac{I_0}{(1 + at)^p}, \tag{2.88}$$

where I_0 is initial intensity, a is a constant, and p is the power between 1 - 2. [49, 50]

2.3.4.3.2 Stretched exponential function In practice, thermal processes of phosphorescence are complex due to the diversity of impurities and charge transfer paths, as well as the random distribution of traps. [51] As a sum of exponential decays, the stretched exponential function is robust to describing such luminescence decay without a constant decay rate. [52] In particular, during phosphorescence decay, the number of available luminescence centres reduce, thereby free carriers in the conduction band or the valence band must travel for a longer distance before activating recombination at luminescence centres, leading to a decrease in the phosphorescence decay rate. The assumptions of the stretched exponential phosphorescence also include at least one trapping state and one variety of luminescence centre involved, direct band-to-band recombination is negligible, and retrapping is considered. [53] The intensity of phosphorescence decay described by a stretched exponential function, which is also called Kohlrausch function, is written as

$$I(t) = I_0 \exp\left[-(t/\tau_0)^{\beta}\right], \tag{2.89}$$

where I_0 is the initial intensity, t is a delay time, τ_0 is a parameter with the dimensions of time, β is a dispersion exponent with a range of $0 < \beta < 1$. [52, 53]

The time-dependent rate coefficient $k(t)$ is

$$k(t) = (\beta/\tau_0)\,(t/\tau_0)^{\beta-1}. \tag{2.90}$$

When $k(t)$ is constant, the decay is an exponential decay. When $k(t)$ increases or decreases with time, the decay described is a super-exponential decay or a sub-exponential decay, respectively. [52]

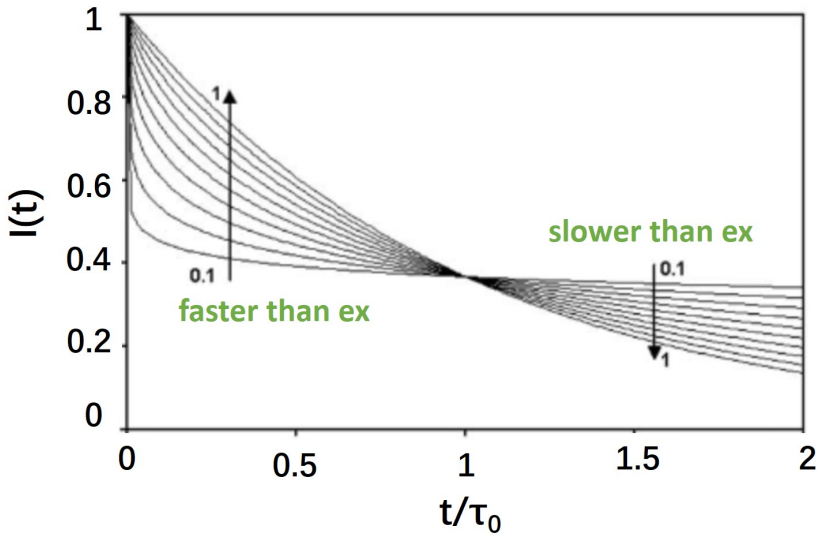

Figure 2.21: The stretched exponential on a log plot for several values of β (0.1, 0.2,..., 0.9, 1). Adapted from [52].

The stretched exponential decay in figure 2.21 including two regimes: for $t < \tau_0$, a faster-than-exponential decay with a infinite initial rate, for $t > \tau_0$, a slower-than-exponential decay. [52]

The infinite initial decay rate of the stretched exponential function is obviously not in accordance with the understanding of phosphorescence decay. To solve the problem of fitting the first several experimental data points of the decay curve, a modified stretched exponential function is created to enable the selection of the origin of times t_0 comparing with τ_0. A parameter α is defined as t_0/τ_0. Hence, the modified exponential function for phosphorescence decay is

$$I(t) = \exp\left[\alpha^{\beta} - (\alpha + t/\tau_0)^{\beta}\right]. \tag{2.91}$$

The time-dependent rate coefficient is

$$k(t) = \beta/\tau_0 \, (\alpha + t/\tau_0)^{\beta-1}. \tag{2.92}$$

The lifetime of phosphorescence is given by

$$\tau = \tau_0 \, (\tau^{1-\beta}/\beta). \tag{2.93}$$

In summary, a better approach of experimental fits for phosphorescence decay of complex thermal processes is provided by a modified stretched exponential function. [44] Whilst the modified stretched exponential function is not a complete model of phosphorescence decay, it does achieve better accuracy in calculating the activation energy.

2.3.4.3.3 Multiple components decay curve fitting In addition, multiple varieties of traps and luminescence centres may participate in the thermal and tunnelling processes. The phosphorescence decay, therefore, could be considered as the combination of multiple decay components. Accordingly, the intensity of phosphorescence is described by

$$I(t) = \sum_m \frac{I_0}{(t+\sigma)} + \sum_n I_0 \, \exp(-t/\tau) + \sum_p \frac{I_0}{(n_0 \, \alpha t + 1)^2} \tag{2.94}$$

Where m, n, p are integers ≥ 0, representing the number of components belongs to 1/t law decay, simple exponential decay, and hyperbolic decay in phosphorescence, respectively.

2.3.5 Thermoluminescence (TL)

Thermoluminescence (TL) is thermally stimulated light emission after excitation has been removed. [54] Semiconductors are excited by various radiation such as photons or nuclear irradiation at low temperatures where the phosphorescence intensity is relatively low. During this process, the free charge carriers are created in the conduction band and valence band, some of which are trapped at the meta-stable states. Hence the radiation energy is stored in the solids. By steadily increasing the

temperature, the trapped carriers are thermally released then retrapped at defects, directly recombine with an opposite charge carrier, or radiatively recombine at luminescence centres generating thermoluminescence. [28, 54, 55] Experimentally, the samples are heated for a range of temperatures at which TL becomes bright gradually and then decays until finally disappearing as all trapped carriers are released. [28]

A TL glow curve is plotted as intensity versus temperature or heating time, with each peak corresponding to one type of trap in the bandgap. [27] The position, shape and intensity of each TL glow peak depend on the parameters (trap depth, trapping rates, etc.) of the relevant trap in the luminescent material, as well as on the existence of other traps. [28, 55] At the high-T side of TL glow peaks, the thermal process dominates, and tunnelling events are negligible. [44]

2.3.5.1 Order of kinetics

In the following discussion, a simplification to the charge transfer process is taken relative to the TL mechanism. It considers only one trap and one luminescence centre, as shown in figure 2.22. The assumption of linear heating rate β is utilised for all the models in this chapter.

$$T = T_0 + \beta t. \tag{2.95}$$

where T_0 is the initial temperature. In addition, the free carrier compensation is assumed to be constant, namely, compared to trapped carriers, the amount free carriers in CB and VB are very small ($n_c \ll n$), and their lifetime is short. [27]

Three key parameters: the activation energy for each trap E_{Trap}, the frequency factor s, and the order of kinetics b is important for the determination of the TL glow curve, which will be discussed in detail below. [54]

2.3.5.1.1 First-order kinetics In the first-order case, recombination at luminescence centres dominates, the retrapping is negligible. Hence the thermoluminescence intensity $I(t)$ is given by:

$$I(t) = -\frac{\mathrm{d}n}{\mathrm{d}t} = s\,\exp\left(-\frac{E_{Trap}}{k_B T}\right) n, \tag{2.96}$$

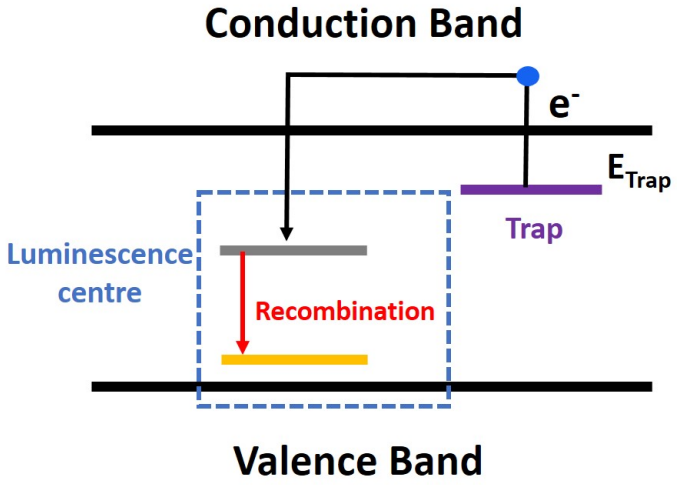

Figure 2.22: The schematic energy levels representation of a luminescent material-containing one trap with an activation energy of E_{Trap} and one luminescence centre.

where n is the number of electrons in traps.

$$\frac{\mathrm{d}n}{n} = -s \exp\left(-\frac{E_{Trap}}{k_B T}\right) \mathrm{d}t, \tag{2.97}$$

Assuming linear heating rate ($\mathrm{d}T = \beta\,\mathrm{d}t$) :

$$\int_{n_0}^{n} \frac{\mathrm{d}n}{n} = \ln\left(\frac{n}{n_0}\right) = -\int_{T_0}^{T} (s/\beta) \exp\left(-\frac{E_{Trap}}{k_B T}\right) \mathrm{d}T \tag{2.98}$$

$$n(t) = n_0 \exp\left[-\int_{T_0}^{T} (s/\beta) \exp\left(-\frac{E_{Trap}}{k_B T}\right) \mathrm{d}T\right] \tag{2.99}$$

where n_0 is the number of electrons in traps at $t = 0$, T_0 the initial temperature. Hence

$$I(T) = n_0 s \exp\left(-\frac{E_{Trap}}{k_B T}\right) \exp\left[-\int_{T_0}^{T} (s/\beta) \exp\left(-\frac{E_{Trap}}{k_B T}\right) \mathrm{d}T\right] \tag{2.100}$$

This is the so-called Randall & Wilkins 1945 expression. [27, 54, 55]

The first-order TL peaks are asymmetrical, and most of the peak area is on the low-temperature side, as shown in figure 2.23. [27, 28] The temperature at which the TL intensity is maximum (T_m) of a first-order kinetics TL glow peak is independent of the initial concentration of trapped carriers n_0, which means the dose of excitation does not affect T_m. For a specific trap, T_m shifts to a higher

temperature as the heating rate increases. When the heating rate is constant, the value of T_m increases as the frequency factor decreasing or for a deeper trap. [28]

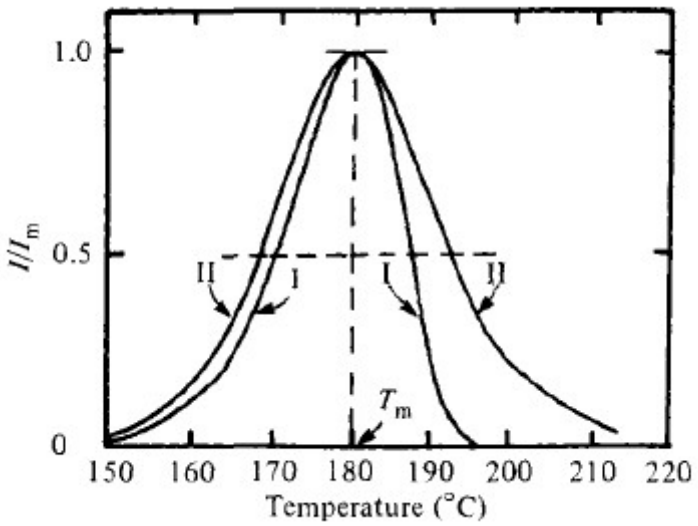

Figure 2.23: An example for TL glow peaks of first-order kinetics and second-order kinetics are asymmetrical and relatively symmetrical, respectively. Adapted from [27].

For a first-order process, the frequency factor s is typically less than the vibration frequency of the crystal ($\sim 10^{12}$ s^{-1}), is determined by the intrinsic crystal lattice, presence of traps and is also independent of temperature. [28, 54, 56]

2.3.5.1.2 Second-order kinetics Garlick and Gibson discussed the circumstances where retrapping dominates when thermoluminescence is of second-order kinetics. [27, 54, 55] The intensity of the glow peak is described as

$$I(t) = -\frac{\mathrm{d}n}{\mathrm{d}t} = s' \exp\left(-\frac{E_{Trap}}{k_B T}\right) n^2 \tag{2.101}$$

where s' is a pre-exponential factor with dimensions of cm^{3}s^{-1} but not a frequency factor. [28] Assuming a linear heating rate ($\mathrm{d}T = \beta \mathrm{d}t$):

$$n(t) = [1/n_0 + s' \exp\left(-\frac{E_{Trap}}{k_B T}\right) t]^{-1} \tag{2.102}$$

The second-order expression of Garlick and Gibson (1948) for a linear heating rate is [27, 54, 55]

$$I(T) = n_0^2 s' \exp\left(-\frac{E_{Trap}}{k_B T}\right) / [1 + (n_0 s'/\beta) \int_{T_0}^{T} \exp\left(-\frac{E_{Trap}}{k_B T}\right) \mathrm{d}T]^2. \quad (2.103)$$

As shown in figure 2.23, the second-order peak is more symmetrical compared to the first-order peak. For a given trap, T_m shifts to a higher temperature when the heating rate increases or the constant s' decreases. For a constant heating rate, the position and shape of the second-order peak strongly depend on the initial concentration of trapped carriers n_0, namely the dose of excitation. The value of T_m is proportional to the trap depth E and increases as the decrease of n_0. [27, 28]

2.3.5.1.3 General-order kinetics In most circumstances, the TL glow peaks do not present either pure first-order or second-order dynamics characteristics. Thermoluminescence of general-order kinetics (the kinetic order b varying from 1 to 2) as shown in figure 2.24, is therefore described by May & Partridge in 1964, which is

$$I(t) = s' \exp\left(-\frac{E_{Trap}}{k_B T}\right) n^b \quad (2.104)$$

where s' is the pre-exponential factor. [27, 54] Assuming linear heating rate ($\mathrm{d}T = \beta \mathrm{d}t$):

$$n(t) = [n_0^{(1-b)} + s' \exp\left(-\frac{E_{Trap}}{k_B T}\right) t]^{1/(1-b)} \quad (2.105)$$

The general-order expression for TL is

$$I(T) = n_0 s'' \exp\left(-\frac{E_{Trap}}{k_B T}\right) / [1 + ((b-1)s''/\beta) \int_{T_0}^{T} \exp\left(-\frac{E_{Trap}}{k_B T}\right) \mathrm{d}T]^{b/(b-1)}. \quad (2.106)$$

where b is the kinetic order ($1 < \mathrm{b} < 2$); $s'' = s'n$ being equivalent to s in the first-order case and having no specific physical meaning here. [54, 55] T_m in general-order case has a dependence on n, hence the dose of excitation. [28, 55]

2.3.5.1.4 Mixed-order kinetics In practice, some charge carriers do not participate in the thermoluminescence process due to the presence of thermal disconnected traps whose depth is much greater than normal trapping levels or

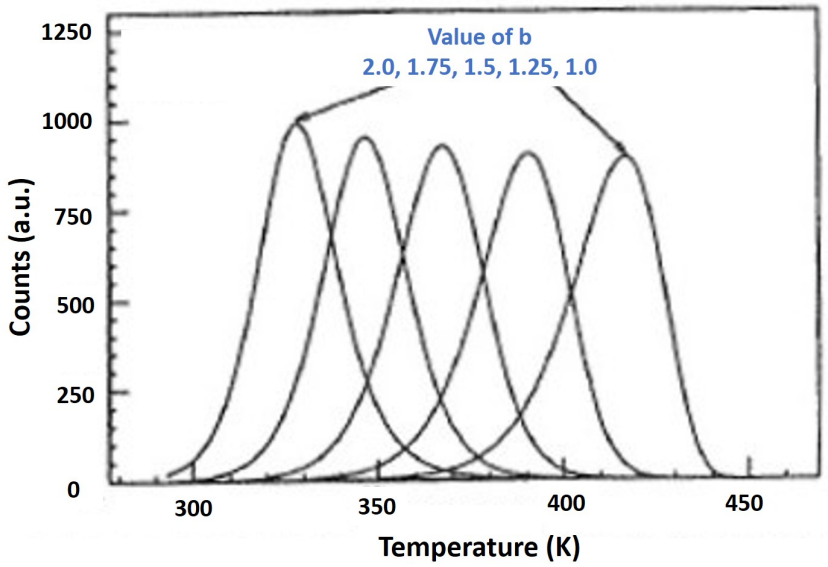

Figure 2.24: The shape and position of TL glow peak when kinetic order b equals 2.0, 1.75, 1.5, 1.25 and 1.0, respectively. [28]

recombination centers with low recombination probabilities. Taking those charge carriers into account, a mixed-order kinetic is suggest by Chen by adding two parameters: m the number of those carriers not involved in the TL process and $\alpha = n_0/(n_0 + m)$. [27, 28] When $\alpha = 1$, the high T side of TL peak tends to be first-order; for $\alpha = 2$, it tends to be second-order. [28] Chen's equations are a combination of first and second-order kinetics, which are

$$I(t) = s'n(n+m)\,\exp\left(-\frac{E_{Trap}}{k_B T}\right) \tag{2.107}$$

and

$$I(T) = \frac{s'm^2\alpha\,\exp\left[(ms'/\beta)\int_{T_0}^{T}\exp\left(-\frac{E_{Trap}}{k_B T}\right)\mathrm{d}T\right]\exp\left(-\frac{E_{Trap}}{k_B T}\right)}{\left\{\exp\left[(ms'/\beta)\int_{T_0}^{T}\exp\left(-\frac{E_{Trap}}{k_B T}\right)\mathrm{d}T\right]-\alpha\right\}^2}. \tag{2.108}$$

2.3.5.2 TL cleaning

Multiple types of traps and recombination centres in luminescent crystals lead to multiple TL glow curve peaks. The shape and intensity of each TL peak can be affected by other traps. Due to sharing electrons or holes, the low T peaks can be weaker. [55] For those traps of very different depths, the corresponding TL peaks are clearly separated, while for two traps with similar depths, the peaks overlap or

even present as one peak. [54]

Fitting such TL peak by the normal methods obtains the value of b greater than 2 and activation energy close to the average for two traps. TL cleaning is a robust tool for plotting an individual variety of traps and obtaining accurate values of their depth E and frequency factor s. [27, 55] In more detail, TL cleaning is the heating temperature to just beyond the maximum of the first peak to empty the traps corresponding to this peak, cooling down rapidly and then heating up again to just beyond the maximum of the second peak until the whole TL glow curve is plotted. [27] Another method to distinguish overlap peaks is based on their TL spectrum if they originate from different luminescent centres.[54]

2.3.5.3 TL glow curve analysis methods

Once a TL glow curve is obtained in the experiment, several analysis methods enable the calculation of relevant traps parameters, mainly the activation energy E and the frequency factor s. In this section, some of the methods picked will be briefly introduced, and their advantages and disadvantages will be discussed.

2.3.5.3.1 The initial rise method The initial rise method is based on the initial part of the TL glow curve that is exponentially dependent on temperature (equation (2.109)) in which the region for detrapping is negligible. By plotting $\ln(I)$ against $1/T$, the gradient is equal to $-E/k_B$. The benefit of this method is quick and simple and independent of kinetic orders. To deal with multiple types of traps, TL cleaning must ensure each peak corresponds to traps of only one depth. [27, 57] There are several limitations to the initial ascent method, which one should be aware of. Firstly, the activation energy obtained is affected by thermal quenching. [27] Secondly, if the recombination in the related TL process is exponentially dependent on temperature, the TL intensity should be given by

$$I(T) = K\, sn_0 \exp[(W-E)/k_BT] \exp\left[-(s/\beta)\int_{T_0}^{T} \exp(-E/k_BT')\,\mathrm{d}T'\right] \quad (2.109)$$

where W is an energy depth for a non-radiative process. [54] This method yields activation energy as $E - W$ rather than E. Thirdly, for the circumstances where the pre-exponential factor is T-dependent, a large error will be generated. However,

due to its simplicity, this method is preferentially utilised to estimate the trap depth. [27]

2.3.5.3.2 TL glow curve fitting A much more accurate calculation of the values of E, s and b is achieved by computerized curve fitting based on the equations for different kinetic order cases discussed above. A simulated curve is generated by varying those parameters and compared with the experimental data. The quality for fitting is evaluated by a root-mean-square (RMS) deviation. The [27] software can be used to deconvolute the complicated TL glow curve with overlap peaks. [57–63]

More methods for TL data analysis are mentioned in the literature. [27, 54] For example, the isothermal decay method is only applied to the first-order cases, and it is hard to resolve multiple peaks. The peak position - heating rates method has difficulty giving an accurate value of E when recombination is T-dependent. The fractional glow method for which large experimental effort is required, etc. [27, 54] For all the above methods for TL glow curve analysis, temperature control is important.

More TL glow curve analysis methods are given in the literature. [27] For example, the peak shape method is also a quick and simple method that gives the kinetic order b, and the frequency factor and the trap depth are based on only three data points: T_m, T_1 and T_2. (Figure 2.23) T_1 and T_2 are the temperature for half peak height at low T and high T sides, respectively. [27, 57] It is noticeable that thermal quenching can affect both the initial rise method and peak shape method, which is the loss of light emission caused by the non-radiative transition at high temperatures. [27, 54, 64]

2.3.6 Cathodoluminescence (CL)

Cathodoluminescence (CL) differs from PL and TL in that the emission is a result of electron beam excitation. As shown in figure 2.25, due to electron bombardment, various signals other than CL can also be detected, such as backscattered electrons (or secondary electrons with energy loss), Auger electrons, inelastically and elastically transmitted electrons, and x-rays. [26]

Microscopic and spectroscopic CL can be performed by a scanning electron microscopy (SEM) system. Due to the absorption of incident electron energy, electrons and holes are generated in the conduction band and valence band of diamond, respectively, resulting in the light emission in the ultraviolet, visible and infrared spectral ranges. Unlike optical excitation, the energy of the electron beam excitation is several orders of magnitude greater and is not limited by different wavelengths of the light source. Therefore, CL is very beneficial for studying wide-bandgap materials like diamond and can drive all light emission mechanisms in such semiconductors. The incident electron energies should be selected carefully to avoid atomic displacement damage on samples. [26] For diamonds, it should be less than approximately 145 keV. [65] Furthermore, CL can be used to identify the concentration and distribution of defects (or luminescence centres) in diamond, such as dislocations, nitrogen-related defects and boron. As an example, the determination of substitutional boron concentration by CL is introduced in Chapter 4.1.2.1.

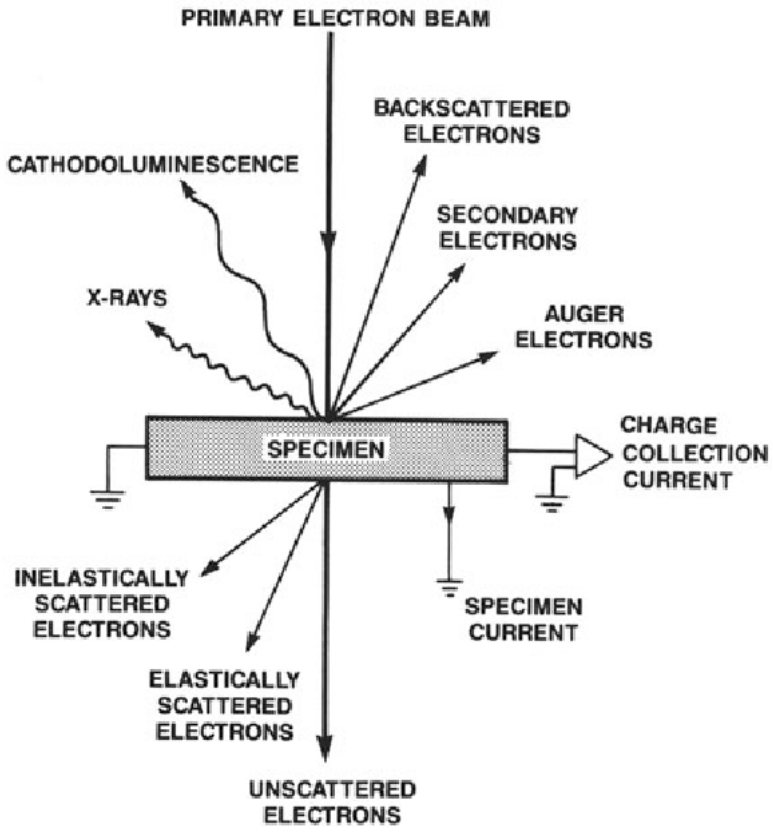

Figure 2.25: Schematic of various signals due to the incident electron beam interaction with solids. Adapted from [26].

2.4 Electron paramagnetic resonance

Electron paramagnetic resonance (EPR) is a robust technique based on the interaction between electromagnetic radiation and magnetic moments arising from unpaired electron interactions with the local environment.

2.4.1 The spin Hamiltonian

The spin Hamiltonian $\hat{\mathcal{H}}$ ((2.110)) is a complete description for the interactions between unpaired electrons and their environment, which could include applied magnetic fields, nuclear spins, other unpaired electron spins, electronic fields, etc. Important interactions include (1) electronic Zeeman interaction, (2) zero-field splitting, (3) hyperfine splitting, (4) quadrupole interaction, and (5) nuclear Zeeman interaction (higher-order terms are omitted).

$$\hat{\mathcal{H}} = \underbrace{\mu_B \mathbf{B}^T \cdot \mathbf{g} \cdot \hat{\mathbf{S}}}_{(1)} + \underbrace{\hat{\mathbf{S}}^T \cdot \mathbf{D} \cdot \hat{\mathbf{S}}}_{(2)} + \sum_i^n \left\{ \underbrace{\hat{\mathbf{S}}^T \cdot \mathbf{A}_i \cdot \hat{\mathbf{I}}_i}_{(3)} + \underbrace{\hat{\mathbf{I}}_i^T \cdot \mathbf{P}_i \cdot \hat{\mathbf{I}}_i}_{(4)} - \underbrace{\mu_N \mathbf{g}_{ni} \mathbf{B}^T \cdot \hat{\mathbf{I}}_i}_{(5)} \right\} \tag{2.110}$$

where μ_B (the Bohr magneton) is the natural unit of the electron's magnetic moment, $\mathbf{g}$ is the g-factor matrix, $\mathbf{D}$ is the zero-field splitting matrix, $\mathbf{A}_i$ is the hyperfine matrix, $\mathbf{P}_i$ is the nuclear quadrupole coupling matrix, $\hat{S}$ is spin, and $\hat{I}_i$ is the nuclear spin.

The zero-field splitting arises from the interaction between two or more unpaired electrons ($S \geq 1$). The quadrupole interaction is caused by non-spherical charge distributions inside a nucleus of spin $I \geq 1$.

2.4.1.1 Electronic Zeeman interaction

An unpaired electron has two allowed spin state $m_s = +\frac{1}{2}$ and $m_s = -\frac{1}{2}$, which are at the same energy level. When an external magnetic field $\mathbf{B}$ interacts with the magnetic moment μ_B of the electron, the spin state splits into two energy levels as shown in figure 2.26. Here, the spin that aligns parallel to the magnetic field occupies a lower energy level, whilst the opposite is true for the anti-parallel aligned spin. As an external magnetic field is varied, the energy difference between

the two spin states changes, which is given by

$$\Delta E = \pm \frac{1}{2} g_e \mu_B B \tag{2.111}$$

When a photon with a frequency ω matching ΔE is absorbed, the resonant transitions between these two spin states can be driven,

$$\Delta E = h\omega = g_e \mu_B B \tag{2.112}$$

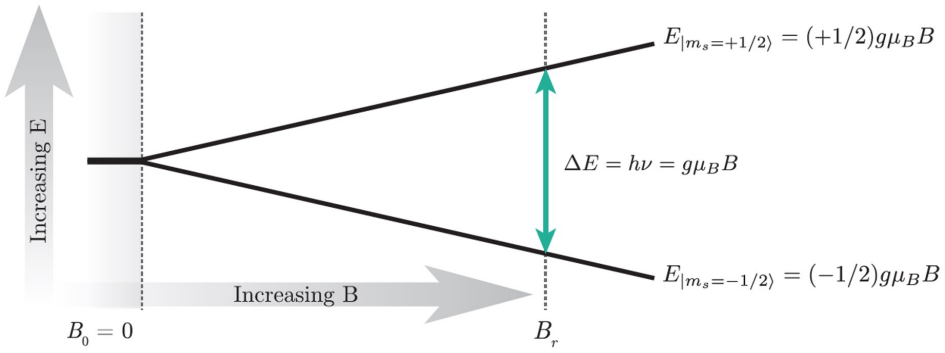

Figure 2.26: The electronic Zeeman effect for an electron with $S = \frac{1}{2}$. Energy levels change as a function of the applied magnetic field $\mathbf{B}$. The resonance transitions occur when the frequency of the incident photon matches the energy difference ΔE.

2.4.1.2 Electron nucleus hyperfine interaction

The hyperfine interaction occurs between the magnetic moments arising from the spins of both the nucleus and electrons and leads to a hyperfine splitting structure in the EPR spectrum.

Fermi contact interaction (isotropic) and dipole interaction (anisotropic) are the two most common electron nucleus interactions with different mechanisms: Fermi contact interaction only occurs when the electron is inside the nucleus, namely only s-shell electrons contribute to this; dipole interactions occurs when an electron moves around a nucleus, therefore depending on the distance between the electron and nuclei, and the orbital shape. The local environment, symmetry, structure and spin localisation of a defect with a non-zero nuclear spin can be studied by utilising hyperfine coupling.

As shown in figure 2.27, there are three allowed EPR transitions by selection rules ($\Delta m_S = \pm 1$; $\Delta m_I = 0$) considering electronic Zeeman interaction and hyperfine interaction of a system with $S = \frac{1}{2}$, $I = 1$ (such as neutral substitutional ^{14}N) . It is noticeable that in some conditions, hyperfine interactions can become comparable to the Zeeman interactions, the spin states have probability to be mixed (neither m_S nor m_I are good quantum numbers) and give rise to weak "forbidden transitions" ($\Delta m_s \neq \pm 1$), $\Delta m_I \neq 0$)).

The hyperfine coupling constant $\mathbf{A}$ determines how far the EPR absorption signal shifts from the original signal. The hyperfine term in equation (2.110) is

$$\hat{\mathbf{S}}^T \cdot \mathbf{A}_i \cdot \hat{\mathbf{I}}_i = \mathbf{A}(\theta) m_S m_I \tag{2.113}$$

$\mathbf{A}(\theta)$ is given by

$$\mathbf{A}^2(\theta) = [\ \mathbf{A}_\parallel^2 cos^2\theta + \mathbf{A}_\perp^2 sin^2\theta\ ] \tag{2.114}$$

where θ is the angle between the symmetry axis of the defect and the applied magnetic field direction.

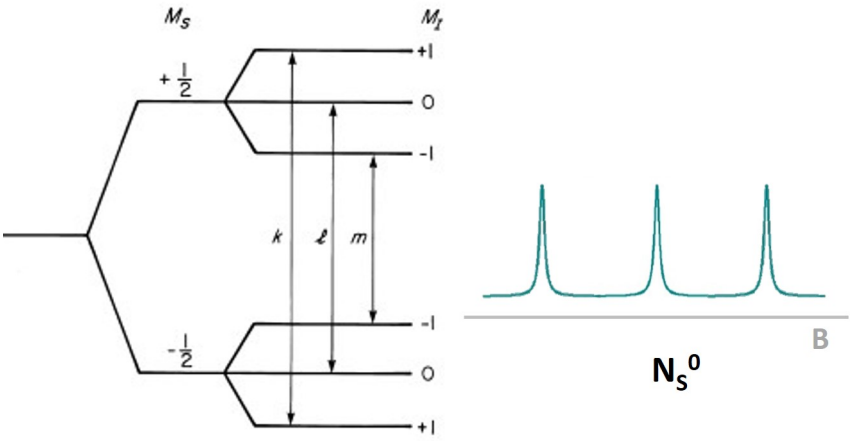

Figure 2.27: Energy levels and allowed EPR transitions at the constant magnetic field for a system with $S = \frac{1}{2}$, $I = 1$ considering electronic Zeeman interaction and electron nucleus hyperfine interaction with a schematic of EPR spectra of N_S^0.

2.4.1.3 Nuclear Zeeman interaction

Nuclear Zeeman interaction is similar to the electronic Zeeman interaction, which arises from the magnetic moment of the nuclear spin ($I \neq 0$) and the external magnetic field. Since the proton magnetic moment μ_N is approximately 2000 times

smaller than the electronic moment μ_B, the impact of nuclear Zeeman on the EPR spectrum is not obvious when the hyperfine interaction is much greater. [19]

2.4.2 Spin lattice relaxation

To understand the spin relaxation, an ensemble of isolated spins with $S = \frac{1}{2}$ (spin system of two energy levels $m_S = +\frac{1}{2}$ and $m_S = -\frac{1}{2}$) is discussed below; only the Zeeman term in the spin Hamiltonian is considered.

The relative population distribution of those two states when a static magnetic field B_0 is applied at a certain temperature T is described by the **Boltzmann distribution**

$$\frac{n_u}{n_l} = \exp\left(-\frac{\Delta E}{k_B T}\right) = \exp\left(-\frac{g_e \mu_B B_0}{k_B T}\right) \tag{2.115}$$

where n_u and n_l are the number of spins in the upper state ($m_S = +\frac{1}{2}$) and the lower state ($m_S = -\frac{1}{2}$), respectively. Quantitative EPR can be utilised in variable temperature studies. [66] At very high temperature, the Boltzmann distribution equals 1, the upwards and downwards transitions are driven by microwaves are equal, hence no EPR signal is seen. When the temperature is lower, the increase of Boltzmann distribution gives rise to a larger EPR signal. More details for the EPR signal at various temperatures are presented by Breeze [42].

Bibliography

[1] C. J. H. Wort and R. S. Balmer, Materials Today **11**, 22 (2008).

[2] C. E. Nebel, arXiv:2005.03884 , 1 (2020).

[3] W. Saslow, T. K. Bergstresser, and M. L. Cohen, Physical Review Letters **16**, 354 (1966).

[4] M. Grundmann, *Physics of Semiconductors*, Vol. 11 (Springer, 2010).

[5] C. Kittel, P. McEuen, and P. McEuen, *Introduction to Solid State Physics*, Vol. 8 (Wiley New York, 1996).

[6] J. Isberg, J. Hammersberg, E. Johansson, T. Wikström, D. J. Twitchen, A. J. Whitehead, S. E. Coe, and G. A. Scarsbrook, Science **297**, 1670 (2002).

[7] J. Singleton, *Band Theory and Electronic Properties of Solids*, Vol. 2 (Oxford University Press, 2001).

[8] B. Van Zeghbroeck, *Principles of Electronic Devices* (University of Colorado, 2011).

[9] C. Kittel, H. Kroemer, and H. L. Scott, American Journal of Physics **66**, 164 (1998).

[10] R. Jones, J. P. Goss, and P. R. Briddon, Physical Review B **80**, 033205 (2009).

[11] A. T. Collins and A. W. S. Williams, Journal of Physics C: Solid State Physics **4**, 1789 (1971).

[12] A. T. Collins, Journal of Physics: Condensed Matter **14**, 3743 (2002).

[13] R. Mildren and J. Rabeau, *Optical Engineering of Diamond* (John Wiley & Sons, Germany, 2013).

[14] V. Y. Yurov, E. V. Bushuev, A. F. Popovich, A. P. Bolshakov, E. E. Ashkinazi, and V. G. Ralchenko, Journal of Applied Physics **122**, 243106 (2017).

[15] F. Peter, Zeitschrift für Physik **15**, 358 (1923).

[16] D. F. Edwards and E. Ochoa, JOSA **71**, 607 (1981).

[17] C. D. Clark, P. J. Dean, and P. V. Harris, Proceedings of the Royal Society A **277**, 312 (1964).

[18] M. Fox, *Optical Properties of Solids* (Oxford University Press, New York, 2001).

[19] B. L. Green, *Optical and magnetic resonance studies of point defects in single crystal diamond*, Ph.D. thesis, University of Warwick (2013).

[20] A. T. Collins, Physica B: Condensed Matter **185**, 284 (1993).

[21] M. Kozák, F. Trojánek, B. Dzurňák, and P. Malỳ, Journal of the Optical Society of America B **29**, 1141 (2012).

[22] R. S. Krishnan, Nature **155**, 171 (1945).

[23] J. R. Hardy and S. D. Smith, Philosophical Magazine **6**, 1163 (1961).

[24] P. L. Diggle, *Single point defect imaging studies in diamond*, Ph.D. thesis, University of Warwick (2019).

[25] J. Barjon, T. Tillocher, N. Habka, O. Brinza, J. Achard, R. Issaoui, F. Silva, C. Mer, and P. Bergonzo, Physical Review B **83**, 073201 (2011).

[26] B. G. Yacobi and D. B. Holt, *Cathodoluminescence Microscopy of Inorganic Solids* (Plenum Press, New York, 1990).

[27] S. W. S. McKeever, *Thermoluminescence of Solids*, Vol. 3 (Cambridge University Press, 1985).

[28] C. Furetta and P. S. Weng, *Operational Thermoluminescence Dosimetry* (World Scientific, 1998).

[29] S. Kamiyama, T. Maeda, Y. Nakamura, M. Iwaya, H. Amano, I. Akasaki, H. Kinoshita, T. Furusho, M. Yoshimoto, T. Kimoto, *et al.*, Journal of Applied Physics **99**, 093108 (2006).

[30] K. Watanabe, S. C. Lawson, J. Isoya, H. Kanda, and Y. Sato, Diamond and Related Materials **6**, 99 (1997).

[31] P. Bäume, M. Behringer, J. Gutowski, and D. Hommel, Physical Review B **62**, 8023 (2000).

[32] D. G. Thomas, M. Gershenzon, and F. A. Trumbore, Physical Review **133**, A269 (1964).

[33] N. A. Bogoslovskiy, P. V. Petrov, Y. L. Ivánov, N. S. Averkiev, and K. D. Tsendin, Semiconductors **50**, 888 (2016).

[34] J. J. Hopfield, D. G. Thomas, and M. Gershenzon, Physical Review Letters **10**, 162 (1963).

[35] F. Williams, Physica Status Solidi (b) **25**, 493 (1968).

[36] J. Krustok, T. Raadik, R. Kaupmees, F. Ghisani, K. Timmo, M. Altosaar, V. Mikli, and M. Grossberg, Journal of Physics D: Applied Physics **54**, 105102 (2021).

[37] Y. Hamanaka, K. Ozawa, and T. Kuzuya, The Journal of Physical Chemistry C **118**, 14562 (2014).

[38] N. A. Bogoslovskiy, P. V. Petrov, Y. L. Ivánov, K. D. Tsendin, and N. S. Averkiev, Physical Review B **98**, 075209 (2018).

[39] A. Alkauskas, J. L. Lyons, D. Steiauf, and C. G. Van de Walle, Physical Review Letters **109**, 267401 (2012).

[40] A. Alkauskas, M. D. McCluskey, and C. G. Van de Walle, Journal of Applied Physics **119**, 181101 (2016).

[41] K. Huang and A. Rhys, in *Selected Papers Of Kun Huang*, Vol. 23, edited by B. F. Zhu (World Scientific, 2000) pp. 74–92.

[42] B. G. Breeze, *Electron paramagnetic resonance studies of point defects in diamond: quantification, spin polarisation and preferential orientation*, Ph.D. thesis, University of Warwick (2016).

[43] U. F. S. D'Haenens-Johansson, *Optical and magnetic resonance studies of point defects in CVD diamond*, Ph.D. thesis, University of Warwick (2011).

[44] A. Vedda and M. Fasoli, Radiation Measurements **118**, 86 (2018).

[45] J. T. Randall and M. H. F. Wilkins, Proceedings of the Royal Society of London. Series A. Mathematical and Physical Sciences **184**, 365 (1945).

[46] P. Avouris and T. N. Morgan, The Journal of Chemical Physics **74**, 4347 (1981).

[47] P. Avouris, I. F. Chang, D. Dove, T. N. Morgan, and Y. Thefaine, Journal of Electronic Materials **10**, 887 (1981).

[48] D. J. Huntley, Journal of Physics: Condensed Matter **18**, 1359 (2006).

[49] M. N. Berberan-Santos, E. N. Bodunov, and B. Valeur, Chemical Physics **317**, 57 (2005).

[50] W. L. Medlin, Physical Review **122**, 837 (1961).

[51] J. C. Phillips, Reports on Progress in Physics **59**, 1133 (1996).

[52] M. N. Berberan-Santos, E. N. Bodunov, and B. Valeur, Chemical Physics **315**, 171 (2005).

[53] R. Chen, Journal of Luminescence **102**, 510 (2003).

[54] R. Chen, Journal of Materials Science **11**, 1521 (1976).

[55] S. Basun, G. F. Imbusch, D. D. Jia, and W. M. Yen, Journal of Luminescence **104**, 283 (2003).

[56] J. T. Randall and M. H. F. Wilkins, Proceedings of the Royal Society of London. Series A. Mathematical and Physical Sciences **184**, 390 (1945).

[57] N. P. Patel, V. Verma, D. Modi, K. V. R. Murhty, and M. Srinivas, RSC Advances **6**, 77622 (2016).

[58] M. Benabdesselam, P. Iacconi, D. Briand, A. Berkane-Krachaï, E. Gheeraert, and H. Kanda, Journal of Applied Physics **88**, 4648 (2000).

[59] M. Puchalska and P. Bilski, Radiation Measurements **41**, 659 (2006).

[60] M. Puchalska and P. Bilski, The thermoluminescence glow-curve analysis using Glowfit-the new powerful tool for deconvolution (2005), `https://www.osti.gov/etdeweb/biblio/20693060`. Accessed September 2021.

[61] A. J. J. Bos, T. M. Piters, J. M. Gómez-Ros, and A. Delgado, Radiation Protection Dosimetry **47**, 473 (1993).

[62] A. J. J. Bos, T. M. Piters, J. M. Gómez-Ros, and A. Delgado, Radiation Protection Dosimetry **51**, 257 (1994).

[63] K. S. Chung, H. S. Choe, J. I. Lee, and J. L. Kim, Radiation Measurements **42**, 731 (2007).

[64] Y. Chen, B. Yu, J. Gou, and S. F. Liu, Journal of Materials Chemistry C **6**, 10687 (2018).

[65] B. Campbell and A. Mainwood, Physica Status Solidi (a) **181**, 99 (2000).

[66] G. R. Eaton, S. S. Eaton, D. P. Barr, and R. T. Weber, *Quantitative EPR* (Springer Science & Business Media, 2010).

Chapter 3

Experimental details

3.1 Samples

3.1.1 GE81-107a-A/B/C

The single-crystal diamond samples GE81-107a-A/B/C were grown using the temperature gradient method by General Electric using an iron and cobalt solvent-catalyst and an aluminum nitrogen getter. From the as-grown sample a {110} oriented plate (approximately 0.85 mm thick) was prepared consisting primarily of {111} and {100} growth sectors (Figure 3.1). This sample was subsequently cut and polished to obtain separate specimens consisting primarily of different {100} (GE81-107a-B) and {111} (GE81-107a-C) growth sectors, as shown in Figure 3.1. Sample GE81-107a-B and GE81-107a-C weigh 7.8 mg and 4.2 mg, respectively. It is worth noting that sample GE81-107a-B is dominated by {100} growth sector, but also involves some other growth sectors. Both GE81-107a-B and GE81-107a-C samples were near colourless but weakly boron-doped and showed characteristic blue to greenish blue fluorescence after UV excitation, with subsequent long-lived phosphorescence.

The average concentration of B_S^0 (uncompensated boron) and N_S^0 in samples GE81-107a-B and GE81-107a-C in the "meta-stable state" (e.g. at room temperature after daylight/laboratory illumination for $>$ 1 hour) were determined by Fourier transform infrared (FTIR) absorption and electron paramagnetic resonance (EPR) spectroscopy, respectively. Those are listed in table 3.1. The distribution

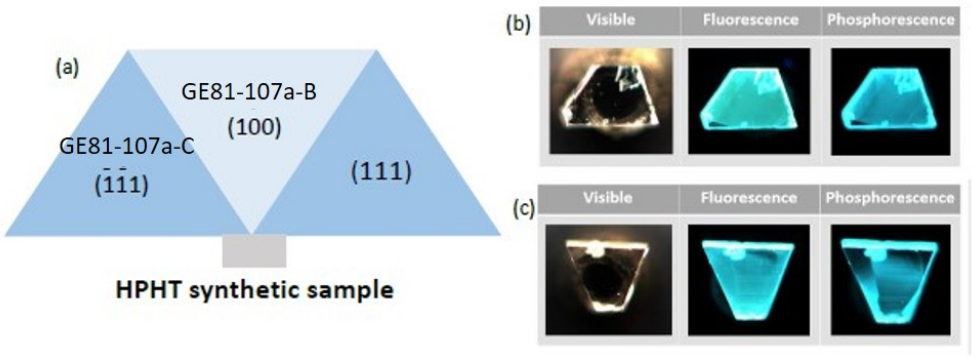

Figure 3.1: Schematic and DiamondView™ images of GE samples
(a) A schematic diagram showing the different growth sectors in a {110} orientated plate taken from an HPHT diamond, with the position of seed shown in grey. The images presented in (b) sample GE81-107a-C ({111} growth sector) and (c) sample GE81-107a-B ({100} growth sector), were recorded with DiamondView™ and show the samples when observed in visible light, room temperature (RT) UV excited photoluminescence (fluorescence) and phosphorescence.

of substitutional boron and substitutional nitrogen are significantly different in {111} and {100} growth sectors. Further measurement of boron and nitrogen concentrations in GE samples under different optical and temperature conditions are presented in Chapter 4 and 5.

Table 3.1: The concentrations of B_S^0 and N_S^0 in samples GE81-107a-B and GE81-107a-C in the "meta-stable state".

(ppb)	GE81-107a-B	GE81-107a-C
$[B_S^0]$ by FTIR	67 ± 10	332 ± 40
$[N_S^0]$ by EPR	145 ± 20	< 4

3.1.2 Sino-01

Single-crystal HPHT diamond sample Sino-01 was grown with iron-cobalt solvent catalyst by Sino-Crystal Diamond Co. Ltd. Sino-01 is a colourless brilliant-cut sample showing blue-green fluorescence and unusual phosphorescence. After UV excitation, Sino-01 shows blue-green phosphorescence for a few seconds, which turns to orange for longer times (Figure 3.2). Sino-01 can be attracted by a magnet, indicating the presence of metal inclusions.

An unknown PL doublet at 693/694 nm is observed in photoluminescence

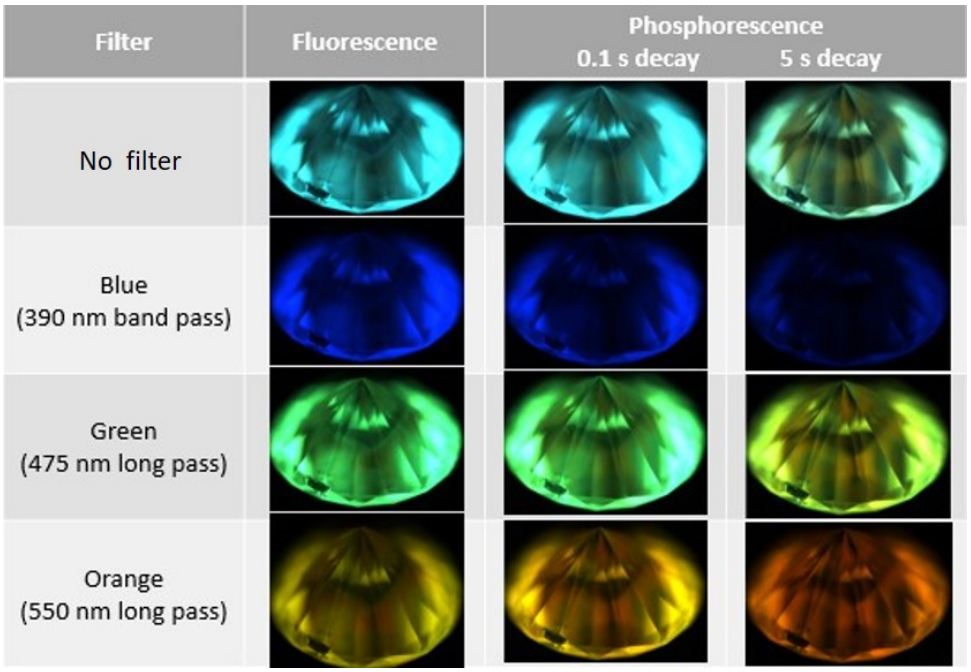

Figure 3.2: DiamondView^{TM} images of Sino-01 sample. UV excited photoluminescence (fluorescence) and phosphorescence (0.1 s and 5 s delay time) with different DiamondView^{TM} filters at RT.

spectra, also reported by NGTC [1]. CL peaks centred at 484 nm and 703.6 nm related to nickel-containing defects are seen, as well as a CL peak at 575 nm indicating the presence of NV^0 defect [2]. Due to the heterogeneity of this diamond sample, it is difficult to determine the boron concentration by CL measurements.

3.1.3 SYN4-10

SYN4-10 is a colourless brilliant-cut HPHT diamond sample on loan from GIA, showing characteristic blue-green fluorescence in DiamondView^{TM}. The blue-green phosphorescence is dominant for a short delay time after a broadband UV lamp excitation, while orange phosphorescence lasts for hours afterwards as shown in figure 3.3.

When sample SYN4-10 was in the "meta-stable state", the concentration of B_S^0 is 350 ± 20 ppb (determined by FTIR), and the average concentration of N_S^0 is 15.5 ± 5 ppb (determined by EPR). Nickel-related defects are seen in the PL spectrum with peaks at 484 nm, 679.5 nm and doublet at 884 nm [2, 3].

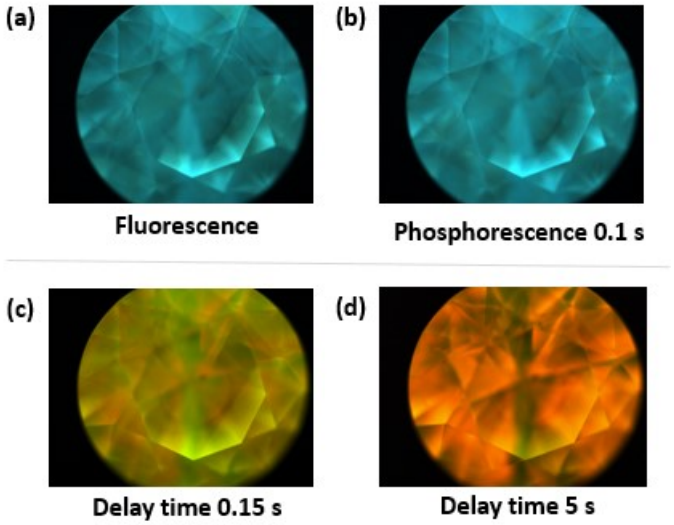

Figure 3.3: DiamondView^{TM} images (a) characteristic blue-green fluorescence (b) phosphorescence in 0.1 s delay time (c)(d) phosphorescence under orange filter in the delay time of 0.15 s and 5 s, respectively.

3.2 Variable-T time-gated luminescence

3.2.1 "Garfield" experimental setup

An experimental system, nicknamed "Garfield", was built to study phosphorescence and TL in diamonds. This system enabled time-resolved bulk spectral data and hyperspectral images to be recorded. (Figure 3.4) The light source is replaceable to adapt different optical excitation requirements, including a pulsed 224 nm laser (HEAG70-224SL, LASER 2000) with 50 mW peak power and a series of continuous wave (CW) lasers of different wavelengths (375 nm, 405 nm, or 450 nm). A five times beam condenser can be used for the adjustment of beam size.

The excitation beam is reflected by a UV-Enhanced mirror, through a beam condenser and the 3 mm central hole on a parabolic mirror, finally shoots on the diamond sample, which is mounted in a variable-temperature stage (THMS600 Linkam) with a quartz window transparent to UV excitation light. The working temperature range of the Linkam stage is from 87 K to 873 K, and the linear heating rate is up to 130 K/min with 0.01 K accuracy. The Linkam stage is mounted on a manual XYZ translation stage to achieve beam focus and optical alignment. The two inch off-axis parabolic mirror collects the sample luminescence. Most of the excitation light reflected by the diamond sample goes through the

central hole on the parabolic mirror and is not collected. An aperture is placed at the focal point of the first achromatic lens (50 mm diameter, $f = 75$ mm) to increase image spatial resolution. The second achromatic lens collimates the light (25 mm diameter, $f = 30$ mm) with an image magnification of approximately 0.8.

The detection beam path is selected by a flip mirror, either to a focus lens and detected by a fibre-coupled spectrometer (ANDOR Shamrock i303) operating between 400 and 1000 nm, or to a replaceable filter, a focus lens and a camera (CMOS, HAMAMATSU, C11440-36U) operating between 400 nm and 1100 nm with a pixel size of 5 μm. The package of replaceable filter involves ten 40 nm-wide bandpass filters centred from 400 nm to 850 nm is used to create time-resolved hyperspectral images of the sample.

As preparation for low-temperature measurement, the air in the Linkam stage chamber is pumped out and replaced by nitrogen gas at 373 K for 5 min to avoid ice formation on the window.

3.2.2 "Garfield" hardware control

An Arduino platform is utilised to control hardware components such as the laser excitation, temperature stage, and detection via the camera or spectrometer with ms time accuracy in phosphorescence and TL experiments. The Arduino platform consists of a micro-controller (Arduino Uno) and the Arduino IDE (Integrated Development Environment) for programming using the C++ language.

3.2.2.1 Phosphorescence experiment

The temperature of the diamond sample is cooled or heated to a certain temperature by the Linkam stage and held till the end of each phosphorescence decay scan. (Figure 3.5) When the temperature is stable, pulsed excitation light source is triggered by TTL signals at a frequency of 10 Hz for a chosen number of pulses; alternatively, the length of CW laser excitation is controlled by triggering a 0.5" shutter (Thorlabs: SH05R) whose reaction time is 26 ± 2 ms. After a variable delay time (generally 0 ms), the detector is triggered by a TTL signal. The number of frames and exposure time (time between two adjacent TTL signals) is set by the Arduino program, the integration time of each frame is set on *HCImage*

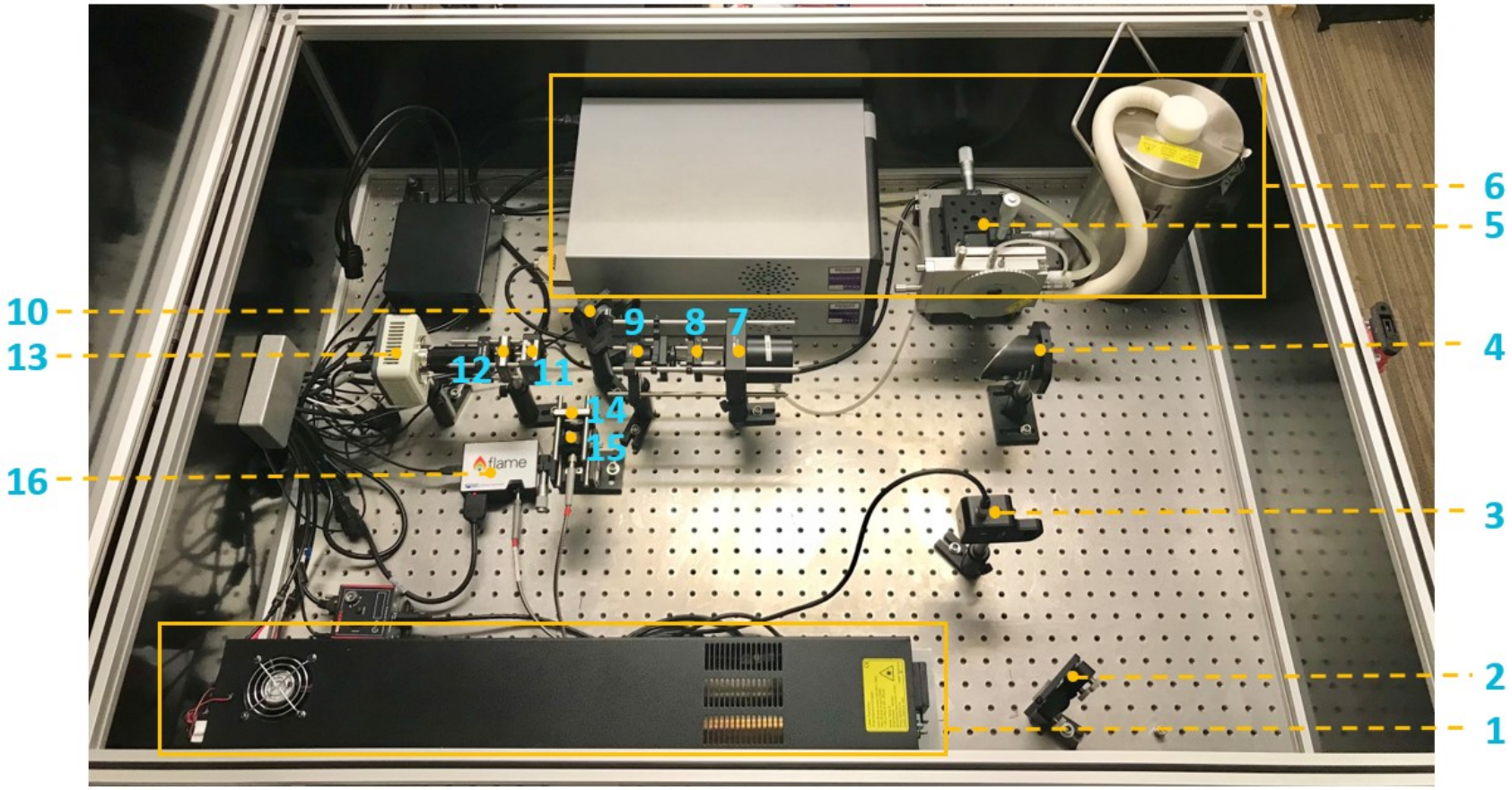

Figure 3.4: Variable-temperature time-gated luminescence experimental arrangement.
1.Excitation light source 2.UV-enhanced mirror 3.Optical beam shutter 4.Off-axis parabolic mirror with holes parallel to focused beam 5.XYZ translation stage 6.THMS600 Linkam temperature-variable stage 7.UV-Vis Plano-convex lens 8.Aperture 9.UV-Vis Plano-convex lens 10.Flip mirror 11.Replaceable filters 12.UV-Vis Plano-convex lens 13.Quantalux CMOS camera 14.UV-Vis Plano-convex lens 15.XY translation stage 16.Fibre-coupled spectrometer.

Live (camera) or *Andor Solis* (spectrometer) software. A *MATLAB* programme is used to obtain average luminescence intensity for the selected area on the phosphorescence images.

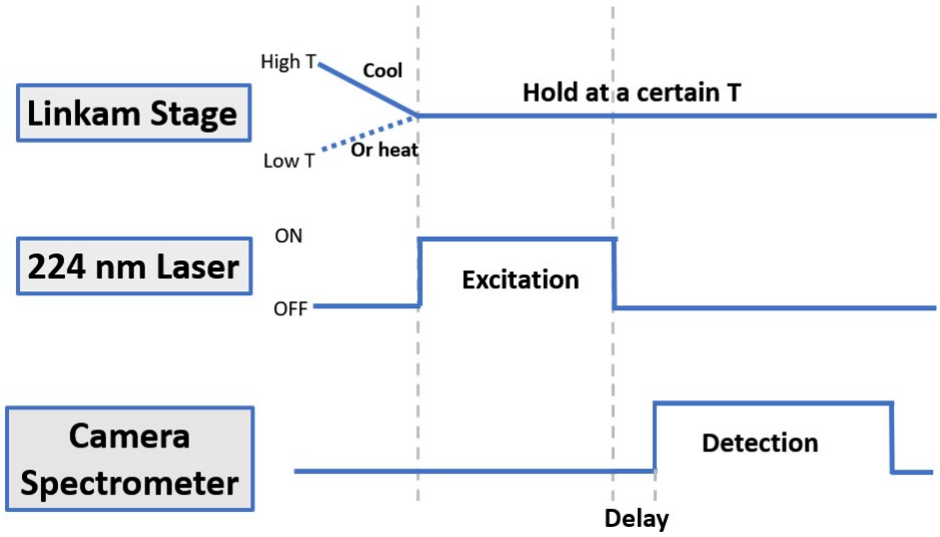

Figure 3.5: Schematic diagram of the phosphorescence experiment sequence.

3.2.2.2 Thermoluminescence experiment

Similar to the phosphorescence experiment, the TL experiment (Figure 3.6) starts with light excitation at a chosen temperature, which is typically in the range 83 K to 300 K. After excitation is removed, the sample is heated up to a final temperature at a linear rate of typically 100 K/min after a variable delay time. Thermoluminescence is detected during the heating stage by a camera or spectrometer. By programming the LINKAM *LINK* software with the required number of ramps, the TL is recorded in real-time. The Linkam variable temperature stage informs the Arduino controller of the start and end of each ramp by sending a TTL signal so that synchronisation of the variable temperature stage, light source, and the detector is possible. As described in Chapter 7, TL glow peaks can also be deconvoluted by setting multiple temperature ramps with the heating rate, limit temperature and TL detection period, all controlled this accurate thermal cleaning process.

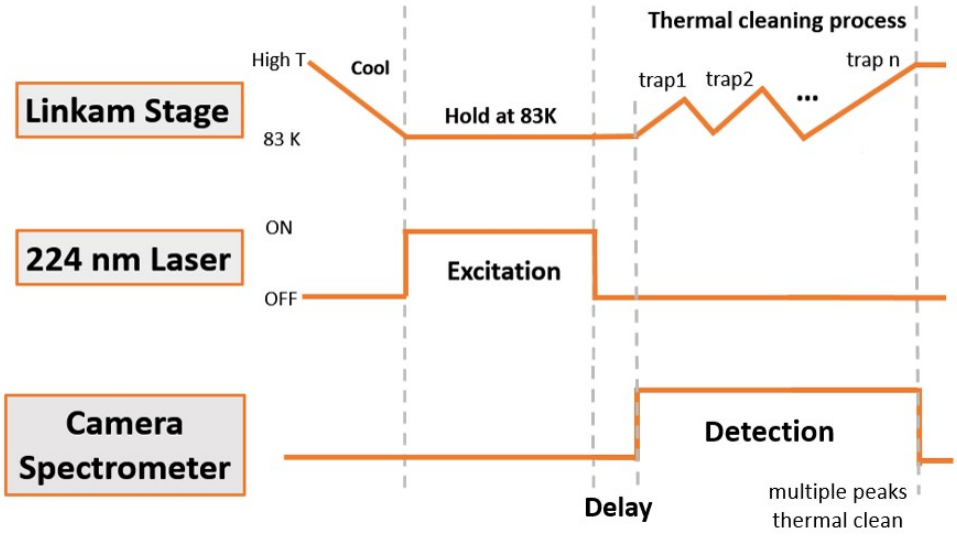

Figure 3.6: Schematic diagram of the thermoluminescence experiment sequence

3.3 EPR

Electron paramagnetic resonance (EPR) is a robust tool for determining the concentration of defects with unpaired spin. An experimental arrangement based on a Bruker E580 EPR spectrometer coupled to an X-band microwave bridge (frequencies between 8-12 GHz) described in this chapter, is utilised to investigate the concentration of the neutral substitutional nitrogen defect (also known as P1 centre or N_S^0) during or after optical excitation at chosen temperatures. The results of these experiments are presented in this thesis.

3.3.1 The EPR spectrometer

3.3.1.1 The magnetic field

The iron-core electromagnet generates a stable and uniform magnetic field B_0 (350 mT with a field homogeneity of $\pm 3 \times 10^{-5}$ mT) over the sample volume. [5] Since the generated field is not linearly related to supplied current and the is also hysteresis, a temperature-stabilized Hall probe (externally calibrated against a known NMR signal) is used to control the current supplied to the magnet and ensure that the field is always at the chosen value. The magnetic field controller provides a reproducible linear scan over a range of the magnetic field around the centre field B_0 for EPR spectrum acquisition.

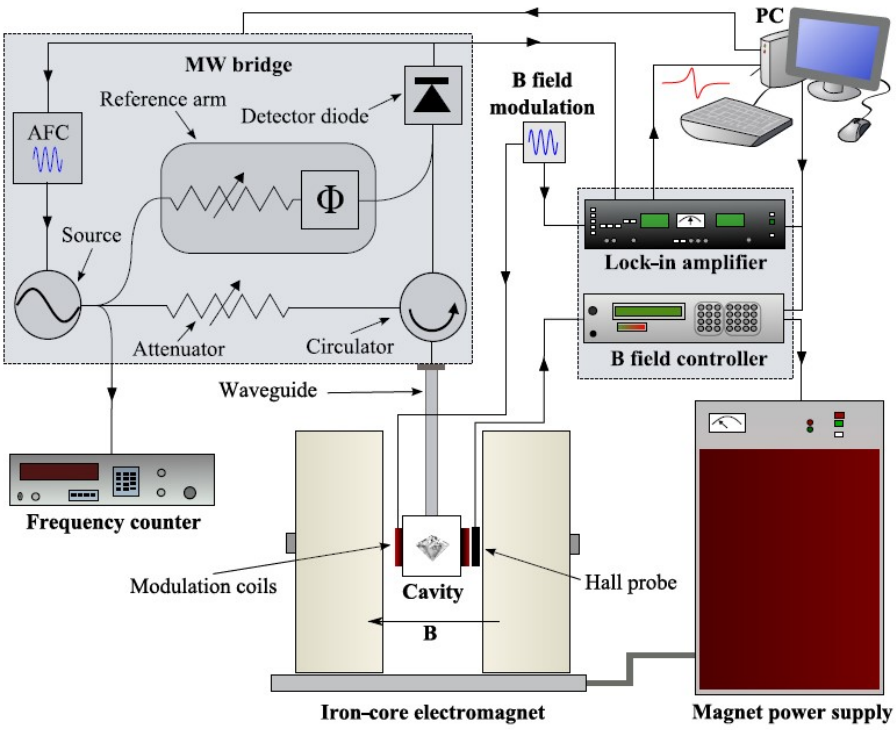

Figure 3.7: A standard EPR spectrometer schematic consists of the magnetic system, the microwave source, the resonance detection system, and control equipment. Figure adapted from [4].

3.3.1.2 The microwave bridge

The microwave radiation at 9.3-9.8 GHz for band microwave bridges is from a Gunn diode. An attenuator precisely controls the microwave power incident on the sample cavity. The microwave output passes through a circulator en route to the microwave resonator/cavity containing the sample. The circulator ensures that only microwaves reflected from the cavity can reach the detector—the Schottky barrier diode as detector coverts the microwave power to an electrical current. An AFC (auto-frequency control) is used to lock the microwave source frequency to the centre frequency of the resonator.

Microwave power from the reference arm is used to "bias" the detector to ensure operation in the linear response regime to optimise sensitivity. The phase shifter ensures the reference arm microwaves are in phase with the signal microwaves reflected from the cavity.

3.3.1.3 Resonators

The resonator, where the sample is mounted, amplifies the EPR signal by increasing the energy density stored. The microwave electromagnetic waves induce currents in the resonator walls which leads to energy dissipation (Ohmic loss). The Q-quality factor shows how efficiently the cavity stores energy and is defined as the ratio of energy stored to that dissipated per cycle. Adjusting the iris (a hole between waveguide and cavity) can achieve impedance matching of the waveguide to the loaded resonator. The system is "critically coupled" when no microwave power is reflected at this interface.

Table 3.2: List of resonators used in this research. All resonators are manufactured by Bruker, adapted from [5].

Resonator	Description	Mode	Q	Frequency
ER 4102ST	Standard rectangular	TE102	2500	X-band
ER 4122SHQ-E	Cylindrical super high Q	TE011	7000	X-band

3.3.1.4 Detection

Phase-sensitive detection of the EPR signal can enhance the spectrometer's sensitivity by several orders of magnitude and is achieved through magnetic field modulation and phase-sensitive or lock-in detection. The magnetic field modulation (amplitude B_m and modulation frequency ω_m (usually 100 kHz)) is superimposed on the much larger Zeeman field. When the field modulation quickly sweeps through part of an EPR signal, the microwave signal reflected from the cavity is modulated at the same frequency ω_m. Lock-in detection works by multiplying the modulated signal with a reference signal of the correct phase that has the same frequency ω_m. After low pass filtering, the amplitude resulting signal is proportional to the first harmonic (derivative) of the EPR line. Noise and electrical interference are suppressed.

The modulation amplitude B_m should be chosen carefully to achieve experiment goals: if an accurate signal lineshape is desired, B_m should not exceed one-tenth of the linewidth; otherwise, a higher B_m can further improve the signal-to-noise ratio, though the EPR signal will be broadened.

The time constant can filter out noise by slowing down the response time of the detection circuit. The longer the time constant, the better the signal-to-noise ratio. To avoid distorting or missing EPR lines, the time constant should be shorter than the conversion time (the length of holding at one magnetic field when scanning).

Defects such as N_S^0 have very long spin-lattice relaxation times (T_1). In order to avoid saturating the EPR signal, very low microwave powers are required resulting in poor sensitivity (slow passage EPR signal proportional to $\sqrt{P_{\mu\omega}}$ in absence of microwave power saturation). An alternative approach is to use "rapid passage" through the EPR transitions (EPR lines swept through in a time short compared to T_1). This approach is described by Edmonds, Cann, and Breeze. [4–6] The rapid passage EPR signal is out of phase with the field modulation. Typical conditions are given in Table 3.3.

Table 3.3: List of experimental parameters used on RP-EPR measurement

Time Constant (ms)	Conversion Time (ms)	Microwave Power (W)	Modulation Amplitude (mT)	Modulation Phase (°)	Sweep Rate (mT/s)
1.28	2.56	Optimised	0.040	90	200

3.3.2 Simulation and fitting of EPR spectra

EPRsimulator is used for simulation and fitting of EPR spectra [7]. It is based on EasySpin [8] in the programming environment MATLAB. EasySpin enables spectral simulation of EPR signals from spin systems with an arbitrary number of electrons and nuclear spins based on the spin Hamiltonian parameters provided. The EPR spectra are loaded into EPRsimulator, as well as the mass of both samples and the $[N_S^0]$ of the reference sample. The linewidths and relative intensities are then optimized by least-squares fitting to obtain $[N_S^0]$ of the test sample. The software can simulate EPR spectra for defects with arbitrary orientation of the applied magnetic field and facilitates the quantitative fitting of multiple defects with overlapping EPR spectra.

3.3.3 Optical-excited variable temperature EPR

In order to investigate the N_S^0 concentration using EPR in the dark, under UV excitation and after UV excitation is removed, an experimental system as shown in figure 3.8 was built.

In terms of optical excitation, a pulsed 224 nm laser (HEAG70-224SL, LASER 2000) with 50 mW peak power, or a 60 W xenon flash lamp (L7685, Hamamatsu) is used as UV excitation light source. The UV light is reflected by a UV-enhanced reflection mirror and focused on a diamond sample mounted on a quartz rod in the EPR resonator. The system is enclosed to ensure laser/UV light safety.

A Bruker ER4131 VT temperature controller is used to control the sample temperature from 160 K to 400 K. The liquid nitrogen cooling system is shown in figure 3.9. The diamond sample is mounted on the top of a hollow quartz rod and placed into the centre of the EPR cavity. The cold nitrogen gas flow is delivered from above. A thermocouple is inserted into the quartz rod and as close as possible to the sample position without extending into the EPR cavity. The temperature difference of the sample position and the thermocouple is calibrated before measurement. In addition, a room temperature nitrogen gas flow keeps passing through the cavity from back to front to ensure no water condenses in the resonator when performing cryogenic measurements.

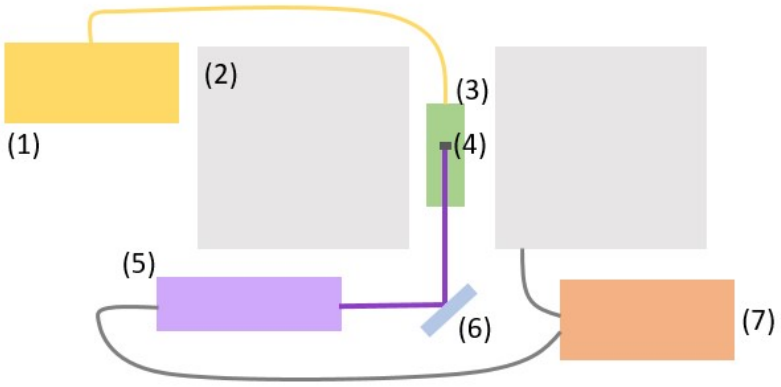

Figure 3.8: Schematic of experimental setup utilised for optical-excited variable T EPR, (1) A Bruker ER4131VT temperature controller as cryostat (2) Bruker E580 spectrometer coupled to an X-band microwave bridge (3) ER4102ST/ ER 4122SH1-E resonator (4) Diamond sample (5)224 nm pulsed laser (6) UV-enhanced reflection mirror (7) National Instruments CompactRIO with NI-9219 and NI-9264 Modules handling a sweeping coil to achieve a faster sweep rate. A black box for safety encloses the UV laser path.

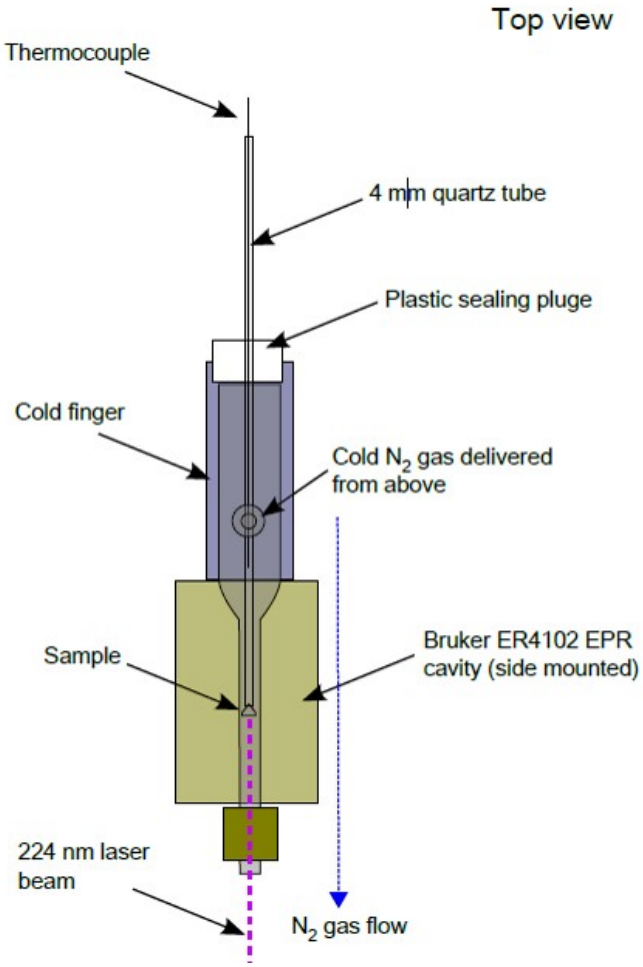

Figure 3.9: Schematic of a partial experimental setup for optical-excited T-variable EPR measurement. The figure is drawn by Andrew Edmonds.

3.3.3.1 Dark vs light measurement at various T

To perform concentration measurements of N_S^0 in the dark and under illumination at each temperature, the sample is first heated up to 400 K to reset the charge distribution, then cooled down to the measurement temperature. The RP-EPR measurement in the dark is conducted first for 500 scans (average the data of 500 scans) at sweep frequency of 10 Hz, spectrum resolution of 1024, and sweep width of 20 mT (sweep rate 200 mT/s). The other experimental parameters are listed in table 3.3. The diamond sample is then illuminated with UV light until saturation of the N_S^0 EPR signal is reached. The RP-EPR measurement is then repeated under UV excitation.

3.3.3.2 Time-resolved EPR

The time-resolved EPR measurement aims to observe the change of $[N_S^0]$ with time after UV excitation is removed, the EPR signal can either decay or recover. As shown in figure 3.10, the UV excitation is maintained on the diamond sample until the EPR signal is optically saturated. The illumination is removed and the EPR spectrometer triggered by LabVIEW software to start RP-EPR measurement in the dark at sweep frequency of 10 Hz, resolution of 1024, sweep width of 10 mT (sweep rate 100 mT/s), and other parameters as in table 3.3. The duration of measurement depends on the decay or recovery lifetime of the N_S^0 EPR signal in the sample of interest. The substitutional nitrogen concentration, given by the integrated area of the central peak in EPR spectra, is calculated by a script written in MATLAB software. Hence the decay or recovery curve of the N_S^0 concentration versus delay time can be plotted.

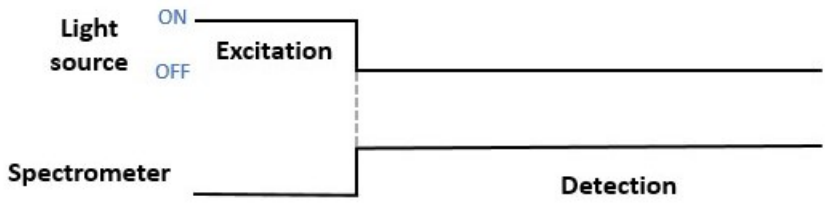

Figure 3.10: Time-resolved EPR to measure the decay or recovery of the concentration of substitutional nitrogen neutral after optical excitation. The measurement is repeated multiple times to improve the SNR.

3.4 Fourier-transform infrared absorption

The Fourier-transform infrared (FTIR) spectrometer simultaneously collects high-resolution spectral data over a wide spectral range, instead of measuring intensity in a narrow wavelength range, incrementing the wavelength and repeating, like a dispersive spectrometer. Modern dispersive spectrometers use array detectors rather than single point detectors.

The raw data (so-called interferogram) is generated by a Michelson interferometer as shown in Figure 3.11. A broadband light source containing the full spectrum of wavelengths to be measured enters into the Michelson interferometer.

The light is split into two beams by the beamsplitter: ideally, 50% of the light is reflected to the fixed mirror, and 50% is transmitted to a moving mirror. An interferogram is generated by recording the intensity of the resulting interference from the two beams as the optical path difference between those two arms is varied. The FTIR absorption spectrum can be obtained from the inverse Fourier-transform of the interferogram.

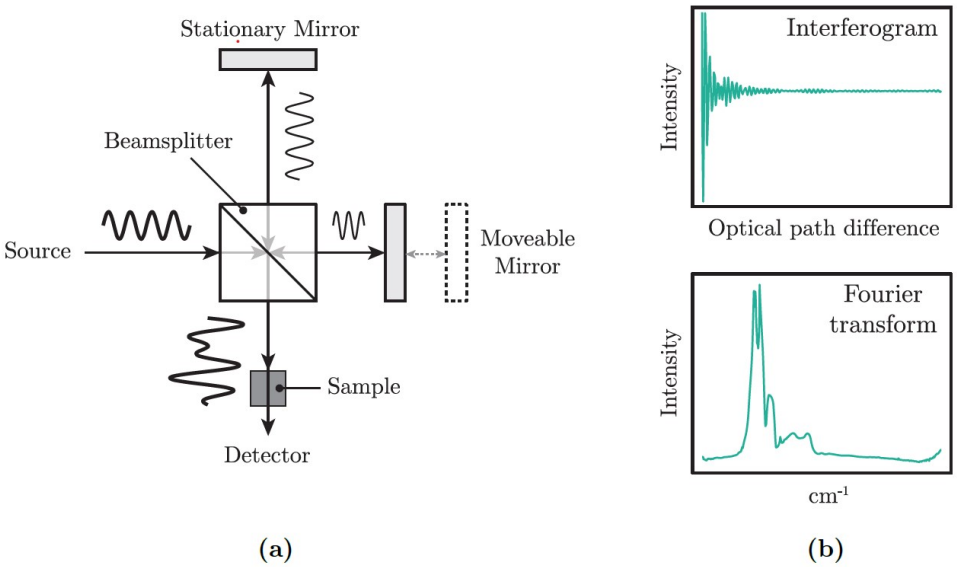

Figure 3.11: (a) The Michelson interferometer setup. (b) an example is a background-corrected interferogram (top), which reveals the absorption in wavenumbers upon taking the Fourier transform (bottom). Adapted from [9].

3.4.1 Optical-excited variable temperature FTIR

The experimental arrangement (Figure 3.12) utilizes a Thermo Fisher Scientific Nicolet iS50R FTIR spectrometer to perform the optical-excited variable temperature FTIR measurements in this thesis. The key components of the commercial FTIR spectrometer are ETC Ever-Glo IR source (20-9600 cm^{-1}), KBr beamsplitter (350-7400 cm^{-1}), and KBr coated DGTC detector (350-12500 cm^{-1}).

The light source for optical excitation is a 224 nm pulsed laser (HEAG70-224SL, LASER 2000), reflected by a UV-enhanced mirror towards the diamond sample. This is mounted on a 1 mm or 1.25 mm aperture in the IR optical path (the aperture allows only the central area of the samples to be measured) in the variable temperature stage (THMS600 Linkam) using silver thermal paste. The cryostat

operates across a temperature range of 273 K to 573 K. An Arduino triggers the optical excitation and the FTIR spectrometer according to the programming procedure.

To investigate the change of $[B_S{}^0]$ in diamond under various optical excitation and temperature conditions, the FTIR spectrum was collected as follows. When measuring in the dark, the background spectrum is taken without a diamond sample in the cryostat. When measuring boron concentration under UV excitation, the background is taken with the diamond sample mounted in the Linkam stage and in the dark. Then the diamond sample is illuminated with the 224 nm laser light at a frequency of 10 Hz for sufficient time to drive the B_S^0 concentration to an optical saturation value and the FTIR spectrum is acquired with the UV light source on. Hence the boron defect FTIR spectrum and the difference of $[B_S{}^0]$ between the dark and illuminated state is obtained.

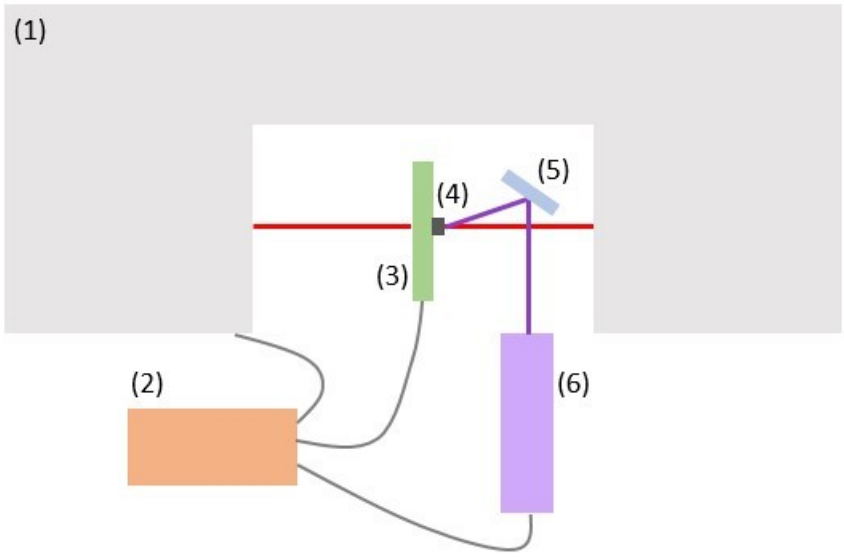

Figure 3.12: Schematic of optical-excited variable T FTIR experimental setup. (1) Nicolet iS50R FTIR spectrometer (2) Arduino (3) THMS600 Linkam Stage (4) Diamond sample (5) UV-enhanced Mirror (6) 224 nm pulsed laser. A black box for laser safety encloses the UV light.

3.4.2 Time-resolved FTIR

The time-dependent changes in the concentration of boron neutral in diamond after optical excitation is removed can be studied by time-resolved FTIR using the experimental setup described above. Similar to the phosphorescence and time-

resolved EPR experiment, the diamond sample is cooled or heated to a certain temperature, then the optical excitation applied (224 nm pulsed laser at a frequency of 10 Hz, a pulse with of 100 μs). When saturation of the B_S^0 signal is reached, the excitation is removed and the FTIR spectrometer is triggered to start data collection immediately (Figure 3.10). With a scanning resolution of 10 cm^{-1}, a spectrum can be recorded every 210 ms over a time interval chosen to allow study of the recovery of the B_S^0 signal. The measurement was repeated multiple times to improve the signal to noise. The background for this measurement is taken with the diamond in the cryostat in the dark at the room temperature.

3.4.3 FTIR mapping

FTIR mapping was utilized to study the distribution of B_S^0 in diamond samples. This was carried out with a Thermo Scientific Nicolet iN10 MX FTIR microscope with a spectral range of 4000 to 650 cm^{-1}. In order to achieve faster acquisition time, higher sensitivity and spatial resolution, a liquid nitrogen cooled MCT-A detector was used. The LN_2 cooled detector requires 30 min for cooling and stabilization before collection. The FTIR mapping spectra were obtained in transmission mode with a scanning step size of 25 μm and a spectral resolution of 4 cm^{-1}.

3.5 Photoluminescence

Apart from the homemade Garfield experimental system mentioned above, several Raman/photoluminescence spectrometers with a series of different laser excitation wavelengths were employed for photoluminescence measurements. The details are listed in table 3.4. All these Raman/photoluminescence spectrometers are equipped with a motorised XYZ stage for sample focusing and mapping.

For variable temperature PL measurements, a liquid nitrogen stage (THMS600 Linkam) operating over a temperature range of 83 K up to 873 K was installed in the Raman microscopes. Silver thermal paste is used to mount the diamond samples in the cryostat for good thermal contact. For cryogenic measurement, air and water vapour should be pumped out of the Linkam stage by N_2 flow at 473 K before cooling.

Table 3.4: The lasers and grating densities used for PL measurements.

Raman Microscope	**Laser type**	**Laser line (nm)**	**Grating ($\mathbf{l\,mm^{-1}}$)**
Renishaw inVia Reflex Raman Microscope	HeCd	325.0	3600
	HeCd	441.6	2400
	HeNe	632.8	1800
Renishaw inVia Raman Microscope	Solid State	514.5	1800
	Solid State	785.0	1200
Renishaw inVia Reflex Raman Microscope	Solid State	531.7	1800

An Edinburgh Instruments FS5 spectrofluorometer has been employed to measure the excitation dependence of photoluminescence in diamonds at room temperature. The excitation wavelength range is selected as 200 - 500 nm in this research. The built-in grating spectrometer is equipped with a single-photon PMT detector to measure the emission spectrum over a range of 200 - 800 nm.

3.6 Cathodoluminescence(CL)

A scanning electron microscope (SEM) equipped with a Gatan Mono CL system (so-called SEM-CL) was employed for CL imaging and spectral analysis. Diamond samples were coated with a layer of amorphous carbon with a thickness of approximately 10 nm in order to avoid a build-up of charge at the surface under electron beam excitation. To determine the substitutional boron concentration in the GE samples, bound exciton CL measurements were performed at liquid nitrogen temperature (77 K). The accelerating voltage of the incident electron beam is set to 15 keV. The focused electron beam spot size is approximately 100 nm. Hence the boron concentration obtained by this method is a point or local measurement. In the CL study of sample Sino-01, the CL images were collected with a chamber pressure of 20 Pa, 15 keV accelerating voltage and a 1.0 nA probe current. The CL spectra were collected at a resolution of approximately 11 nm, which causes some spectral features to broaden.

Bibliography

[1] Z. Song, T. Lu, S. Tang, J. Ke, J. Su, B. Gao, N. Hu, J. Zhang, J. Zhou, *et al.*, Journal of Gemmology **35** (2016).

[2] A. M. Zaitsev, *Optical Properties of Diamond: A Data Handbook* (Springer Science & Business Media, New York, 2001).

[3] I. A. Dobrinets, V. G. Vins, and A. M. Zaitsev, *HPHT-Treated Diamonds*, Vol. 181 (Springer Science & Business Media, New York, 2013).

[4] A. M. Edmonds, *Magnetic resonance studies of point defects in single crystal diamond*, Ph.D. thesis, University of Warwick (2008).

[5] B. G. Breeze, *Electron paramagnetic resonance studies of point defects in diamond: quantification, spin polarisation and preferential orientation*, Ph.D. thesis, University of Warwick (2016).

[6] B. L. Cann, *Magnetic resonance studies of point defects in diamond*, Ph.D. thesis, University of Warwick (2009).

[7] M. W. Dale, *Colour centres on demand in diamond*, Ph.D. thesis, University of Warwick (2015).

[8] S. Stoll and A. Schweiger, Journal of Magnetic Resonance **178**, 42 (2006).

[9] P. L. Diggle, *Single point defect imaging studies in diamond*, Ph.D. thesis, University of Warwick (2019).

Chapter 4

Substitutional boron-related charge transfer

4.1 Background

Boron atoms can be introduced into the diamond lattice as a substitutional impurity during the growth. Boron can present as a mantle element for natural diamonds or as a dopant for synthetic diamonds. [1] The boron-induced absorption in the visible region leads to blue to dark-blue appearance of diamonds. [1, 2] Boron aggregates have been theoretically predicted to exist, but no experimental evidence has been discovered. [3]. This research focuses on a time-resolved spectroscopic study of the substitutional boron defect, using Fourier-transform infrared (FTIR) absorption, to understand the role of substitutional boron in charge transfer processes, which is essential to be able to interpret subsequent measurements of the phosphorescence and thermoluminescence described in Chapters 6 and 7.

4.1.1 Substitutional boron

Substitutional boron is a shallow acceptor in diamond with an ionization energy of 368.5 ± 1.5 meV. [1, 4–6] Boron doping makes diamond a p-type semiconductor and at high doping concentrations ($\geq 5 \times 10^{20}$ cm^3), the diamond becomes metallic and at low temperatures a superconductor. [7] Hence boron is widely used as a dopant in the CVD and HPHT synthesis of diamond. For HPHT growth under different conditions, the incorporation efficiency of boron in various growth sectors

is very different. [1, 6, 8, 9] The higher HPHT crystallization temperature results in increased uncompensated boron concentration in the {111} and {001} growth sector. [8] The rate of uptake boron by various growth sectors of HPHT diamond is {111} > {110} > {100}, {113}. [10]

A boron atom in a substitutional site in the diamond lattice bonds to the four neighbouring carbon atoms. This system can be treated as a negatively charged nucleus and a bound positive hole. Therefore, the spectral features of boron, as a shallow acceptor in diamond, can be described by a quasi-hydrogen model. [11] The electronic states follow a Rydberg series (figure 4.1)

$$E_n = \frac{e^4\, m^*}{8\,\varepsilon_0{}^2 \varepsilon_r{}^2 h^2}\,\frac{1}{n^2} \qquad (n = 1, 2, 3, ...), \tag{4.1}$$

where e is the elementary electric charge, m^* the effective mass of a bounded hole, ε_0 the electric constant, ε_r the relative permittivity of diamond, and h Planck's constant. A small splitting of the excited states results from states at the top of the valence band. [12]

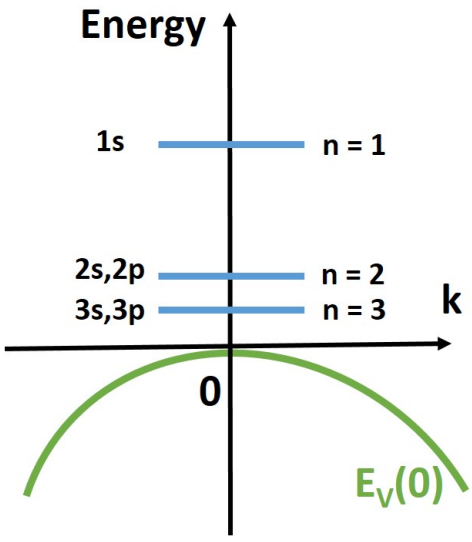

Figure 4.1: The schematic of electronic states of a hydrogen-like boron acceptor. $E_V(0)$ is the energy of the maximum of the valence band.

4.1.2 Determination of substitutional boron concentration

Several spectroscopic methods, such as cathodoluminescence (CL) spectroscopy, FTIR absorption spectroscopy, Raman spectroscopy have been correlated with the

boron concentration. Secondary ion mass spectrometry (SIMS) can be used to determine the atomic boron concentration in sample. [1, 13] The hole concentration in a diamond can be determined by Hall effect measurements. [4] The determined concentration needs some work since the Hall effect measurement gives the free hole concentration, if there is no compensation or if the fraction of acceptors which are compensated is known, then the boron acceptor concentration can be calculated from the measured hole concentration. [4] The intensity of the boron bound exciton CL signal is assumed to be independent of the boron acceptor charge states, therefore, it is used to quantify the total substitutional boron concentration. The method for determining uncompensated boron concentration by FTIR is developed by Collins and widely used for boron acceptor studies. [14] Raman spectroscopy is applied for heavily boron-doped diamond samples since boron-related features can only be induced when the boron concentration greater than 10^{20} cm^{-3} [1].

4.1.2.1 Determination of [B_S] by CL

In a doped diamond, the phonon-assisted luminescence lines from bound exciton recombination are shifted to lower energy by the localization energy E_{loc} (binding energy) compared to the free exciton recombination. E_{loc} is equal to 55.0 meV for the neutral boron-bound exciton (BE). [15] The luminescence line from neutral-boron bound exciton and TO phonon recombination is at 237.7 nm (5.217 eV). [15]

At low temperature (77 K to 170 K), the total boron concentration in a diamond sample can be quantified using equation (4.2) or (4.3), since the peak intensity ratio between FE_{TO} and BE_{TO} is proportional to the boron concentration when it is below 6×10^{17} cm^{-3} (3.4 ppm). [2, 15–17]

$$[B_S] = 1.26 \times 10^{17} R \ [\text{cm}^{-3}] \tag{4.2}$$

$$[B_S] = 7.16 \times 10^{2} R \ [\text{ppb}] \tag{4.3}$$

where R equals I_B/I_F (the ratio of bound exciton over free exciton). The concentration is determined irrespective of the charge state of B_S because of carrier injection neutralisation. [15]

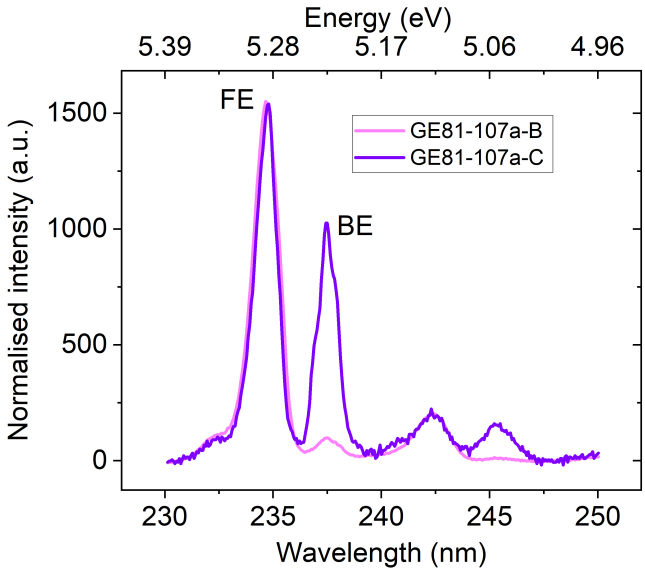

Figure 4.2: The CL spectra of sample GE81-107a-B ({001} growth sector) and GE81-107a-C ({111} growth sector) at 80 K with the free exciton peak (FE) and boron bound exciton peak (BE) labelled.

The concentration of substitutional boron in GE samples measured by bound exciton CL at 80 K is given in Table 4.1. The boron concentration in the {111} growth sector is significantly higher than that in the {001} growth sector. The boron is heterogeneously incorporated into each growth sector, and this boron concentration was obtained by a single spot measurement.

Table 4.1: The concentration of total substitutional boron (B_S) in GE samples determined by CL measurement at 80 K. The error given is for single spot measurement. For an inhomogeneous sample the average concentration value could differ significantly from this point measurement.

GE81-107a-B {001}	GE81-107a-C {111}
$[N_S] > [B_S]$	$[N_S] < [B_S]$
39 ± 5 ppb	405 ± 20 ppb

4.1.2.2 Determination of $[B_S^0]$ by FTIR

The characteristic FTIR absorption spectra of B_S^0 recorded at room temperature is shown in figure 4.3. It consists of a series of bands including the boron-induced one-phonon absorption broadband from approximately 1000 to 1332 cm^{-1} with a hump at 160 meV (1290 cm^{-1}). IR absorption peaks in the two- and three-phonon intrinsic region arise from internal transitions to excited states which are at 304

meV (2457 cm^{-1}), 347 meV (2802 cm^{-1}), and 363 meV (2929 cm^{-1}), respectively. [4, 6, 14] Similar absorption spectra of boron can be seen in ^{13}C diamond with the bands shifts to higher energies by 0.4 - 1.5 meV. [18] The photoconductivity threshold places the ground state of the boron acceptor at 368 meV above the valence band edge. [1]

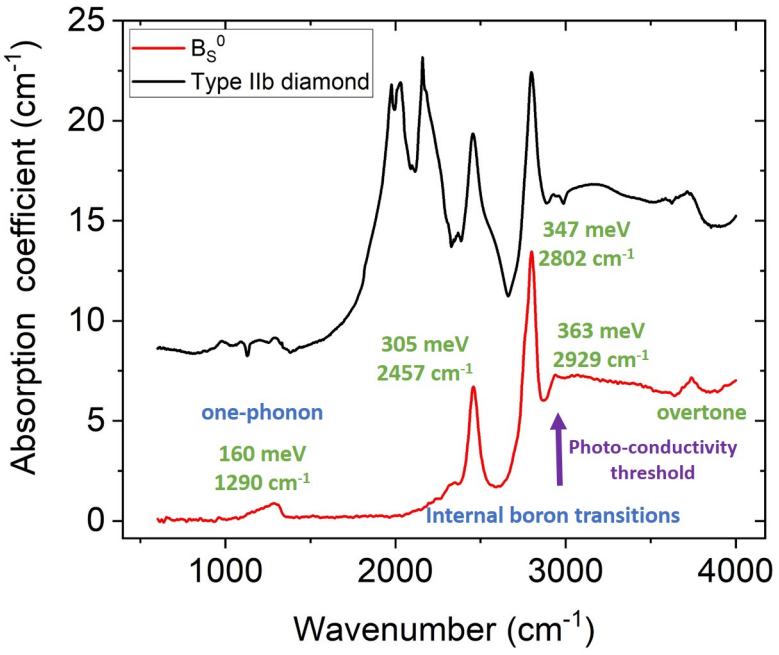

Figure 4.3: The FTIR spectra of a type IIb diamond sample GE81-107a-C and uncompensated substitutional boron with boron-related peaks at 160 meV (one-phonon absorption), 305 meV, 347 meV, 363 meV labelled (intrinsic type IIa spectrum has been removed, leaving only the boron-related features).

The population distribution of different energy levels are T-dependent, so the relative height of these boron internal transitions are temperature-dependent. [9] The peaks at 2457 cm^{-1} and 2802 cm^{-1} sharpen up at low temperature: there is no substructure under 2457 cm^{-1} peak, while the 2802 cm^{-1} exhibits substructure at 77 K. [9] The fine structure of excited states consisting of 31 lines has been observed by Fourier-transform photocurrent spectroscopy (FTPS) at 77 - 160 K. [19]

The following determination of uncompensated boron concentration by FTIR absorption are all limited to measurements at room temperature.

The integrated intensity of the 2802 cm^{-1} absorption band, which is approxim-

ately 50 times stronger than that of 1290 cm^{-1} band, therefore is usually used to quantify boron when concentration is low. The uncompensated boron concentration in ppm is given by

$$[N_A - N_D] = (0.0350 \pm 0.0028) \times H_{2802} \tag{4.4}$$

where H_{2802} in cm^{-1} is measured from the maximum to a straight-line baseline which is tangential to the spectrum at 2664 cm^{-1} to 2891 cm^{-1} [14]; Or

$$[N_A - N_D] = (5.53 \pm 10^{-4}) \times I_{2802} \tag{4.5}$$

where I_{2802} in cm^{-2} is the integrated intensity of 2802 cm^{-1} peak. [1]

As the boron concentration increased up to 5 ppm, the 2802 cm^{-1} peak is significantly broadened compared to the 2457 cm^{-1} peak. The uncompensated boron concentration in ppm determined by 2457 cm^{-1} peak height in cm^{-1} is given by [14]

$$[N_A - N_D] = (0.105 \pm 0.008) \times H_{2457} \tag{4.6}$$

For heavily boron-doped diamond, the line width of the electronic transitions at 2457 cm^{-1} and 2802 cm^{-1} can dramatically increase from approximately 7 meV to 30 meV due to the overlapping boron bound hole orbitals, or peak intensity can be saturated when measuring. [6, 14] Therefore, the one-phonon absorption can be used to determine the boron concentration up to 50 ppm by [14]

$$[N_A - N_D] = (1.00 \pm 0.15) \times H_{1290} \tag{4.7}$$

4.1.3 The decay of 2802 cm^{-1} absorption peak

In type IIa natural diamonds that show long-lived blue-green phosphorescence at room temperature, the decay of the boron-induced 2802 cm^{-1} absorption peak, which lasts for a few seconds after UV excitation, has been observed. [20, 21] In this work, the decay of the 2802 cm^{-1} absorption peak in different growth sectors of type II HPHT diamonds is measured as a function of temperature.

4.2 Experimental results

4.2.1 Distribution of uncompensated substitutional boron

The FTIR mapping on GE samples has been performed at room temperature using a Thermo Scientific Nicolet iN10 MX FTIR microscope described in Chapter 3.4. The concentration of uncompensated substitutional boron is calculated by equation 4.5. As shown in figure 4.4, overall, the [B_S^0] in the {111} growth sector is significantly greater than that in the {001} growth sector.

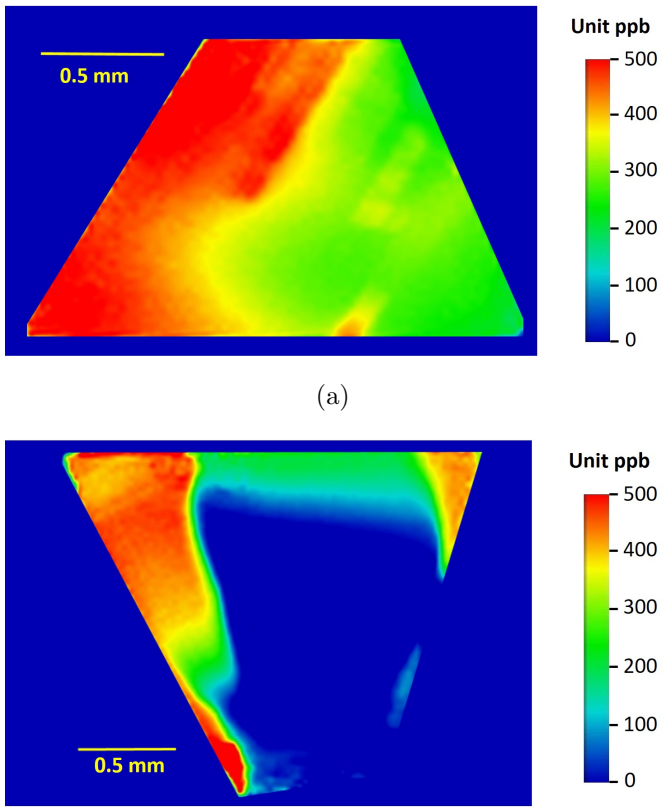

Figure 4.4: Distribution of uncompensated boron concentration in GE samples determined from the height of 2802 cm^{-1} peak at RT. (a) GE81-107a-C ({111} growth sector). (b) GE81-107a-B ({001} growth sector)

In sample GE81-107a-C ({111} growth sector), the distribution of B_S^0 is relatively homogeneous, varying by a factor of 2. In sample GE81-107a-B ({001} growth sector), the low boron-doped middle area is homogeneous, and the high concentration of boron at the edges on both sides indicates higher [B_S^0] in other neighbouring growth sectors in the plate. Therefore, for FTIR measurements on

{001} growth sector, an aperture is placed in front of the GE81-107a-B sample to block the edge areas.

The point CL measurements shown in Table 4.1 give the total boron concentration and the FTIR mapping gives the distribution of the uncompensated boron acceptor concentration. CL imaging of the boron bound exciton would allow direct comparison of the total boron concentration with the uncompensated boron acceptors concentration, which would be expected to correlate with the concentration of substitutional nitrogen compensating the boron acceptor (e.g. N_S^+).

4.2.2 T-dependence of B_S^0 concentration

The experimental method for obtaining the FTIR spectra presented in figure 4.5 and 4.6 is introduced in Chapter 3.4. In both GE samples, the height of boron-related absorption peaks collected in "dark" (no visible/UV excitation) decreases as temperature increases when varying from RT to 423K (Figure 4.5).

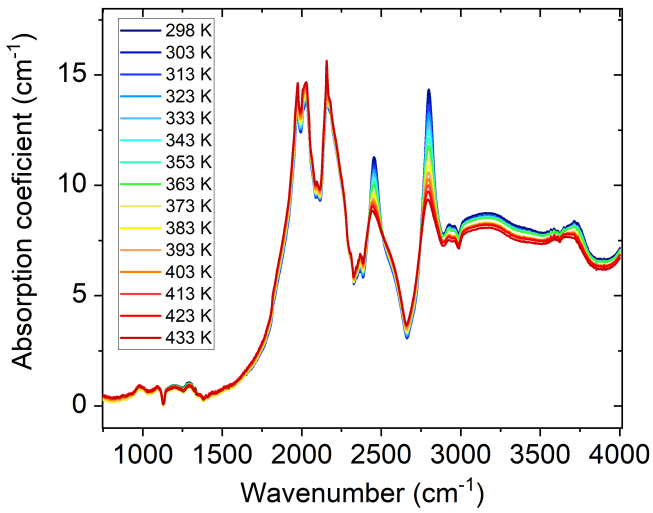

Figure 4.5: FTIR spectra of sample GE81-107a-C were recorded in the dark at temperatures between RT to 433 K.

Each FTIR spectra shown in figure 4.6 presents the spectral difference between under 224 nm excitation and in the "dark" at a specific temperature between room temperature and 433 K. Only boron-related absorption features are seen. Hence, no other defects are detected by FTIR absorption in GE samples when excited by the

224 nm pulsed laser excitation. The concentration change of uncompensated boron by UV excitation is temperature-dependent, it decreases when the temperature climbs. At temperatures above 400 K for GE81-107a-B ({001} growth sector) or 430 K for GE81-107a-C ({111} growth sector), the neutral boron concentration can be barely increased by 224 nm excitation.

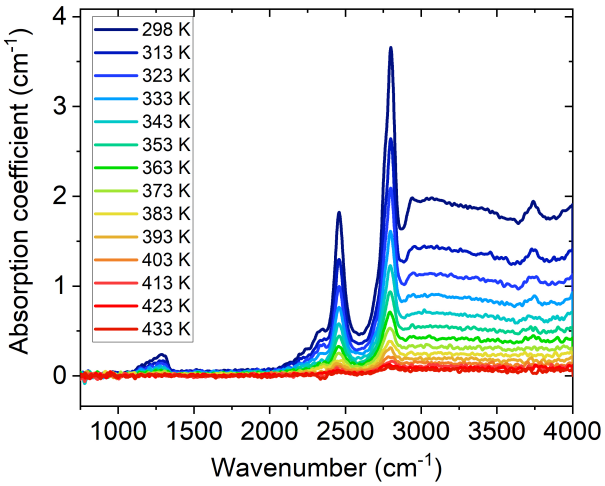

Figure 4.6: FTIR spectra of sample GE81-107a-C recorded under 224 nm laser excitation using the sample in the dark background at each temperature between RT to 433 K.

Figure 4.7 shows that the height of change in boron-related absorption peaks at 1290 cm^{-1}, 2457 cm^{-1}, 2802 cm^{-1}, and 2935 cm^{-1} vary differently with temperature. This is because the energy level population distribution varies with temperature. The equations (Chapter 4.1.2.2) proposed in the literature for determining uncompensated boron concentration calculation can only be applied for room temperature. [1, 4]

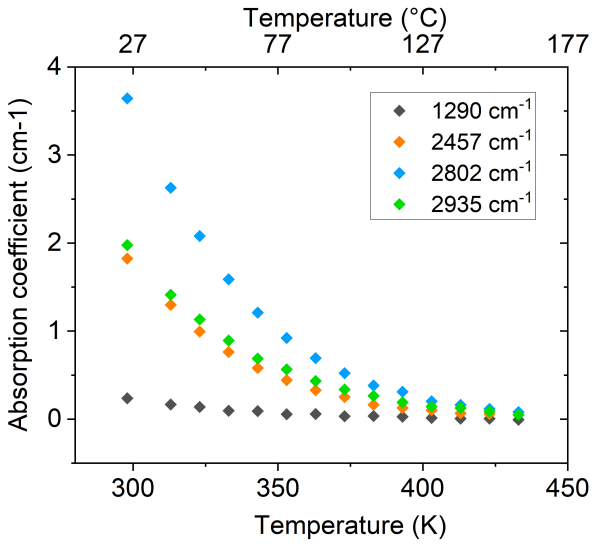

Figure 4.7: Variation in selected absorption peaks in the FTIR spectra of sample GE81-107a-C in figure 4.6 vary with temperatures between RT to 433 K.

Figure 4.8 summarizes the temperature dependence of 2802 cm^{-1} absorption peak in GE samples under different conditions. $[B_S^0]$ in the dark gradually decreases as the temperature increasing. Almost all substitutional boron defects are compensated in the dark when the temperature approaches 540 K for GE81-107a-B or 575 K for GE81-107a-C. In addition, the bandgap excitation always increases $[B_S^0]$, at a temperature between RT and approximately 400 K for sample GE81-107a-C or RT to around 430 K for sample GE81-107a-B. The origin of different transitions within the 2802 cm^{-1} peak are complex: some arise due to transitions from a thermal ground state and will decrease with temperature, while others originating at a thermally excited state will increase with temperature. [22] Without knowledge of the transition moments, it is not possible to predict the intensity of the band as a function of temperature and therefore it is presented phenomenologically here.

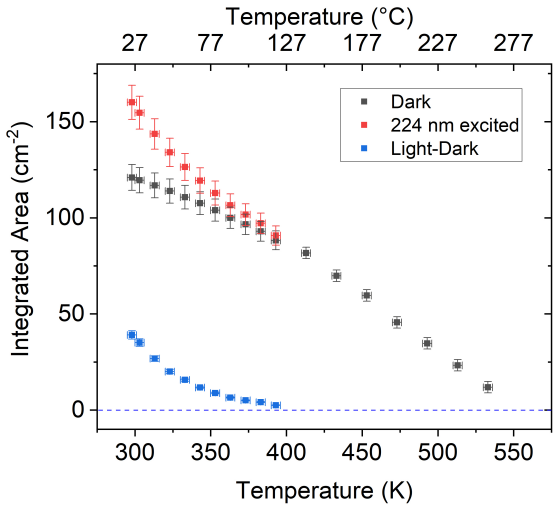

(a)

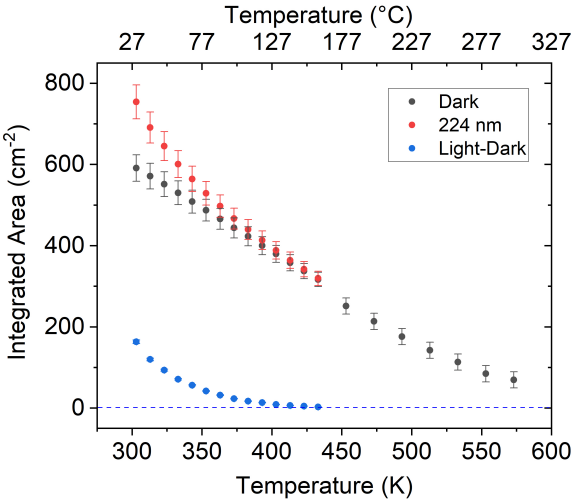

(b)

Figure 4.8: The T-dependence of the integrated area of 2802 cm^{-1} peak in the dark, under 224 nm laser excitation, and the difference between in dark and under light. (a) GE81-107a-B ({001} growth sector). (b) GE81-107a-C ({111} growth sector)

4.2.3 The decay of 2802 cm^{-1} absorption peak

The decay of 2802 cm^{-1} absorption peak in GE samples after 224 nm pulsed laser excitation has been monitored by the time-resolved FTIR experiment described in Chapter 3.4.

4.2.3.1 Decay curves

The decay curves of 2802 cm^{-1} absorption peak integrated intensity at selected temperatures between 303 K to 373 K in GE81-107a-B and GE81-107a-C recorded in the "dark" after UV excitation was removed are plotted in figure 4.9. The data is plotted on a log time scale to emphasise the change in the decay rates. Consistent with literature reports, the decay of 2802 cm^{-1} absorption peak occurs during phosphorescence. [20, 21] At a specific temperature, the $[B_S^0]$ decay rate in {111} growth sector where boron concentration is greater, is slower than that in {001} growth sector.

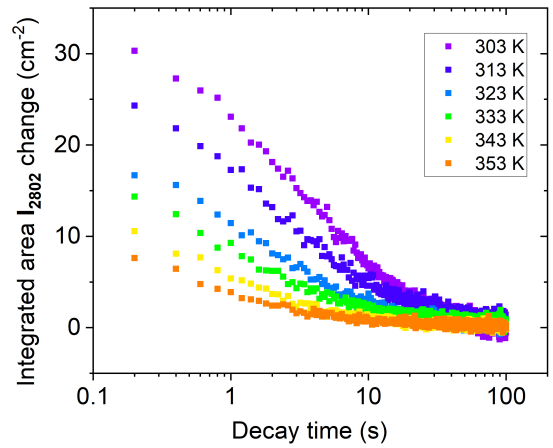

(a)

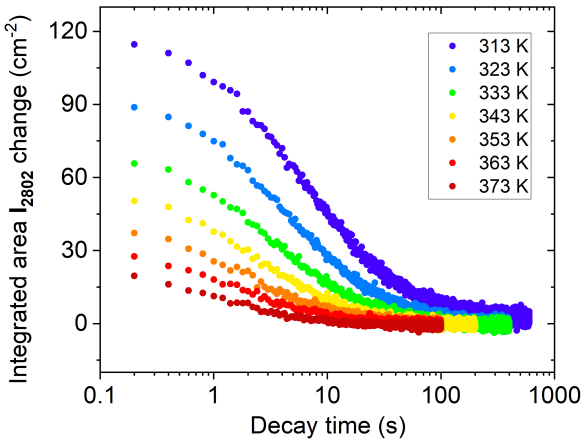

(b)

Figure 4.9: The integrated area of 2802 cm^{-1} peak decay curves in sample GE81-107a-C recorded after excitation with 224 nm laser at a series of temperatures between 303 K to 373 K. (a) GE81-107a-B ({001} growth sector). (b) GE81-107a-C ({111} growth sector)

4.2.3.2 The fitting of decay curves

The decay curves of 2802 cm^{-1} absorption peak integrated intensity can be fitted by various functions introduced in Chapter 2.3.4, including multiple components fitting function (two simple exponential components), modified stretched exponential function (MSE), and complex power-law function (CPL). For decay curves at most temperatures, two components are obtained when using multiple components fitting functions. However, three simple exponential components (with an additional very weak and short-lived component) are required to achieve a reasonable fitting for

the decay curves obtained at room temperature and 313 K.

Figure 4.10 presents examples for the experimental data and fitting curves at 323 K. The decay curves are equally well-fitted by these three different functions. The half-lifetime of the decay curve obtained by different fitting functions, the parameter β for MSE function and the power p for CPL function are listed in table 4.2.

Table 4.2: The half-lifetime of 2802 cm^{-1} peak integrated area decay curves at 323 K in sample GE81-107a-B and GE81-107a-C by the fitting of (a) multiple components method (equation 2.94), (b) modified stretched exponential function (MSE) (equation 2.91), and (c) complex power law decay function (CPL)(equation 2.88), respectively.

	GE81-107a-B {001} $[N_S] > [B_S]$	GE81-107a-C {111} $[N_S] < [B_S]$
2Exp	$\tau_1 = 15.39$ s, $I_1 = 4.42$ $\tau_2 = 1.89$ s, $I_2 = 12.99$	$\tau_1 = 53.34$ s, $I_1 = 19.09$ $\tau_2 = 5.72$ s, $I_2 = 64.50$
MSE	$\tau = 1.02$ s $\beta = 0.28$	$\tau = 3.88$ s $\beta = 0.28$
CPL	$\tau = 1.68$ s $p = 1.01$	$\tau = 5.03$ s $p = 1.24$

4.2.3.3 T-dependence of initial integrated intensity

The initial integrated area of 2802 cm^{-1} peak decay in GE sample obtained by experiment and the three different fitting methods are plotted in figure 4.11. For the two simple exponential components fitting, the initial integrated area is the sum of the initial integrated area of all components. For all the fitting functions, there is good agreement between the experimental data and fitting results. However, the initial concentration of uncompensated boron obtained by the CPL function is slightly higher than the fitting results of the two simple exponential components fitting and the MSE function fitting.

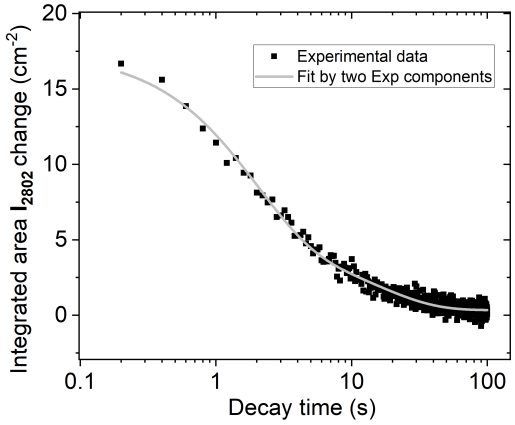

(a)

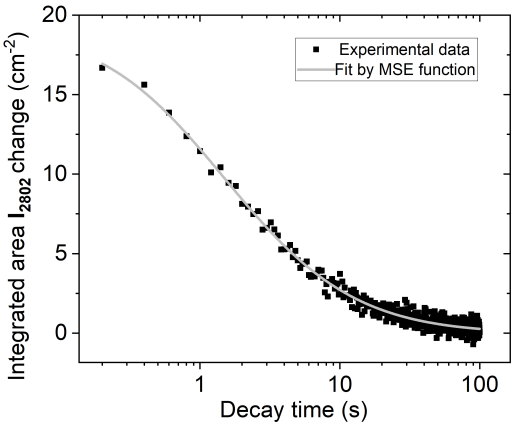

(b)

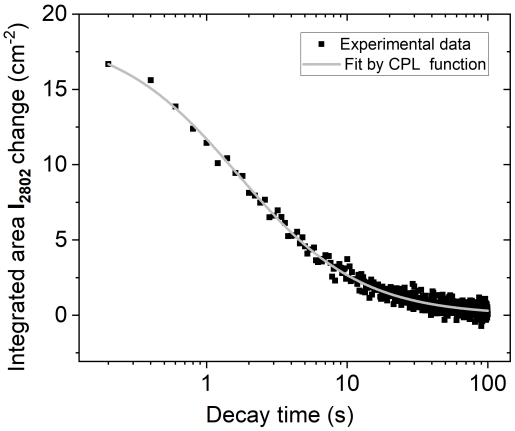

(c)

Figure 4.10: The decay curves of 2802 cm^{-1} peak integrated area in GE81-107a-B recorded after 224 nm excitation at 323 K by fitting of (a) multiple components method (equation 2.94), (b) modified stretched exponential function (MSE) (equation 2.91), and (c) complex power law decay function (CPL) (equation 2.88).

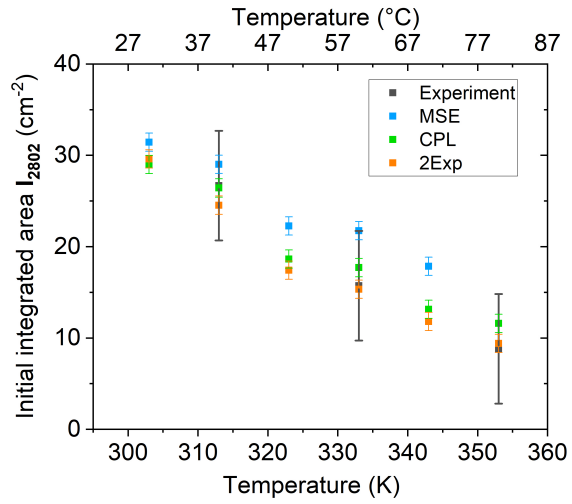

(a)

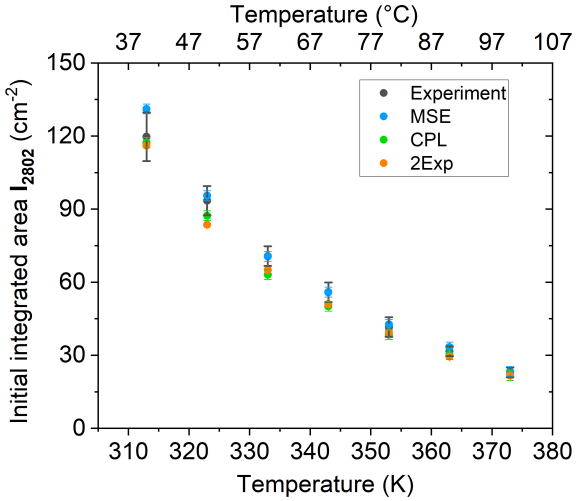

(b)

Figure 4.11: The initial integrated area of 2802 cm^{-1} peak decay in sample GE81-107a-C recorded after 224 nm laser excitation at a series of temperatures between 303 K to 373 K. (a) GE81-107a-B ({001} growth sector). (b) GE81-107a-C ({111} growth sector). Experimental data and results of different fitting methods are included.

4.2.3.4 T-dependence of decay lifetime

Figure 4.12 (a) indicates that two decay components with different half-lifetime are obtained by multiple components fitting for the 2802 cm^{-1} absorption peak decay above room temperatures. In sample GE81-107a-C, when the temperature is heated from room temperature to 363 K, the half-lifetime of the slow component and the fast component change from approximately 140 s to 5 s and 20 s to 1 s, respectively. In sample GE81-107a-B, in the temperature range between room

temperature and 353 K, the half-lifetime of the slow and the fast decay components vary from around 20 s to 6 s and 3 s to 0.7 s, respectively.

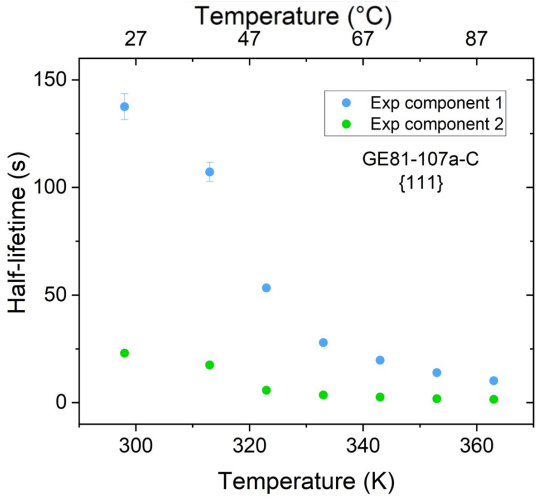

(a)

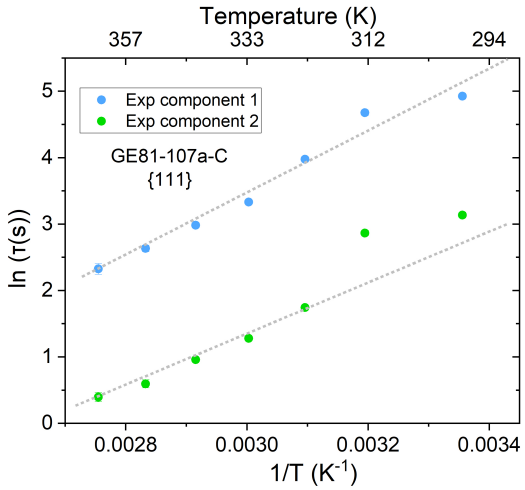

(b)

Figure 4.12: Temperature dependence of the uncompensated substitutional boron decay half-lifetime in sample GE81-107a-C ({111} growth sector) between 298 K to 363 K. (a) half-lifetime versus temperature. (b) The logarithm of half-life time versus reciprocal of temperature. The grey dash lines are the results of the fitting to an Arrhenius function.

The activation energy of uncompensated boron concentration decay can be determined using equation 2.80 as shown in figure 4.12 (b) and 4.13. At high temperatures, the expected thermal activation behaviour (straight line) is obtained. The activation energies obtained from the uncompensated decay lifetimes by different fitting methods are listed in the following table 4.3. In both samples

GE81-107a-B and GE81-107a-C, the activation energies are very close and slightly smaller than the ionization energy of the substitutional boron, which is 0.368 eV. [1, 4]

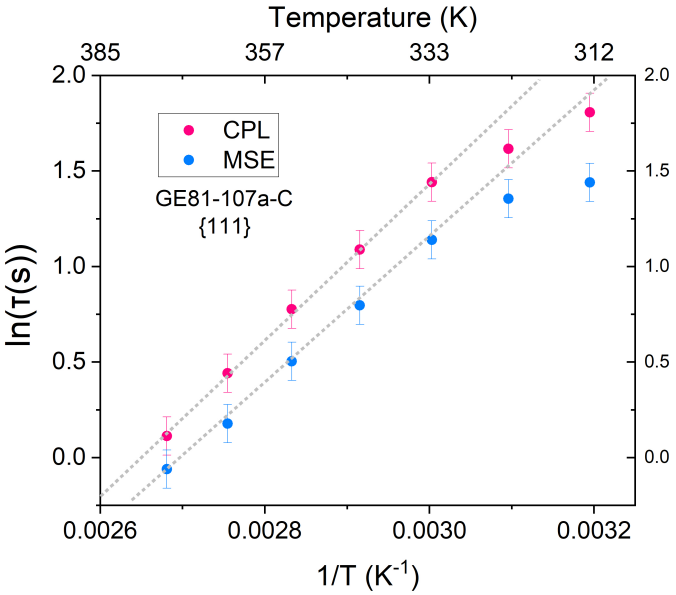

Figure 4.13: The logarithm of half-lifetime (fit by MSE function and CPL function, respectively) in GE81-107a-C versus reciprocal temperature. The dash lines are the results of the fitting to an Arrhenius function.

Table 4.3: Activation energies determined from uncompensated boron concentration decay lifetimes for GE samples by the fitting of multiple components method (equation 2.94), modified stretched exponential function (MSE) (equation 2.91) and complex power law decay function (CPL) (equation 2.88). See Table 3.1 for "metastable state" nitrogen and boron concentrations.

	GE81-107a-B {001} $[N_S] > [B_S]$		GE81-107a-C {111} $[N_S] < [B_S]$	
	Exp 1	Exp 2	Exp 1	Exp 2
2Exp	0.34(3) eV	0.32(3) eV	0.41(5) eV	0.34(3) eV
MSE	0.32(5) eV		0.32(5) eV	
CPL	0.37(3) eV		0.35(3) eV	

4.3 Discussion and conclusions

As discussed in Chapter 4.1, substitutional boron is a relatively shallow acceptor in diamond. Boron can be compensated by donors and at room temperature only a fraction of the boron acceptor are thermally ionized.

The bandgap UV (224 nm laser) excitation creates electrons in the conduction band and holes in the valence band:

$$h\omega_{BG} \rightarrow \mathrm{e}^- + \mathrm{h}^+ \tag{4.8}$$

$[\mathrm{B_S^0}]$ is increased during excitation:

$$\mathrm{B_S}^- + \mathrm{h}^+ \rightarrow \mathrm{B_S}^0 \tag{4.9}$$

until the absorption signal is saturated for the available light intensity and hole trapping/detrapping rates.

After the optical excitation is removed, in the temperature range studied thermal ionization of $\mathrm{B_S^0}$

$$\mathrm{B_S}^0 \rightarrow \mathrm{B_S}^- + \mathrm{h}^+ \tag{4.10}$$

is expected to dominate over charge carrier tunneling. Thus it is expected that the decay time would vary exponentially with reciprocal temperature with an activation energy equals to the $\mathrm{B_S^0}$ acceptor energy of ~ 0.37 eV. It can be seen from table 4.3 that within the experimental uncertainties this is indeed the case. However, the average activation energy of 0.35 eV is slightly lower than the acceptor activation energy. This point will be returned to in Chapter 8.

The research can be improved on several aspects for future work. Firstly, the current experimental arrangement can only be utilised above room temperature. To monitor the boron-related charge transfer between liquid nitrogen temperature and room temperature is meaningful to understand the phosphorescence process in the low temperature and intermediate temperature windows (Chapter 6). Secondly, the temperature dependence of $\mathrm{B_S^0}$ IR absorption is not quantitatively understood. It would be very useful to be able to determine the uncompensated substitutional boron concentration from $\mathrm{B_S^0}$ related absorption peaks at different temperatures.

Bibliography

[1] D. Howell, A. T. Collins, L. C. Loudin, P. L. Diggle, U. F. S. D'Haenens-Johansson, K. V. Smit, A. N. Katrusha, J. E. Butler, and F. Nestola, Diamond and Related Materials **96**, 207 (2019).

[2] A. J. Neves and M. H. Nazaré, *Properties, Growth and Applications of Diamond*, 26 (The Institution of Electrical Engineers, 2001).

[3] J. P. Goss and P. R. Briddon, Physical Review B **73**, 085204 (2006).

[4] A. T. Collins and A. W. S. Williams, Journal of Physics C: Solid State Physics **4**, 1789 (1971).

[5] R. M. Chrenko, Physical Review B **7**, 4560 (1973).

[6] K. Thonke, Semiconductor Science and Technology **18**, S20 (2003).

[7] J. V. Macpherson, Physical Chemistry Chemical Physics **17**, 2935 (2015).

[8] V. D. Blank, M. S. Kuznetsov, S. A. Nosukhin, S. A. Terentiev, and V. N. Denisov, Diamond and Related Materials **16**, 800 (2007).

[9] G. Davies, *Properties and Growth of Diamond*, 9 (Inst of Engineering & Technology, 1994).

[10] R. C. Burns, V. Cvetkovic, C. N. Dodge, D. J. F. Evans, M. L. T. Rooney, P. M. Spear, and C. M. Welbourn, Journal of Crystal Growth **104**, 257 (1990).

[11] K. W. Böer and U. W. Pohl, *Semiconductor Physics* (Springer, 2018).

[12] E. Gheeraert, S. Koizumi, T. Teraji, H. Kanda, and M. Nesladek, physica status solidi (a) **174**, 39 (1999).

[13] M. Werner, R. Job, A. Zaitzev, W. R. Fahrner, W. Seifert, C. Johnston, and P. R. Chalker, Physica Status Solidi (a) **154**, 385 (1996).

[14] A. T. Collins, in *Diamond Conference, University of Warwick, July* (2010) pp. 13–16.

[15] P. L. Diggle, *Single point defect imaging studies in diamond*, Ph.D. thesis, University of Warwick (2019).

[16] J. Barjon, T. Tillocher, N. Habka, O. Brinza, J. Achard, R. Issaoui, F. Silva, C. Mer, and P. Bergonzo, Physical Review B **83**, 073201 (2011).

[17] H. Kawarada, H. Matsuyama, Y. Yokota, T. Sogi, A. Yamaguchi, and A. Hiraki, Physical Review B **47**, 3633 (1993).

[18] H. Kim, A. K. Ramdas, S. Rodriguez, and T. R. Anthony, Solid State Communications **102**, 861 (1997).

[19] R. Kravets, M. Vanecek, C. Piccirillo, A. Mainwood, and M. E. Newton, Diamond and Related Materials **13**, 1785 (2004).

[20] J. Li, C. Fan, S. Chen, and G. Li, The Journal of Gemmology **35**, 248 (2016).

[21] S. Eaton-Magaña, Gems & Gemology **53**, 412 (2016).

[22] S. G. Pavlov, D. D. Prikhodko, S. A. Tarelkin, V. S. Bormashov, N. V. Abrosimov, M. S. Kuznetsov, S. A. Terentiev, S. A. Nosukhin, S. Y. Troschiev, V. D. Blank, *et al.*, Physical Review B **104**, 155201 (2021).

Chapter 5

Substitutional nitrogen related charge transfer

5.1 Background

Substitutional nitrogen N_S, also known as the C-centre or P1 defect in EPR studies, forms when a nitrogen atom substitutes a carbon atom in the diamond lattice. Substitutional nitrogen defects are rare in natural diamonds due to the aggregation of nitrogen atoms under the conditions in the mantle of Earth. [1, 2] In lab-grown diamonds, the preference for nitrogen incorporation depends on the growth sector: in HPHT synthetic diamonds, the nitrogen content usually follows $\{111\} > \{100\} > \{113\} > \{110\}$; whereas in CVD growth diamonds, it follows $\{111\} > \{113\} > \{110\} > \{100\}$. [1, 3] As introduced in Chapter 1.2.1.1, the use of nitrogen getters can reduce the nitrogen content during HPHT growth. [1] In addition, introduced by implantation: a fraction of nitrogen ions implanted into the diamond lattice with keV to MeV energies and then annealed at over 600 °C will migrate to substitutional lattice sites. [1] Substitutional nitrogen can exist in neutral, positive or negative charge states, as N_S^0, N_S^+, and N_S^-. In previous studies of charge transfer and phosphorescence in near colourless HPHT grown diamond, the role of N_S^- has not been considered. It is shown here that the results in this and subsequent chapters cannot be explained without the existence of significant metastable concentrations of N_S^- after UV excitation.

5.1.1 N_S^0

Substitutional nitrogen in a neutral charge state (N_S^0), the P1 centre, was firstly observed using the EPR technique by Smith *et al.* in 1959 [4–6], and has since been thoroughly studied [7–10]. The P1 centre has a C_{3v} trigonal symmetry. [11] The nitrogen forms equivalent bonding orbitals with four adjacent carbon atoms, whilst the remaining unpaired electron (S =1/2) can relax into any of these N-C bond anti-bonding orbitals along ⟨111⟩ direction. [6, 11, 12] The unique N-C bond is elongated by approximately 30 % over the normal C-C bond length. [1, 6, 13] The unpaired electron (elongated N-C) bond can reorient between four sites either by hopping at high temperatures above 600 K with a reorientation activation energy of around 0.7 eV or by tunnelling at lower temperatures. When above 1200 K, the unpaired electron is "hopping" so fast between these four sites on a timescale comparable to that of an EPR experiment, so the P1 centre is observed to have T_d symmetry. [1, 8, 11]

N_S^0 acts as a deep donor with its energy level lying 1.7 eV below the conduction band (activation energy determined by resistivity measurement as a function of temperature). [14, 15] Hence the substitutional nitrogen donor is too deep to be thermally ionized at room temperature. [16] When substitutional nitrogen donor and an acceptor such as boron is present, N_S^0 donates an electron to the acceptor and turns into N_S^+ [17].

$$N_S{}^0 + B_S{}^0 \rightarrow N_S{}^+ + B_S{}^- \tag{5.1}$$

The threshold for optically ionizing an electron from N_S^0 to the conduction band is 2.2 eV, which is different from the thermal ionization energy (1.7 eV) because of the change in "configuration". [5, 15, 18, 19]

The quantification of N_S^0 can be achieved by various measurements such as FTIR absorption and EPR. In type Ib diamond, substitutional nitrogen is the dominant impurity species and detectable by FTIR absorption. [1, 2, 12, 17, 20] N_S^0 gives rise to characteristic IR absorption features: a peak maximum at 1130 cm^{-1}, which shifts to lower energy by 0 - 15 cm^{-1} if diamond contains a both ^{14}N and ^{15}N; as well as a sharp LVM at 1344 cm^{-1} related to an A ↔ E transition in a defect of trigonal symmetry, with no detectable shift on changing the isotope of nitrogen.

[1, 12, 21] The concentration of N_S^0 by IR absorption (at 1 cm^{-1} resolution) is given by

$$[N_S^0]\ (\text{ppm}) = (25 \pm 2) \times \mu_{1130}\ (cm^{-1}) \tag{5.2}$$

and

$$[N_S^0]\ (\text{ppm}) = 37.5 \times \mu_{1344}\ (cm^{-1}) \tag{5.3}$$

where μ_{1130} and μ_{1344} are the absorption coefficients at 1130 cm^{-1} and 1344 cm^{-1}, respectively. [17, 20]

In type II diamond, the concentration of neutral substitutional nitrogen is too low to be detectable by FTIR absorption. Therefore, the EPR technique is usually utilised to determine the N_S^0 concentration in type IIa diamond with a detection limit of approximately 0.02 ppb at room temperature (see Chapter 5.2). [1, 11, 13, 22]

5.1.2 N_S^+

When N_S^0 donates an electron and forms N_S^+, the diamond lattice distortion disappears. Therefore, N_S^+ has four identical N-C bonds to the adjacent carbon atoms and has a T_d tetrahedral symmetry. [12, 22] The N_S^+ defect is EPR inactive. [1, 17]

The infrared spectrum of N_S^+ presents IR absorption peaks at 1332 cm^{-1}, 1046 cm^{-1}, 950 cm^{-1}. [12, 17] The peaks at 1046 cm^{-1}, 950 cm^{-1} shift to lower wavenumber by approximately 5 cm^{-1} on replacing ^{14}N by ^{15}N. The 1332 cm^{-1} vibrational mode of N_S^+ infrared absorption spectrum arises from the neighbouring carbon atoms but does not involve the nitrogen atom so shows no $^{14}N/^{15}N$ isotope shift. [1, 17] The concentration of N_S^+ in type Ib diamond can be determined from the IR absorption (at 1 cm^{-1} spectral resolution),

$$[N_S^+]\ (\text{ppm}) = (5.5 \pm 1) \times \mu_{1332}\ (cm^{-1}) \tag{5.4}$$

where μ_{1332} is absorption coefficient at 1332 cm^{-1}. [17] However, other defects can also contribute to the absorption at 1332 cm^{-1}, while the 1046 cm^{-1}, 950 cm^{-1} peaks uniquely arise from the positive-charge substitutional nitrogen. [1, 17] The ratio of N_S^0 and N_S^+ in diamond can be changed by optical excitation (depending

on other traps in the sample). [17]

5.1.3 N_S^-

Substitutional nitrogen is predicted to have an acceptor level below the minimum of the conduction band. This negatively charged N_S^- could exist. [5]

$$N_S{}^0 + e^- \rightarrow N_S{}^- \tag{5.5}$$

In 2011, the experimental evidence of N_S^- based on the ultra-fast spectroscopic technique was reported by Ulbricht *et al.*. [23] A transient infrared absorption feature at 1349 cm^{-1} is assigned to the LVM of N_S^- state. [23] The formation of N_S^- in the {100} growth sector of a type Ib HPHT synthetic diamond is explained by the electron originally excited from N_S^0 into the conduction band by an ultra-short laser pulse, recombining into a N_S^0 defect rather than N_S^+. [1, 23]

$$2N_S{}^0 \overset{h\omega}{\rightarrow} N_S{}^+ + N_S{}^- \tag{5.6}$$

The existence of N_S^- is crucial for the interpretation of the phosphorescence and thermoluminescence date in the Chapter 6 and 7.

5.2 Determination of $[N_S{}^0]$ by EPR

5.2.1 Quantitative EPR measurement

The integrated intensity of the recorded EPR lines originating from the N_S^0 centre is proportional to the number of related spins present. The concentration of N_S^0 in a diamond, therefore, can be accurately identified by performing an EPR measurement under the same conditions on both the unknown sample [X] and a reference sample [ref] with a known concentration of N_S^0. The reference samples are listed in table 5.1. The relationship between [X] and [ref] involving many other

factors can be described as

$$[X] = \frac{I_S}{I_{\text{ref}}} \underbrace{[\text{ref}] \frac{S(S+1)_{ref}}{S(S+1)_S} \frac{g_{ref}^2}{g_S^2}}_{\text{known paramters}} \underbrace{\frac{\eta_{\text{ref}}}{\eta_S} \frac{Q_{ref}}{Q_S}}_{\text{measurable}} \underbrace{\frac{\sqrt{P_{\mu w_{ref}}}}{\sqrt{P_{\mu w_s}}} \frac{B_{m_{\text{ref}}}}{B_{m_{\text{S}}}} \frac{G_{\text{ref}}}{G_S} \frac{T_{\text{ref}}}{T_S} \frac{t_{aq_{\text{ref}}}}{t_{aq_{\text{S}}}} \frac{N_{\text{ref}}}{N_S}}_{\text{spectrometer settings}} \quad (5.7)$$

where

- I is the double integrated intensity of the EPR spectrum,
- S is the total spin,
- g is the g factor of the system (2.0024 ± 0.0002 for N_S^0),
- η is the filling factor of the microwave resonator for the sample under investigation,
- Q is the loaded quality factor of the microwave resonator,
- $P_{\mu w}$ is the incident microwave power in the absence of microwave power saturation ($B_1 \propto \sqrt{P_{\mu w}}$),
- B_m is the field modulation amplitude,
- G is the spectrometer gain,
- T is the temperature of the measurement,
- t_{aq} is the acquisition (or dwell time) at each point on the spectrum,
- N is the number of scans.[6, 24]

Table 5.1: The reference samples for quantitative EPR measurement.

Sample name	**Type**	**N_S^0 in ppm**	
Syn93-04	HPHT	270(20)	SP-EPR
0577207-C(ii)	CVD	0.040(4)	RP-EPR

Microwave power saturation should be avoided for quantitative EPR measurement (the EPR signal should be linear to the square root of microwave power). In addition, the test sample and reference sample should be carefully placed in the same position in the microwave resonator when the measurement is made.

5.2.2 Slow passage regime versus rapid passage regime

CW (continuous wave) EPR is usually carried out in the slow passage (SP) regime to quantify the concentration of substitutional nitrogen in a diamond when N_S^0 is higher than 2 ppm. [25] The detection limit for the N_S^0 centre in diamond with

SP-EPR is approximately 20 ppb. [11] In an ideal situation, the measurement is performed under steady-state conditions; namely, the rate of the magnetic field's change is slow compared to τ_1 or τ_2. Assuming the concentration of N_S^0 in the diamond at room temperature is much greater than other paramagnetic defects, τ_1 and τ_2 are 2 - 3 ms and 7 - 7000 µs, respectively. [25] The lower the concentration of neutral charge state substitutional nitrogen in diamond, the longer the spin relaxation time τ_2. When $[N_S^0]$ is below 1 ppm, τ_2 is almost independent of the concentration. [11]

Compared with conventional CW-EPR, the rapid passage (RP) EPR is closer to pulsed EPR, introduced in detail in references [11, 26]. To be brief, for the rapid passage regime, the applied magnetic field sweeps through the EPR transitions faster than the relaxation time τ_1 and τ_2 of a spin packet, which means that the spin system can not fully reach the thermal equilibrium. [13] Experimentally RP-EPR is performed with demodulation phase at 90 degree to the modulation phase, and enables quantitative measurement in a lower concentration range of 0.02 - 1000 ppb (at room temperature). [13, 25, 27] RP-EPR is not as easily saturated by the microwave (MW) power as SP-EPR during the scan; therefore, higher MW power can be applied to obtain a better SNR. [13]

5.2.3 Sweep rate

The maximum sweep rate of RP-EPR measurements performed by the Bruker E580 spectrometer described in Chapter 3.3, is 2 mT/s. [11] However, a faster sweep rate is required for the research in this thesis, especially for the time-resolved EPR experiment since the lifetime of N_S^0 change after optical excitation is short. To achieve this, an experimental method to significantly improve the sweep rate in EPR measurement developed by B. G. Breeze is utilised, details can be seen in section 5.2.3 in his thesis. [11] The large electromagnet of the Bruker E580 system is used to generate a static magnetic field at approximately 348 mT while using small coils creating a much smaller field to sweep the EPR spectrum. The sweep coils and data recording is handled by a software written in LabVIEW. In this way, sweep rates can reach 200 mT/s. [11]

5.2.4 Temperature

To investigate the variation of N_S^0 concentration and monitor the N_S related charge transfer after UV excitation in diamond at different temperatures, temperature variable RP-EPR measurements are performed in this research. For a diamond containing a constant concentration of N_S^0 at different temperatures, when reducing the temperature, the Boltzmann population difference between ground and excited states is increased (Chapter 2.4). The SP-EPR signal is inversely proportional to temperature as long as $P_{\mu W}$ is well below the levels required for microwave power saturation. [11, 13] In addition, SNR is improved as temperature decreases between 300 K and 150 K, as shown in figure 5.1. Further reduction in temperature does not contribute to better SNR. [11] The loaded quality factor of the cavity Q is improved at lower temperatures within the range of 150 K to room temperature. [11]

When the temperature decreases below 200 K, the spin-lattice relaxation time τ_1 starts to increase (Figure 5.1), and so the EPR signal is easily saturated in the SP-EPR. [13, 24] Therefore, the rapid passage regime is suitable for quantitative measurement instead of SP-EPR. At temperatures lower than 150 K, τ_1 is significantly increased, the intensity of N_S^0 EPR signal is distorted because of the insufficient time between resonances to restore equilibrium population, and the "forbidden" transition is driven. [11]

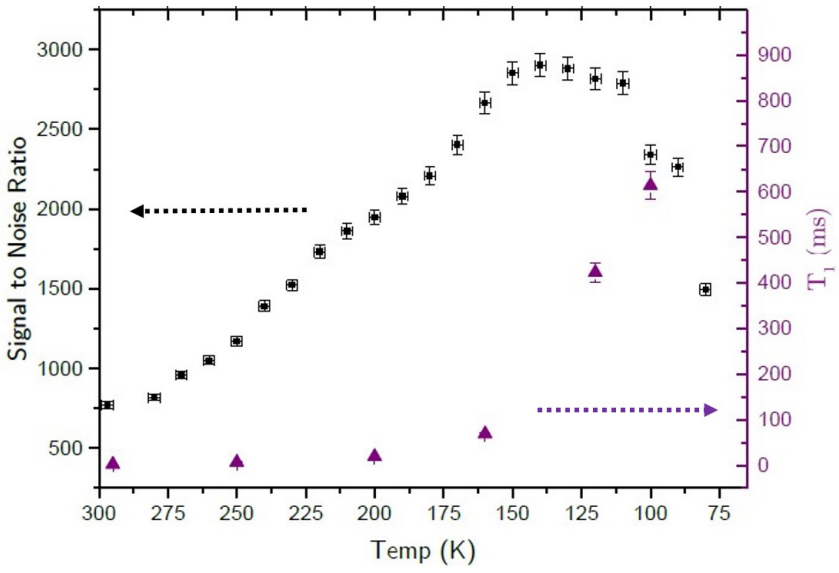

Figure 5.1: The temperature dependence of SNR and τ_1 for N_S^0 by RP-EPR. The MW power is optimised for each measurement. Adapted from [11].

Considering the low nitrogen concentration in the diamonds studied and the requirement for low-temperature measurement, RP-EPR is mainly used in this thesis. The specific experimental methods, including setup and parameters, are introduced in Chapter 3.3.

5.2.5 Reference sample for T-variable measurement

A type II CVD growth diamond 2446789-E1 weighing 89.2 mg is used as the reference sample to calibrated the EPR signal of N_S^0 in the studied diamond samples between 180 K to 360 K. The concentration of N_S^0 contained in this sample is 106 ± 6 ppb measured by [25] and it has been shown that $[N_S^0]$ does not vary with temperature in this CVD sample (concentration of traps is too low to affect the $[N_S^0]$).

The EPR spectra of N_S^0 in reference sample 2446789-E1 obtained by the Bruker E580 spectrometer and by the fast sweep setup is shown in figure 5.2. As introduced in Chapter 3.3, the diamond sample is mounted on the top of a quartz rod which means the diamond sample is in a random orientation in the magnetic field, which leads to approximately $\pm$ 5 % error in concentration calculation. [11]

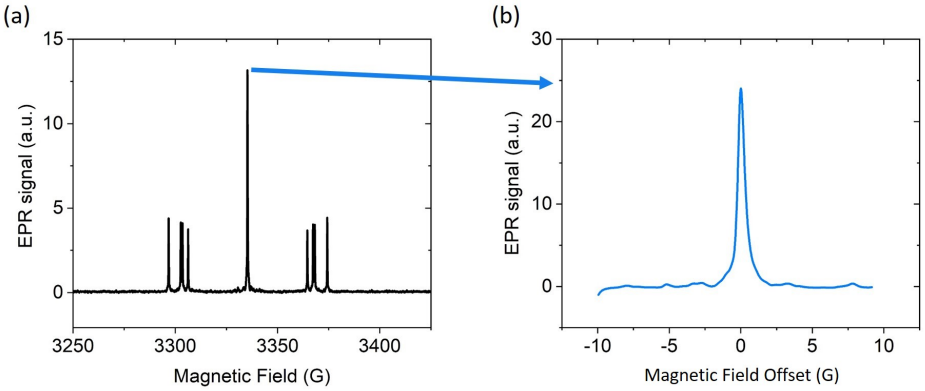

Figure 5.2: (a) Example of an RP-EPR spectrum for sample 2446789-E1 (random orientation) by Bruker E580 spectrometer. (b) The RP-EPR spectra of the central peak of N_S^0 centre scanned with a self-modified fast sweep setup (described in Chapter 5.2.3).

Figure 5.3 shows that when performing an RP-EPR scan at the same unsaturated MW power, the EPR signal intensity of N_S^0 in the reference sample increases as temperature drops from 360 K to 220 K and then decreases as lowering the temperature below 220 K.

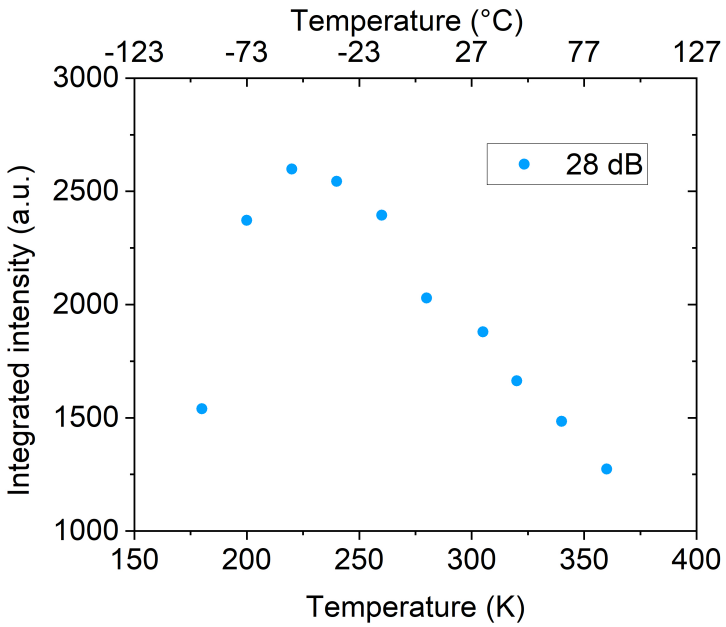

Figure 5.3: The RP-EPR integrated intensity of the N_S^0 signal in a CVD reference sample 2446789-E1 measured with 28 dB microwave power attenuation at a temperature range of 180 K to 360 K, sweep rate at 200 mT/s.

5.3 Sample GE81-107a-C {111}

5.3.1 Temperature dependence of N_S^0 concentration

The concentration of N_S^0 in sample GE81-107a-C in dark and under UV radiation between 180 K to 360 K is measured using the experimental method described in Chapter 3.3. Since the RP-EPR signal of the N_S^0 centre is temperature-dependent, as discussed above, the concentration is calibrated by the measurement of the reference sample 2446789-E1 (figure 5.3). As shown in figure 5.4, in sample GE81-107a-C almost all substitution nitrogen defects are not in the neutrally charged state in the dark across the entire measuring temperature range. As the temperature increases, the number of substitutional nitrogen neutralised by the 224 nm pulsed laser excitation decreases. When the temperature is above approximately 340 K, the change in concentration of N_S^0 under UV excitation is negligible.

Here the assumption that the spectrometer sensitivity is not changing with temperature (e.g. the loaded quality factor of the cavity Q_S in equation 5.7 is constant) is problematic, since number of thermal activated charge carriers increases with temperature, and therefore the sample conductivity decreases (dielectric loss) with decreasing temperature, which results in higher Q and hence overestimation of

N_S^0 concentration at low temperatures. In addition, the electrons in the conduction band and the holes in the valence band created by the UV illumination leads to higher electric conductivity, therefore, reducing the Q_S factor. Hence the concentration of N_S^0 under UV excitation measured at relatively high temperatures shown in figure 5.4 is slightly underestimated. However, it is uncertain that whether the N_S^0 concentration under UV excitation obtained at low temperatures is overestimated or underestimated.

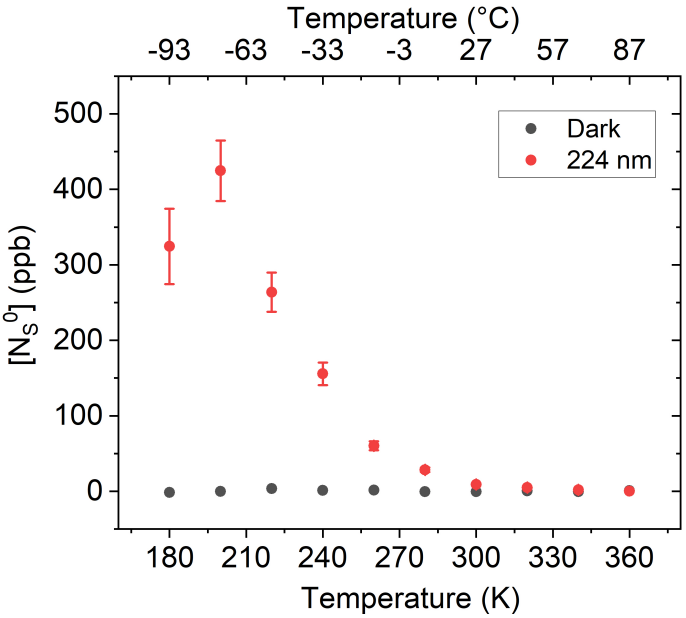

Figure 5.4: The temperature dependence of N_S^0 concentration in GE81-107a-C ({111} growth sector) determined by RP-EPR in dark and under 224 nm laser excitation. Calibrated by the CVD reference sample 2446789-E1 and assuming the EPR spectrometer sensitivity is independent of temperature.

When performing the RP-EPR scan at a temperature below 180 K, either in the dark or under UV radiation, there is an unknown feature presented by the side of the central peak of the N_S^0 centre EPR spectra in both samples, spectra for sample GE81-107a-C is shown in figure 5.5. The signal of this unknown feature is more significant when the temperature drops. Further study is required to figure out the origin. But it does not influence the $[N_S^0]$ measurement we reported here.

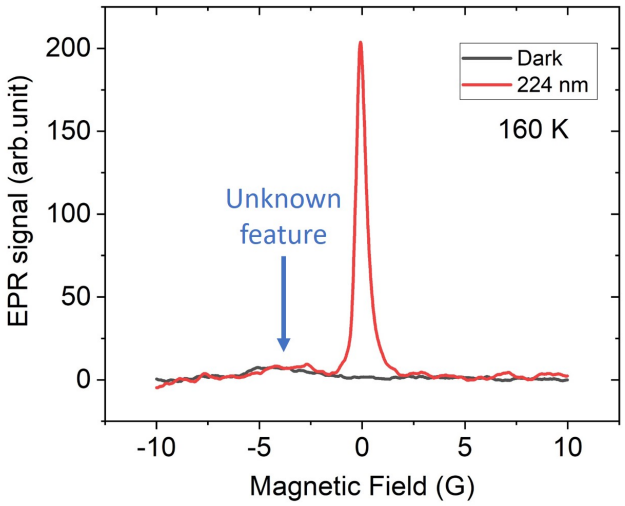

Figure 5.5: The RP-EPR spectra of the N_S^0 central peak in GE81-107a-C recorded at 160 K showing an undetermined feature by its side. (the magnetic field x axis is relative to the central peak)

5.3.2 Time-resolved EPR

The change of the central peak of N_S^0 EPR spectra in sample GE81-107a-C after 224 nm pulsed laser excitation has been monitored by the time-resolved EPR experiment described in Chapter 3.3 in the temperature range between 210 K to 250 K. Above 250 K, it takes too long to record decay curves with a reasonable SNR due to the weak signal and long lifetime of the decay.

5.3.2.1 Decay curves

Figure 5.6 shows the decay of the integrated intensity of N_S^0 central peak after 224 nm laser excitation between 210 K to 250 K. The data is plotted on a log time scale to emphasize the change in the decay rates. The lifetime of the N_S^0 concentration decay is temperature-dependent: the higher the temperature, the shorter the lifetime (see Figure 5.9 where can be seen the lifetime varies by a factor of > 5 between 210 K to 250 K).

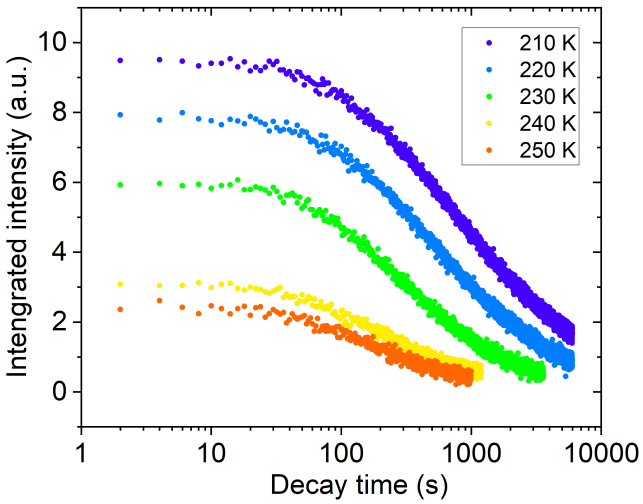

Figure 5.6: The integrated intensity of N_S^0 central peak decay curves in GE81-107a-C ({111} growth sector) recorded after 224 nm laser excitation at different temperatures.

5.3.2.2 Curve fitting

The decay curves of the integrated intensity of N_S^0 central EPR peak presented above are fitted by various functions introduced in Chapter 2.3.4, including multiple components fitting function (two simple exponential components), modified stretched exponential function, and complex power-law function. The decay curve at 210 K obtained by experiment and fitting are shown in figure 5.7, respectively, as an example. These three different fitting methods all provide reasonably good fitting results for the whole temperature range.

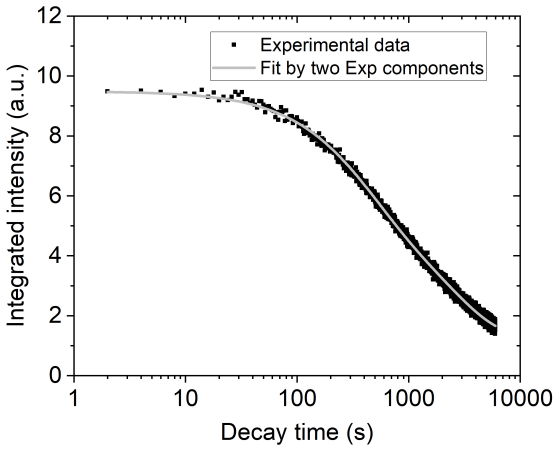

(a)

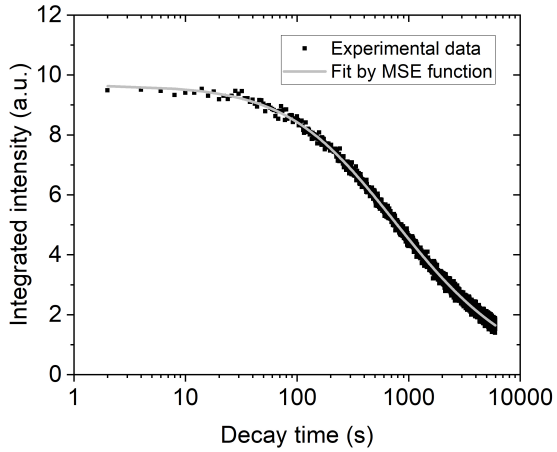

(b)

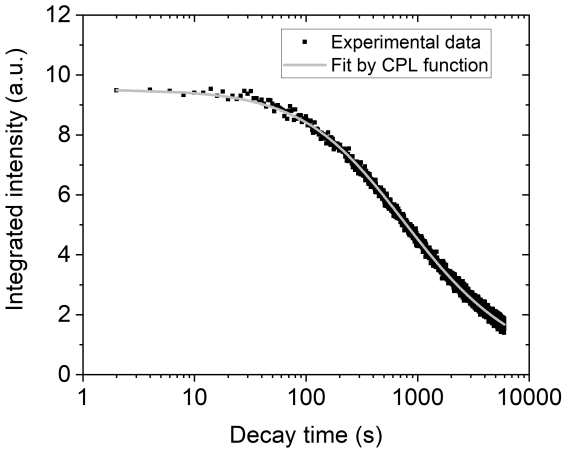

(c)

Figure 5.7: The decay curves of N_S^0 central peak integrated intensity in sample GE81-107a-C recorded after 224 nm excitation at 210 K by the fitting of (a) multiple components method (equation 2.94), (b) modified stretched exponential function (MSE) (equation 2.91), and (c) complex power law decay function (CPL) (equation 2.88).

5.3.2.3 T-dependence of initial integrated intensity

Figure 5.8 presents the initial integrated intensity of the N_S^0 centre EPR signal decay after UV illumination obtained by experiment and three fitting methods. For the two simple exponential components fitting, the initial integrated area is the sum of two components. These three fitting methods provide reasonable results compared to the experimental data, except the fitting for decay at 210 K and 220 K by two simple exponential components fitting gives sightly lower initial intensity.

The increase in the initial intensity with lowering the temperatures is attributed to the increase in Boltzmann distribution and the concentration of substitutional nitrogen neutralised by UV radiation.

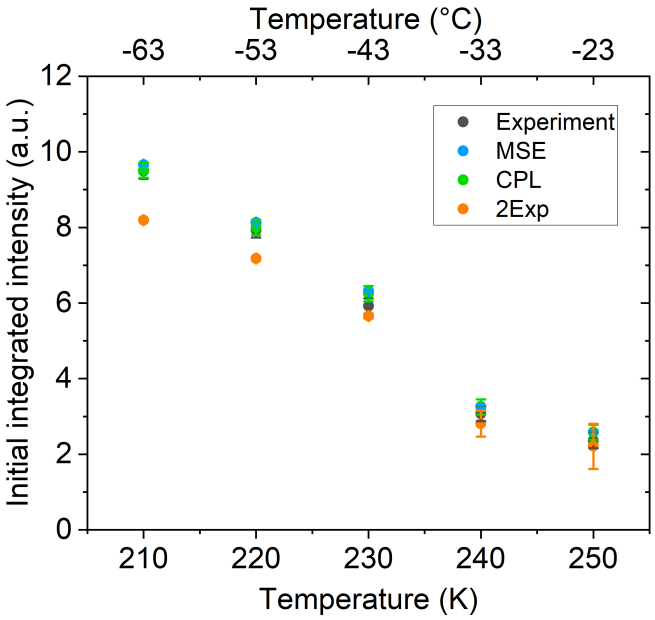

Figure 5.8: The initial integrated intensity of N_S^0 central peak decay curves in GE81-107a-C ({111} growth sector) was recorded after 224 nm laser excitation at temperatures between 210 K to 250 K. Experimental data and results of different fitting methods are included.

5.3.2.4 T-dependence of nitrogen concentration decay lifetime

Two simple exponential components are obtained by the fitting of the N_S^0 EPR integrated intensity decay curve using the multiple components function (equation 2.94). As shown in figure 5.9(a), the lifetime of the short-lived component varies from 382 s to 126 s when the temperature increases from 210 K to 250 K. In the same temperature range, the lifetime of the long-lived component is much

greater, which varies from 2402 s to 422 s.

The half-lifetime given by CPL and MSE fitting is very similar at each experimental temperature, which varies from 892 s to 185 s and 860 s to 184 s, respectively, between 210 K to 250 K.

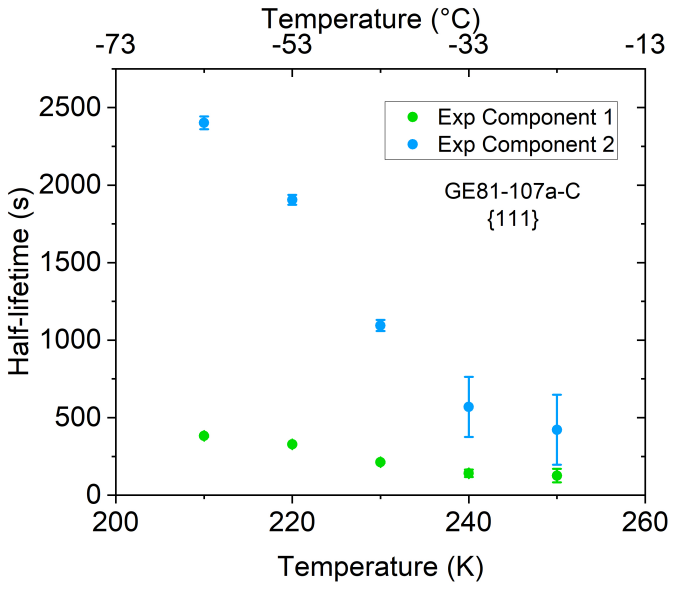

(a)

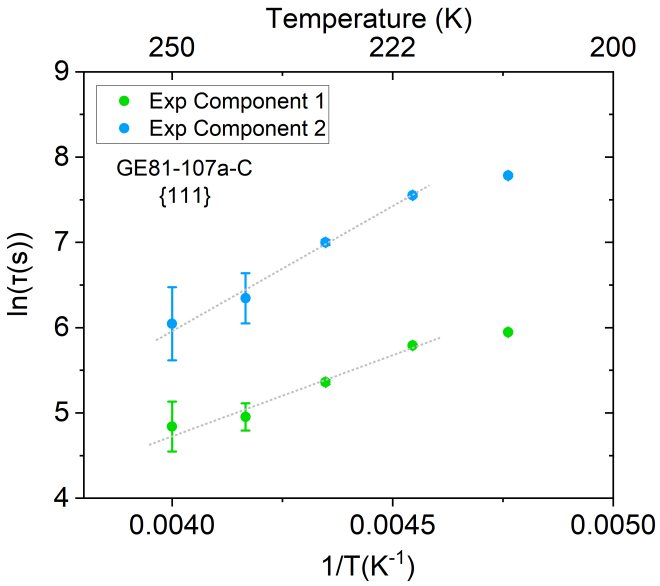

(b)

Figure 5.9: Temperature dependence of N_S^0 decay half-lifetime in sample GE81-107a-C ({111} growth sector) between 210 K to 250 K. (a) half-lifetime versus temperature. (b) The logarithm of half-lifetime versus reciprocal of temperature. The grey dash lines are the results of the fitting to an Arrhenius function.

The activation energy of N_S^0 concentration decay in sample GE81-107a-C ({111}

growth sector) after 224 nm pulse laser excitation is calculated using equation 2.80 based on the fitting results by three different fitting functions, which are presented in figure 5.9(b) and figure 5.10. The activation energies obtained from the lifetime of N_S^0 concentration decay are listed in table 5.2 (see page 146). It is more reasonable to select higher temperatures for the activation energy calculation based on the temperature windows defined by thermoluminescence measurement in Chapter 7. However, as discussed above, the experimental temperature is limited by the weak EPR signal and slow decay rate at higher temperatures.

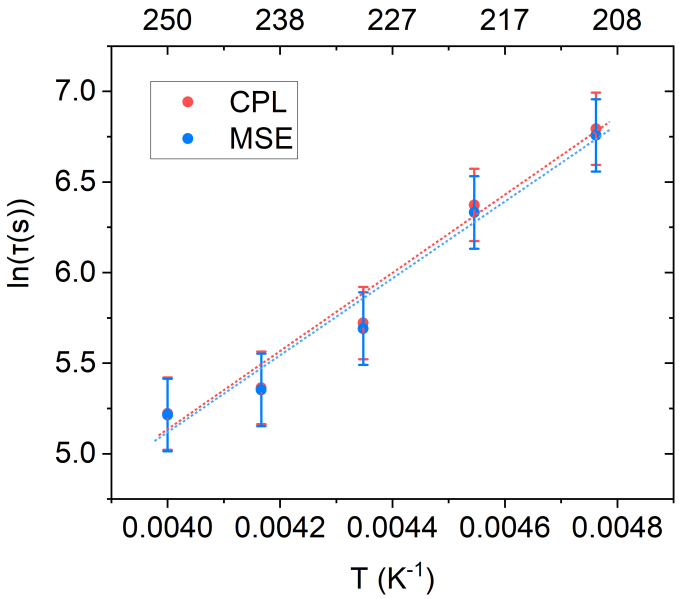

Figure 5.10: The logarithm of half-lifetime (fit by MSE function and CPL function, respectively) in GE81-107a-C versus reciprocal temperature. The dash lines are the results of the fitting to an Arrhenius function.

5.4 Sample GE81-107a-B {001}

5.4.1 Temperature dependence of N_S^0 concentration

The concentration of N_S^0 in sample GE81-107a-B ({001} growth sector) in the dark and under 224 nm pulsed laser illumination between 180 K to 370 K (Fig. 5.11) is obtained using the experimental method described in Chapter 3.3. The concentration is calibrated by the EPR signal of N_S^0 in the reference sample 2446789-E1. As the loaded quality factor of the cavity Q_S decreases under the bandgap UV excitation, the concentration of N_S^0 under UV excitation obtained in this measurement tends to be slightly underestimated. When the temperature is below approximately 200 K, the concentration of N_S^0 defect is barely changed by UV illumination (Fig. 5.11). At higher temperatures the UV excitation decreases the neutral substitutional nitrogen concentration. The change of N_S^0 concentration by UV radiation is relatively constant above room temperature. The substitutional related charge transfer at various temperatures will be detailed discussed in the following section. We would not expect thermal ionization of N_S^0 since it is a deep donor.

The band-edge absorption structure of diamond is complex and highly temperature sensitive. The maximum penetration depth of the 224 nm laser will be less than half the thickness of both GE samples studied, and significantly less at elevated temperatures. (See Chapter 2.2.1) Hence only the substitutional nitrogen defects located in a relatively thin layer of diamond GE81-107a-B and GE81-107a-C are optically excited in this measurement. However, electrons and holes created by UV excitation can transport throughout the whole diamond.

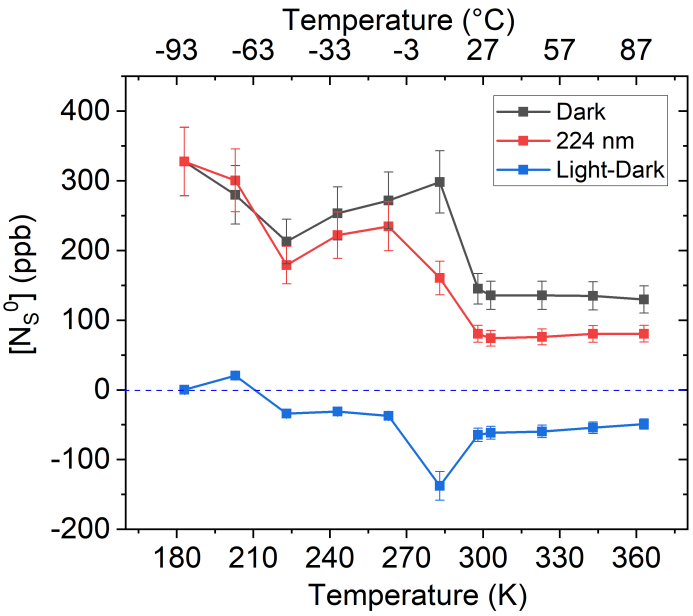

Figure 5.11: The temperature dependence of N_S^0 concentration in GE81-107a-B ({001} growth sector) determined by RP-EPR in the dark (black line) and under 224 nm laser excitation (red line). The change of N_S^0 between under light and in the dark are labelled as blue line. Calibrated by the CVD reference sample 2446789-E1 and assuming the EPR spectrometer sensitivity is independent of temperature.

5.4.2 Time-resolved EPR

The change of the EPR signal of the N_S^0 centre in sample GE81-107a-B after 224 nm pulse laser excitation between approximately 270 K to 350 K has been recorded by the time-resolved EPR experiment described in Chapter 3.3, to understand the substitutional related charge transfer during phosphorescence decay.

5.4.2.1 Recovery curves

The N_S^0 concentration in GE81-107a-B is reduced by 224 nm laser excitation at a selected temperature range (270 K to 347 K), the integrated intensity of the central peak of N_S^0 centre's RP-EPR spectra recovers on a time scale of tens seconds after optical excitation is removed to the pre-excitation value (Figure 5.12). The data is plotted on a log time scale to emphasize the change in the recovery rates. The recovery rate of the curves is dramatically temperature-dependent when varying from 270 K to 318 K, whereas it becomes slightly faster with increasing temperature when above 318 K.

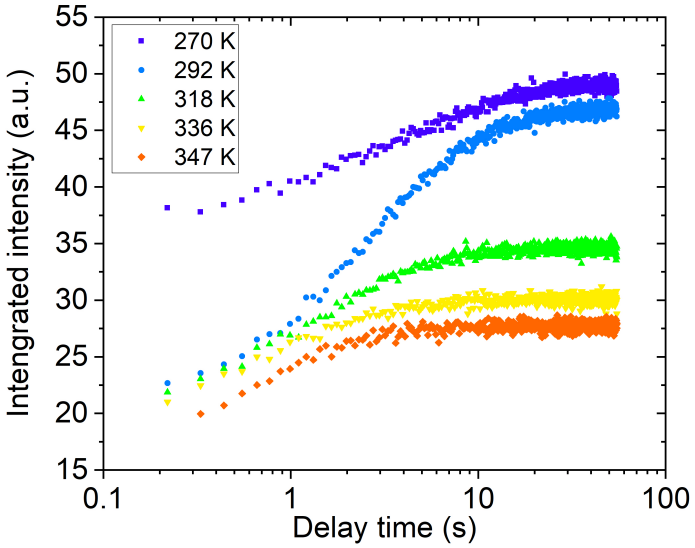

Figure 5.12: The integrated intensity of N_S^0 central peak recovery curves in GE81-107a-B ({001} growth sector) was recorded after 224 nm laser excitation at different temperatures.

5.4.2.2 Curve fitting

The recovery curves of the integrated intensity of N_S^0 central EPR peak presented above are fitted by various functions introduced in Chapter 2.3.4, including multiple components fitting function (two simple exponential components), modified stretched exponential function, and complex power-law function. The decay curve at 292 K obtained by experiment and fitting are shown in figure 5.7, respectively, as an example. These three different fitting methods all provide reasonably well-fitting results at variable temperatures.

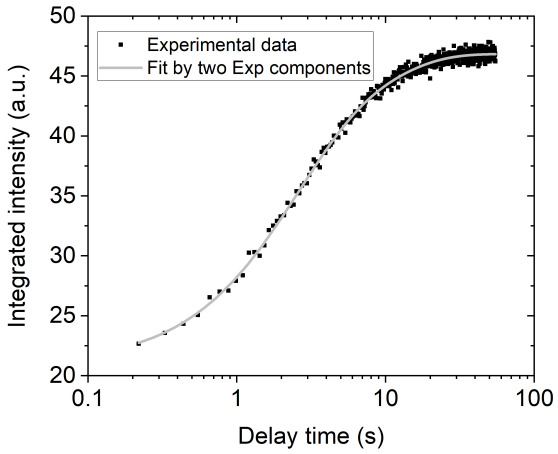

(a)

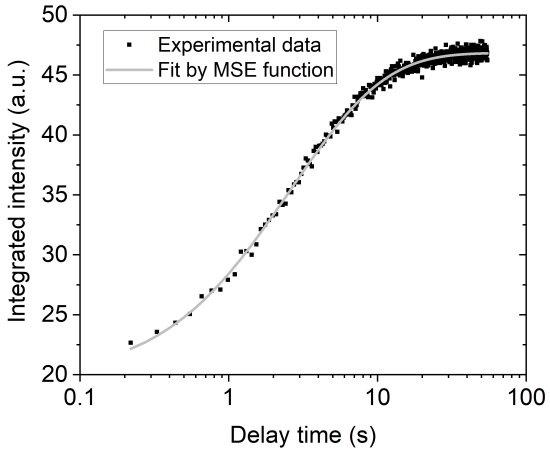

(b)

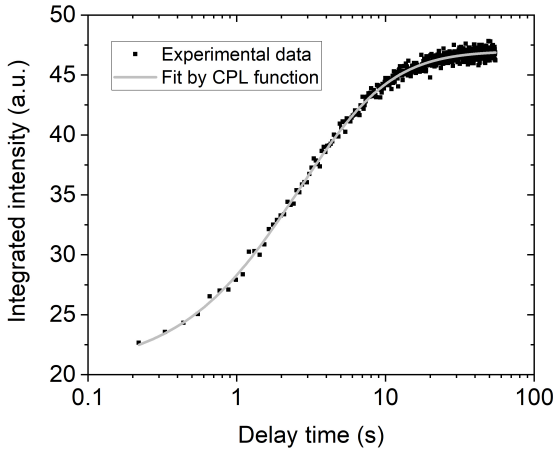

(c)

Figure 5.13: The decay curves of N_S^0 central peak integrated intensity in sample GE81-107a-B recorded after 224 nm excitation at 292 K by the fitting of (a) multiple components method (equation 2.94), (b) modified stretched exponential function (MSE) (equation 2.91), and (c) complex power law decay function (CPL) (equation 2.88).

5.4.2.3 T-dependence of initial and final integrated intensity

The initial and final integrated intensity of the N_S^0 EPR signal recovery after UV excitation in GE81-107a-B obtained by three different fitting methods are plotted in figure 5.14. For the two simple exponential components fitting, the initial and final integrated intensity is the sum of two components. The final intensity of N_S^0 EPR signal after recovery given by various fitting functions at each experimental temperature are highly coincident. The initial intensity obtained by three different methods is consistent at most temperatures, except the initial intensity calculated by MSE function at 336 K and 347 K, slightly lower than the other two results but still within the error bar.

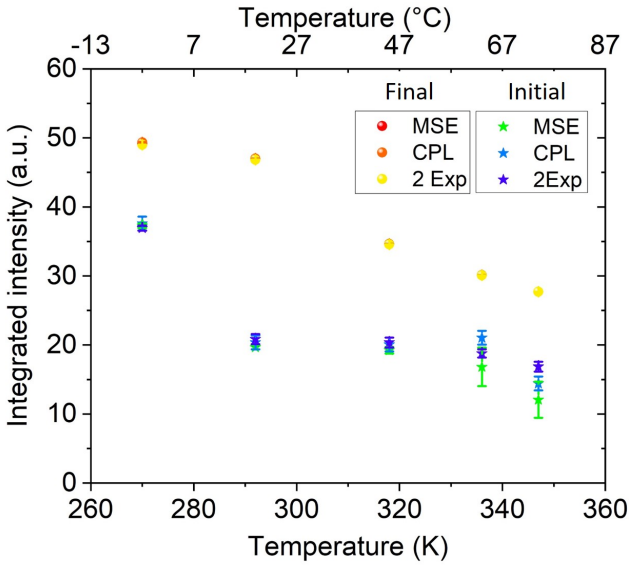

Figure 5.14: The initial and final integrated intensity of N_S^0 central peak recovery curves in GE81-107a-B ({001} growth sector) recorded after 224 nm laser excitation at temperatures between 270 K to 350 K. Final intensities obtained from different fitting methods are highly coincident.

5.4.2.4 T-dependence of nitrogen concentration recovery lifetime

Two simple exponential components are obtained by fitting the recovery curves presented above using the multiple components fitting function (equation 2.94). Figure 5.15 shows the lifetime of two recovery components between 270 K to 347 K. The lifetime of the fast and slow recovery components both decrease as temperature increases above 292 K, varying from 2.27 s to 0.61 s and 8.28 s to 2.76 s, respectively. The substitutional nitrogen related charge transfer process

in GE81-107a-B after UV excitation probably has different mechanisms at the temperatures below and above room temperature.

The differences between the half-lifetime given by CPL and MSE fitting functions are within approximately 0.1 s. At a temperature range of 270 K to 347 K, the half-lifetime of the $[N_S^0]$ recovery after UV radiation in GE81-107a-B obtained by CPL and MSE fitting methods varies from 3.12 s to 0.46 s and 3.00 s to 0.35 s, respectively.

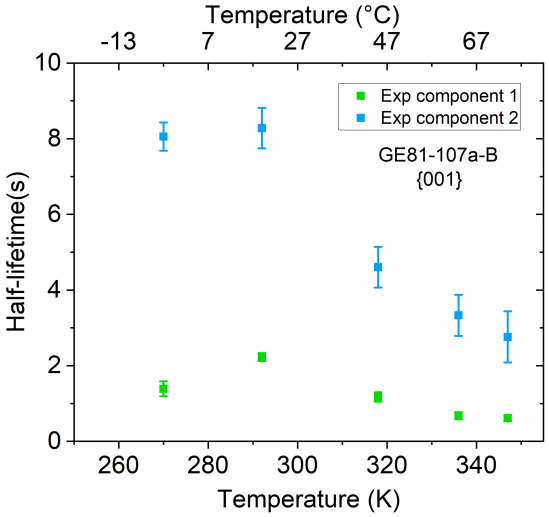

(a)

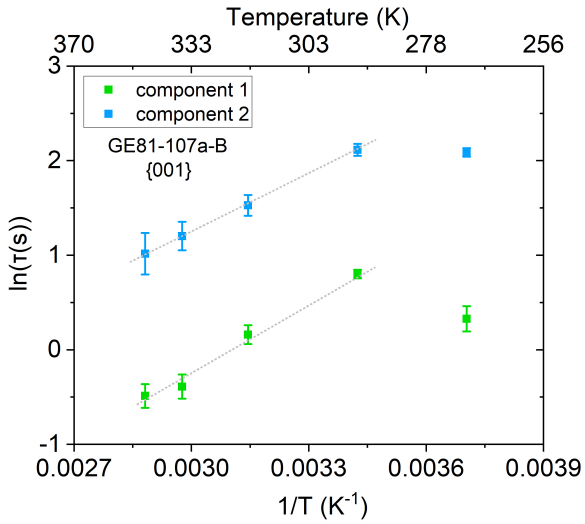

(b)

Figure 5.15: Temperature dependence of N_S^0 recovery half-lifetime in sample GE81-107a-B ({001} growth sector) between 270 K to 350 K. (a) half-lifetime versus temperature. (b) The logarithm of half-lifetime versus reciprocal of temperature. The grey dash lines are the results of the fitting to an Arrhenius function.

The activation energy for the recovery of N_S^0 in sample GE81-107a-B ({001} growth sector) after 224 nm pulsed laser excitation is calculated using equation 2.80 based on the fitting results by three different fitting functions as shown in figure 5.15(b) and figure 5.16. The activation energies obtained from the lifetime of N_S^0 concentration recovery in GE81-107a-B by different fitting methods, which are listed in table 5.2, is consistent and approximately 0.2 ± 0.05 eV.

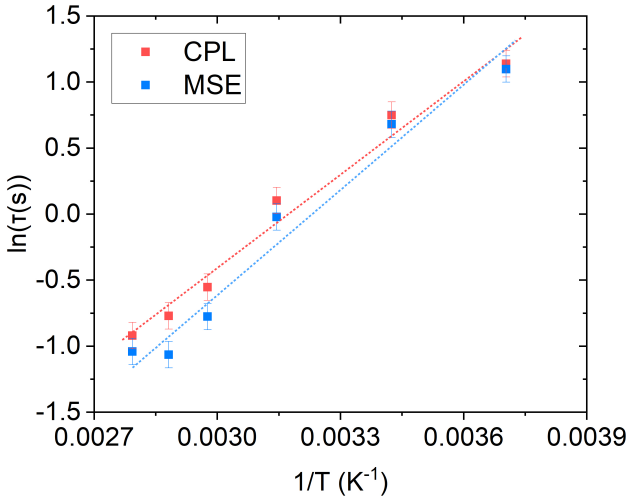

Figure 5.16: The logarithm of half-lifetime (fit by MSE function and CPL function) in GE81-107a-B versus reciprocal temperature. The dash lines are the results of the fitting to an Arrhenius function.

Table 5.2: Activation energies determined from N_S^0 concentration decay or recovery lifetimes for GE samples by the fitting of multiple components method (equation 2.94), modified stretched exponential function (MSE) (equation 2.91) and complex power law decay function (CPL) (equation 2.88).

	GE81-107a-B {001} $[N_S] > [B_S]$		GE81-107a-C {111} $[N_S] < [B_S]$	
	Exp 1	Exp 2	Exp 1	Exp 2
E_A	0.18(2) eV	0.21(2) eV	0.18(5) eV	0.26(5) eV
	MSE		MSE	
E_A	0.22(5) eV		0.18(3) eV	
	CPL		CPL	
E_A	0.21(5) eV		0.19(3) eV	

5.4.2.5 Different excitation

To investigate the influence of excitation light source on the substitutional nitrogen charge transfer dynamics during phosphorescence, a 224 nm pulsed laser and a pulsed broadband UV lamp described in Chapter 3.3 are used to irradiate sample GE81-107a-B. Observation during pulsed UV lamp illumination is impossible since the generation of high concentration carriers increases the electric conductivity and causes dielectric loss, which dramatically changes the Q_S value and detunes the resonator. The recovery curves of the N_S^0 EPR signal recorded after different excitation are plotted in figure 5.17. The concentration of N_S^0 changed by different UV illumination is similar, whereas the recovery rate after UV lamp excitation with a higher power is faster. For further research of interest, the comparison between the current results and recovery curve after the continuous wave (CW) UV excitation would be helpful.

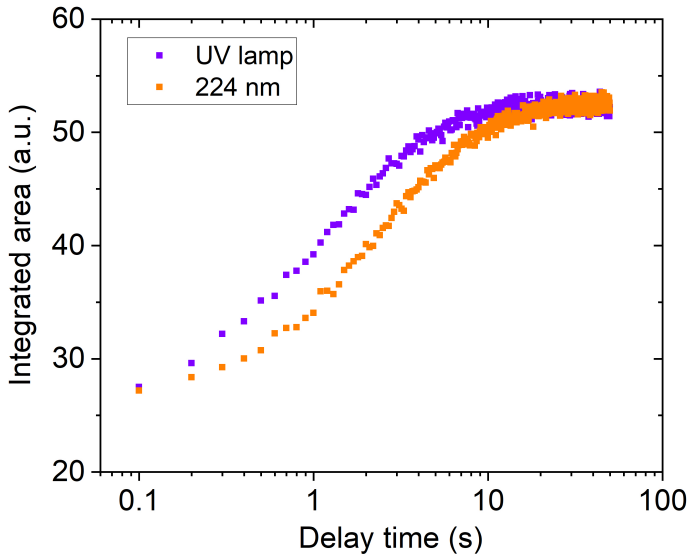

Figure 5.17: The recovery curve of N_S^0 central peak integrated intensity in sample GE81-107a-B was recorded at room temperature after UV lamp and 224 nm pulsed laser excitation, respectively.

5.5 Sample SYN4-10

The UV lamp excitation increases the concentration of N_S^0 in HPHT synthetic diamond sample SYN4-10 from 15 ± 2 ppb to 21 ± 2 at room temperature when

pump to saturation. The central peak of the N_S^0 RP-EPR spectra in dark and after UV excitation recorded using the experimental methods described in Chapter 3.3 is shown in figure 5.18.

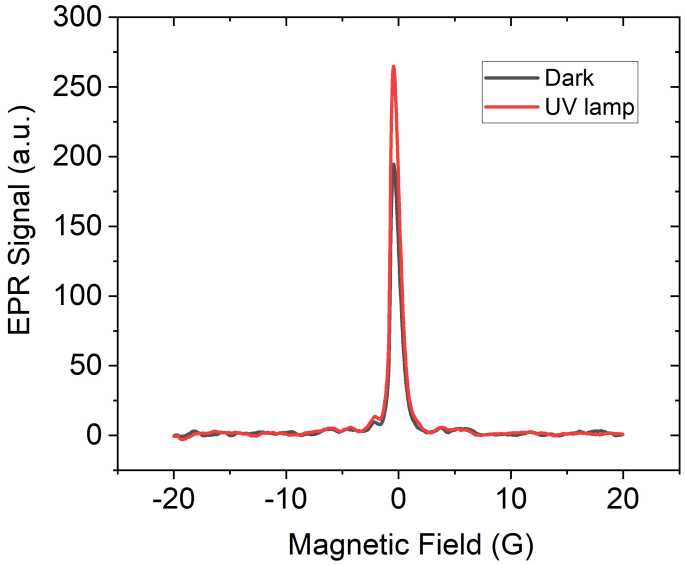

Figure 5.18: EPR spectra of N_S^0 centre central peak of sample SYN4-10 recorded under UV lamp excitation and in the dark at room temperature.

After turning off the UV lamp, the concentration of neutral substitutional nitrogen further increases for approximately 10 s, then begins to drop by a dramatically slower rate (figure 5.19). Due to the detection time constraints, the dynamics monitoring of N_S^0 concentration after UV excitation did not continue to allow the concentration back to the level before the UV excitation; namely, the charge equilibrium has not reached yet when finishing the record of the curve shown in figure 5.19. The decay of N_S^0 EPR signal lasts for $>$ 12 hours.

5.6 Discussion

5.6.1 During bandgap UV excitation

Bandgap UV excitation creates electrons in the conduction band and holes in the valence band, respectively:

$$h\omega_{BG} \rightarrow e^- + h^+ \tag{5.8}$$

In a compensated {111} sample where $[B_S] > [N_S]$, it is expected that $[N_S^+] \gg$

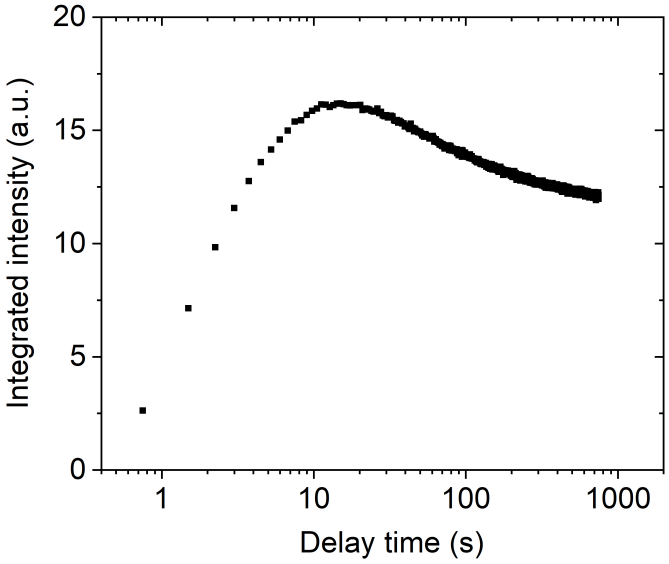

Figure 5.19: The N_S^0 central peak integrated intensity recovery-decay curve in sample SYN4-10 was recorded after UV lamp excitation at room temperature. The entire curve is not recorded due to the limitation of detection time.

$[N_S{}^0]$ in dark. During bandgap excitation, for the isolated N_S defect, it is expected that the dominant process will be

$$N_S{}^+ + e^- \rightarrow N_S{}^0 \tag{5.9}$$

the concentration of N_S^0 is expected to **increase**. This is consistent with the charge transfer observed in the {111} growth sector containing more boron acceptor than substitutional nitrogen. Substitutional boron is also neutralized by bandgap UV excitation:

$$B_S{}^- + h^+ \rightarrow B_S{}^0 \tag{5.10}$$

However, the concentration of N_S^0 in the {001} growth sector is seen to decrease under bandgap UV illumination, which can only be explained by the existence of substitutional nitrogen in negative charge state. If $[N_S] \gg [B_S]$, it is expected that $[N_S{}^0] > [N_S{}^+], [B_S{}^-]$ in dark. Under bandgap illumination, although $[N_S^0]$ and $[B_S^0]$ might be expected to increase, it is possible that if N_S^0 can also act as an electron trap,

$$N_S{}^0 + e^- \rightarrow N_S{}^- \tag{5.11}$$

$$2N_S{}^0 \overset{h\omega}{\rightarrow} N_S{}^+ + N_S{}^- \tag{5.12}$$

$[N_S^0]$ could in fact **decrease**. Substitutional boron is also neutralized by the bandgap UV excitation:

$$B_S{}^- + h^+ \rightarrow B_S{}^0 \tag{5.13}$$

Jones *et al.* have theoretically predicted that in addition to a deep donor level for N_S^0, the substitutional nitrogen defect has an acceptor level (N_S^-) in the bandgap lying approximately 1.1 eV below the conduction band minimum. [5] N_S^- has been experimentally observed in high nitrogen-doped diamond samples by Ulbricht *et al.* [23] The production of N_S^- under bandgap illumination can explain the observed experiment results. However, in this research the data shows that the N_S^- level is only $\sim$ 0.2 eV below the conduction band minimum. This value for the activation energy is determined from the thermal ionization measurements (see Chapters 5.3.2.4 and 5.4.2.4)

5.6.2 After bandgap UV excitation

Figure 5.20 shows at room temperature, after bandgap excitation $[N_S^0]$ reached equilibrium faster in the {001} growth sector than in the {111} growth sector.

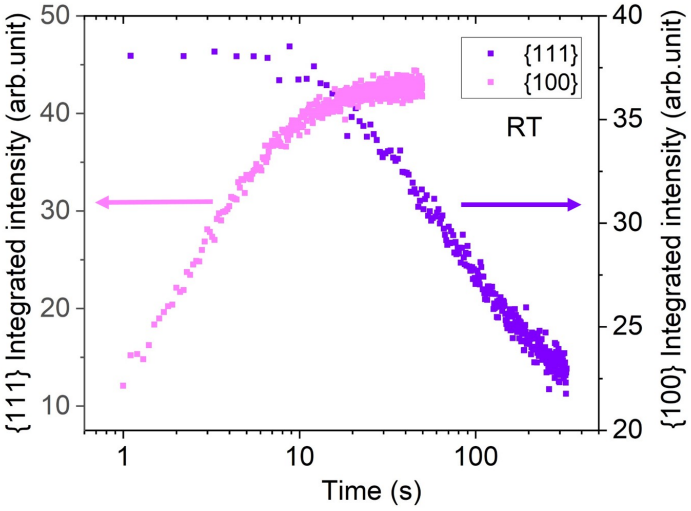

Figure 5.20: The N_S^0 central peak decay in sample GE81-107a-C ({111} growth sector) and recovery in sample GE81-107a-B ({100} growth sector) were recorded at room temperature after 224 nm pulsed laser excitation. Sample GE81-107a-B and GE81-107a-C weigh 7.8 mg and 4.2 mg, respectively.

In the {001} growth sector (GE81-107a-B) where $[N_S] > [B_S]$, the $[N_S^0]$ recovery is driven by both

$$N_S{}^- \rightarrow N_S{}^0 + e_{CB}^- \tag{5.14}$$

(released electron can be trapped by luminescence centres and phosphorescence results) and

$$N_S{}^+ + N_S{}^- \rightarrow 2N_S{}^0 \tag{5.15}$$

Isolated boron can be thermally ionized

$$B_S{}^0 \rightarrow B_S{}^- + h_{VB}^+ \tag{5.16}$$

and the released hole trapped by luminescence centres and phosphorescence results.

In the {111} growth sector (GE81-107a-C) where $[B_S] > [N_S]$, even though the activation energy for B_S^0 ionization

$$B_S{}^0 \rightarrow B_S{}^- + h_{VB}^+ \tag{5.17}$$

is higher than that for ionization of N_S^-, the decay in the excess isolated N_S^0 concentration is expected to be dominated by hole capture

$$N_S{}^0 + h^+ \rightarrow N_S{}^+ \tag{5.18}$$

in addition to tunneling of N_S^0 electron to luminescence centres (temperature too low for thermal ionization of N_S^0). Thus in the {111} growth sector, the decay of $[N_S^0]$ is expected to be slower than the recovery of $[N_S^0]$ in the {001} growth sector. But also

$$N_S{}^- \rightarrow N_S{}^0 + e_{CB}^- \tag{5.19}$$

and

$$N_S{}^+ + N_S{}^- \rightarrow 2N_S{}^0 \tag{5.20}$$

can occur. The electrons and holes released can be trapped by isolated defects and luminescence centres (e.g. DAPs), thereby resetting these defects so they can emit multiple times.

The activation energy for N_S^0 decay after bandgap excitation was found to be less than the B_S acceptor activation energy and similar to that determined in the sample where $N_S > B_S$. This result is surprising without the knowledge of discovery reported here that the N_S^- is a shallow donor. The measurements on the sample where $B_S > N_S$ are taken over a narrow temperature range (different to that for the sample where $N_S > B_S$) and a temperature calibration error could effect the activation energy determined. Further, in the temperature range studied, thermal activation and carrier tunnelling both contribute significantly. Therefore, the measurements should be at higher temperatures but this was prohibited here by low SNR.

The data presented here suggests that the N_S defect can form a shallow (close to the bottom of CB) electron trap. The ionization data indicates that this trap level is only ~ 0.2 eV beneath the bottom of the conduction band, and is thus more easily thermally ionized than the B_S acceptor (0.37 eV). It is reasonable that the electron wavefunction for N_S^- is more delocalised than for N_S^0. Less configurational change is expected between N_S^- and N_S^0 than between N_S^0 and N_S^+. For both N_S^0 and N_S^-, a large trigonal distortion is expected. It is therefore likely that tunneling between close N_S^0 and N_S^- defects is reasonably easy and that this would contribute to the resetting of luminescence centres at low temperatures (see Chapter 6).

In diamonds containing a relatively low concentration of defects, we would expect, after bandgap excitation, a distribution of isolated N_S defects in different charge states: N_S^+, N_S^0, and N_S^-. Measuring low concentrations of N_S^- is challenging as no EPR or localized electronic optical signal is expected. However we can estimate the concentration of N_S^-.

Table 5.3 shows the measured $[N_S^0]$ (EPR) and $[B_S^0]$ (FTIR) for sample GE81-107a-B annealed in the dark to 400 K or excited with bandgap optical excitation. For GE81-107a-B in the dark/annealed state, we can reasonably assume that $[N_S^-] = 0$. Furthermore, for GE81-107a-B in the illuminated state $[B_S^-]$ would tend to be zero at sufficiently high light intensities. Thus using charge balance and concentration of total N_S and B_S, we can simply calculate $[B_S^-]$, $[N_S^+]$, and $[N_S^-]$ (table 5.3). This shows that there could be a significant concentration of isolated N_S^-. Thus for diamonds containing isolated N_S, isolated B_S, and suitable luminescence

centres such as donor-acceptor pairs (the nature of these is discussed in Chapters 6, 7, and 8), after bandgap illumination we would have excess concentration of N_S^- and B_S^0. At sufficiently high temperatures the former would release electrons and the latter holes into the CB and VB, respectively. These carriers could be trapped by luminescence centres, and phosphorescence observed. At low temperatures charge tunneling would dominates.

Table 5.3: The concentrations of N_S and B_S in different charge states in GE81-107a-B at room temperature: annealed in the dark to 400 K or excited with the bandgap optical excitation.

Heated in dark			UV illumination	
Determination	Conc.		Conc.	Determination
Measured by EPR	145	N_S^0	80	Measured by EPR
Assumed that heating in dark empties shallow N_S^- trap	0	N_S^-	44	Derived from measured change in $[N_S^0]$ and charge neutrality
Derived from charge neutrality, $[N_S^-]$ and $[B_S^-]$	23	N_S^+	44	Derived from measured change in $[N_S^0]$ and charge neutrality
Measured by FTIR	67	B_S^0	90	Measured by FTIR
Derived from measured change in $[B_S^0]$ on UV excitation and ①	23	B_S^-	0	① Assumed that bandgap excitation neutralises boron acceptor

Below bandgap excitation could also result in the redistribution of charge and produce excess population of both isolated N_S^- and B_S^0 leading in turn to phosphorescence. This should be investigated further.

It is clear from the data presented that the results of bandgap optical excitation depend on the concentrations of N_S and B_S in the sample studied. This is exemplified in the multi-sectors sample SYN4-10 where after excitation is removed $[N_S^0]$ increases and then decreases. Studies on N_S and B_S co-doped CVD samples could be very interesting especially if the impurities concentration could be accurately controlled.

5.7 Conclusion and future work

In conclusion, it has been shown that it is necessary to consider three charge states for substitutional nitrogen: N_S^+, N_S^0, and N_S^-. UV illumination can either increase or decrease the concentration of N_S^0. The N_S^0 defect is a deep donor and at the temperatures studied and it cannot be thermally ionized. However, N_S^-, as a shallow trap, is readily thermally ionized over a temperature range which overlaps with that for thermal ionization of the neutral boron acceptor (charge transfer process 5.14). The activation energy for this thermal ionization estimated as ~ 0.2 eV.

This study can be further improved on the following aspects: firstly, the influence of boron concentration and dose of UV excitation on the value of the loaded quality factor Q of the cavity when performing the RP-EPR experiment should be confirmed; secondly, the method for low-temperature quantification of EPR technique should be developed; thirdly, utilise the CW UV excitation to irradiate the diamond sample and investigate the concentration of N_S^0 changed under intensive excitation; fourthly, the SNR of RP-EPR measurement above room temperature should be further improved to confirm the activation energy of the N_S^0 decay after UV excitation in sample GE81-107a-C; finally, the diamond sample can be sliced to a thinner diamond plate to achieve a more accurate quantitative understanding of the proportion of the total substitutional nitrogen concentration that participates in the charge transfer processes under and after UV excitation.

Bibliography

[1] M. N. R. Ashfold, J. P. Goss, B. L. Green, P. W. May, M. E. Newton, and C. V. Peaker, Chemical Reviews **120**, 5745 (2020).

[2] A. T. Collins, Diamond and Related Materials **1**, 457 (1992).

[3] R. C. Burns, V. Cvetkovic, C. N. Dodge, D. J. F. Evans, M. L. T. Rooney, P. M. Spear, and C. M. Welbourn, Journal of Crystal Growth **104**, 257 (1990).

[4] W. V. Smith, P. P. Sorokin, I. L. Gelles, and G. J. Lasher, Physical Review **115**, 1546 (1959).

[5] R. Jones, J. P. Goss, and P. R. Briddon, Physical Review B **80**, 033205 (2009).

[6] G. Davies, *Properties and Growth of Diamond*, 9 (Inst of Engineering & Technology, 1994).

[7] A. Cox, M. E. Newton, and J. M. Baker, Journal of Physics: Condensed Matter **6**, 551 (1994).

[8] C. A. J. Ammerlaan and E. A. Burgemeister, Physical Review Letters **47**, 954 (1981).

[9] R. C. Barklie and J. Guven, Journal of Physics C: Solid State Physics **14**, 3621 (1981).

[10] J. H. N. Loubser and W. P. Van Ryneveld, British Journal of Applied Physics **18**, 1029 (1967).

[11] B. G. Breeze, *Electron paramagnetic resonance studies of point defects in diamond: quantification, spin polarisation and preferential orientation*, Ph.D. thesis, University of Warwick (2016).

[12] A. J. Neves and M. H. Nazaré, *Properties, Growth and Applications of Diamond*, 26 (The Institution of Electrical Engineers, 2001).

[13] D. G. Mitchell, M. Tseitlin, R. W. Quine, V. Meyer, M. E. Newton, A. Schnegg, B. George, S. S. Eaton, and G. R. Eaton, Molecular Physics **111**, 2664 (2013).

[14] R. G. Farrer, Solid State Communications **7**, 685 (1969).

[15] A. T. Collins, Diamond and Related Materials **8**, 1455 (1999).

[16] A. T. Collins and A. W. S. Williams, Journal of Physics C: Solid State Physics **4**, 1789 (1971).

[17] S. C. Lawson, D. Fisher, D. C. Hunt, and M. E. Newton, Journal of Physics: Condensed Matter **10**, 6171 (1998).

[18] R. P. Messmer and G. D. Watkins, Physical Review Letters **25**, 656 (1970).

[19] K. Iakoubovskii and G. J. Adriaenssens, Journal of Physics: Condensed Matter **12**, L77 (2000).

[20] G. Davies, Physica B: Condensed Matter **273**, 15 (1999).

[21] A. T. Collins, M. Stanley, and G. S. Woods, Journal of Physics D: Applied Physics **20**, 969 (1987).

[22] A. M. Edmonds, *Magnetic resonance studies of point defects in single crystal diamond*, Ph.D. thesis, University of Warwick (2008).

[23] R. Ulbricht, S. T. Van Der Post, J. P. Goss, P. R. Briddon, R. Jones, R. U. A. Khan, and M. Bonn, Physical Review B **84**, 165202 (2011).

[24] G. R. Eaton, S. S. Eaton, D. P. Barr, and R. T. Weber, *Quantitative EPR* (Springer Science & Business Media, 2010).

[25] B. L. Cann, *Magnetic resonance studies of point defects in diamond*, Ph.D. thesis, University of Warwick (2009).

[26] U. F. S. D'Haenens-Johansson, *Optical and magnetic resonance studies of point defects in CVD diamond*, Ph.D. thesis, University of Warwick (2011).

[27] A. M. Edmonds, U. F. S. D'Haenens-Johansson, R. J. Cruddace, M. E. Newton, K. M. C. Fu, C. Santori, R. G. Beausoleil, D. J. Twitchen, and M. L. Markham, Physical Review B **86**, 035201 (2012).

Chapter 6

Phosphorescence

6.1 Background

With the assistance of other properties, phosphorescence is important for the characterisation and identification of natural and synthetic diamonds. [1, 2] Phosphorescence in natural diamond was first reported in 1946 [3], the blue afterglow caused by sunlight passing through a Wood's glass filter (320 - 400 nm) lasted for several seconds to minutes. More investigation on phosphorescence in natural and synthetic diamonds (mainly HPHT synthesis) afterwards indicated that phosphorescence was rare and most commonly shown in type II diamonds. [1, 4–6] For those diamonds showing phosphorescence after radiation, the natural ones are usually blue in appearance, and the synthetic ones are boron-doped. [1, 2, 4, 5] Therefore, boron is believed to play a key role in the phosphorescence mechanism. [1]

Three different phosphorescence bands are commonly reported in diamond. "Blue-green", "orange", and "red" phosphorescence were observed in various diamonds after different radiation and temperature conditions, which appeared as broad, featureless bands on the spectrum. [1, 2, 4–7]

The "blue" (or "blue-green") emission band at a peak energy of 2.5 eV (490 nm - 503 nm) was observed in type II natural, HPHT synthetic, and HPHT treated diamonds. [1–10] Almost all phosphorescence in natural and HPHT synthetic or treated diamonds detected after UV radiation ($\lambda \leq 254$ nm) at room temperature contains this "blue" component. For the phosphorescence with only one "orange"

band in the boron-doped synthetic diamond reported by Walsh *et al.* [6], "blue" bands still possibly exist due to the large width of broadband. A shoulder of the 2.5 eV band at a shorter wavelength (440 nm to 470 nm), usually shown after relatively intense radiation, is considered to be generated by the same donor-acceptor pair (DAP) recombination, with the shift in energy a consequence of different distances between the donor and acceptor [4, 10, 11]. The "blue" phosphorescence is quenched at higher temperatures. The band position is temperature independent in a range of 250 K to 400 K. [7, 11] The "blue" emission band centred at 2.5 eV was not seen after excitation at longer wavelengths such as 365 nm and 458 nm. [1, 4]

The peak energy of the "orange" or "yellowish-orange" phosphorescence band has a wider distribution from 575 nm [4, 5] to 590 nm [1, 6], which was referred to as the 2.1 eV band. The "orange" emission band centred at 2.1 eV is generally observed in HPHT synthetic or HPHT treated diamonds after UV and visible excitation. [1, 2, 4–6] The "orange" phosphorescence band centred at 580 nm was once reported to have been seen in natural diamond. [5] Compared to the "blue-green" band centred at 2.5 eV, the "orange" band is not common and has a weaker initial intensity and longer half-life time from several seconds to tens of seconds. [1, 5] After radiation, the phosphorescence can be seen to change from blue to orange. The "blue" and "orange" phosphorescence is distributed in the different regions of HPHT synthetic diamonds: the "orange" emission is more concentrated near the seed crystal. Also, the "orange" emission band and "blue-green" emission band have a different excitation threshold, so should have a different origin. [1]

Like the "orange" emission band, a "red" phosphorescence band has peak energies ranging from 1.80 eV to 1.88 eV (660 nm) [2, 4], 680 nm [7], or 690 nm [6], observed in natural diamonds is always accompanied by the "blue-green" band centred at 2.5 eV. The "red" phosphorescence can be excited by either UV or visible light. [4] The decay of the "red" emission band with a lifetime ranging from several seconds to tens of seconds, is slower than that of the 2.5 eV "blue-green" band. [4] As the concentration of boron in diamond increases, the ratio of the initial intensity of the "blue-green" band and the "red" band decreases, and the half-lifetime of phosphorescence bands becomes shorter. [2]. Sometimes the "red"

phosphorescence cannot be seen until the diamond is heated up to 350 K. [7] Eaton *et al.* only found the "red" emission band centred at 660 nm in natural diamonds. [2] In contrast, a weak "red" phosphorescence band was seen in a HPHT synthetic diamond grown with cobalt and titanium as nitrogen getters by Watanabe *et al.*. [1] Since the spectrum was not published, it is uncertain whether they are the same variety of phosphorescence bands.

The phosphorescence decay curve usually follows a hyperbolic decay function. [1, 2, 10] The "blue-green", "orange" and "red" phosphorescence bands above were not observed in CVD diamond. [5] There is a lack of research on phosphorescence in CVD synthetic diamonds in the literature.

A model based on a T-dependent recombination process for the mechanism of phosphorescence in type II diamond has been suggested. [1] As shown in figure 6.1, both DAP and isolated acceptor are involved in the model. During excitation, the pair of neutral donor and neutral acceptor recombine and emit fluorescence. Meanwhile, the holes created are trapped by the isolated acceptor. After excitation, the holes are thermally released from isolated acceptors, transport through the valence band, and are captured by the ionized acceptor in close proximity to a neutral donor. The donor-acceptor recombination generates delayed light emission, namely phosphorescence. Alternately, the thermally released hole from the isolated acceptor can be re-trapped by other non-radiative centres. [1] As a shallow acceptor with an activation energy of 0.35 eV, boron is widely considered to play a key role in the phosphorescence process. [1, 6]

Further improvement for the above model is required: although the luminescence centre is considered donor-acceptor pairs, the specific candidates are not certain. [1] Moreover, considering the low concentration distribution of related defects in type II diamond, the relatively strong phosphorescence intensity is not consistent with the above model. Finally, phosphorescence decay observed at low temperatures can not be explained by such a thermal process with a vanishingly low probability of thermal excitation. [12]

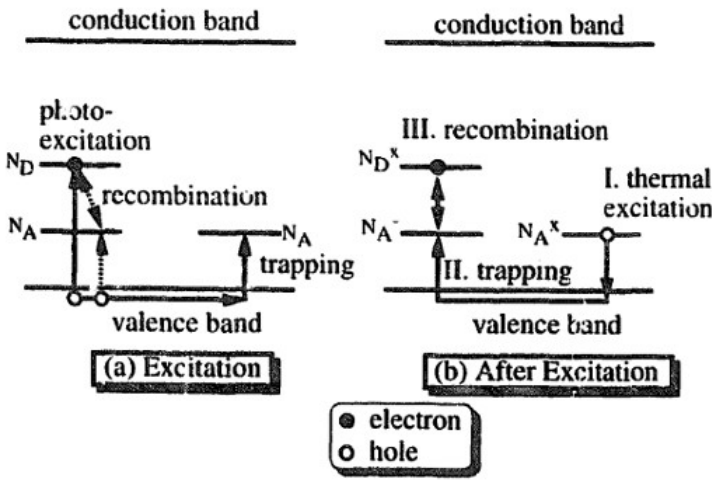

Figure 6.1: Schematic energy level representation of the basic model for phosphorescence published by [1].

6.2 Sample GE81-107a-B/C

6.2.1 Cathodoluminescence

The CL emission bands in sample GE81-107a-B and GE81-107a-C at 80 K and room temperature are recorded as shown in figure 6.2.

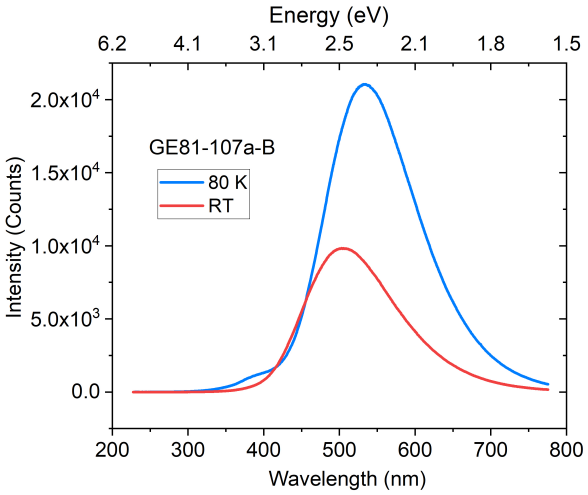

(a)

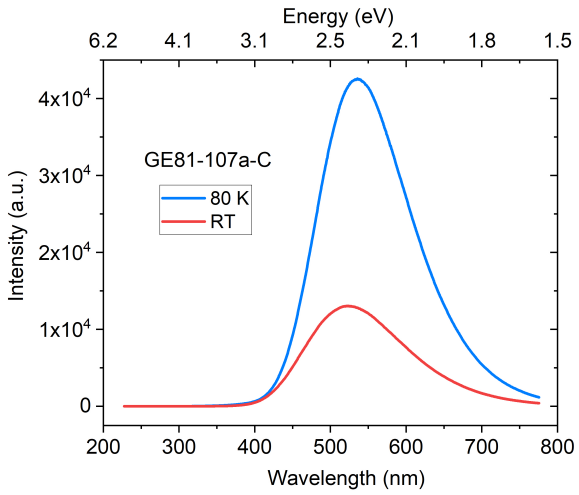

(b)

Figure 6.2: The CL spectra show the visible emission band in GE samples at 80 K and room temperature. (a) GE81-107a-B (b) GE81-107a-C.

The centre of the emission band at room temperature is located at a shorter wavelength than the emission band at the liquid nitrogen temperature. Specifically, the CL emission band in GE81-107a-B is centred at 532 nm (2.33 eV) and 503 nm (2.46 eV) at 80 K and RT, respectively. In addition, a shoulder can be seen

at the higher energy side of the emission band at 80 K, which is likely to be the "blue-green" CL emission band near 2.8 eV observed by Klein *et al.* previously. [13] The CL emission band in GE81-107a-C peaks at 535 nm (2.32 eV) and 520 nm (2.38 eV) at 80 K and RT, respectively. Those emission bands gradually decay after turning off the electron gun, and the decay at room temperature is significantly faster than that at low temperature.

6.2.2 Photoluminescence

Figure 6.3 shows that the "blue-green" luminescence band centred at approximately 2.5 eV is excited by the UV light ranging from around 200 nm (short wavelength limitation of this measurement) to 235 nm. The centre of the band shifts from 490 nm to 480 nm as the excitation wavelength varies from 200 nm to 270 nm. The luminescence band is most intense under approximately 222.5 nm excitation. As shown in figure 6.4, there is a significant UV excitation edge at approximately 235 nm. For a longer-wavelength excitation, the intensity of luminescence drops. Such luminescence behaviour is very similar for samples GE81-107a-B and GE81-107a-C.

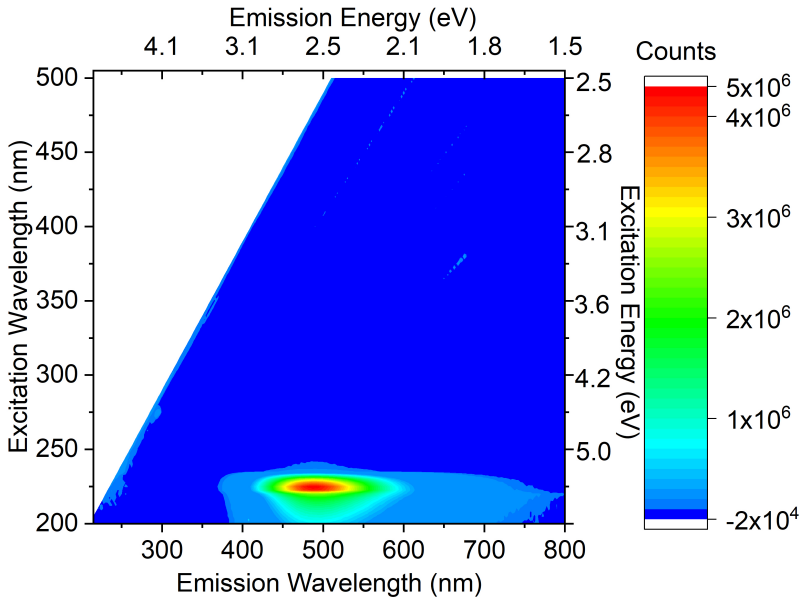

Figure 6.3: Photoluminescence spectra of GE81-107a-B by excitation ranging from 200 nm to 500 nm at room temperature.

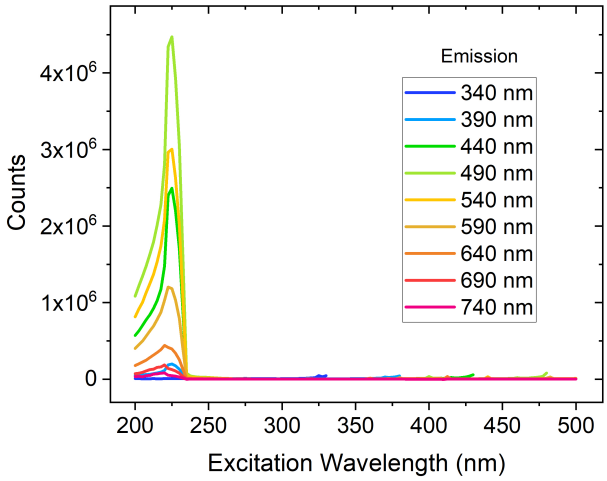

Figure 6.4: Photoluminescence intensity of emission at a series of different wavelengths versus excitation wavelengths in sample GE81-107a-B.

6.2.3 Phosphorescence spectra

Phosphorescence spectra in type II HPHT synthetic diamond samples GE81-107a-B ({001} growth sector) and GE81-107a-C ({111} growth sector) have been investigated by the Garfield experimental setup described in Chapter 3.2. After 224 nm excitation, the phosphorescence spectra were recorded in a temperature range of 83 K to 573 K at intervals of 20 K.

The characteristic "blue" (or "blue-green") phosphorescence is shown in both GE81-107a-B ({001} growth sector) and GE81-107a-C ({111} growth sector) samples after 224 nm excitation in the whole operating temperature range. The other phosphorescence bands centred at approximately 2.1 eV and 1.8 eV reported in the literature are not seen. [1, 5]

As shown in figure 6.5, the phosphorescence band in GE81-107a-C peaks at 2.25 eV (550 nm) in the low-temperature range of 83 K to 173 K, and approximately 2.5 eV (494 nm) at high temperature (273 K to 473 K). The 2.5 eV band corresponds to the results in the literature. [1, 2, 4–6] There is no shift in phosphorescence band peak energies during decay after radiation when the temperature is below 173 K or above 273 K. However, in the intermediate temperature range (173 K to 273 K), the position of emission bands shifts to higher energy significantly during decay, which suggests the phosphorescence consists of different components: one

phosphorescence band at lower energies decays faster, another phosphorescence band at higher energies decays more slowly. As the temperature increases in this range, the initial phosphorescence spectra recorded at a delay time of 0.01 s after UV radiation gradually shifted to higher energies. This is due to an increase in the intensity of the high energy component and a decrease in the intensity of the low energy component until the temperature reaches 273 K, where only the high energy component (the 2.5 eV band) remains.

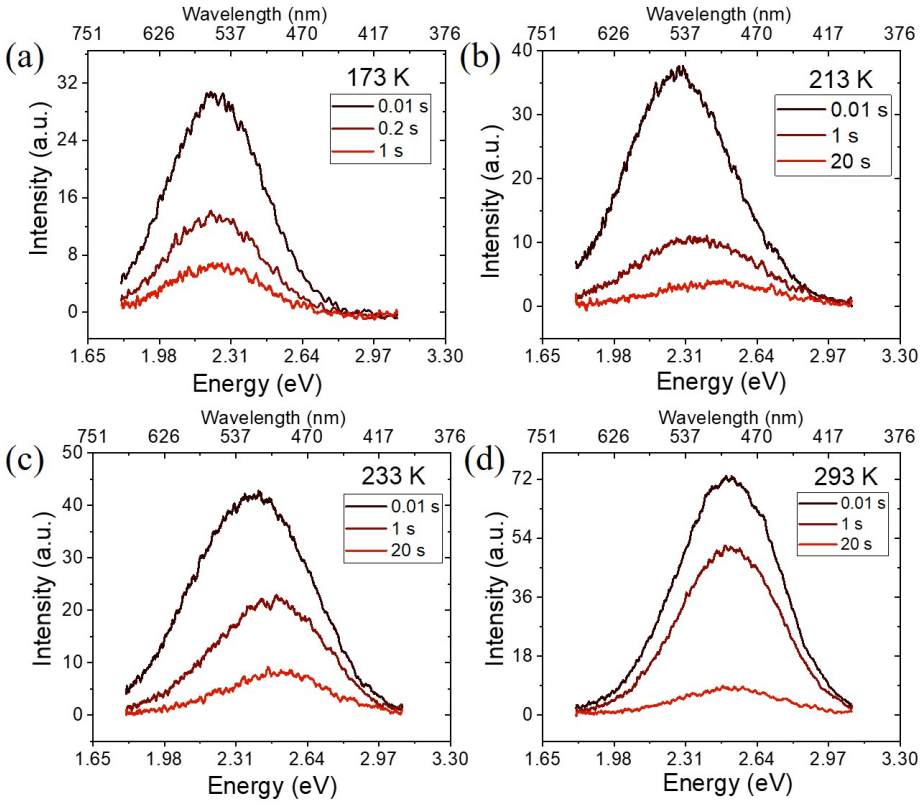

Figure 6.5: Phosphorescence spectra from sample GE81-107a-C recorded using 224 nm excitation at (a) 173 K, (b) 213 K, (c) 233 K, and (d) 293 K, respectively.

The variation in emission band position in the two diamonds after different temperature conditions is similar. The "blue-green" emission band in GE81-107a-B is centred at 484 nm, slightly shorter in wavelengths than that of GE81-107a-C (494 nm) when temperature above 273 K. The phosphorescence band at low temperature is the same as that in {111} growth sector, which is at 2.25 eV (550 nm). The phosphorescence intensity in GE81-107a-B is lower than that in GE81-107a-C. The differences in intensity of the "blue-green" phosphorescence between different growth sectors result from the concentration and distribution of related defects.

6.2.4 Phosphorescence decay curve

Phosphorescence decay by 224 nm pulsed laser radiation in HPHT synthetic diamond samples GE81-107a-B ({001} growth sector) and GE81-107a-C ({111} growth sector) were measured using the camera of the "Garfield" experimental setup at a temperature range of 83 K to 473 K (Fig 6.6). Although the phosphorescence intensities are plotted in arbitrary units in figure 6.6, a comparison can be made between the relative intensities at different temperatures since the acquisition parameters are the same for all measurements. The data is plotted on a log time scale to emphasise the change in the decay rates at higher temperatures.

The 224 nm laser-excited phosphorescence was more intense for sample GE81-107a-C than sample GE81-107a-B at all temperatures studied, but the difference was largest for the measurements at low and high temperatures. Both samples' low-temperature phosphorescence decay rate (temperature below 173 K) was approximately independent of temperature. At temperatures above 173 K, the lifetime of phosphorescence decay dropped rapidly as the temperature increased until the decay was too rapid to detect by the experimental setup when reaching 473 K.

6.2.5 Phosphorescence decay curve fitting

Phosphorescence decay curve can be fitted by various functions introduced in chapter 2.3.4, such as simple exponential function, hyperbolic function, power-law decay function, stretched exponential function, or a combination of those functions, depending on different mechanisms of phosphorescence processes. The three fitting methods based on different functions are described in detail as follows.

6.2.5.1 Multiple components fitting

The multiple components fitting methods based on function 2.94 are useful for investigating the components in a phosphorescence decay curve, which have different mechanisms such as tunnelling process ($1/(t+\gamma)$ power-law decay), the first order of kinetics (simple exponential decay) and second-order of kinetics (hyperbolic exponential decay) thermal processes. When fitting the phosphorescence decay

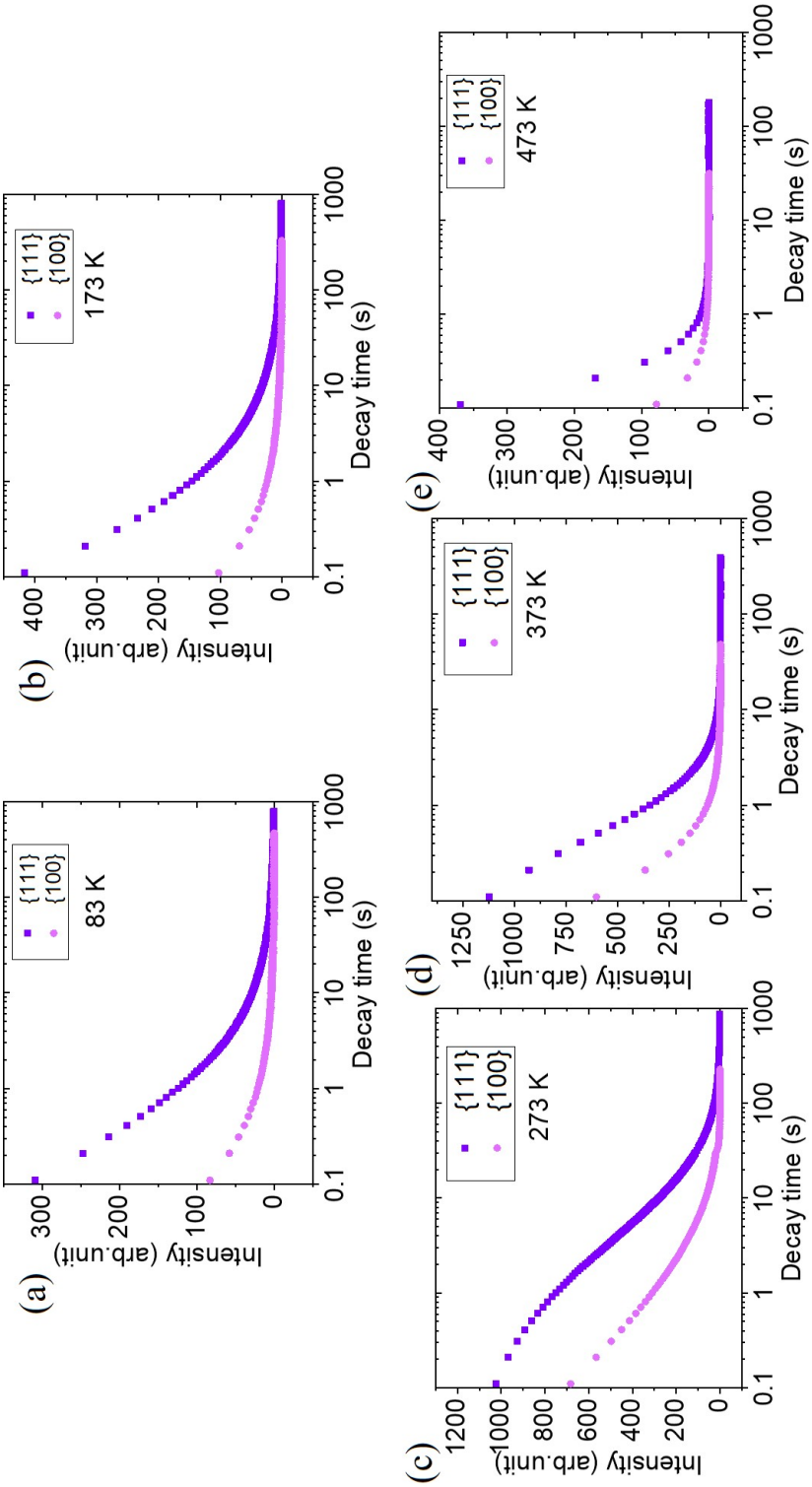

Figure 6.6: Phosphorescence intensity decay curves in growth sector {111} and {100} recorded (50 ms acquisition time for each frame) after excitation with 224 nm laser for GE samples at different T (a) 83 K (b) 173 K (c) 273 K (d) 373 K (e) 473 K.

curve by these functions, parameters are adjusted to make the coefficient of determination (R-squared) reach 0.999 to get a proper fit.

As shown in figure 6.7, the phosphorescence decay curves recorded at a low-temperature range (83 K to 173 K) can be satisfactorily fit using two $1/(t+\gamma)$ power-law decay components with different parameters, which indicates that the phosphorescence decay origins from athermal tunnelling processes.

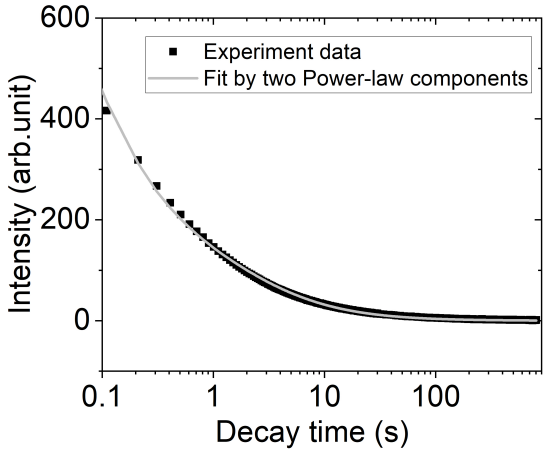

(a)

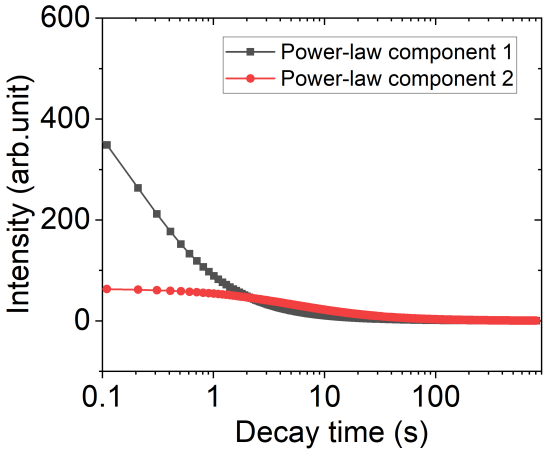

(b)

Figure 6.7: The different components are the results of fitting the phosphorescence decay curve in sample GE81-107a-C at low-temperature range by function 2.94, taking the decay at 173 K as an example here. Compared to one power-law component fitting, the R-squared is improved from 0.932 to 0.999; the chi-squared is reduced from 170.53 to 1.08. (a) shows the experimental data and the fitting curve. (b) shows the two power-law components decay curves: power-law component 1 and power-law component 2 labelled as black and red lines follow a $1/(t+\gamma)$ power-law decay.

In the intermediate temperature range of 173 K to 273 K, the phosphorescence decay (Figure 6.8) is best fitted using a combination of $1/(t+\gamma)$ power-law decay functions and simple exponential decay functions. Therefore, both the tunnelling process and the thermal process contribute to phosphorescence.

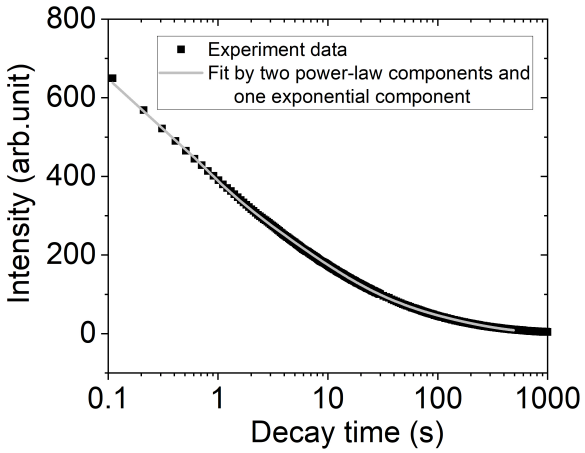

(a)

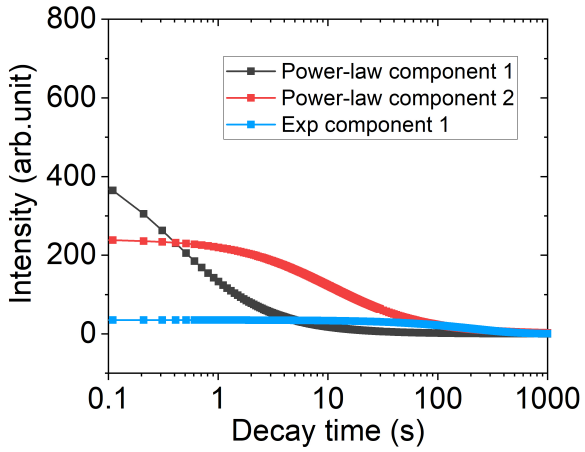

(b)

Figure 6.8: The different components are the results of fitting the phosphorescence decay curve in sample GE81-107a-C at intermediate temperature range by function 2.94, taking the decay at 233 K as an example here. Compared to two power-law components fitting, the R-squared is improved from 0.997 to 1.000; the chi-squared is reduced from 16.93 to 1.96. (a) shows the experimental data and the fitting curve. (b) shows the individual components decay curves: power-law component 1 and power-law component 2 labelled as black and red lines follow a $1/(t+\gamma)$ power-law decay, Exp component 1 labelled as blue line follow a simple exponential decay.

Two components following simple exponential decay are involved in the phos-

phorescence when the temperature is above 273 K (Figure 6.9), suggesting the phosphorescence at high temperature is dominated the thermal processes. Moreover, simple exponential functions are better than the hyperbolic functions to fit the phosphorescence decay curves, which shows that once the charge carriers are thermally released into the conduction band or valence band, the probability of retrapping is negligible. This is consistent with the low concentration of defects by our measurement results.

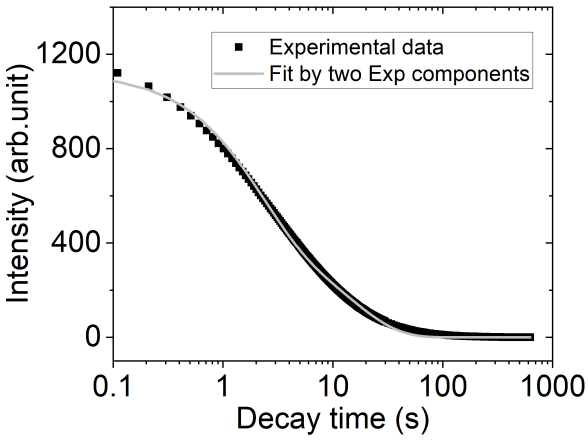

(a)

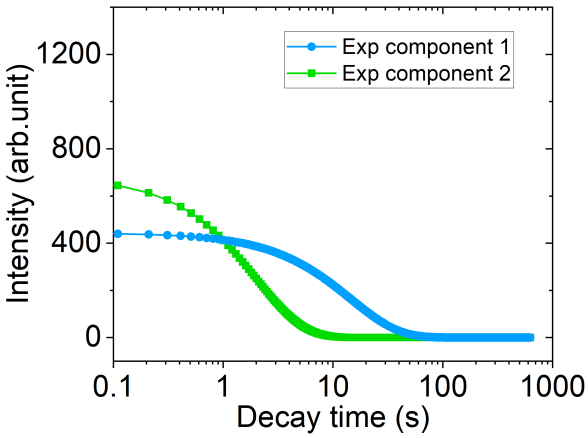

(b)

Figure 6.9: The different components are the results of fitting the phosphorescence decay curve in sample GE81-107a-C at high-temperature range by function 2.94, taking the decay at 293 K as an example here. Compared to one simple exponential component fitting, the R-squared is improved from 0.937 to 0.999; the chi-squared is reduced from 2796.79 to 63.83. (a) shows the experimental data and the fitting curve. (b) shows the two exponential components decay curves: Exp component 1 and Exp component 2 labelled as blue and green lines follow a simple exponential decay.

a. T-dependence of phosphorescence intensity

Figure 6.10 shows the initial intensity variation of phosphorescence in the GE samples with temperature in a range of 83 K to 473 K. In the low-temperature range (83 K to 173 K), the initial intensity of two phosphorescence components is approximately temperature independent.

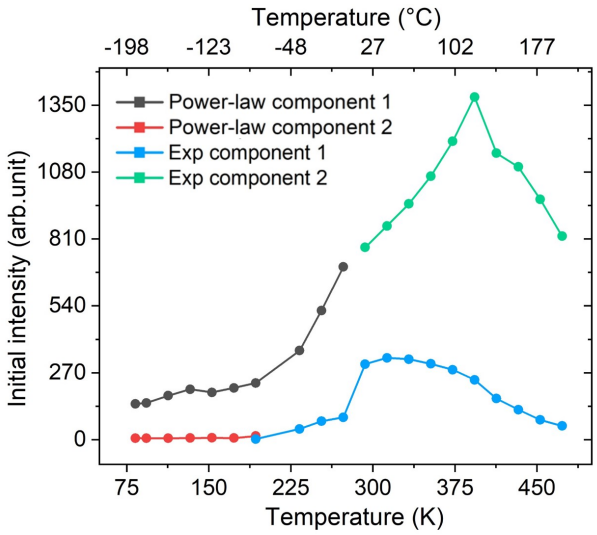

(a)

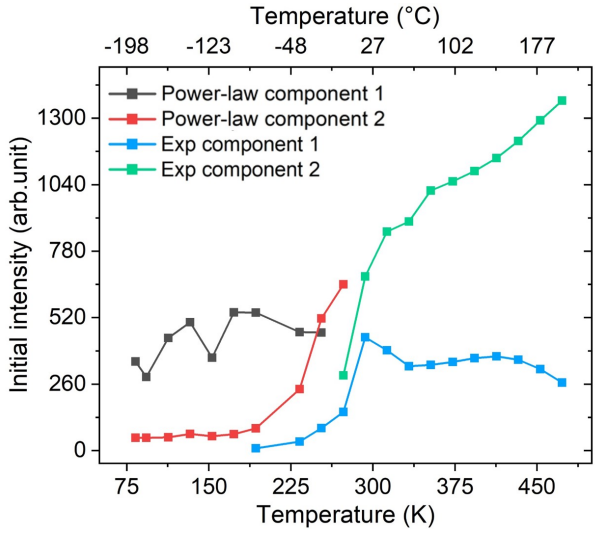

(b)

Figure 6.10: Initial intensity of different components of phosphorescence decay curve versus temperature (a) GE81-107a-B ({001} growth sector) (b) GE81-107a-C ({111} growth sector).

As shown in figure 6.11, the ratio of the initial intensity of power-law component 1 and power-law component 2 is approximately 28±4 in GE81-107a-C ($[B_S] > [N_S]$),

and 7 ± 2 in GE81-107a-B ($[N_S] > [B_S]$), respectively. When the temperature is higher (173 K to 273 K), the initial intensity of one of those two phosphorescence components significantly increases with temperature. Meanwhile, one additional phosphorescence component (labelled as EXP component 1 in figure 6.10) appears, whose initial intensity is also increased by higher temperature. At a temperature higher than 273 K, the initial intensity of phosphorescence is obviously temperature-dependent. It is important to note that due to the speedy decay rate, the initial intensity of phosphorescence may have a relatively large error at a temperature close to 473 K.

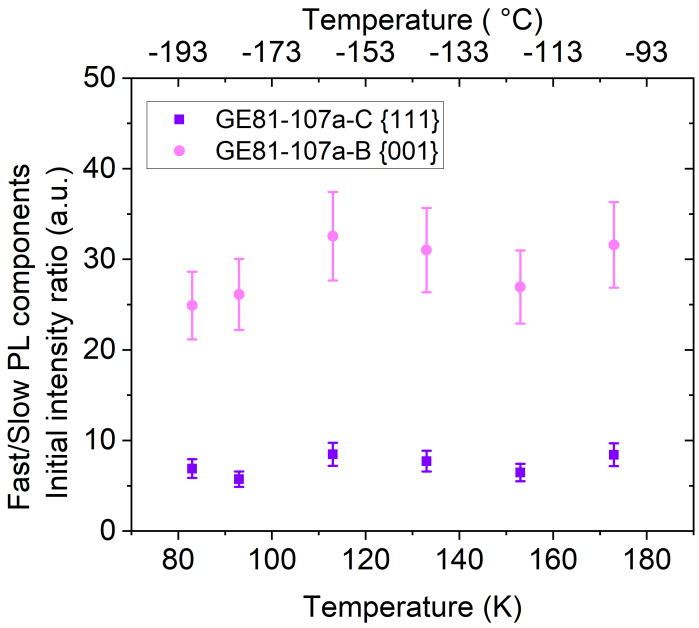

Figure 6.11: The ratio of power-law component 1 (strong and short-lived) initial intensity and power-law component 2 (weak and long-lived) initial intensity in the low-temperature range in GE81-107a-C ({111} growth sector) and GE81-107a-B ({001} growth sector), respectively.

The total emission of phosphorescence components of various mechanisms can be calculated from the integrated area under the corresponding decay curves. As shown in figure 6.12, the total emission light of two phosphorescence components origin from tunnelling processes is stable at a low-temperature range. At temperatures above 173 K, thermal processes begin to become important and subsequently dominate the decay. For exp component 1 and phosphorescence exp component 2, which follow the simple exponential decay, their total emission of light increases when temperature increases at the intermediate range (173 K to 273 K) while

gradually decreasing as temperature increases 273 K to 473 K.

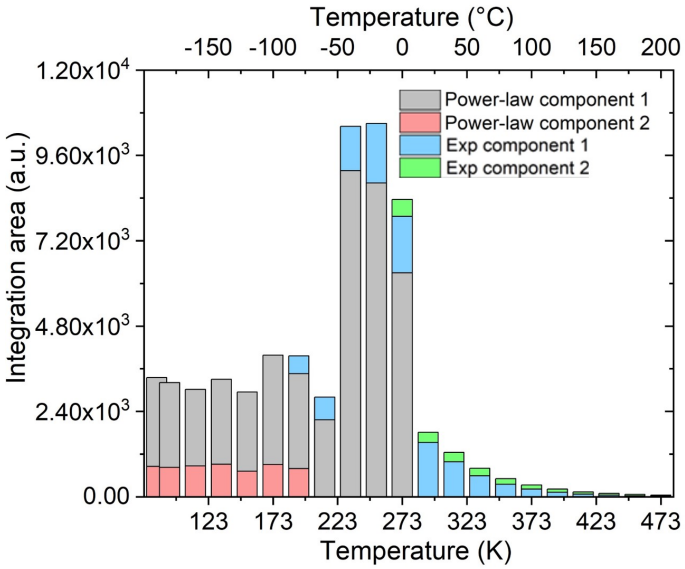

(a)

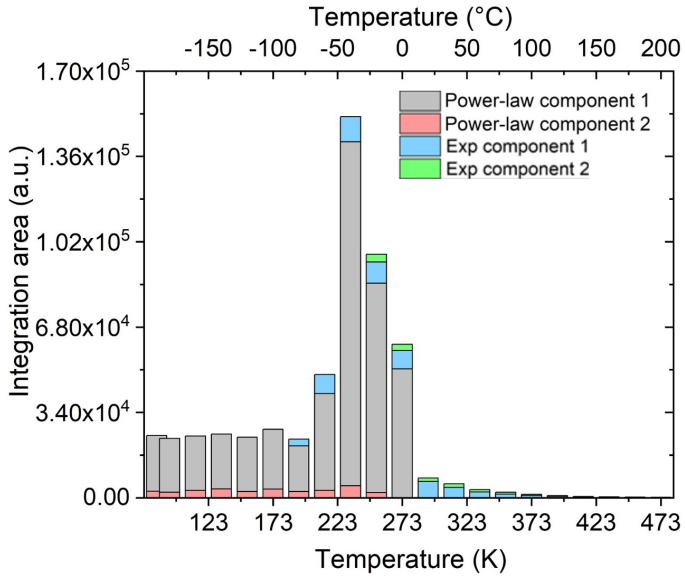

(b)

Figure 6.12: Total counts of different components (power law decay component or single exponential component) of phosphorescence decay versus temperature. (a) GE81-107a-B ({001} growth sector) (b) GE81-107a-C ({111} growth sector).

b. T-dependence of the lifetime of phosphorescence decay

The half-lifetime represents the delay time when the intensity becomes half of the initial intensity, which is a conventional measure of the phosphorescence decay rate. The half-lifetime of different phosphorescence components based on the multiple components fitting methods at the low-temperature range is shown in

figure 6.13. The half-lifetime of those two athermal phosphorescence components is approximately 6 s and 0.3 s, respectively, independent of temperature. The half-lifetime of athermal phosphorescence components in different growth sectors ({111} and {001}) is very similar, which means that it is not affected by the relative concentration of boron and single substitutional nitrogen.

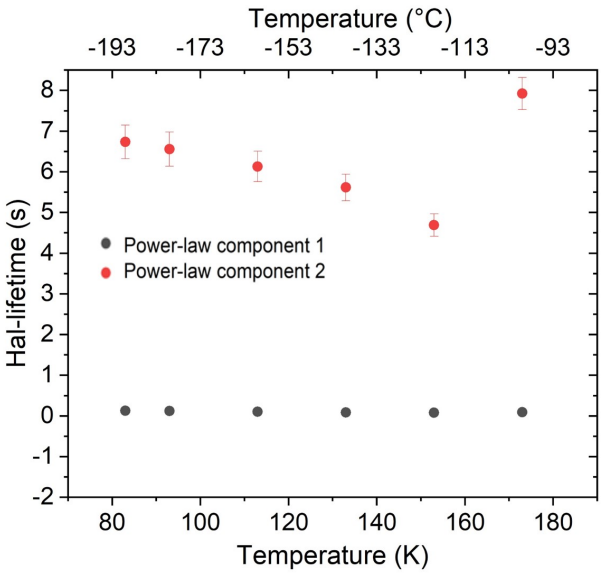

(a)

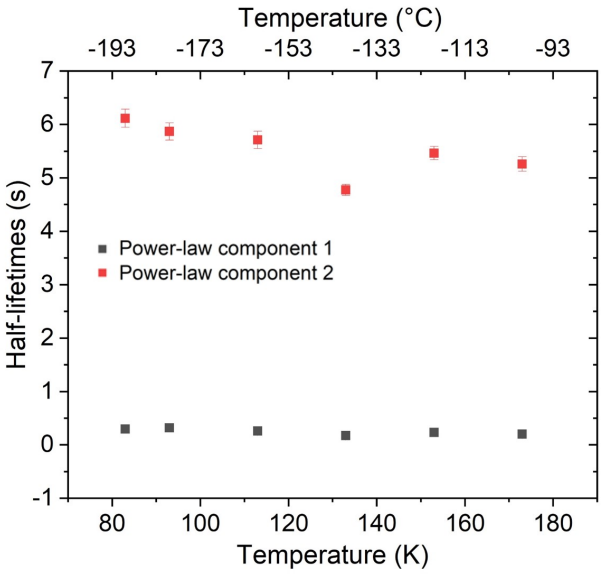

(b)

Figure 6.13: Half-lifetime of different components of phosphorescence decay curve versus temperature in the low T range (83 K to 173 K) (a) GE81-107a-B {001} (b) GE81-107a-C {111}.

As shown in figure 6.14, at temperatures above 273 K, the lifetimes determined

from both components of the fit to the phosphorescence decays varied exponentially with reciprocal temperature. The activation energy ΔE is given by equation 2.80.

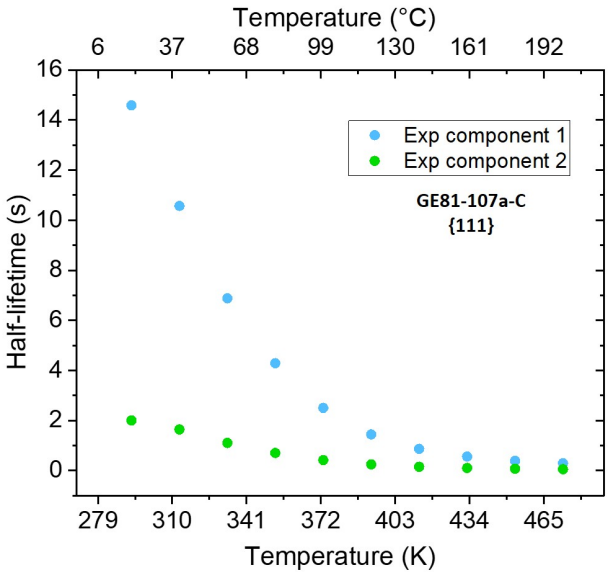

(a)

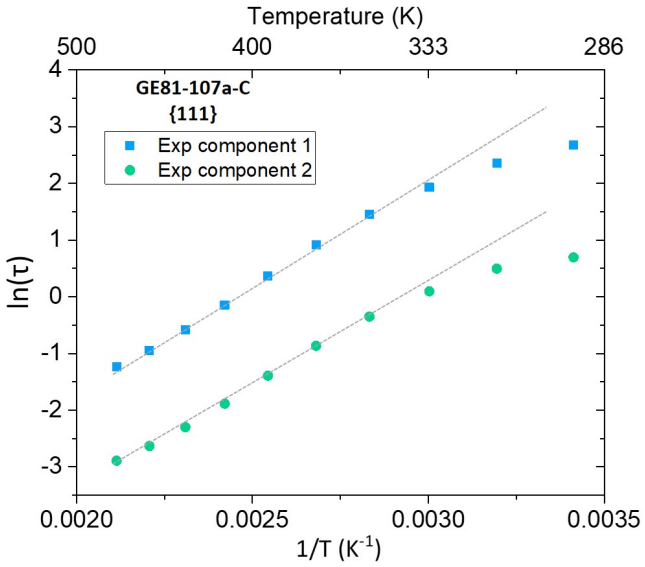

(b)

Figure 6.14: Temperature dependence of the phosphorescence half-lifetime at high-temperature range (273 K to 473 K). (a) Half-lifetime versus temperature. (b) The logarithm of half-life time versus reciprocal of temperature. The grey dash lines are the results of the fitting to an Arrhenius function.

The activation energies determined for both samples are shown in table 6.1 on page 177. A measurable difference in activation energies is determined from the temperature variation of phosphorescence lifetimes in samples GE81-107a-B and

GE81-107a-C. In the {111} growth sector, phosphorescence lifetime is expected to be dominated by the thermal excitation of electrons to B_S^0 (and subsequent trapping of the holes), and indeed the activation energy determined is that of the boron acceptor. In {001} growth sector, it is not clear what the origin of the 0.22 eV activation energy is.

6.2.5.2 Other phosphorescence curve fitting methods

Although the multiple components fitting method offers a clear physics explanation of phosphorescence processes, it is not sufficient to describe the real circumstances in diamond with an inhomogeneous distribution of traps and luminescence centres. The stretched exponential function, the modified stretched exponential function, and the complex power-law decay function, as introduced in Chapter 2.3.4.3, provide a better mathematical fitting for phosphorescence decay curves, hence a chance for more accurate calculation of activation energy for thermal process in the high-temperature range.

As predicted, the stretched exponential function is difficult to fit the phosphorescence decay curve because the infinite initial decay rate it describes is not suitable for phosphorescence decay. Both modified stretched exponential function and complex power-law decay function give reasonable fitting results. In comparison, the latter is slightly better. Figure 6.15 shows that the power varying from 1 to 2 in the high-temperature range and increasing as the temperature climbs.

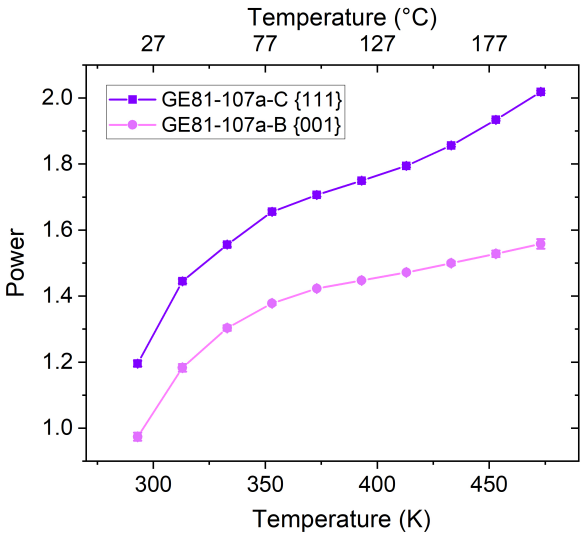

Figure 6.15: The power values are obtained by fitting of phosphorescence curves using the complex power-law function (equation 2.88) in the GE samples at a temperature between 273 K and 473 K.

The activation energies of the thermal process between 273 K to 473 K in the GE samples can be determined using equation 2.80 as shown in figure 6.14(b) and 6.16, and are listed in table 6.1. The activation energies given by MSE fitting method and CPL fitting method are very close to the multiple components fitting activation energy, thus confirming that boron as the trap dominates the phosphorescence process in sample GE81-107a-C and the phosphorescence process in the sample GE81-107a-B is dominated by a trap with a shallower energy level, shown here to be N_S^-.

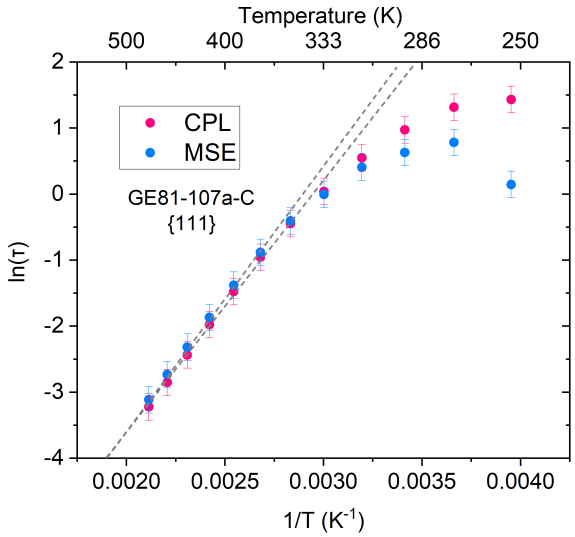

Figure 6.16: The logarithm of half-lifetime (fit by MSE function and CPL function, respectively) in GE81-107a-C versus reciprocal temperature. The dash lines are the results of the fitting to an Arrhenius function.

Table 6.1: Activation energies determined from phosphorescence lifetimes for GE samples by the fitting of multiple components method (equation 2.94), modified stretched exponential function (MSE) (equation 2.91) and complex power law decay function (CPL) (equation 2.88).

	GE81-107a-B {001}		GE81-107a-C {111}	
	$[N_S] > [B_S]$		$[N_S] < [B_S]$	
	Exp 1	Exp 2	Exp 1	Exp 2
E_A	0.23(5) eV	0.21(5) eV	0.33(5) eV	0.31(5) eV
	MSE		MSE	
E_A	0.30(1) eV		0.34(1) eV	
	CPL		CPL	
E_A	0.25(1) eV		0.35(1) eV	

6.3 Sample Sino-01

Sample Sino-01 is introduced in Chapter 3.1.2.

6.3.1 Cathodoluminescence

Figure 6.17 shows the cathodoluminescence images of the panchromatic sum of the CL signal over all wavelengths in the detection range from part of the “table” of the

brilliant-cut sample Sino-01 collected at 100 K and room temperature, respectively. Multiple growth sectors can be observed. Six measurement positions were selected for the acquisition of CL spectra.

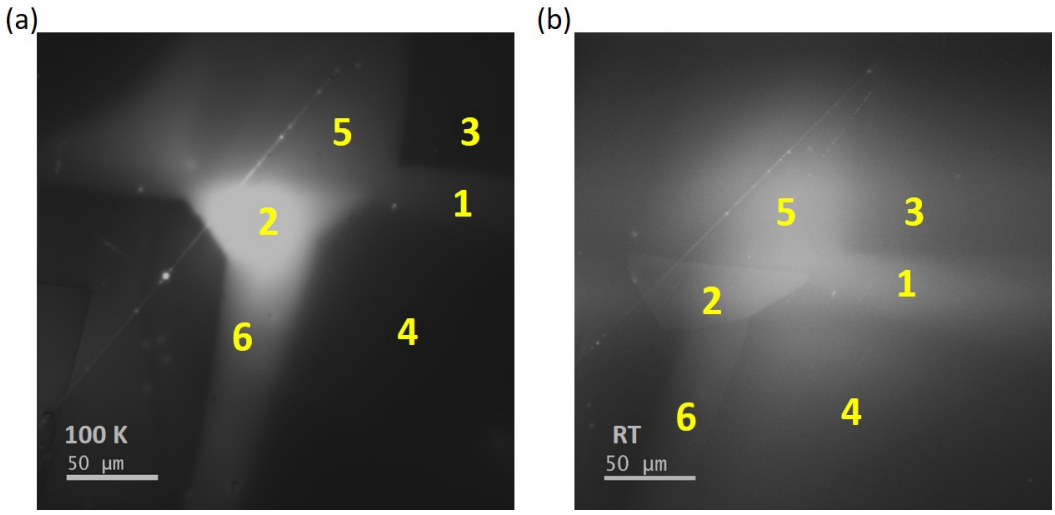

Figure 6.17: Cathodoluminescence images of a partial table of the brilliant-cut sample Sino-01 at (a) 100 K, (b) RT. Scale bars represent 50 µm. Six measurement positions for CL spectra acquisition are labelled.

Figure 6.18 and 6.19 present the CL spectra of six measurement positions on sample Sino-01 at 100 K and room temperature, respectively. Limited by the experimental setup conditions, these spectra were collected at a spectral resolution of approximately 11 nm. In figure 6.18, at 100 K boron bound exciton emission is observed at approximately 5.21 eV, with higher-order replica peaks at around 2.6 eV and 1.74 eV. Other CL emission peaks are observed at approximately 4.6, 3.4, 3.0, 2.8, 2.3 and 1.8 eV. At room temperature, the CL emission is complicated consisting of several overlapping broad band, CL emission peaks are observed around 3.4, 3.0, 2.5, and 1.8 eV. At room temperature (Fig 6.19), the CL emission band centred at 2.5 eV is also commonly observed in the photoluminescence and phosphorescence spectra of the HPHT grown diamond samples studied in this thesis. The 1.8 eV "red" broadband is also observed as a phosphorescence emission band in sample SYN4-10 (Chapter 6.4). Another spectral feature at 3.4 eV (360 nm) presents at all the measurement positions and requires further research.

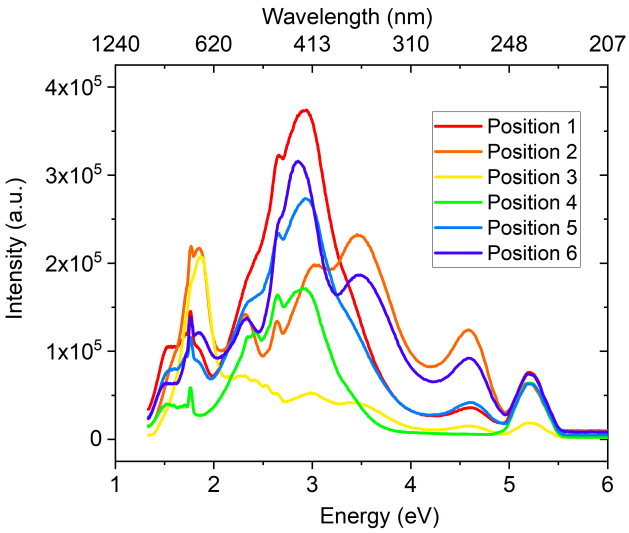

Figure 6.18: Cathodoluminescence spectra of six measurement positions on sample Sino-01 at 100 K. The spectral resolution is ∼ 11 nm.

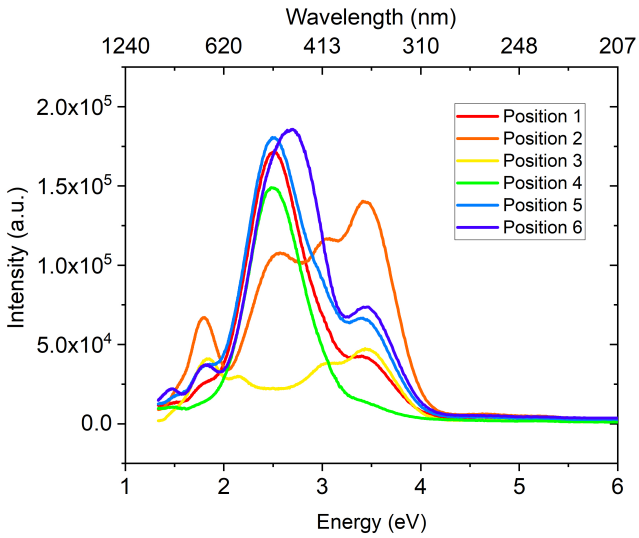

Figure 6.19: Cathodoluminescence spectra of six measurement positions on sample Sino-01 at RT. The spectral resolution is ∼ 11 nm.

6.3.2 Photoluminescence

As shown in figure 6.20, the "blue-green" broadband spectrum centred at 2.5 eV at room temperature can be strongly excited by light with a wavelength of approximately 220 nm to 235 nm. However, the "orange" emission band at 2.1 eV is observed with excitation in a range of 200 nm to 500 nm.

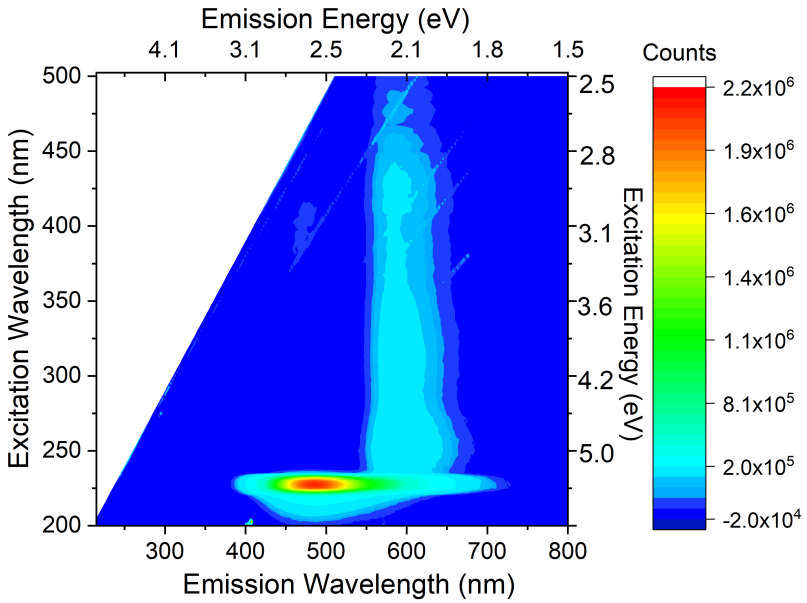

Figure 6.20: Photoluminescence spectra of Sino-01 by excitation ranging from 200 nm to 500 nm at room temperature.

6.3.3 Phosphorescence spectra

Phosphorescence spectra in several type II HPHT synthetic diamond samples have been investigated using the Garfield experimental setup described in Chapter 3.2. After 224 nm (or 375 nm) excitation, the phosphorescence spectra were recorded over a temperature range of 83 K to 573 K at intervals of 20 K. For multi-sector samples, such as Sino-01, this measurement cannot distinguish the phosphorescence from different growth sectors. Moreover, it is confusing to use any decay curve fitting methods to analyse and calculate the activation energies of the phosphorescence in such samples due to the variations between different growth sectors.

Figure 6.21 shows the phosphorescence from sample Sino-01 following excitation with a 224 nm laser. Two separate luminescence bands are observed: a "blue-green" band centred at approximately 2.5 eV (493 nm) and an "orange" band centred at 2.1 eV (580 nm - 590 nm), respectively. Similar "blue-green" and "orange" phosphorescence bands were observed in HPHT synthetic diamonds previously. [1, 2, 6]

At 223 K, one broad phosphorescence band at 2.5 eV (493 nm) is observed, decaying relatively slowly. There is no shift in band position during phosphorescence decay, and the emission lasts for tens of seconds. Above 253 K, the "orange"

phosphorescence band and the 2.5 eV "blue-green" band are both observed. The lifetime of "orange" emission is longer than that of "blue-green" emission, consistent with the observation of Watanabe *et al.*. [1] The higher the temperature, the stronger the initial intensity of the "orange" phosphorescence compared to that of the "blue-green" band. The "orange" band shifts slightly to lower energy as the temperature is increased. The "orange" band shifts to lower energy (by approximately 0.04 eV) during phosphorescence decay.

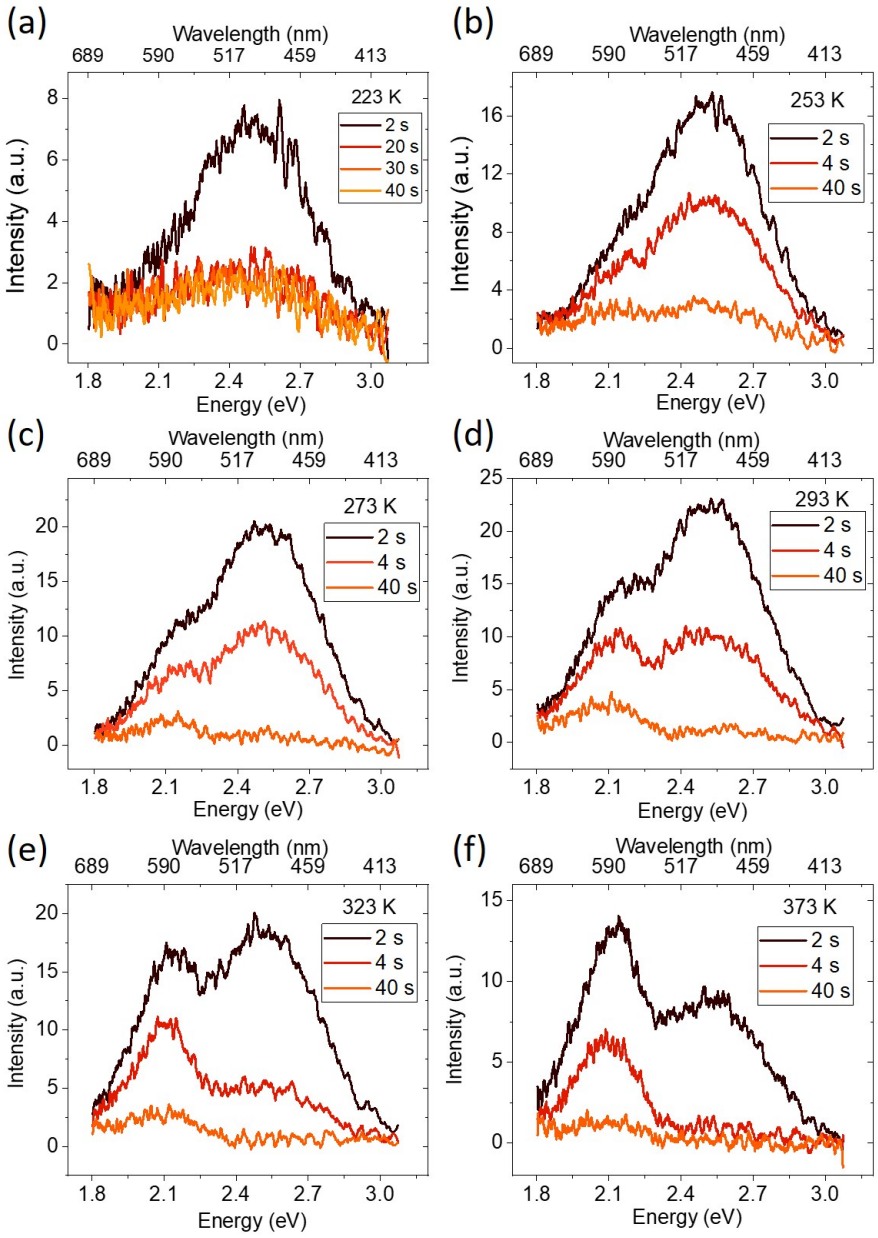

Figure 6.21: Phosphorescence spectra diamond Sino-01 after 224 nm excitation is measured by the Garfield experimental setup at (a) 223 K, (b) 253 K, (c) 273 K, (d) 293 K, (e) 323 K, and (f) 373 K.

6.4 Sample SYN4-10

Sample SYN4-10 is introduced in Chapter 3.1.3.

6.4.1 Photoluminescence

Figure 6.22 shows the excitation dependence of the photoluminescence from sample SYN4-10 at RT. The band centred on 2.5 eV is strongly excited by light in a range of 220 - 237 nm, but in this sample this emission is weakly excited by wavelength up to approximately 370 nm. "Orange" (approximately 2.1 eV) and "red" (approximately 1.8 eV) emission bands are excited by light from around 220 nm to much longer wavelengths.

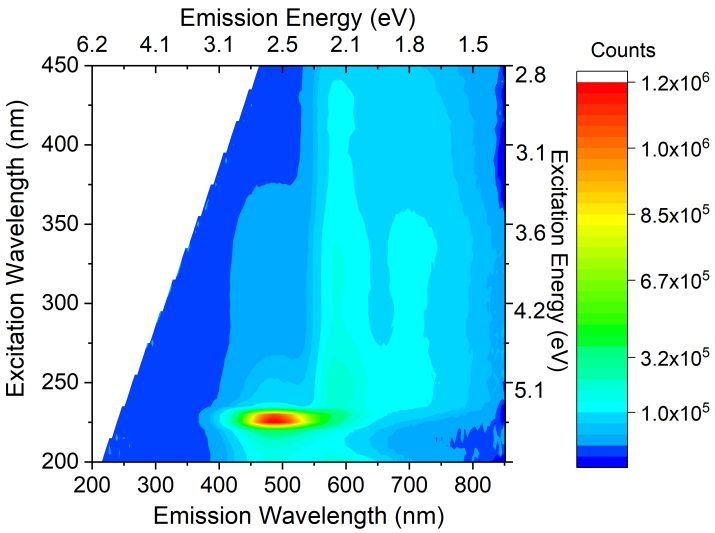

Figure 6.22: Photoluminescence spectra of SYN4-10 by excitation ranging from 200 nm to 450 nm at room temperature.

Phosphorescence in sample SYN4-10 is studied over a temperature range of 83 K to 513 K using both the 224 nm pulsed laser (bandgap excitation) and 375 nm CW laser excitation with the "Garfield" experimental setup. Phosphorescence bands in "blue-green", "orange" and "red" colours are observed in this sample under different experimental conditions.

6.4.2 Phosphorescence spectra

6.4.2.1 Phosphorescence after 224 nm excitation

In the low-temperature range between 83 K to 173 K, a "blue-green" phosphorescence band centred at 2.25 eV (550 nm) was observed in sample SYN4-10, and the band position did not shift during the phosphorescence decay (Figure 6.23). This is similar to the phosphorescence exhibited by the GE samples at low temperatures.

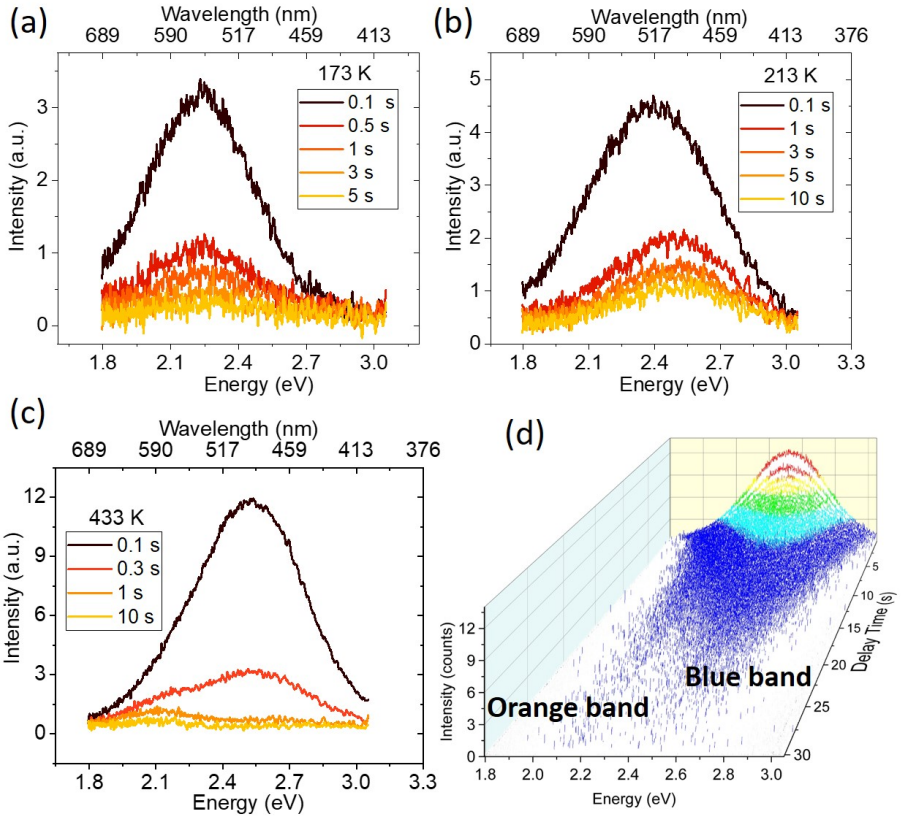

Figure 6.23: Phosphorescence spectra from sample SYN4-10 recorded using 224 nm excitation at (a) 173 K, (b) 213 K, (c) 433 K. (d) 3D plot of phosphorescence decay after 224 nm UV radiation at room temperature.

In the temperature range of 173 - 273 K, during the phosphorescence decay the peak shifts to higher energies, and as the temperature is increased the peak emission is also blue shifted. The peak emission at long times and higher temperatures is approximately 2.5 eV (see Fig 6.23(c)).

Besides the "blue-green" phosphorescence band centred at 2.5 eV, an additional "orange" band with a peak energy at approximately 2.1 eV (590 nm) is observed at temperatures above approximately 273 K. The decay of the 2.1 eV "orange"

phosphorescence band is significantly slower than the 2.5 eV "blue-green" band. However, it is uncertain whether the band position of the "orange" band shifts during decay because of the weak intensity.

The peak emission of the "blue-green" and "orange" luminescence bands are consistent with those reported in the literature [1, 6].

6.4.2.2 Phosphorescence after 375 nm excitation

Figure 6.24(a) shows two phosphorescence bands observed at 83 K following 375 nm excitation: one weak "blue-green" band centred at 556 nm (2.23 eV) lasts approximately 1 s and one much stronger "red" phosphorescent band peak energies at 1.8 eV (680 nm) with a lifetime of around 10 s. The "blue-green" band could be either one emission band or a combination of two bands at different energies (e.g. 2.25 eV and 2.1 eV). The peak of this broad band is seen at a longer wavelength (570 nm) as the temperature rises to 213 K. The spectral position of this "red" band is the same as Krumme's observation in a natural diamond. [7] Unlike other phosphorescence bands observed previously which are all broad and featureless, there is previously unreported resolved vibronic structure the "red" emission band (see Fig 6.24(b)). [1, 2, 4–6, 10, 11] The vibronic structure of the "red" band is not resolved at temperatures above 173 K. Meanwhile, the band position shifts to 690 nm, consistent with the "red" phosphorescent band position report by Walsh *et al.* [6] The centre of the emission band (690 nm) does not change during the phosphorescence decay. The red-NIR phosphorescence band centred at 690 nm is observed over a temperature range of 173 K to 373 K; the initial intensity increases, and the lifetime decreases as temperature increases. When the temperature is above approximately 373 K, it is uncertain whether the "red" band disappears or masked by the stronger "orange" band.

At least three emission bands can be simultaneously observed during the phosphorescence decay at temperatures between 253 K and 353 K. For example see figure 6.25; all three bands show a significant shift to higher energies during the first approximately 1 s at RT. After that, the emission bands are centred at 490 nm (2.5 eV), 580 nm (2.1 eV), and 690 nm (1.8 eV), respectively. The phosphorescence lifetime is shortest for the 1.8 eV "red" band, and longest for

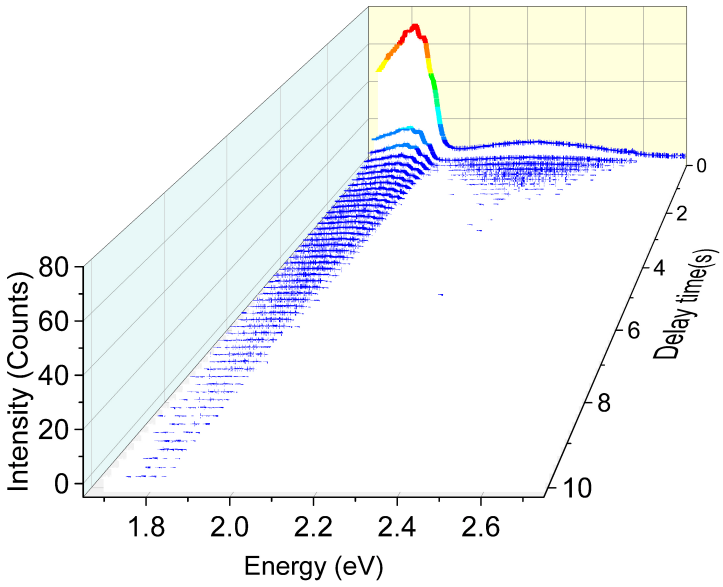

(a)

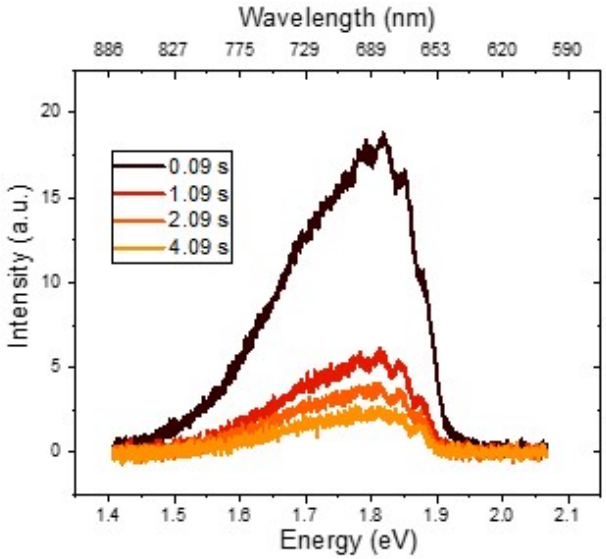

(b)

Figure 6.24: Phosphorescence spectra in sample SYN4-10 excited by 375 nm CW laser light at 83 K recorded using the "Garfield" experimental setup. (a) The 3D plot of phosphorescence decay in the wavelength range of 450 nm to 750 nm. (b) "Red" phosphorescence band decay with vibronic structure but no clear ZPL.

the 2.1 eV "orange" band, with the 2.5 eV band in between. The peak of those three phosphorescence bands are observed at the same spectral position at higher temperatures up to around 373 K. The intensity of the "orange" phosphorescence band increases dramatically with increasing temperature. When the temperature is above 433 K (Figure 6.25), the broad band phosphorescence band centred at

590 nm is asymmetric. It has a long tail on the low energy side, which suggests that both the "orange" and "red" bands are contributing to the overall emission. The 2.5 eV "blue-green" band is weak or not efficiently excited by the 375 nm radiation.

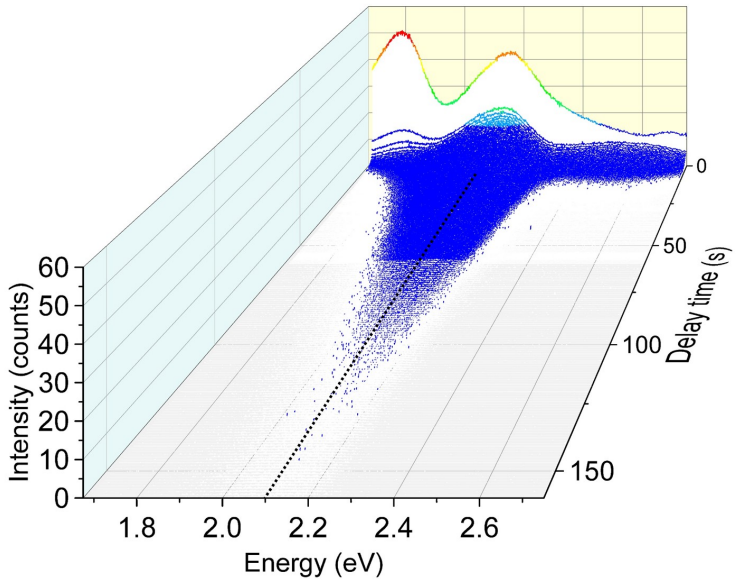

(a)

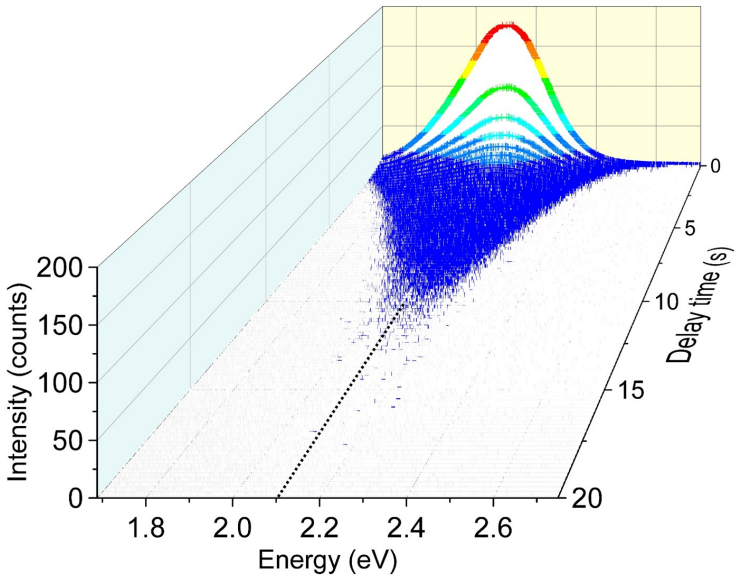

(b)

Figure 6.25: The 3D plot of phosphorescence decay spectra in sample SYN4-10 by 375 CW laser excitation recorded using Garfield experimental setup (a) at 293 K (b) at 513 K.

6.4.3 Phosphorescence decay curves

The panchromatic (all wavelengths) phosphorescence decay curves recorded from sample SYN4-10 following 224 nm pulsed laser excitation are shown in figure 6.26 with the time plotted on a logarithmic scale. At the low-temperature range below 173 K, the phosphorescence decay is temperature-independent. At higher temperatures, the decay rate of phosphorescence becomes faster as the temperature increases. As discussed above, the "blue-green" emission dominates following 224 nm excitation, while following 375 nm excitation, the "orange" band dominates. Therefore, figure 6.26(a) and figure 6.26(b) suggest differences in the temperature dependence of phosphorescence decay curves of the "blue-green" and "orange" bands.

Sample SYN4-10 is a brilliant-cut sample comprising different growth sectors in which the types and concentration distributions of phosphorescence-related defects are different. Therefore, phosphorescence decay curve analysis has not been performed. Further phosphorescence research should be done on the individual growths sector.

6.5 Discussion

6.5.1 Photoluminescence

The data from GE samples in figure 6.3 shows that there is a clear threshold for the excitation of the broad "blue-green" emission band; at room temperature this band is only excited with light of wavelength shorter than approximately 235 nm. This equates to 5.28 eV, which is approximately 0.2 eV less than the diamond indirect bandgap. At room temperature, the main onset of intrinsic absorption occurs at 236 nm (0.21 eV below the indirect bandgap energy) and results from the excitation of an electron from the top of the valence band to the excitonic state just below the conduction band minimum and assisted by the absorption of a high energy optical phonon (see Chapter 2.2.4). [14, 15] The emission band is most intense with excitation at approximately 222.5 eV (2.572 eV) which is above the threshold for creation of an unbound electron-hole pair and optical phonon.

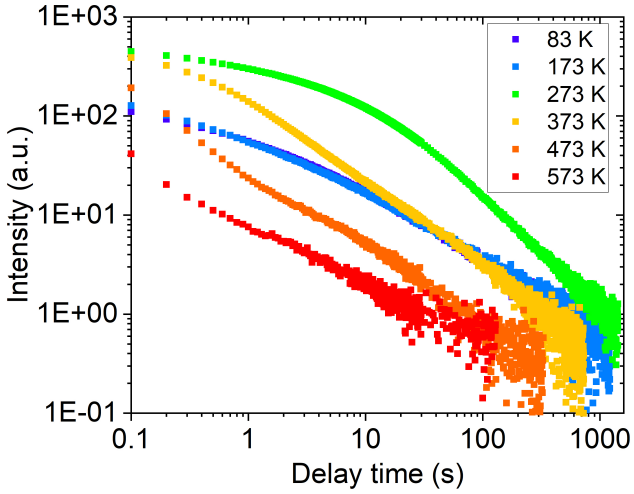

(a)

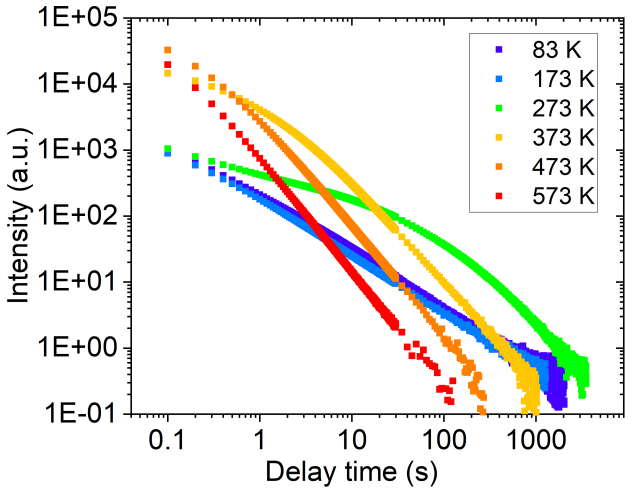

(b)

Figure 6.26: Phosphorescence decay curves in sample SYN4-10 at 83 K, 173 K, 273 K, 373 K, 473 K, and 573 K after 224 nm pulsed laser excitation and 375 CW laser excitation, respectively.

The reduction in the photoluminescence intensity as the photon energy increases is likely to be due to the rapid fall of in output intensity of the xenon lamp source at shorter wavelengths.

This experimental evidence suggests that the broad "blue-green" emission band is directly related to the creation of free electrons and holes. This is of course consistent with the optical excitation creating free carriers that neutralize donors and acceptors, and the broad "blue-green" emission band arising from

donor-acceptor pair recombination. For excitation at 224 nm (5.53 eV), the room temperature absorption coefficient of intrinsic diamond is approximately 50 cm^{-1} [14], meaning that more than 90 % of the light transmitted through the air-diamond interface will be absorbed in the first 0.5 mm of diamond. Thus for thick samples the creation of free electrons and holes will vary significantly with depth. Reducing the temperature from room to 77 K significantly reduces the optical absorption coefficient in the region 5.28 eV to 5.47 eV, as the number of phonons is reduced, meaning that the light in this energy range will penetrate more deeply into the diamond.

The "blue-green" emission band is also observed in samples Sino-01 and SYN4-10, but in these samples is accompanied by an additional broad "orange" band (peak $\sim$ 2.1 eV RT) and a "red" band (peak $\sim$ 1.8 eV RT). Figure 6.20 and 6.22 show that the "orange" and "red" bands are excited by light of lower energy than the "blue-green" band. Note weak "blue-green" luminescence is stimulated with light in the range 235 - 380 nm in sample SYN4-10, but not Sino-01 or the GE samples. This could suggest that the concentration of defects with mid gap levels is higher in sample SYN4-10.

6.5.2 Cathodoluminescence

The room temperature cathodoluminescence spectrum, figure 6.2, for the GE samples is similar to the room temperature photoluminescence spectrum, with the peak intensity shifted slightly. Given the differences in electron beam and optical excitation (e.g. higher density of free electrons and holes produced by CL) it is unsurprising that there are differences in the emission spectra. As the temperature is reduced the CL spectra shift to lower energy, which consistent with the behaviour observed in phosphorescence emission (see Chapter 6.2.3). From the position and intensity of the CL emission band at low temperatures, it is reasonable to infer that it consists of the emission from both distant DAP recombination (lower energy) and close DAP recombination (higher energy) (see Chapter 2.3.1.2).

The CL spectra for sample Sino-01 is much more complicated than that for the GE samples with additional peaks (see Fig 6.18 and 6.19). The CL emission is heterogeneous.

6.5.3 "Blue-green" phosphorescence

This discussion focuses on the "blue-green" phosphorescence that is observed in all samples and is the only emission observed in GE samples. The phosphorescence data in figure 6.5 was recorded following the specified delay after the 224 nm laser excitation to saturation. The integration period to record the entire spectra was 50 ms. We see from figure 6.5(a), that at 173 K in sample GE81-107a-C (and lower temperatures) the phosphorescence spectrum is centred on approximately 2.25 eV and does not shift over the first $\sim$ 1 s after the excitation was removed. However, the phosphorescence peak recorded after a delay of 10 ms at 213 K and 233 K (figures 6.5(b) and 6.5(c)) shifts to higher energy with increasing temperature and the spectra recorded after a 1 and 20 s delay continue to shift to higher energy with increasing delay. The phosphorescence spectra recorded at 293 K (6.5(d)) is centred on approximately 2.5 eV and does not shift with increasing time.

For more discussion of the phosphorescence processes in different temperature ranges, see Chapter 8.

6.5.3.1 The "blue-green" phosphorescence band energy

The characteristic narrow lines associated with DAP emission from close pairs (separation of order or less than the sum of the donor and acceptor radii) that accompany the broad emission from distant pairs in other materials (e.g. GaP, 3C-SiC) with shallow, delocalised donors and acceptors are not observed in this work. Given the compact donor and acceptor wavefuncions in diamond, there are very few neighbours that should even be considered as close pairs. Although Dischler *et al.* tentatively interpreted CL emission features as arising from close DAP in CVD diamond this assertion has not been confirmed and the intensities were not in accord with theory [16].

In the sample with $[N_s] < [B_s]$, the activation energy determined from the high temperature phosphorescence lifetime is consistent (see tables 4.3 and 6.1) with thermal excitation of boron acceptors predominantly controlling the emission. Previously, given the assumption that the acceptor is substitutional boron equation 2.61 has been used to estimate the donor activation energy [1]. However, equation 2.61 should only be used when the donor and acceptor electron

wavefunction probability density is highly delocalised (the case for shallow defects) and very low at the donor atom such that it does not exert significant influence on the atomic positions. For the deep nitrogen donor in diamond this is not the case. When the nitrogen donor changes charge state from N_S^0 to N_S^+, there is a large configuration change (N_S^0 has C3v symmetry with one N-C bond 25 % longer than the diamond C-C bond, and the other three smaller, whereas N_S^+ has $\mathbf{T_d}$ symmetry with all N-C bonds approximately equal to the diamond C-C bond length). [17] However, when the boron acceptor changes charge state from B_S^0 to B_S^-, there is little configurational change (in both charge states the defect has $\mathbf{T_d}$ symmetry; any symmetry lowering distortion is negligible [18]). It can be seen from a 1D configuration coordinate diagram, figure 6.27, that for a N_S^0...B_S^0 pair to emit a photon, a substantial amount of energy must be lost to the emission of a significant number of phonons. Figure 6.27 has been drawn assuming a typical N_S^0 phonon energy of 1130 cm^{-1} ($\hbar\omega_0$ = 141 meV) and a B_S^0 phonon energy of 427 cm^{-1} ($\hbar\omega_0$ = 53 meV) and that the energy lost to phonons in the configuration change associated with emission is approximately 1.2 eV. [19] Taking this into account, the energy of the DAP recombination transition should be given by

$$h\nu = E_g - (E_D + E_A) + \Delta E_C - \Delta_{FC}^g \tag{6.1}$$

where Δ_{FC}^g is the Frank-Condon shift, which equals to SE_{ph}. The Huang-Rhys factor S essentially qualifies the average number of phonons emitted (in this case approximately 23) and E_{ph} is the average phonon energy. [20] Such strong electron-phonon coupling is unsurprising for such a deep localised donor. This is consistent with the description of N-B pair recombination emission by Ščajev *et al.*. [21]

The Frank-Condon shift Δ_{FC}^g = 1.2 eV, would result in a distant N_S^0...B_S^0 pair emission energy of approximately 2.25 eV, consistent with the observations reported here and elsewhere. Given the large configuration change, such a large Frank-Condon shift appears reasonable, indeed in molecules the shifts can be as large as several eV. [22] We note that the barrier to reorientation of the N_S^0 C3v axis has been estimated as approximately 0.8 eV [23], and the energy of the N_S^0 donor level is deeper than the value predicted for a hydrogenic donor ($\sim$ 0.4 eV) by $\sim$ 1.3 eV. Both values are large compare to shifts observed in other materials

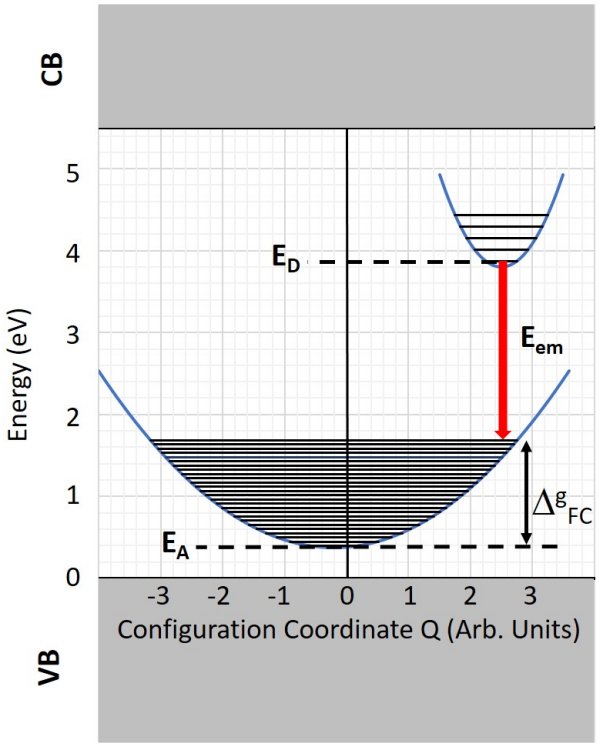

Figure 6.27: The configuration diagram for the energy levels of boron-nitrogen pair recombination at 0 K. The electronic state of substitutional nitrogen is 1.7 eV below the conduction band, and the ionisation energy of boron is 0.37 eV.

and demonstrate the large distortion associated with N_S^0. Further theoretical calculations of the Frank-Condon shift for emission from a N_S^0...B_S^0 pair would be very valuable.

To describe the vibrational broadening of the N_S^0...B_S^0 pair emission, it is necessary to sum all possible transitions between the accessible vibrational levels of the N_S^0 donor and all those of the associated B_S^0 acceptor. Assuming a typical N_S^0 phonon energy of $\hbar\omega_0 = 141$ meV, then at room temperature ($k_BT \sim 26$ meV) only the ground vibrational state of the N_S^0 donor will be occupied, and thus using the 1D model it is only necessary to sum over all the vibrational levels of B_S^0 (equation 2.68; strictly speaking this equation is derived assuming that the vibrational energy of the ground and excited state are equal but a similar result is obtained if they are not) [24]. For defects with large electron-phonon coupling ($S \gg 1$), resolved phonon replicas are not observed, and contributions from individual phonon modes cannot be identified. Furthermore, the luminescence intensity from the zero-phonon line of each different N_S^0...B_S^0 pair is practically zero. Figure 6.28 shows a simulation

of the distant (small coulomb shift) $N_S^0...B_S^0$ pair emission in the limit of strong electron-phonon coupling ($S \sim 23$), using equation 2.68. The agreement between simple theory and experiment is reassuring. The broadening of the emission lines from the few close pairs means that they are undetectable and the overlapping contributions from differently separated distant pairs (with different relaxation times) provides a natural explanation of the complex non-exponential decay.

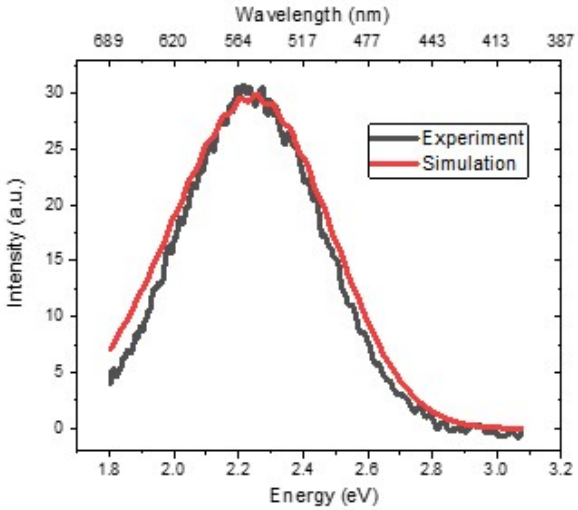

Figure 6.28: Phosphorescence spectrum at 173 K in GE81-107a-C (black line), and simulated spectrum with parameters $E_g = 5.47$ eV, $E_D = 1.7$ eV (N_S^0), $E_A = 0.37$ eV (B_S^0), $E_{ph} = 0.053$ eV, $S = 22.7$.

6.5.3.2 Low temperature phosphorescence

In diamond without optical excitation at low temperatures, there is a negligible concentration of holes (electrons) in valence band (conduction band). After illumination and the neutralization of donors and acceptors in the absence of tunnelling, there is no way that a donor-acceptor pair can reset, therefore under this constraint each neutral DAP could only emit once. The atypically close pairs will have the greatest optical transition probability and thus shorter radiative lifetimes but are few so have a small relative contribution to the emission intensity. At low temperatures (e.g. below approximately 170 K) many of the numerous $N_S^0...B_S^0$ DAPs with long radiative lifetimes eventually emit and will dominate the emission simply by weight of numbers. The more distant a pair the lower the coulomb shift and the emission energy, but distant pairs are not isolated pairs (i.e. pairs with

a separation very small compared to the distance between the pair and another donor or acceptor) and perturbations will broaden the emission and result in non-exponential decays (see Chapter 2.3.1.2).

We would expect the number of free carriers and the electrical conductivity of a diamond to be vanishingly small at low temperature where all free carriers are frozen into donor or acceptor centres. However, it is known that when both donors and acceptors (compensated semiconductor) are present even at concentrations of 10^{15} - 10^{16} cm^{-3} (10's - 100's ppb) significant conductivity can be observed even at very low temperatures. [25] Consider, a compensated p-type semiconductor with $n_A > n_D$, where before illumination we will have n_D ionized acceptors and $n_A - n_D$ un-ionized acceptors. The ionized acceptors with be spread throughout the material and holes from neutral acceptors might be able to tunnel from one vacant site to another. Given the compact boron acceptor wavefunction in diamond ($r_{Bohr} \approx 0.3$ nm), and the relatively large impurity separations at low concentrations (e.g. for a concentration of 0.5 ppm the typical impurity separation will be $\sim$ 13 nm) only a small fraction of the acceptors will be sufficiently close to facilitate tunnelling and the overall rate is expected to be low.

We have assumed that the acceptor can only exist in two charge states, B_S^0 or B_S^-. If the nitrogen donor can only exist in two charge states, N_S^0 or N_S^+, then after sufficiently intense near band gap excitation with equal concentrations of donors and acceptors we would expect all the N_S donors and B_S acceptors to be neutral. Low temperature DAP emission would result in only a very small fraction of the donors (acceptors) becoming ionized, and tunnelling of electrons from N_S^0 to N_S^+ (or holes from B_S^0 to B_S^-) would be very improbable because $N_S^0 \gg N_S^+$ ($B_S^0 \gg B_S^-$). The majority of donors and acceptors would be isolated and remain neutral. Nevertheless, tunnelling does provide a mechanism (albeit with a low probability) to convert an ionized acceptor in the vicinity of a neutral donor, or ionized donor in the vicinity of a neutral acceptor, back to neutral, enabling this DAP to re-emit. Given the different localizations of the donor electron probability density on N_S^0, and the hole probability density on B_S^0 we would expect, if present in the similar concentrations and ionized fractions, different tunnelling rates for the donor electrons and acceptor holes. The overall tunnelling rate after illumination

will depend on the degree of donor and acceptor neutralization achieved. It could also vary during the phosphorescence emission decay, and depend on the local concentration of impurities present.

The low temperature phosphorescence lifetime was investigated by monitoring the total emission (integrated over wavelengths between 400 nm and 750 nm) as a function of time after the excitation (sufficient number of pulses from 224 nm laser to achieve saturation of the initial phosphorescence intensity) was removed. Figure 6.6(a) and 6.6(b) show the phosphorescence intensity decay for samples GE81-107a-B and GE81-107a-C at 83 K and 173 K. Below approximately 170 K the emission lifetime is temperature independent. In this low temperature regime the decay curves fits to a power law function produced by two components of the form as equation 2.87. This type of decay is expected for tunneling of carriers to recombination centres. [26] Figure 6.13 shows that below 170 K $\tau = 6.0 \pm 0.5$ s for one component and 0.3 ± 0.1 s for the other in sample GE81-107a-B, and approximately the same in sample GE81-107a-C. The initial intensity (figure 6.11) of the fast-decaying component is 7.5 times larger than the more slowly decaying component in sample GE81-107a-C, and 30 times larger in sample GE81-107a-B.

In GE81-107a-C $n_A > n_D$, and GE81-107a-B $n_D > n_A$. Since $N_S^+ ... B_S^0$ pair requires the ionized donor to capture an electron before emission is possible, $N_S^0 ... B_S^-$ requires the ionized acceptor to capture a hole before emission is possible ($N_S^+ ... B_S^-$ requires both electron and hole capture), one might tentatively assign the two distinctly different tunneling rates identified (fitting the data to two power law decays) at low temperature to tunneling between ionized and neutral donors and similarly ionized and neutral acceptors. Since it has been shown that the N_S donor can exist in three charge states, N_S^-, N_S^0, and N_S^+, then after bandgap illumination we could anticipate all three charge states being created. At sufficiently low temperature such that N_S^- was not thermally ionized (releasing an electron into CB) back to N_S^0, there could be tunnelling between different charge states of the N_S defect. Tunneling is governed by many factors (e.g. donor/acceptor effective radius, distribution of donors/acceptors, relative compensation, etc.) so it would be unwise to speculate further, but the relative intensities of the fast and slow components in samples GE81-107a-B and GE81-107a-C are consistent with the

assertion of faster tunnelling between N_S^- and N_S^0 and slower tunnelling between B_S^- and B_S^0. Figure 6.29 shows the model for the low temperature "blue-green" phosphorescence involving tunneling between nitrogen donors and boron acceptors.

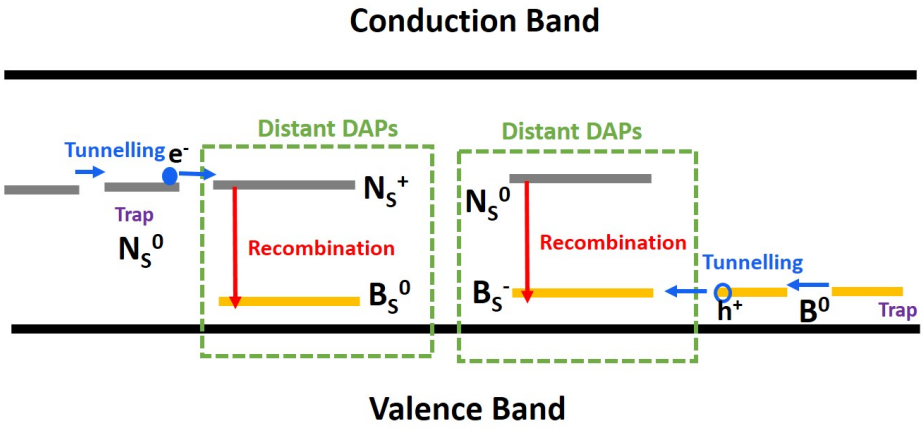

Figure 6.29: Schematic energy level representing the model for phosphorescence in GE samples at low temperatures (83 K to 173 K). The distant DAPs refer to the donor-acceptor pairs where the donor and the acceptor are far apart in the diamond lattice. The luminescence centre emits the phosphorescence broadband centred at 2.25 eV.

6.5.3.3 Intermediate temperature phosphorescence

As already mentioned, the "blue-green" phosphorescence band recorded after a delay of 10 ms at 213 K and 233 K (Figure 6.5(b) and 6.5(c)) shifts to higher energy with increasing temperature and the spectra recorded after a 1 s and 20 s delay continue to shift to higher energy with increasing delay. We now have a situation where although the number of thermally excited carriers after the optical excitation is removed is still relatively small, it is sufficient to influence the donor acceptor pair recombination. For a diamond where the number boron acceptors exceed the number of deep donors between 173 K and 233 K, the concentration of free holes increases by a factor of approximately 1000 (see Chapter 2.1.2). For a deep donor such as N_S^0 at these temperatures there is still a very low probability of thermal ionization, but if there were a shallow trap such as N_S^- that was ionized, electrons would also be released to the conduction band. The probability that distant neutral DAPs (with long lifetimes) are ionized before they can emit increases with increasing temperature, and the near DAPs with short lifetimes have the opportunity to reset and can emit more than once. Thus we would expect the

peak of the broad $N_S^0...B_S^0$ DAP emission band shift to higher energy. This is precisely what is observed with a shift of approximately 0.25 eV between 173 K and 293 K. On first inspection this might seem to be a large shift to associate with the Coulomb attraction term in equation 2.61. Derivation of equation 2.61 assumes that the separation of the DAP is large compared to the effective diameter of the neutral donor and acceptor states. The low frequency dielectric constant ϵ_r is used in the final terms of equation 2.61 because it is assumed that we are considering the interaction of an electron (hole) with a charge removed a large distance compared with the diameter of the bound electron (hole) state. For diamond $\epsilon_r = 5.7$, whereas for silicon the value is 11.7, 3C-SiC 9.72 and GaP 11.1. [27] Furthermore, the lattice parameter for diamond ($a_0 = 0.3567$ nm at 298 K) is smaller than these other materials (e.g. Si: $a_0 = 0.5430$ nm, GaP: $a_0 = 0.5451$ nm, 3C-SiC: $a_0 = 0.4360$ nm) so that the Coulomb term in equation 6.1 is 2 to 3 times bigger for diamond than in these other materials.

For an acceptor concentration of 500 ppb, and an equal concentration of donors, the mean DAP separation is approximately 12.5 nm, corresponding to a Coulomb shift of 0.02 eV. A DAP with a separation of 0.922 nm (shell number 27; see Chapter 2.3.1.2) is shifted by more than 0.25 eV to higher energy. If the donor and acceptors are randomly distributed then for a concentration of 500 ppb the probability of DAPs with a mean separation of up to 0.922 nm is very small (less than 0.03%). This motivates the question, are there sufficient close DAPs to explain the strength of emission observed. It should be remembered that close pairs will be much more efficient emitters and they will dominate the emission when free carriers are available to "reset" close pairs multiple times. The thermoluminescence data presented in the next Chapter (Figure 7.6) shows strong emission on heating after the low-temperature phosphorescence has been allowed to decay. This emission must arise from close DAPs. Luminescence images (Figure 3.1) indicate that the DAP emission is not uniform. The incorporation efficiency of both nitrogen and boron is known to depend on the growth surface orientation and in some local regions (especially at dislocations and steps) the concentrations of donors and acceptors could be much higher than the average value substantially increasing the local probability of close DAPs forming. Furthermore, it is not possible to rule

out the possibility that close pairs are grown in at greater concentrations than would be expected for a purely random chance of formation. Further, work is required to determine the absolute concentration of DAPs. An investigation of CVD diamonds co-doped with different concentrations of nitrogen and boron could be very informative.

No attempt has been made to measure the "blue-green" phosphorescence decay at different emission energies in this intermediate temperature range, but it is clear from figure 6.5 that the lifetime is different at different emission energies. Thus it is unsurprising that satisfactory fitting of the overall emission decay in this temperature range can require multiple components (e.g. Figure 6.10) as different process have similar rates.

It is interesting that in this intermediate temperature range the integrated intensity (obtained by integrating under the fitted decay curves from $t = 0$ to infinity) after the excitation is removed is greatest (see Figure 6.12). This behaviour has been discussed by Lawson *et al.*, who noted that carrier recombination processes other than those that results in DAP recombination must be considered. [1] At low temperatures (negligible thermal excitation of free charge carriers), sufficiently close neutral DAPs will eventually emit and only those pairs close enough to other donors/acceptors to facilitate tunneling can emit more than once. Therefore, a metastable concentration of isolated neutral acceptors and donors can remain long after the excitation is removed. As the temperature is increased free holes and electrons are thermally excited from these previously isolated acceptors and donors and contribute to the resetting of those sufficiently close DAPs that contribute to the emission. Thus, the overall emission intensity increases. As the temperature is increased further the neutral donor-acceptor pairs are thermally ionized before they can emit, the integrated phosphorescence intensity decreases and the carriers released are trapped. Figure 6.30 shows the model for the intermediate temperature "blue-green" phosphorescence involving tunneling and thermal-activated charge transfer between nitrogen donors and boron acceptors.

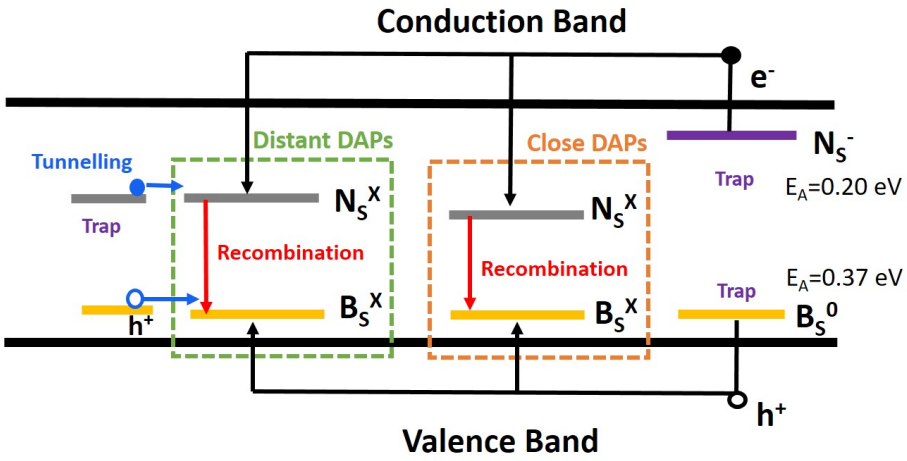

Figure 6.30: Schematic energy level representing the model for phosphorescence in GE samples at intermediate temperature (173 K to 273 K). The recombination between distant DAPs may occur via the athermal process or thermally-excited process. The close DAPs refers to the donor-acceptor pairs where the donor and the acceptor are in close proximity to each other. The close DAPs recombination is enabled by the free carriers thermally released from traps, albeit with low probability.

6.5.3.4 High temperature phosphorescence

At temperatures above approximately 273 K the broad "blue-green" phosphorescence band is centred on 2.5 eV, and does not shift position during the decay (Figure 6.5). The integrated intensity (obtained by integrating under the fitted decay curves from $t = 0$ to infinity) after the excitation is removed decreases rapidly with increasing temperature, which as explained above is consistent with increased thermal ionization on acceptors and donors (Figure 6.12).

At temperatures above approximately 273 K the phosphorescence decay can be successfully fitted with either a combination of two exponential decays, a modified stretched exponential decay (Equation 2.91) or a power law function (equation 2.88) with the relevant parameter, β or p varying with temperature (Figure 6.15). For all these approaches at high temperatures the characteristic phosphorescence lifetime(s) follow equation 2.80. Table 6.1 shows the different activation energies E_A obtained. The activation energies determined in the sample with $[N_S] > [B_S]$ are systematically lower than those in sample with $[N_S] < [B_S]$. This again suggests that there is a second shallow trap presented that is thermally ionized. With the data it is not possible to determine if this is an electron/hole trap, but as

discussed in Chapter 8, the shallow N_S^- defect is the most likely electron trap. Figure 6.31 shows the model for the high temperature "blue-green" phosphorescence involving thermal-activated charge transfer between substitutional nitrogen and substitutional boron.

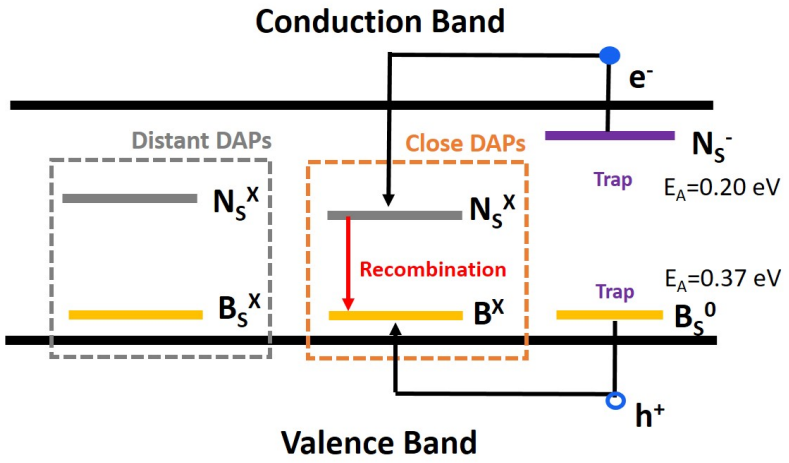

Figure 6.31: Schematic energy level representing the model for phosphorescence in GE samples at high temperatures (273 K to 473 K). The thermal process dominates and quenches distant DAPs recombination. The luminescence centres for the 2.5 eV phosphorescence band are close nitrogen and boron pairs, which can be reset by free charge carriers and emit multiple times. The activation energy of thermally de-trapping in {111} growth sector and {001} growth sector is approximately 0.37 eV and 0.20(5) eV, respectively.

6.5.4 Origin of "orange" and "red" emission bands

As discussed, the "orange" and "red" emission bands observed in sample Sino-01 and SYN4-10 have a different excitation dependence to that of the "blue-green" band and are absent from the GE samples grown from a Co-Fe solvent. This suggests that samples Sino-01 and SYN4-10 contain additional defects/impurities.

The low temperature "red" emission band can be satisfactorily simulated with a simple "1D model" using equation 2.68 (see Fig 6.32, ZPL at $\sim$ 1.883 eV) with Gaussian lineshape and asymmetric (Gaussian and Lorentzian) lineshape, respectively. [20, 28] The resolved vibronic structure suggests that this emission originates from an isolated defect rather than donor-acceptor pairs. There are many Ni related defects in diamond (e.g. 1.883 eV ZPL defect, among in high [N] diamond grown with Ni solvent catalyst), but none can be conclusively associated with the defect reported here. [29–31]

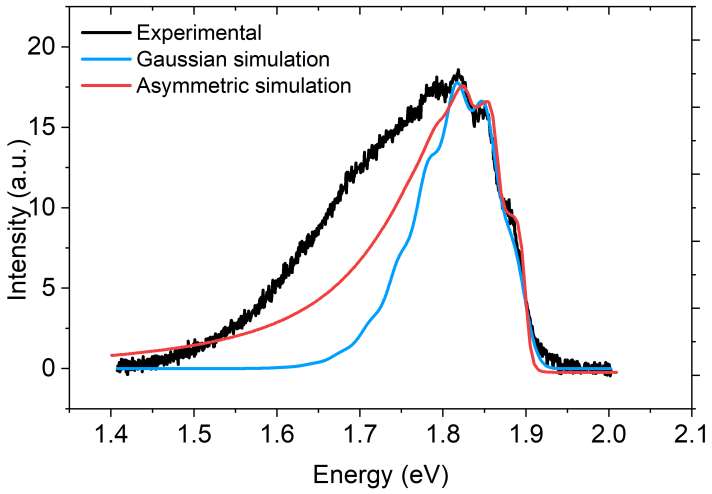

Figure 6.32: The phosphorescence spectrum at 83 K in SYN4-10 following 375 nm excitation (black line). Two different simulations are shown here: simulation spectrum with parameters $E_{ZPL} = 1.883$ eV, $E_{ph} = 0.034$ eV, $S = 2.20$. Gaussian lineshape simulation $\Gamma = 0.015$ eV (blue line); asymmetric (Gaussian and Lorentzian) lineshape simulation spectrum with $\Gamma = 0.050$ eV, asymmetry factor $a = 0.03$ (see equation 4 in [28]) (red line).

However, it is possible that this is a Ni defect. Although it was not possible to measure the activation energy associated with the phosphorescence decay of the "red" band, the temperature dependence is consistent with the process involving the capture of a hole released from a boron acceptor. It is well known that in electro-luminescence/CL hole capture by NV^- results in the emission from NV^0 (i.e. upon hole capture the defect arrives in an excited state of NV^0, and emission follows). It appears that the defect responsible for the "red" band could be excited in a similar manner. After 224/375 nm excitation, the defect X traps an electron as X^-, and the concentration of $B_S{}^0$ is increased. At low T, there are very few holes in the VB, but tunnelling is still possible, and X^- could capture a hole to produce X^0 in an excited state. As the temperature is increased, thermal excitation to $B_S{}^0$ dramatically increased the number of holes, and the lifetime of the "red" emission decreases (as observed). Furthermore, the population of excited vibration levels would result in the "red" emission shifting to higher energies, and the emission would broaden, washing out the vibronic structure (as observed).

The "orange" emission band could be similarly explained, but again the defect responsible is unknown and given the lack of information available, it would be

unwise to speculate further.

It is worth considering if the "orange" and "red" PL/phosphorescence/CL emission band could originate from DAP recombination, with a DAP other than N_S^0...B_S^0. As previously stated, the resolved vibronic structure of the "red" band would suggest this is unlikely. Also finding no alternative donor (acceptor) in sufficiently high concentration (similarity of N_S^0 and B_S^0) is challenging, but the possibility cannot be ruled out especially for the "orange" emission band. The "orange" emission band observed in thermoluminescence experiment will be discussed in Chapter 7.4.5.

6.6 Conclusion and future work

Phosphorescence related defects (traps and luminescence centres) have a very different distribution in various growth sectors of HPHT synthetic diamond. Hence it is crucial to distinguish them for phosphorescence study.

A model based on N_S^0...B_S^0 donor-acceptor pair recombination to fully explain the mechanism of characteristic "blue-green" phosphorescence over a wide temperature range (83 K to 473 K) has been proposed. At low temperatures, the tunnelling process based on distant DAPs gives rise to a T-independent phosphorescence after 224 nm radiation, whose emission band is centred at relatively lower energy (2.25 eV). At high temperature, thermal process dominates and enable the T-dependent phosphorescence to arise from close DAPs. The phosphorescence band peaks at 2.5 eV.

It is accepted that B_S^0 is a relatively shallow acceptor in diamond and N_S^0 a deep donor. The large configuration change when N_S^0 loses an electron is consistent with the N_S^0...B_S^0 donor-acceptor pairs giving rise to the emission at 2.25 - 2.5 eV. However, the phosphorescence decay rates strongly suggest that another shallow trap is involved; N_S^- is proposed as this defect and was discussed in Chapter 5.

Excitation with higher light intensities could be beneficial to study the phosphorescence in diamonds. Moreover, phosphorescence in natural and CVD synthetic diamonds should be studied in future research.

Bibliography

[1] K. Watanabe, S. C. Lawson, J. Isoya, H. Kanda, and Y. Sato, Diamond and Related Materials **6**, 99 (1997).

[2] S. Eaton-Magaña and R. Lu, Diamond and Related Materials **20**, 983 (2011).

[3] V. Chandrasekharan, in *Proceedings of the Indian Academy of Sciences-Section A*, Vol. 24 (Springer India, 1946) pp. 182–186.

[4] S. Eaton-Magaña, J. E. Post, P. J. Heaney, J. Freitas, P. Klein, R. Walters, and J. E. Butler, Geology **36**, 83 (2008).

[5] U. F. S. D'Haenens-Johansson, A. Katrusha, K. S. Moe, P. Johnson, and W. Wang, Gems & Gemology **51**, 260 (2015).

[6] P. S. Walsh, E. C. Lightowlers, and A. T. Collins, Journal of Luminescence **4**, 369 (1971).

[7] J. B. Krumme and W. J. Leivo, in *Proceedings of the Oklahoma Academy of Science* (1964) pp. 105–114.

[8] V. Chandrasekharan, in *Proceedings of the Indian Academy of Sciences-Section A*, Vol. 24 (Springer India, 1946) pp. 193–197.

[9] Z. Song, T. Lu, S. Tang, J. Ke, J. Su, B. Gao, N. Hu, J. Zhang, J. Zhou, *et al.*, Journal of Gemmology **35** (2016).

[10] T. Shao, F. Lyu, X. Guo, J. Zhang, H. Zhang, X. Hu, and A. H. Shen, Carbon **167**, 888 (2020).

[11] L. X. Su, C. X. Zhao, Q. Lou, C. Y. Niu, C. Fang, Z. Li, C. L. Shen, J. H. Zang, X. P. Jia, and C. X. Shan, Carbon **130**, 384 (2018).

[12] V. Chandrasekharan, in *Proceedings of the Indian Academy of Sciences-Section A*, Vol. 27 (Springer India, 1948) p. 316.

[13] P. B. Klein, M. D. Crossfield, J. A. Freitas Jr, and A. T. Collins, Physical Review B **51**, 9634 (1995).

[14] C. D. Clark, P. J. Dean, and P. V. Harris, Proceedings of the Royal Society A **277**, 312 (1964).

[15] R. Mildren and J. Rabeau, *Optical Engineering of Diamond* (John Wiley & Sons, Germany, 2013).

[16] B. Dischler, W. Rothemund, C. Wild, R. Locher, H. Biebl, and P. Koidl, Physical Review B **49**, 1685 (1994).

[17] A. Cox, M. E. Newton, and J. M. Baker, Journal of Physics: Condensed Matter **6**, 551 (1994).

[18] J. P. Goss and P. R. Briddon, Physical Review B **73**, 085204 (2006).

[19] V. Mortet, A. Taylor, Z. V. Živcová, D. Machon, O. Frank, P. Hubík, D. Trémouilles, and L. Kavan, Diamond and Related Materials **88**, 163 (2018).

[20] A. Alkauskas, M. D. McCluskey, and C. G. Van de Walle, Journal of Applied Physics **119**, 181101 (2016).

[21] P. Ščajev, L. Trinkler, B. Berzina, E. Ivakin, and K. Jarašiūnas, Diamond and Related Materials **36**, 35 (2013).

[22] A. Franceschetti and S. T. Pantelides, Physical Review B **68**, 033313 (2003).

[23] C. A. J. Ammerlaan and E. A. Burgemeister, Physical Review Letters **47**, 954 (1981).

[24] A. Alkauskas, J. L. Lyons, D. Steiauf, and C. G. Van de Walle, Physical Review Letters **109**, 267401 (2012).

[25] R. A. smith, *Semiconductors* (Cambridge University Press, 1978 2nd edition).

[26] P. Avouris, I. F. Chang, D. Dove, T. N. Morgan, and Y. Thefaine, Journal of Electronic Materials **10**, 887 (1981).

[27] L. Patrick and W. J. Choyke, Physical Review B **2**, 2255 (1970).

[28] A. L. Stancik and E. B. Brauns, Vibrational Spectroscopy **47**, 66 (2008).

[29] A. T. Collinss, H. Kanda, and R. C. Burns, Philosophical Magazine B **61**, 797 (1990).

[30] A. Yelisseyev, V. Nadolinny, B. Feigelson, and Y. Babich, International Journal of Modern Physics B **16**, 900 (2002).

[31] A. Yelisseyev, S. Lawson, I. Sildos, A. Osvet, V. Nadolinny, B. Feigelson, J. M. Baker, M. Newton, and O. Yuryeva, Diamond and related materials **12**, 2147 (2003).

Chapter 7

Thermoluminescence

7.1 Background

Early investigation of thermoluminescence (TL) in diamond samples can be traced back to the 1940s. A blue thermoluminescence glow at 540 K was observed from a blue fluorescent diamond. [1] The energy obtained from electromagnetic radiation or ionizing radiation (such as optical excitation, x-rays or electric radiation) can be stored in the diamond by the trapping charge carriers at defects. After excitation, a fraction of the stored energy can be released as phosphorescence; in other cases, the energy can be stored in the dark for a long time and is released as thermoluminescence when heated, via thermally-activated de-trapping of charge carriers. [1, 2] Therefore, thermoluminescence is a useful technique to investigate traps and optically active defects in diamond. The shape, position and intensity of the TL emission ("glow curve") indicate the depth and the relative concentration of traps. [2, 3]

Since the late 1980s, CVD synthetic diamond has been proposed as an attractive TL dosimeter (TLD) material exploiting properties such as human soft tissue equivalence, non-toxicity, chemical stability, well-controlled defects, and it is relatively insensitive to radiation damage. [4–6] For this application, studies mainly focused on reproducibility, the efficiency of thermoluminescence, and the linear relationship of integrated TL intensity and radiation dose. [4, 5, 7–12] However, diamonds are usually irradiated at room temperature, which results in the absence of TL glow peaks corresponding to shallow traps. In addition, there is a lack of

information on the depth of traps and thermoluminescence spectra in those studies. Hence those studies will not be introduced in detail in this thesis.

Table 7.1 summarizes thermoluminescence studies on diamond where the sample were illuminated at liquid nitrogen temperature (approximately 80 K). "Blue-green" and "red" thermoluminescence are seen in natural, HPHT synthetic and boron-doped CVD synthetic diamonds, regardless of type I or type II. Since the published TL spectra are limited, it is uncertain whether the same colour TL emission ("blue-green" or "red") in different samples originate from the same defect. The "red" thermoluminescence band peak at 1.85 eV reported by Walsh *et al.* [13] is very similar to the "red" phosphorescent band [14, 15]. The "blue-green" TL band centred at 2.57 eV [6] or 2.6 eV [13] seen after UV illumination could be linked to the "blue-green" phosphorescence band investigated by Shao *et al.* [16]. After UV radiation in a weakly boron-doped type IIb CVD synthetic diamond film, the 480 K TL emission peak appeared as "blue-green" broad band at about 490 nm. [17] Its spectral position is the same as the commonly seen "blue-green" phosphorescence band. [18–20] Therefore, the same defects may play roles in both thermoluminescence and phosphorescence. [13] Moreover, "red" and "blue-green" thermoluminescence appear in the temperature range belonging to different TL glow peaks, corresponding to traps with different activation energies. [13, 21–24] This indicates that the carriers thermally released from one type of trap can give rise to emission from different luminescence centres. [22] This can be a result of the different cross-sections of luminescence centres. Besides, the emission from the same type of luminescence centre can also be generated by carriers from different traps.

Two TL glow peaks corresponding to traps with activation energies of approximately 0.2 eV and 0.37 eV are commonly observed in type II natural and HPHT synthetic diamonds. [13, 21–24] The thermal activation energy is usually calculated by the methods introduced in Chapter 2.3.5.3. Among them, the initial rise method is very frequently used due to its convenience. However, in cases where TL peaks overlap, or the thermal scan of the TL glow peak does not start with zero intensity, the initial rise region is not well-defined, and this method does not result in the determination of accurate activation energies (e.g. [21]). Thermal cleaning can

be applied to solve this problem. The relative intensity of these two glow peaks (0.2 eV and 0.37 eV) is sample dependent, indicating they correspond to different traps in diamonds. [22] The higher energy (0.37 eV) TL glow peak requires a stronger dose of excitation to reach saturation of intensity in Walsh's research. [13] The TL glow peak of activation energy of 0.37 eV is widely agreed to be assigned to $B_S{}^0$. However, the trap of the lower temperature TL glow peak is uncertain: Walsh considered it as a shallower acceptor [13], while Bourgoin believed its energy level is approximately 0.22 eV below the conduction band [24]. It is noticeable that this TL glow peak is more intense in diamond samples containing a higher concentration of nitrogen [13].

The study of the depth of traps and spectral response in CVD synthetic diamond is obviously insufficient. More investigation is required in future work, especially from liquid nitrogen temperatures to higher temperatures. In addition, discussion of the correlation between phosphorescence and thermoluminescence in diamond, and the comparison of optical activation energy and thermal activation energy, is rare in the literature.

7.2 The simulation of TL glow peak

The TL glow peak is simulated by the equations based on the thermoluminescence model of one trap and one luminescence centre introduced in Chapter 2.3.5.1. It helps to understand how the parameters affect the shape and position of the TL glow peak. These parameters include the physical parameters which are sample-dependent, such as the frequency factor s, the depth of trap E, and the order of the kinetics b depends on the relative concentration of traps and luminescence centres; the experimental parameter heating rate (β); and the concentration of trapped carriers (n_0) determined by both the concentration of traps in samples and the dose of excitation during the experiment. [27, 28]

7.2.1 The frequency factor

For the simple thermoluminescence model of one trap and one luminescence centre, the value of the frequency factor s should be close to typical lattice

Table 7.1: Summary of thermoluminescence glow peaks and activation energies of corresponding traps in various diamonds in the literature

Diamond	Excitation	β (K/min)	Peak T (K)	E_A (eV)	Emission	Year [ref]
type I natural	$\leq$ 300 nm	-	540	-	"blue"	1946 [1]
Type I industrial	365 nm	150	420	0.5	"blue"	1950 [25]
			520	0.7	"blue"	
Type I	UV lamp	15	180	0.12	-	
			330	0.4 -0.5	-	
			525	1	-	
Type IIa	UV lamp	15	113	0.2	-	
			150	0.37	-	1961 [26]
			217	0.55	-	
			375	0.88	-	
			563	1.5	-	
Type IIb	UV lamp	15	140	0.20	"blue"	
			250	0.37	"blue"	
Type IIb	$\geq$ 3 eV	35	150	0.2	"blue"	
			260	0.37	"blue"	1966 [22]
	$\geq$ 1.8 eV	35	175	0.2	"red"	
			285	0.38	"red"	
Type IIb	$\geq E_g$	30	150	0.18 (5)	"red"/"blue"	1971 [13]
			250	0.35 (2)	1.85 eV/2.6 eV	
Type IIb	Electrically	35	265	-	"blue"	
			280	-	"red"	1973 [23]
	225 nm	35	150	-	-	
Type IIb natural	4.88 eV	0.5 - 15	105	0.09	"red"	
			250	-	"red"	
			265	0.37 (2)	"blue"	
			415	0.8	"red"	1978 [24]
Type IIb HPHT	4.88 eV	0.5 - 15	105	0.09	"red"	
			210	0.22 (2)	"blue"	
			265	0.37 (2)	"blue"	
			320	0.38	"red"	
CVD film	200-400 nm	60	336	0.50 (3)	2.57 eV	2007 [6]
			563	1.22 (6)	"blue"	

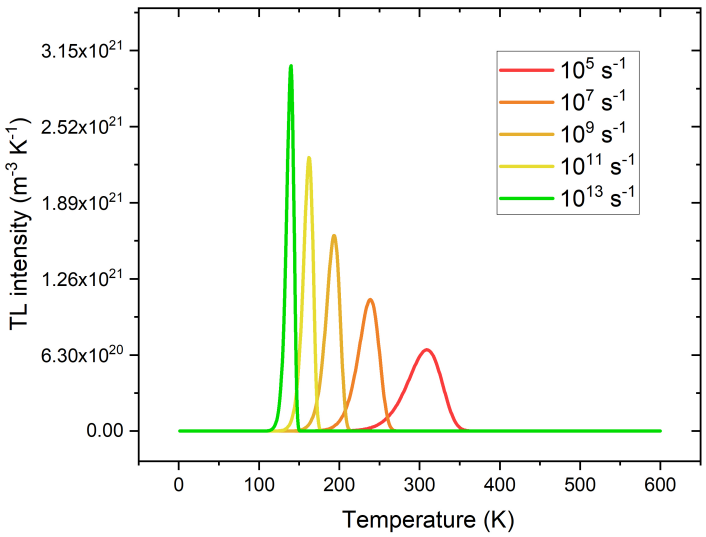

Figure 7.1: Simulation of TL glow peak using the first-order TL equation 2.100 showing the variation with the frequency factor s equals to 10^5 s^{-1}, 10^7 s^{-1}, 10^9 s^{-1}, 10^{11} s^{-1}, 10^{13} s^{-1}, respectively. Parameter values are $E = 0.37$ eV, $n_0 = 3.51 \times 10^{22}$ m^{-3} (200 ppb), $k = 8.617 \times 10^{-5}$ eV/K, $\beta = 2$ K/s.

vibration frequencies, e.g. 10^{12} - 10^{14} s^{-1}. [27] For diamonds, it is 1332 cm^{-1} (3.94×10^{13} s^{-1}), while abnormal values obtained from experiments can sometimes be either surprisingly large or small. [2] For example, the s value corresponding to a TL peak with an activation energy of 0.4 eV has been reported as 2.4×10^3 s^{-1} in a treated CVD lab-grown diamond sample. [29] The explanation of such abnormal low value for s is thought to be that the TL emission is generated from centre-to-centre recombination rather than recombination between a centre and a carrier in the conduction band or the valence band. The value yielded from the calculation is, therefore, closer to the recombination probability at the luminescence centre rather than the s value defined in the first-order TL equation (equation 2.100). [2]

As shown in figure 7.1, the first-order TL peak centre shifts from approximately 140 K to 310 K accompanied by a decrease in peak height and an increase in peak width, as the s value varies from 10^{13} s^{-1} to 10^5 s^{-1}. The area of TL peaks in this figure are equal because the first-order TL peak area is only determined by the concentration of trapped charge carrier n_0, which is kept constant in this simulation.

7.2.2 The depth of the trap

Figure 7.2 shows the theoretical distribution of first-order TL peaks corresponding to traps of different activation energy. The higher the activation energy, the higher temperature where the TL peak is located. The height of the TL peak decreases, and the width of the TL peak increases as the trap depth increases. The area of those peaks in the figure is constant. The activation energy shift of the second-order TL peaks shows the same trend as the first-order TL peaks, although the shape of each second-order peak is more symmetric. [2, 27] Hence in terms of one TL glow curve, the TL peak of a deeper trap is always located at a higher temperature.

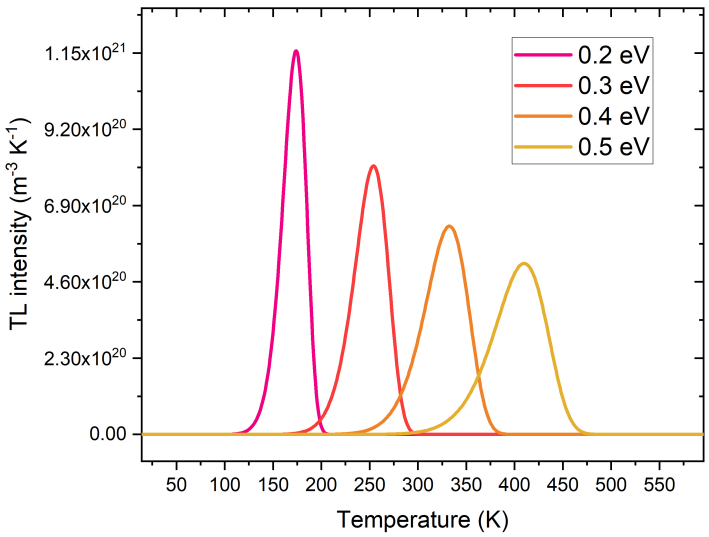

Figure 7.2: Simulation of TL glow peak using the first-order equation 2.100 showing the variation with the depth of trap E equals to 0.2 eV, 0.3 eV, 0.4 eV , 0.5 eV, respectively. Parameter values are $s = 10^5$ s^{-1}, $n_0 = 3.51 \times 10^{22}$ m^{-3} (200 ppb), $k = 8.617 \times 10^{-5}$ eV/K, $\beta = 2$ K/s.

7.2.3 The total number of trapped charge carriers

Figure 7.3 shows a simulation of the variation of first-order TL peak intensity with the initial concentration of trapped carriers n_0. The area under each TL peak equals n_0, and the peak position is independent of n_0. [27] Figure 7.4 shows the second-order TL depending on the initial concentration of trapped charge carriers. Those peaks are more symmetric with a larger width of the high-temperature half than the first-order TL peaks. T_m, the maximum TL intensity temperature, shifts

to a lower temperature when n_0 is higher.

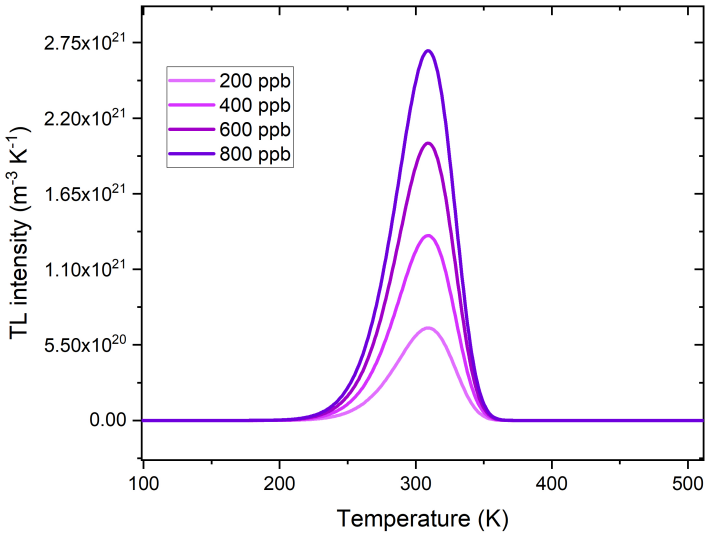

Figure 7.3: Simulation of TL glow peak using the first-order equation 2.100 showing the variation with the concentration of trapped charge carriers n_0 equals to 3.51×10^{22} m^{-3} (200 ppb), 7.02×10^{22} m^{-3} (400 ppb), 1.05×10^{23} m^{-3} (600 ppb) , 1.41×10^{23} m^{-3} (800 ppb), respectively. Parameter values are $s = 10^5$ s^{-1}, $E = 0.37$ eV, $k = 8.617 \times 10^{-5}$ eV/K, $\beta = 2$ K/s.

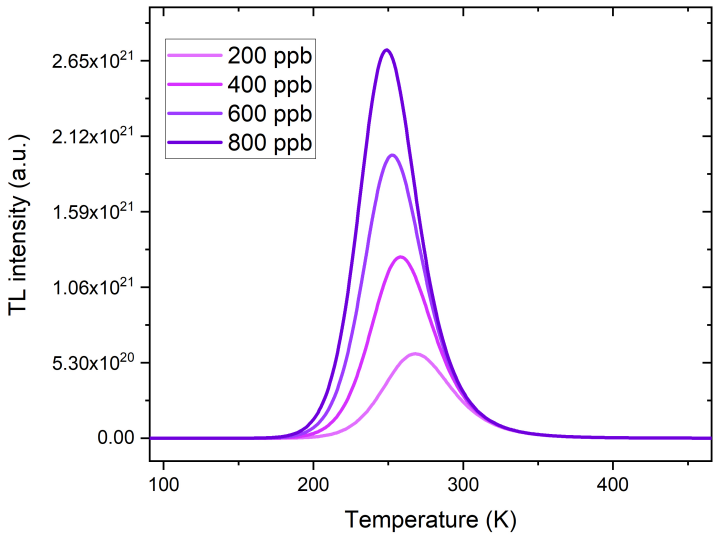

Figure 7.4: Simulation of TL glow peak using the second-order equation 2.103 showing the variation with the concentration of trapped charge carriers n_0 equals to 3.51×10^{22} m^{-3} (200 ppb), 7.02×10^{22} m^{-3} (400 ppb), 1.05×10^{23} m^{-3} (600 ppb) , 1.41×10^{23} m^{-3} (800 ppb), respectively. Parameter values are the concentration of traps $N = 3.51 \times 10^{21}$ m^{-3} (20 ppb), $s = 10^5$ s^{-1}, $E = 0.37$ eV, $k = 8.617 \times 10^{-5}$ eV/K, $\beta = 2$ K/s.

7.2.4 Excitation

The concentration of trapped charge carriers depends on the excitation dose (or integrated photon flux). At a relatively low dose of excitation, the TL signal depends linearly on the dose. However, optical bleaching occurs when the excitation dose reaches a saturation level. [22] The TL peak can also be bleached by applying an electric field after radiation to change the distribution of charge carriers. [23] In addition, different TL peaks can have a different dependence on the wavelength of the optical excitation. [22]

7.2.5 Heating rate

For the thermoluminescence experiment, a constant heating rate β should be applied. As shown in figure 7.5, the position of the TL peak shifts to higher temperatures when the heating rate is increased. The TL peak of a higher heating rate shows a lower height in this figure, while it is noticeable that the unit of the TL intensity here is the concentration of defects per Kelvin. From an experimental point of view, a higher heating rate usually gives rise to more luminescence detected in a certain time window. [27] Namely, at a low heating rate, the TL peaks are broad and relatively weak. [30] Therefore, a high heating rate is beneficial for improving the signal-to-noise ratio. However, for materials having low thermal conductivity, there can be a delay between the temperature of the sample and the heater. There is generally no such concern for diamonds. The TL glow peak area is independent of the heating rate in the absence of thermal quenching. [6]

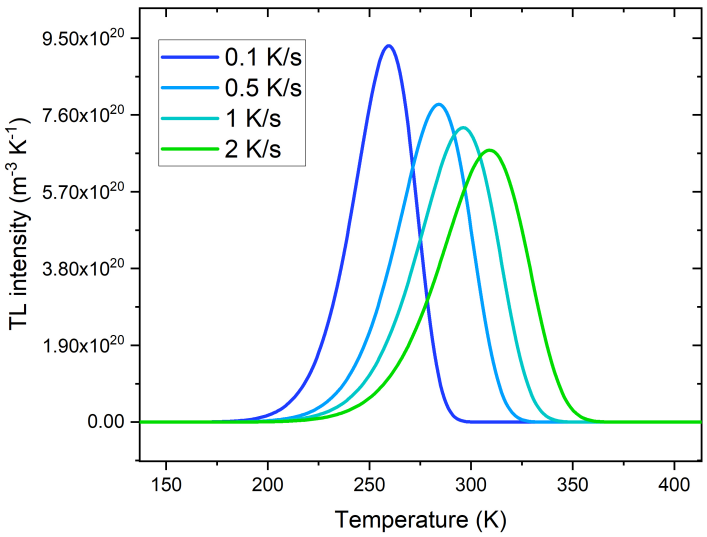

Figure 7.5: Simulation of TL glow peak using the first-order equation 2.100 showing the variation with the linear heating rate equals to 0.1 K/s, 0.5 K/s, 1 K/s, 2 K/s, respectively. Parameter values are $s = 10^5$ s^{-1}, $E = 0.37$ eV, $n_0 = 3.51 \times 10^{22}$ m^{-3} (200 ppb), $k = 8.617 \times 10^{-5}$ eV/K.

7.3 Experimental TL results

Thermoluminescence glow curves and TL spectra in various diamond samples studied were recorded using the "Garfield" experimental setup introduced in Chapter 3.2. Before each TL experiment, the diamond sample was heated to a high temperature generally above 473 K to empty the shallow traps whose TL glow peak was located in the experimental temperature range. The diamond samples were cooled to 83 K. When the temperature stabilized, optical excitation was applied until saturation of the resulting TL signal was achieved. After excitation removed, the diamond was heated at a linear heating rate of 100 K/min, during which time the thermoluminescence was detected by camera or spectrometer. The time window between the excitation and the heating procedure, the so-called delay time, is adjustable to meet different experimental requirements.

7.3.1 Sample GE81-107a-B/C

7.3.1.1 TL glow curve

In figure 7.6, the red solid lines represent the TL glow curves observed from the sample GE81-107-a-B ({001} growth sector) and GE81-107a-C ({111} growth sector) after 224 nm laser excitation is removed and with a delay time. The delay time after excitation removed was set to 900 s based on the experiment results in Chapter 6. This time was sufficiently long for the phosphorescence at 83 K to decay to zero. Hence the luminescence that arises from the tunnelling process was excluded from the detected thermoluminescence. The thermoluminescence detected only arises from the luminescence centres which are located far from the traps. The TL intensity in GE81-107a-C is stronger than that in GE81-107a-B, while the shape and position of the two TL glow curves are very similar. For each sample, a single TL glow peak was observed from 173 K to approximately 400 K and centred at 273 K. The low-temperature half of the TL peak where the thermoluminescence intensity climbs as temperature increasing covers a range of 173 K to 273 K corresponding to the "intermediate temperature range" of phosphorescence (see Chapter 6). Above 273 K, the TL intensity gradually decreases during heating. This corresponds to the high-temperature range of phosphorescence, where phosphorescence arises from a predominated thermal activation of carriers from traps. The high-temperature half of the TL peak has a larger half-width than the low-temperature side. This indicates that the TL peak is likely to consist of two TL peaks overlapping with each other.

The black solid lines in figure 7.6 represent the TL glow curves in GE diamond samples at the same condition as the red lines TL glow curves but with no delay time between the excitation and the heating procedure. Hence the integrated area of the whole TL glow curve depends on the total number of luminescence centres regardless of whether they are spatially close to traps or not. [31] In theory, the proportion of the close pairs of trap and luminescence centre and distant pairs of trap and luminescence centre can be obtained by calculating the difference of integrated area of the red and black curves. In the current experimental set up there is considerable variability in the time taken between removal of the optical

excitation and the starting of the temperature ramp (due to LINKAM software) so this analysis was not undertaken.

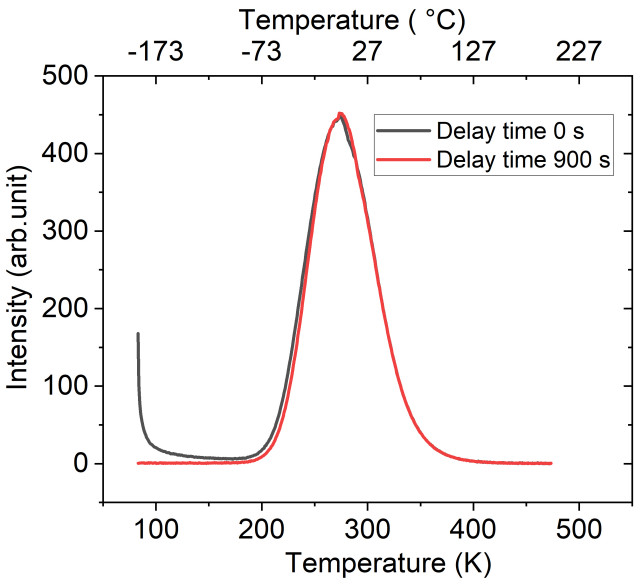

(a)

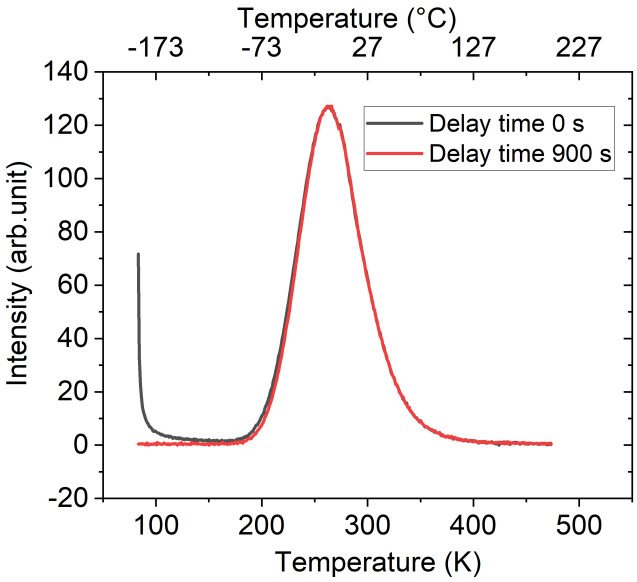

(b)

Figure 7.6: TL glow curve recorded for GE samples after excitation with 224 nm laser at 83 K, after sufficient (900 s) or no delay time, then heated to 473 K. Heating rate at 100 K/min. (a) GE81-107a-C ({111} growth sector). (b) GE81-107a-B ({001} growth sector)

7.3.1.2 Thermal cleaning

The Thermal cleaning method was used to separate individual TL glow peaks. Figure 7.7 (a) and 7.7 (b) show the two TL peaks (labelled as Peak 1 and Peak 2

here) obtained by thermal cleaning in sample GE81-107a-C as TL intensity versus experiment time and temperature, respectively. When the sample started to cool from the peak temperature of Peak 1 at a 50 K/min rate, the thermoluminescence intensity dropped relatively rapidly to zero. The symmetry of Peak 2 is typical of second-order kinetics (indicating retrapping dominates). So if the capture cross section is equal, the number of luminescence centres is significantly less than the number of traps, which is also the case for sample GE81-107a-B.

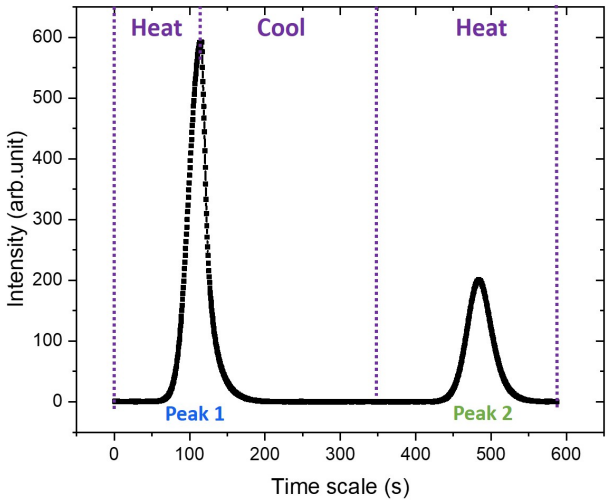

(a)

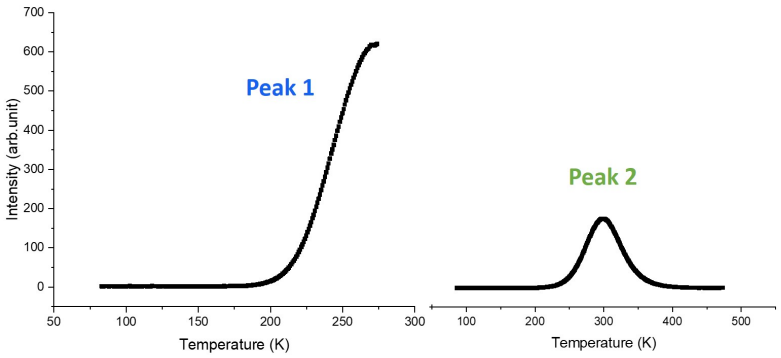

(b)

Figure 7.7: TL glow curve in GE81-107a-C recorded for GE samples after excitation with 224 nm at 83 K. When the first peak in the TL curve was reached, the sample was rapidly cooled to 83 K and the TL glow curve recorded again. Heating rate 100 K/min. (a) TL intensity as a function of time. (b) TL intensity as a function of temperature in K.

Since each TL glow peak's initial region can be clearly selected, the initial

rise method described in Chapter 2.3.5.3 was applied to calculate the thermal activation energy of those traps, which are listed in table 7.2.

Table 7.2: Activation energies determined from TL cleaning peaks for GE samples using the initial rise method

	GE81-107a-B {001}		GE81-107a-C {111}	
	Peak 1	Peak 2	Peak 1	Peak 2
ΔE_A	0.30(5) eV	0.33(5) eV	0.34(5) eV	0.37(5) eV

7.3.1.3 TL spectrum

Thermoluminescence recorded after the phosphorescence has decayed away presents as one featureless broadband with the peak of the thermoluminescent band located at 490 nm and 484 nm (approximately 2.5 eV) for GE81-107a-C and GE 81-107a-B, respectively. (Figure 7.8) This suggests that the recombination pair of substitutional boron and substitutional nitrogen as discussed in Chapter 6.5.3.1 is also responsible for thermoluminescence. There is no shift in TL band position during heating for both samples. The spectral position of TL bands in different growth sectors of diamond ({111} & {001}) is only slightly different.

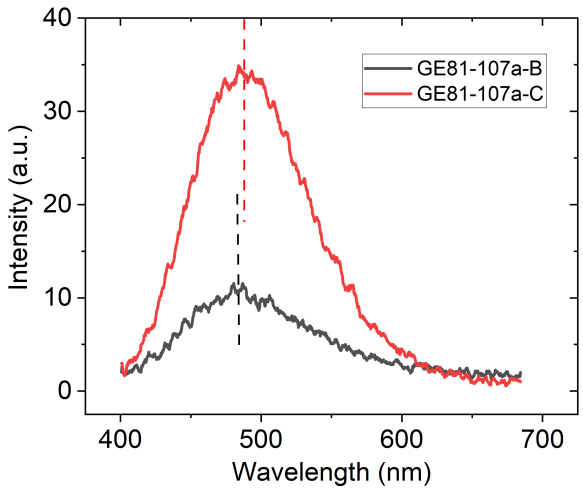

Figure 7.8: TL spectra in sample GE81-107a-B (T_m = 483 K) and sample GE81-107a-C (T_m = 487 K).

Figure 7.9 (a) shows that when heating the diamond sample immediately after the 224 nm radiation, the initial broadband luminescence detected is centred on

550 nm (2.25 eV) in samples GE81-107a-B and GE81-107a-C. This is at the same position as the phosphorescence band at the low-temperature range (83 K to 173 K). The thermoluminescence band appears afterwards during heating, ranging from 273 K to around 410 K, and peaks peaked at 490 nm in GE81-107a-C and 484 nm in GE81-107a-B.

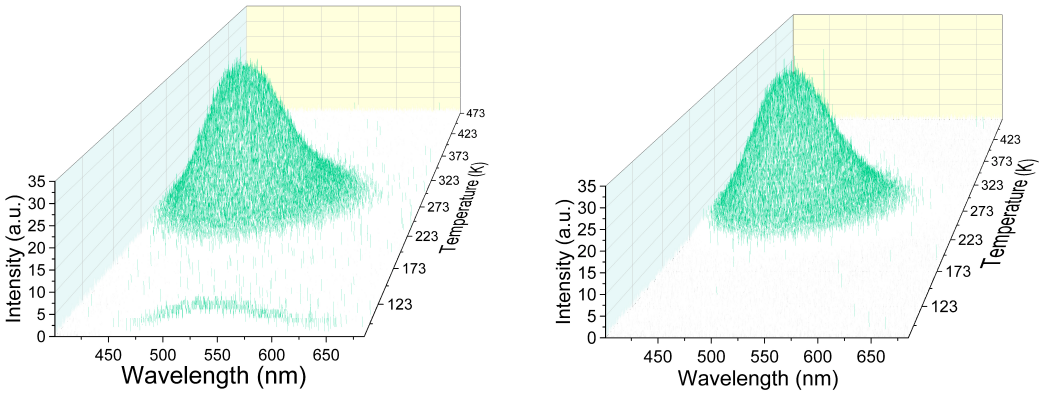

(a) (b)

Figure 7.9: The 3D plot of thermoluminescence in sample GE81-107a-C was recorded after excitation with 224 nm at 83 K at a heating rate of 100 K/min. (a) no delay time (b) with a delay time of 900 s.

As shown in figure 7.10, the spectral position of maximum thermoluminescent emission in sample GE81-107a-C for "Peak 1" and "Peak 2" are both "blue-green" centred at 490 nm. It is similar for GE81-107a-B, where the spectral TL bands peak at 484 nm.

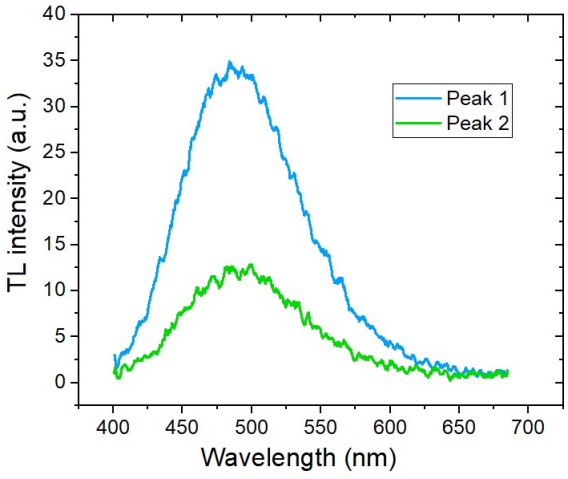

Figure 7.10: TL spectra at the peak temperature of "Peak 1" (269 K) and "Peak 2" (298 K) (after thermal cleaning) in sample GE81-107a-C.

Table 7.3: Activation energies determined from TL cleaning peaks for Sino-01 sample using the initial rise method

	Sino-01	
	Peak 1	Peak 2
ΔE_A	0.24(2) eV	0.35(2) eV

7.3.2 Sample Sino-01

Figure 7.11 presents the TL glow curve for sample Sino-01 which starts to climb at around 173 K and reaches the maximum at approximately 283 K. The TL glow peak is asymmetric with a larger width on the high-temperature side indicating that it consists of more than one TL peak.

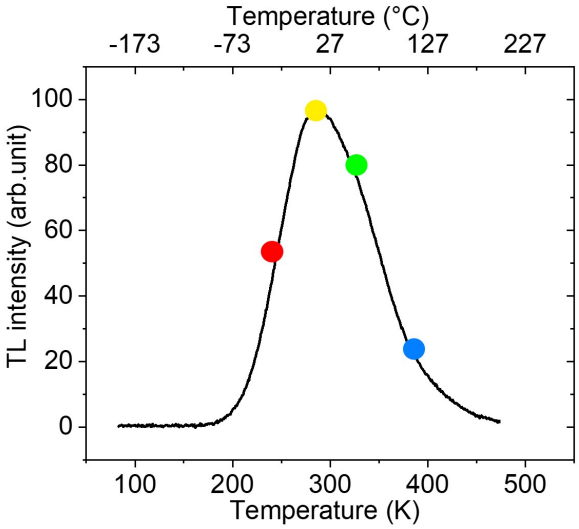

Figure 7.11: TL glow curve recorded for sample Sino-01 after excitation with 224 nm laser at 83 K, delay for 5 min for phosphorescence to decay to zero, then heat to 473 K. Heating rate at 100 K/min. The dots indicate the temperatures for spectra acquisition in figure 7.13, the colours of dots correspond to the line colours.

The activation energies of the TL peaks obtained by the TL cleaning process are therefore, calculated by the initial rise method and listed in table 7.3. The activation energy of the shallower trap, whose TL peak is centred at 284 K, is 0.24 (2) eV. The second peak is centred at 325 K. (Figure 7.12) The depth of the corresponding trap shown in table 7.3 assigns it to B_S^0.

As shown in figure 7.13(a), a "blue-green" band appear firstly at relatively low temperature, then as it fades, another "orange" band appears. Its intensity

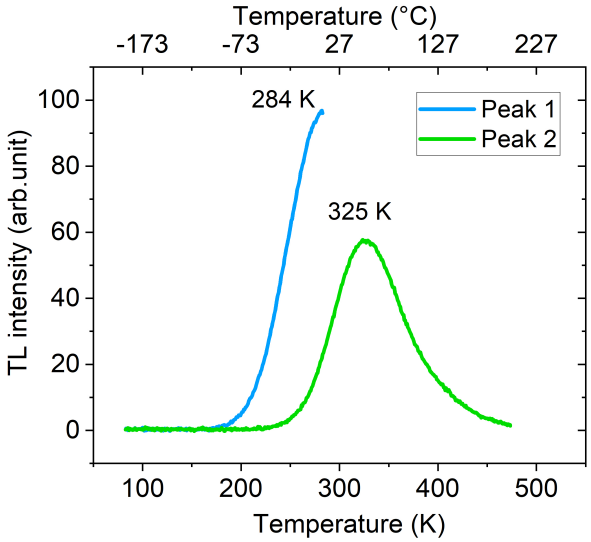

Figure 7.12: TL glow peaks in Sino-01 recorded using a thermal cleaning procedure after excitation with 224 nm at 83 K. Heating rate 100 K/min.

gradually reaches about the same level as the maximum of the "blue-green" band before finally disappearing when the temperature approaches 473 K. The spectral "blue-green" band is centred at 490 nm. There is no shift in the "blue-green" band position during the thermoluminescence emission. By contrast, the centre of the "orange" band shifts from approximately 580 nm to 590 nm as the temperature increases.

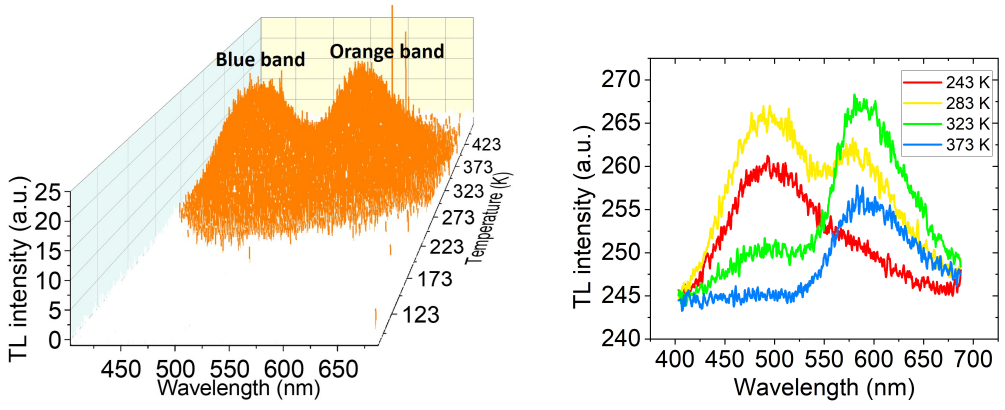

(a) (b)

Figure 7.13: Thermoluminescence in sample Sino-01 recorded after excitation with 224 nm and 5 min delay at 83 K at a 100 K/min heating rate. (a) The 3D of TL plot (b) Selected TL spectra: the line colours correspond to the colour of spots in figure 7.11 indicating the temperatures.

7.3.3 Sample SYN4-10

Figure 7.14(a) and figure 7.14(b) show the thermoluminescence in the brilliant-cut diamond sample SYN4-10 after pumping with a 224 nm pulsed laser (a) and 375 nm CW laser (b), respectively. Following optical excitation at these two wavelengths, the thermoluminescence spectra include both a "blue-green" and an "orange" band. The "blue-green" broadband first appears at lower temperatures, followed by an "orange" band at higher temperatures. The relative intensities of the "blue-green" band and the "orange" band are different for different excitation wavelengths.

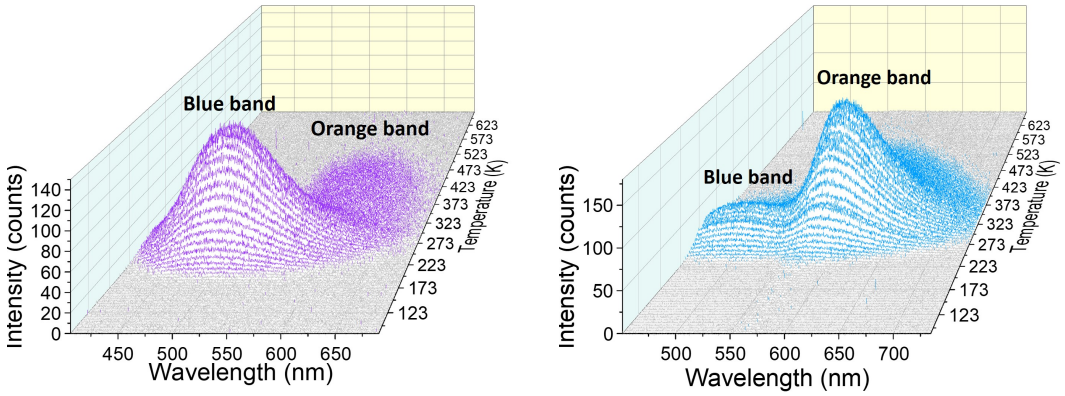

(a) (b)

Figure 7.14: The 3D plot of thermoluminescence in SYN4-10 recorded after excitation and phosphorescence from 83 K to 673 K at a 100 K/min heating rate. (a) after 224 nm pulsed laser excitation and 10 min delay (b) after 375 nm CW laser excitation and 10 min delay.

7.3.3.1 TL after 224 nm excitation

As shown in figure 7.15, after 224 nm excitation and phosphorescence (band centred at 550 nm) at 83 K, sample SYN4-10 was heated at a rate of 100 K/min. The thermoluminescence rises from approximately 173 K and reaches the maximum intensity at 313 K. There is a relatively flat shoulder on the TL glow peak at the high-temperature side, covering around 373 K to 600 K.

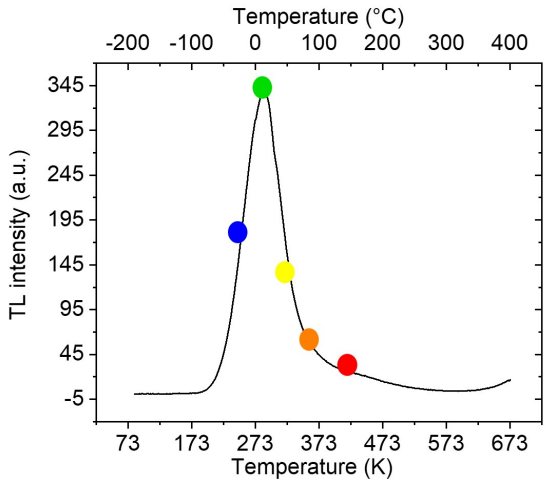

Figure 7.15: TL glow curve recorded for SYN4-10 sample after excitation with 224 nm laser at 83 K and 10 min delay for phosphorescence decay to zero, then heat to 673 K. Heating rate at 100 K/min.

A TL cleaning process was utilised in an attempt to separate the overlapping TL glow peaks. As shown in figure 7.16, at least four TL glow peaks can be obtained for SYN4-10 with their activation energy, calculated by initial rise method, are 0.32(3) eV, 0.36(3) eV, 0.37(3) eV, and 0.38(3) eV. The activation energy of Peak 2, Peak 3, and Peak 4 are very close; they do not necessarily correspond to trap of different depths.

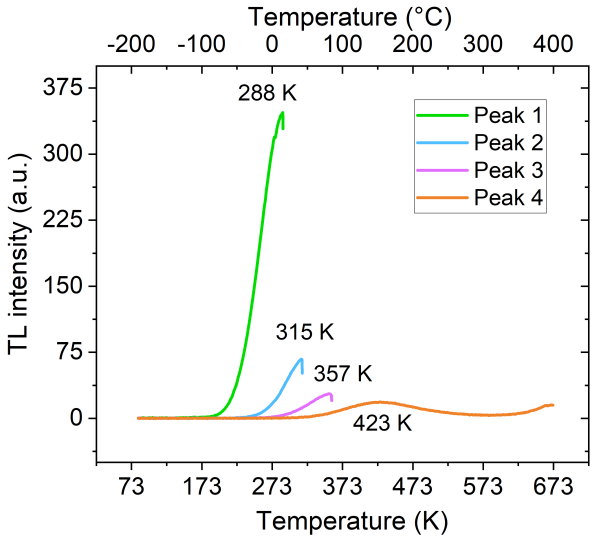

Figure 7.16: TL glow peaks in SYN4-10 were recorded using thermal cleaning procedure after excitation with 224 nm at 83 K and 10 min delay. Heating rate 100 K/min.

Figure 7.17 presents several TL spectra after 224 nm excitation at different

temperatures. In the temperature range where thermoluminescence intensity increases with temperature, an intense featureless broad band is centred at 490 nm, which is the same as the "thermal" phosphorescence band (Chapter 6.4). The spectral position of this "blue-green" thermoluminescence band is temperature independent. Due to the large width of this band, the "orange" band is likely underlying. As the temperature increases above approximately 350 K, the "blue-green" thermoluminescence becomes weak, the "orange" thermoluminescence emerges. For the "orange" TL band, no obvious change in intensity is observed with temperature, while there is a small shift in spectral position from 585 nm to 587 nm with increasing temperature.

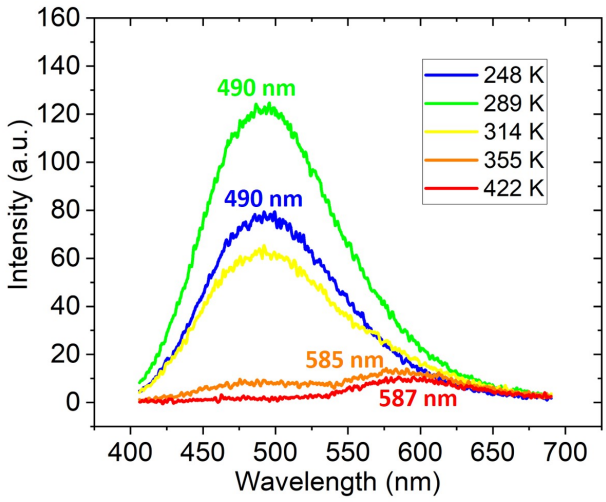

Figure 7.17: Several selected spectra of thermoluminescence in SYN4-10 after 224 nm excitation. The line colours correspond to the colour of spots in figure 7.15 indicating the temperatures.

7.3.3.2 TL after 375 nm excitation

The TL glow peak after 375 nm excitation from sample SYN4-10 is wider than that following 224 nm excitation, ranging from approximately 200 K to 673 K with a shoulder on the low-temperature side. The top of the TL glow peak appears at 335 K (figure 7.18). Extremely weak thermoluminescence is observed from 160 K to 200 K with relatively stable intensity, which presents repeatably for multiple measurements.

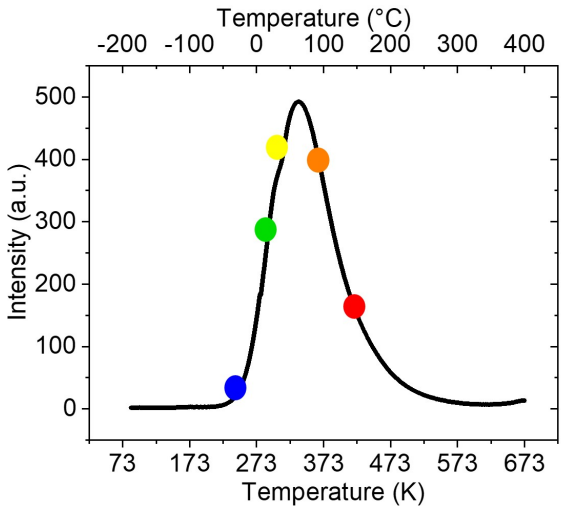

Figure 7.18: TL glow curve recorded for SYN4-10 sample after excitation with 375 nm laser at 83 K and delay for 40 min for phosphorescence decay to zero, then heat to 673 K. Heating rate at 100 K/min.

Figure 7.19 presents three main TL glow peaks obtained by the thermal cleaning process. Peak 1 corresponds to a trap with an activation energy of 0.32(3) eV, peak 2 and peak 3 correspond to trap activation energy of 0.35(3) eV by an initial rise method calculation.

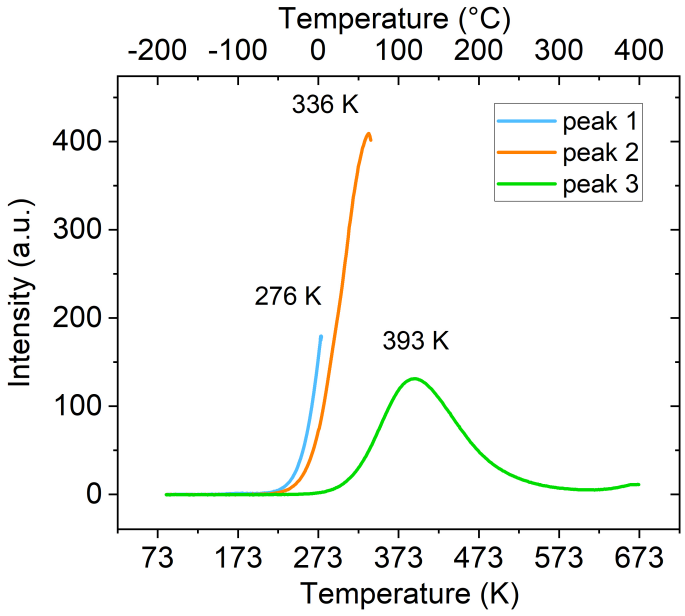

Figure 7.19: TL glow peaks in SYN4-10 recorded using thermal cleaning procedure after excitation with 375 nm at 83 K and 40 min delay. Heating rate at 100 K/min.

Figure 7.20 shows that thermoluminescence after 375 nm excitation in sample SYN 4-10 is dominated by the "orange" rather than the "blue-green" band. The

"blue-green" thermoluminescent band centred at 490 nm (2.5 eV) presents at a temperature range of approximately 200 K to 335 K, which is weaker than the accompanying "orange" band but also the "blue-green" TL band observed following 224 nm excitation in figure 7.17. There is a significant shift in the spectral position of the "orange" thermoluminescence band, whose centre varies from 573 nm (2.16 eV) to 587 nm (2.11 eV) as the temperature increases. The "red" emission band shown in phosphorescence measurement after the same optical excitation (Chapter 6.4) is not observed on thermoluminescence spectra.

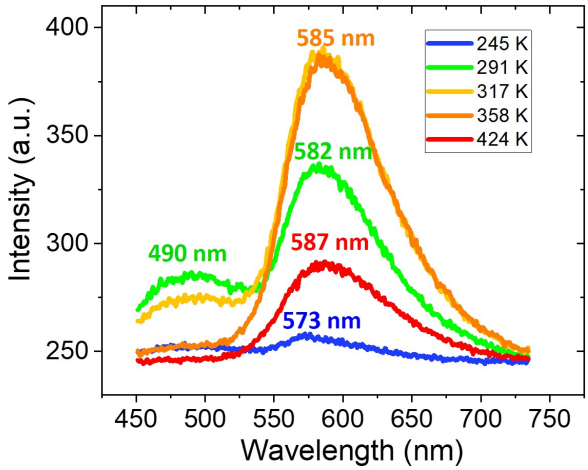

Figure 7.20: Several selected spectra of thermoluminescence in SYN4-10 after 375 nm excitation. The line colours correspond to the colour of spots in figure 7.18 indicating the temperatures.

7.4 Discussion

7.4.1 Summary

In the GE sample cut from a {111} growth sector (GE81-107a-C) and a {001} growth sector (GE81-107a-B) following 224 nm (5.535 eV) excitation a broad glow curve centred on ~ 273 K (FWHH = 70 K; heating rate 1.67 K/s) and 263 K (FWHH = 73 K; heating rate 1.67 K/s) is detected, which shift to higher temperatures upon thermal cleaning. The initial glow curve falls more slowly than it rises, but the second peak recorded after thermal cleaning is almost symmetrical.

In both GE samples the TL spectrum is composed of one broad asymmetric

peak (T_m = 273 K GE81-107a-C and T_m = 263 K GE81-107a-B) centred on approximately 487 nm (2.5 eV).

In sample Sino-01 following 224 nm excitation at 83 K, a broad glow curve centred on 283 K (FWHH = 110 K; heating rate 1.67 K/s) is detected. The glow curve falls more slowly than it rises and shifts to higher temperatures upon thermal cleaning. The TL spectrum is composed of two broad peaks, with similar maximum intensities. The low temperature peak (T_m = 283 K) is centred on 490 nm while the higher temperature peak (T_m = 325 K) shifts from 580 to 590 nm (2.10 - 2.14 eV) as the temperature increases.

In sample SYN4-10 following 224 nm excitation at 83 K, a broad glow curve centred on 313 K (FWHH = 70 K; heating rate 1.67 K/s) is detected. The glow curve falls more slowly than it rises and shifts to higher temperatures upon thermal cleaning. The TL spectrum is composed of two broad TL peaks. The much more intense low temperature peak (T_m = 288 K) is centred on 490 nm while the higher temperature peak (T_m = 355 K) is centred on 586 nm (2.12 eV).

In sample SYN4-10 following 375 nm (3.306 eV) excitation at 83 K, a broad glow curve centred on 335 K (FWHH = 108 K; heating rate 1.67 K/s) is detected. The glow curve falls more slowly than it rises and shifts to higher temperatures upon thermal cleaning. The TL spectrum is composed of two broad TL peaks. The much more intense low temperature peak (T_m = 289 K) is centred on 490 nm while the higher temperature peak (T_m = 355 K) shifts from 573 to 587 nm (2.11-2.16 eV) as the temperature increases.

7.4.2 Order of kinetics

The standard textbook models for thermoluminescence usually assume one type of trap and one type of recombination centre. [32] In these model systems it is assumed that upon illumination electrons (holes) are transferred from the recombination/luminescence centres to the traps and are unable to escape. During heating, electrons (holes) are ejected out of the traps and become free to move in the conduction (valence) band. The "Randall and Watkins" model assumes that these free carriers find the recombination centre with negligible probability of re-trapping (see Chapter 2.3.5.1). This is often referred to as "first-order" thermoluminescence

as the intensity is proportion to the initial concentration of filled traps (which is equal to the initial concentration of available recombination centres in the one type of trap and one type of recombination centre model). The glow curve predicted by this model is asymmetric, rising more slowly than it falls. **This shape of glow curve was not seen in the studies reported here.**

If re-trapping of carriers cannot be ignored, and a free carrier has no preference for recombination or re-trapping then it can be shown that following the one type of trap and one type of recombination centre assumptions, the thermoluminescence intensity is proportional to the square of the initial concentration of filled traps and is known as "second-order" thermoluminescence (see Chapter 2.3.5.1). In contrast to the "Randall and Watkins" model the glow curve arising from this model falls slightly more slowly than it rises. **This is typical of the shape of glow curves seen in the studies reported here.**

7.4.3 Activation energies determined by TL

In this work, the trap activation energies were determined from the thermoluminescence glow curves using the Initial Rise Method. [2] The activation energies determined consistently lie in the range 0.24(2) to 0.38(2) eV. In the early part of a glow peak, the depletion of trapped carriers is assumed to be negligible and the initial part of the glow curve can be approximated as $C\exp\left(-\frac{E_{Trap}}{k_B T}\right)$ independent of the "order" of the process. Accurate determination in the value of the activation energy from the initial rise part of the glow curve requires this emission to be free from any contribution from other glow peaks. In all samples studied, thermal cleaning results in glow curves with progressively higher activation energies, and the highest trap energy is consistent with depth of the neutral substitutional boron acceptor. **Thus, the thermal cleaning measurements suggest the presence of at least one other trap, with a lower trap energy.**

It is interesting to compare the results reported here with those on natural type IIb diamonds. Halperin and Nahum (1961) studied a natural type IIb diamond and found that following bandgap excitation below 100 K, the glow curve (heating rate 15 K/min) contained a weak peak at 140 K, an intense peak at 240 K (actually two overlapping peaks), another at 350 K and a shoulder near 420 K. [26] For the

240 K peak, the TL emission spectrum consisted of a broad band with a maximum at approximately 480 nm. Peak cleaning and the method of initial rise identified multiple activation energies from the glow curves in the range 140 - 253 K, the lowest at 0.20 eV and the highest at 0.37 eV. Similar results have subsequently been reported (see Table 7.1) on both natural and HPHT type IIb diamonds. Thus, there is considerable evidence for the shallow trap, and the new data in Chapter 5 indicates that the substitutional nitrogen donor is also an electron trap, with the trap level (N_S^-) approximately 0.2 eV below the bottom of the conduction band. This was previously discussed in Chapters 5 and 6.

7.4.4 "Blue-green" band observed in TL

Substitutional boron and nitrogen are ubiquitous impurities in near colourless HPHT diamond, and it was shown in Chapter 6.5.3.1 that the only plausible explanation for the long-lived "blue-green" phosphorescence observed in near colourless HPHT diamond was emission from N_S^0...B_S^0 close donor-acceptor pairs, reset with carriers released from isolated boron acceptors and a shallow donor, now identified N_S^- (see Chapter 5 and 6). Thus it is proposed that it is also the N_S^0...B_S^0 close donor-acceptor pairs that are the recombination centre for the "blue-green" band observed in thermoluminescence 7.9. It is unsurprising that this emission band is observed in both natural and lab-grown diamonds containing both nitrogen and boron substitutional impurities.

The average output power of the 375 nm laser (70 mW CW) is much higher than that of the 224 nm laser (average power < 0.1 mW; pulse width 100 μs, pulse frequency 10 Hz, peak power 50 mW), and since the energy of the 375 nm light is more than half of the bandgap energy of diamond, it is possible to pump electrons from the valence band to mid-gap levels, and subsequently pump from these levels to the conduction band. Although potentially relatively inefficient, this below bandgap excitation could facilitate production of isolated B_S^0, N_S^-, N_S^0, N_S^+ defects and give rise to the observed weak thermoluminescence from sufficiently close N_S^0...B_S^0 donor-acceptor pairs.

7.4.5 "Orange" band observed in TL

In samples Sino-01 and SYN4-10 the "blue-green" thermoluminescence band is accompanied by a broad "orange" emission band. In Sino-01 the relative intensities of the two bands are similar after 224 nm excitation (Fig 7.13(a)), whereas in SYN4-10 the "orange" band is considerably weaker than the "blue-green" band (Fig 7.14(a)). For both samples analysis of the glow curves using thermal cleaning and the method of initial rise indicates that there are at least two different trap energies, the largest of which is equal to that of the substitutional boron acceptor. The "orange" thermoluminescence glow curve peaks at higher temperatures than that for the "blue-green" emission. Interestingly, when sample SYN4-10 is excited with 375 nm light (3.31 eV) the relative intensity of the "blue-green" and "orange" thermoluminescence bands is reversed to that observed with 224 nm excitation, with "orange" band now much stronger. Analysis of the glow curves observed in sample SYN4-10 from both 224 nm and 375 nm excitation effectively give the same range of activation energies (0.32 - 0.38 eV). Thus, it can be inferred that one or even both of the traps responsible for the "blue-green" thermoluminescence band are also responsible for the "orange" band.

The origin of the "orange" thermoluminescence emission could be due to another type of donor-acceptor pair e.g. N_S...Z or B_S...Z, but this appears unlikely as the unknown impurity, Z, would need to be present in concentrations comparable to the nitrogen and/or boron impurities. An alternative explanation, based on emission from an unknown negatively charged defect following capture of a hole is proposed. First, the process of colour centre localised photoluminescence is reviewed. Optical pumping of a colour centre with light of energy below the bandgap, but sufficient to drive an internal (optical absorption) transition, can excite an electron from the ground to an excited state of a defect. This excited state relaxes with the emission of a photon and the electron returns to the ground state. In such a photoluminescence experiment the conduction band and valence bands can be ignored; the colour centre can be considered as an isolated atom like system.

Electroluminescence and cathodoluminescence from a colour centre involves trapping of carriers from the valence or conduction bands and is a more complicated process than photoluminescence. For example, it is known that the NV^- defect

can trap a hole from the valence band, which alters the charge state and electronic structure of the defect such that it arrives in an excited sate of NV^0 which relaxes via emission of a photon to the ground state of NV^0 as shown in figure 7.21. [33, 34] The neutral charge state NV^0 can trap an electron but when it does so it returns to the ground state of the NV^- defect and no emission is observed. Both NV^0 and NV^- have optical transitions between localised ground and excited states, but this is not a requirement for hole capture followed by emission. The negatively charged defect need only have one energy level in the band gap.

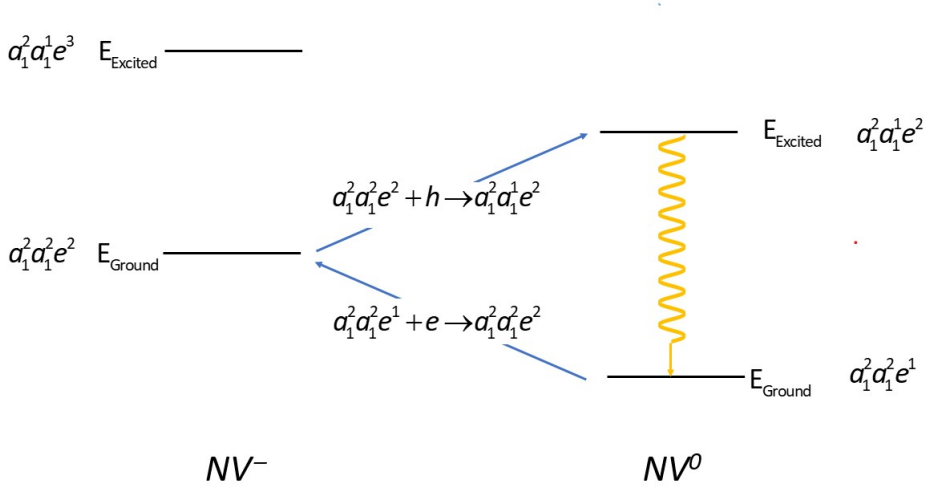

Figure 7.21: Schematic of luminescence from an NV centre involving trapping of carriers.

A possible explanation for the "orange" band thermoluminescence, phosphorescence (see Chapter 6.3 and 6.4) and luminescence (see Chapter 6.3 and 6.4) observed in Sino-01 and SYN4-10 can be postulated. Consider a defect labelled X, that can exist in two charge states X^- and X^0. On optical pumping with 375 or 224 nm light enable the defect X^0 to trap an electron excited from the valence band, or from $N_S{}^0$ via the conduction band (Figure 6.20 and 6.21 show that the related "orange" photoluminescence can be pumped with light up to a wavelength of approximately 440 nm/2.8 eV). This optical pumping also causes the concentration of $B_S{}^0$ to increase. At sufficiently low temperatures X^- is frozen after the light is removed. As the temperature increases, electrons are thermally excited to $B_S{}^0$, creating $B_S{}^-$ and the free holes in the valence band which can be trapped by X^- to produce X^0 in an excited electronic state that emits "orange" light when an electron returns to the ground state of X^0. The fact that no zero phonon

line is observed suggests that there is a large configurational change between the ground and excited state of X^0. The different wavelength dependence of the optical pumping of the $N_S{}^0...B_S{}^0$ donor-acceptor pairs and the defect X are clear from the change in intensity of the "blue-green" and "orange" TL peaks (Figure 7.14). The peak of the "orange" thermoluminescence glow curve is at a higher temperature than that of the "blue-green" emission from $N_S{}^0...B_S{}^0$ DAPs which is consistent with only the deeper trap ($B_S{}^0$) being involved in this emission.

What is the defect X? With the data available it is only possible to speculate. But given the presence of defects incorporating nickel in both Sino-01 and SYN4-10 but not the GE samples, it can be tentatively suggested that X is a nickel related defect. Even for HPHT diamond samples from an iron-cobalt solvent, trace contamination with nickel can results in the incorporation of a variety of nickel related defects. Both Sino-01 and SYN4-10 are brilliant cut gemstones, so it is impossible to determine which growth sectors the "orange" emission originates from, but it is clear that this emission is not uniform over the sample.

It should be noted that "red" phosphorescence band (Fig 6.24) has not yet been detected in thermoluminescence experiments.

7.5 Conclusion and future work

Neither of the simple first-order kinetics and second-order kinetics models is likely to be sufficient to fully explain the results reported in this chapter. The traps and luminescence centres in diamonds responsible for phosphorescence also play very similar roles in thermoluminescence due to the similar activation energy and spectral characteristics. It is noticeable that in thermoluminescence research, the depth of a trap is given according to TL glow peak, while the spectra can indicate the luminescence centre involved. The trap and luminescence centre are not necessarily in a one-to-one relationship. Charge carriers released from the same type of traps can recombine at different luminescence centres and give rise to various colours of thermoluminescence. One thermoluminescence band in spectra can also result from charge carriers released from different types of traps.

In all samples it appears that in addition to the boron acceptor, there is one

or more other shallow trap(s) (e.g. N_S^-) and probably significant re-trapping of thermal excited carriers. From the thermoluminescence measurements it cannot be determined whether the additional trap(s) is close the conduction or valence band (electron or hole trap). Nor is the frequency factor, concentration, or relative capture cross section of the lower energy trap known. In order to better determine the activation energy of the trap (or traps) which are shallower than the substitutional boron acceptor, further thermoluminescence studies are required utilising low temperature bandgap excitation varying levels of saturation, and different heating rates (especially those very much lower than used here). An electrical conductivity glow curve measurement may prove useful for the identification of traps. [26]

The "blue-green" thermoluminescence band observed is arise from the close pairs of $N_S{}^0...B_S{}^0$. Furthermore, in sample Sino-01 and SYN4-10 there are multiple recombination/luminescence centres. Further studies on single growth sectors in samples produced with known solvent chemistries, noting the preference for nickel incorporation in {111} growth sectors of HPHT diamond, should help with unravelling the identity of X. Furthermore, optically detected magnetic resonance (ODMR) could be useful in the identification of X, if a long-lived excited state had non-zero electronic spin. This state could then be detected by ODMR after optical excitation whereas the ground state cannot be detected by EPR or ODMR. [35]

The thermoluminescence experiment to study diamonds should also be further improved in following aspects: firstly, a more precise timing enables the calculating the proportion of distant pairs and close pairs of $N_S{}^0...B_S{}^0$ luminescence centres; secondly, a higher temperature range measurement would enable investigation of deeper traps in diamonds; thirdly, research on CVD diamond samples has been limited so far, where boron is not a major impurity.

Bibliography

[1] V. Chandrasekharan, in *Proceedings of the Indian Academy of Sciences-Section A*, Vol. 24 (Springer India, 1946) p. 187.

[2] S. W. S. McKeever, *Thermoluminescence of Solids*, Vol. 3 (Cambridge University Press, 1985).

[3] L. Paslovsky, J. E. Lowther, T. L. Nam, and R. J. Keddy, Journal of luminescence **55**, 167 (1993).

[4] E. Vittone, C. Manfredotti, F. Fizzotti, A. L. Giudice, P. Polesello, and V. Ralchenko, Diamond and Related Materials **8**, 1234 (1999).

[5] E. Borchi, C. Furetta, G. Kitis, C. Leroy, R. S. Sussmann, and A. J. Whitehead, Radiation Protection Dosimetry **65**, 291 (1996).

[6] A. Petitfils, F. Wrobel, M. Benabdesselam, P. Iacconi, and J. E. Butler, Diamond and Related Materials **16**, 1062 (2007).

[7] C. Furetta, G. Kitis, A. Brambilla, C. Jany, P. Bergonzo, and F. Foulon, Radiation Protection Dosimetry **84**, 201 (1999).

[8] V. Chernov, R. Meléndrez, S. Gastélum, M. Pedroza-Montero, T. Piters, S. Preciado-Flores, and M. Barboza-Flores, Physica Status Solidi (a) **210**, 2088 (2013).

[9] B. Gan, J. Ahn, Q. Zhang, S. F. Yoon, R. Meléndrez, and M. Barboza-Flores, Materials Letters **56**, 80 (2002).

[10] C. Descamps, D. Tromson, M. J. Guerrero, C. Mer, E. Rzepka, M. Nesladek, and P. Bergonzo, Diamond and Related Materials **15**, 833 (2006).

[11] M. I. Gil-Tolano, R. Meléndrez, S. Álvarez-García, D. Soto-Puebla, V. Chernov, and M. Barboza-Flores, Physica Status Solidi (a) **215**, 1800246 (2018).

[12] S. Mazzocchi, M. Bruzzi, M. Bucciolini, G. Cuttone, S. Pini, M. G. Sabini, and S. Sciortino, Nuclear Instruments and Methods in Physics Research Section A: Accelerators, Spectrometers, Detectors and Associated Equipment **476**, 713 (2002).

[13] P. S. Walsh, E. C. Lightowlers, and A. T. Collins, Journal of Luminescence **4**, 369 (1971).

[14] S. Eaton-Magaña, J. E. Post, P. J. Heaney, J. Freitas, P. Klein, R. Walters, and J. E. Butler, Geology **36**, 83 (2008).

[15] S. Eaton-Magaña and R. Lu, Diamond and Related Materials **20**, 983 (2011).

[16] T. Shao, F. Lyu, X. Guo, J. Zhang, H. Zhang, X. Hu, and A. H. Shen, Carbon **167**, 888 (2020).

[17] M. Benabdesselam, P. Iacconi, D. Briand, D. Lapraz, E. Gheeraert, and A. Deneuville, Diamond and Related Materials **9**, 56 (2000).

[18] K. Watanabe, S. C. Lawson, J. Isoya, H. Kanda, and Y. Sato, Diamond and Related Materials **6**, 99 (1997).

[19] U. F. S. D'Haenens-Johansson, A. Katrusha, K. S. Moe, P. Johnson, and W. Wang, Gems & Gemology **51**, 260 (2015).

[20] V. Chandrasekharan, in *Proceedings of the Indian Academy of Sciences-Section A*, Vol. 24 (Springer India, 1946) pp. 193–197.

[21] J. Nahum and A. Halperin, Journal of Physics and Chemistry of Solids **24**, 823 (1963).

[22] A. Halperin and R. Chen, Physical Review **148**, 839 (1966).

[23] J. Levinson, A. Halperin, and V. Bar, Journal of Luminescence **6**, 1 (1973).

[24] J. Bourgoin, B. Massarani, and R. Visocekas, Physical Review B **18**, 786 (1978).

[25] C. Bull and G. F. J. Garlick, Proceedings of the Physical Society. Section A **63**, 1283 (1950).

[26] A. Halperin and J. Nahum, Journal of Physics and Chemistry of Solids **18**, 297 (1961).

[27] A. J. J. Bos, Radiation measurements **41**, S45 (2006).

[28] S. Basun, G. F. Imbusch, D. D. Jia, and W. M. Yen, Journal of Luminescence **104**, 283 (2003).

[29] M. Benabdesselam, P. Iacconi, D. Briand, A. Berkane-Krachaï, E. Gheeraert, and H. Kanda, Journal of Applied Physics **88**, 4648 (2000).

[30] R. Chen and S. A. A. Winer, Journal of Applied Physics **41**, 5227 (1970).

[31] A. Dobrowolska, A. J. J. Bos, and P. Dorenbos, Journal of Physics D: Applied Physics **47**, 335301 (2014).

[32] C. M. Sunta, *Unraveling thermoluminescence*, Vol. 202 (Springer, 2014).

[33] M. Solà-Garcia, S. Meuret, T. Coenen, and A. Polman, ACS Photonics **7**, 232 (2019).

[34] N. Mizuochi, T. Makino, H. Kato, D. Takeuchi, M. Ogura, H. Okushi, M. Nothaft, P. Neumann, A. Gali, F. Jelezko, *et al.*, Nature Photonics **6**, 299 (2012).

[35] J. E. Wertz and J. R. Bolton, *Elementary theory and practical applications* (Springer, 1972).

Chapter 8

Conclusions

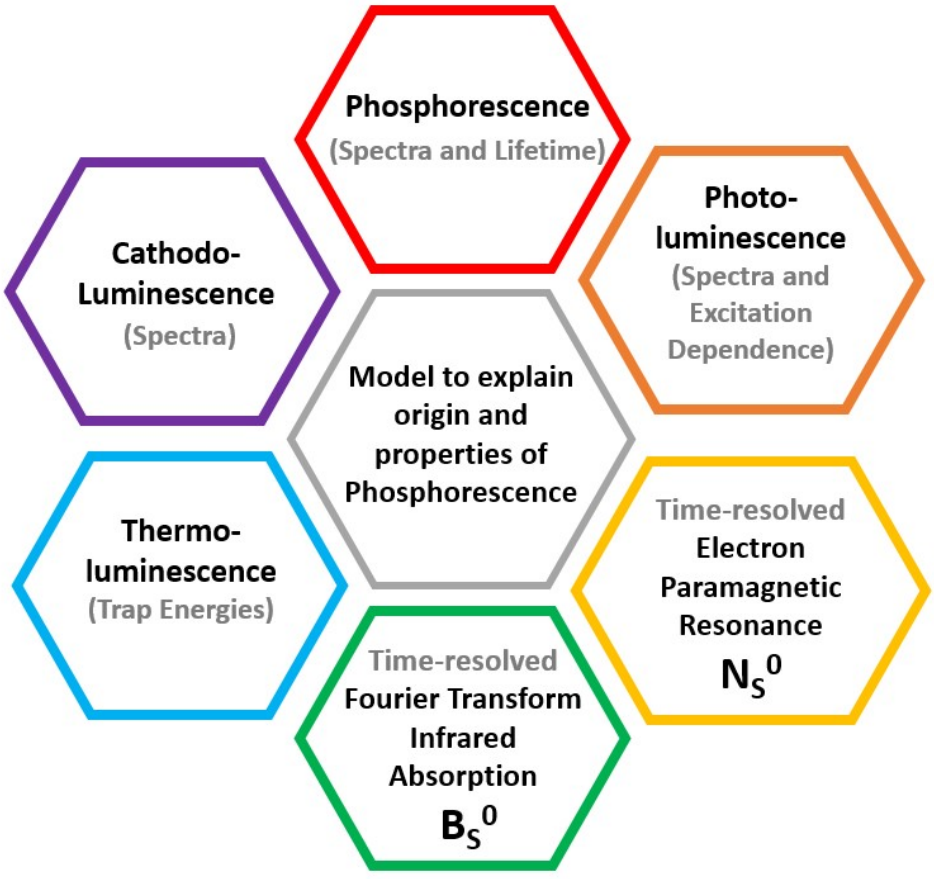

Figure 8.1: Summary of experimental techniques applied to study the physics of phosphorescence in diamond.

In this research, a combination of experimental techniques (Fig 8.1) has been utilised to investigate the physics of the phosphorescence observed from HPHT diamond. Cathodoluminescence and photoluminescence provide information about the emission spectra and their excitation dependence. Phosphorescence spectra

and lifetime measurements provide insights into the emission mechanism, and in combination with thermoluminescence studies reveal information about thermal activation of the emission processes. Finally, time-resolved FTIR absorption and EPR measurements are used to monitor the changes in concentrations of neutral boron acceptors and deep nitrogen donors during UV excitation and the phosphorescence emission.

The incorporation efficiency of substitutional boron (B_S) and substitutional nitrogen (N_S), along with other impurities such as nickel and silicon, is known to vary significantly between different growth sectors in HPHT synthetic diamonds. Studies on diamond samples containing combinations of growth sectors produce confusing results that are difficult to interpret. Hence in this thesis where possible studies have been performed on samples prepared from individual growth sectors.

8.1 Luminescence in GE samples

Cathodoluminescence spectra from both sectors cut from the same original sample (Fig 6.2) at room temperature and 80 K shows a strong emission band and the peak intensity shifts to lower energy as the temperature reduced.

From a 2D map of the intensity of the **photoluminescence** emission versus excitation energy (Fig 6.3), it is clear that in order to excite the "blue-green" emission, an excitation wavelength shorter than $\sim$ 235 nm is required. Interestingly this corresponds to the free exciton emission energy in diamond. It appears that excitation which produces free electrons and holes is required to give rise to the "blue-green" emission. Bandgap excitation is expected to neutralise donors and acceptors such that reasonably close donor-acceptor recombination pairs could emit.

The behaviour of "blue-green" **phosphorescence** in these samples can be summarised as follows:

- At low temperatures when there is negligible probability of thermal excitation of electrons and holes, there is still phosphorescence after UV illumination. The phosphorescence lifetime is independent of temperature (Fig 6.6), which is consistent with the tunneling of carriers between nearby acceptors or

donors. As the phosphorescence decays, the peak position of emission band does not shift and is centred around 2.25 eV (Fig 6.5).

- At high temperatures the phosphorescence lifetime reduces dramatically with increasing temperature (Fig 6.6). In this temperature range the thermal activation of carriers increases significantly. As the phosphorescence decays, the peak position does not shift and is centred at approximately 2.5 eV(Fig 6.5).

- At intermediate temperature as the phosphorescence decays, the peak position shifts to higher energies (Fig 6.5).

The spectra and lifetime data show that the dominant mechanism for charge transfer changes from tunneling at low temperatures to thermal activation at high temperatures.

The logarithmic plots of the phosphorescence lifetime as a function of reciprocal temperature (Fig 6.14 and 6.16) show the expected thermal activation behaviour (straight line) at high temperature. For the {111} sample where $[B_S] > [N_S]$, the activation energy obtained from the phosphorescence decay is shown in table 8.1. In this sample, the value determined approaches that expected for the thermal ionization energy of boron acceptor (0.37 eV). [1] However, in the {100} sample where $[N_S] > [B_S]$, the derived activation energy of phosphorescence shown in table 8.2 is lower.

Table 8.1: Activation energies of phosphorescence decay, TL glow peaks, $B_S{}^0$ decay, and $N_S{}^0$ decay after bandgap optical excitation in GE81-107a-C ({111} growth sector) where $[B_S] > [N_S]$.

E_A (eV)	Multiple components		MSE	CPL
	Component 1	Component 2		
Phosphorescence	0.31(3)	0.33(3)	0.34(1)	0.35(1)
Thermoluminescence	0.34(5)	0.37(5)		
$B_S{}^0$ decay	0.34(3)	0.41(5)	0.32(5)	0.35(3)
$N_S{}^0$ decay	0.18(5)	0.26(5)	0.18(3)	0.19(3)

Table 8.2: Activation energies of phosphorescence decay, TL glow peaks, B_S^0 decay, and N_S^0 recovery after bandgap optical excitation in GE81-107a-B ({001} growth sector) where $[N_S] > [B_S]$.

E_A (eV)	Multiple components		MSE	CPL
	Component 1	Component 2		
Phosphorescence	0.21(5)	0.23(5)	0.30(1)	0.25(1)
Thermoluminescence	0.30(5)	0.33(5)		
B_S^0 decay	0.32(3)	0.34(3)	0.32(5)	0.37(3)
N_S^0 recovery	0.18(2)	0.21(2)	0.22(5)	0.21(5)

When performing **thermoluminescence** measurements, at low temperatures the phosphorescence after the UV optical excitation decays away in approximately 15 minutes. A strong thermoluminescence glow peak can then be recorded when the sample is heated (Fig 7.6). Two conclusions can be drawn: firstly, as mentioned above, at low temperatures charge tunneling occurs and phosphorescence originates from donor-acceptor pairs; secondly, after this decay there is still a significant concentration of neutral donors and acceptors that are physically isolated. It is not until temperature is increased that these impurities are thermally ionized and release carriers that reset the close DAPs (luminescence centres), so they can emit multiple times and give rise to strong thermoluminescence.

In a thermoluminescence "cleaning" experiment (Fig 7.7) — where the sample is heated to just beyond the TL glow peak position, rapidly cooled and then heated again — a different activation energy is derived from the second peak, indicating that more than one trap contributes to the emission. Accurate trap energies are difficult to determine for closely overlapping peaks. The higher activation energy for the TL glow peaks in the sample where $[B_S] > [N_S]$ (Table 8.1) equates to that for the boron acceptor. The data from the other sample (Table 8.2) strongly suggests that there is also a lower energy trap. In addition, the thermoluminescence bands for the two TL glow peaks are at the same spectral position (Fig 7.10) which enables them to be assigned to the same luminescence centre.

8.2 Charge transfer in GE samples

As the temperature is increased, the concentration of neutral **boron** acceptors ($B_S{}^0$) decreases due to increased thermal excitation. The neutral boron acceptor infrared absorption spectra was taken whilst illuminated with 224 nm UV light minus the absorption spectrum recorded in the dark at different temperatures (Fig 4.7). UV illumination increases [$B_S{}^0$] but makes a smaller change as the temperature is increased. The neutral boron acceptor infrared absorption peak at 2802 cm^{-1} decays during phosphorescence after the 224 nm excitation is removed (Fig 4.9). The activation energies (Table 8.1 and 8.2) obtained from the temperature dependence of the decay curves are approximately the same for both samples and are close to the $B_S{}^0$ acceptor energy.

To measure the concentration of the neutral substitutional **nitrogen** defect in diamond, electron paramagnetic resonance has been used. In the sample where [B_S] > [N_S], UV illumination increases the concentration of the neutral substitutional nitrogen defect, and when the illumination is removed the concentration decays back to the value measured in the dark. The decay time decreases with increasing temperature (Fig 5.6). The activation energy for [$N_S{}^0$] decay was obtained over a temperature range when thermal activation and carrier tunnelling both contributed significantly, therefore, it is underestimated (Table 8.1).

In the sample where [N_S] > [B_S], UV illumination decreases the concentration of neutral substitutional nitrogen defect, and when the illumination is removed the concentration recovers back to the value measured in the dark. The recovery time decreases with increasing temperature above RT (Fig 5.12).

If the substitutional nitrogen defect can only exist in neutral charge state and positive charge state, the concentration of the neutral substitutional nitrogen is always expected to be increased (or not changed) by the UV excitation in a sample containing only appearable quantities of substitutional nitrogen and boron defects. However, the fact is that this is not the case reveals that upon UV illumination another charge state is produced. Therefore, it can be proposed that the substitutional nitrogen defect has trapped an electron to produce $N_S{}^-$. The "acceptor level" of the substitutional nitrogen defect has been proposed previously by Jones *et al.* [2]. Analysis of the temperature dependence of the recovery of the

neutral substitutional nitrogen defect indicates that this "acceptor level" is only approximately 0.2 eV below the conduction band minimum (Table 8.2). When N_S^- is thermally ionized the released electron can be trapped by N_S^+ and thus the concentration of N_S^0 can be increased. When boron acceptors are present after UV illumination is removed DAP recombination will act to reduce the concentration of neutral and negatively charged substitutional nitrogen.

Several conclusions about the charge transfer processes can be drawn from the above that:

- For the substitutional nitrogen defect three charge states have to be considered: negative, neutral, and positive. The total concentration of substitutional nitrogen is given by

$$N_T = N_S^- + N_S^0 + N_S^+ \tag{8.1}$$

- For the substitutional boron defect, only the neutral and negatively charged states should be considered. The total concentration of substitutional boron is given by

$$B_T = B_S^- + B_S^0 \tag{8.2}$$

- In diamond containing only substitutional nitrogen and boron impurities, both tunneling and thermal excitation of carriers have to be considered.

- UV excitation creates electrons in the CB and holes in the VB:

$$h\omega_{BG} \rightarrow e^- + h^+ \tag{8.3}$$

- UV excitation will increase the concentration of neutral substitutional boron acceptors:

$$B_S^- + h^+ \rightarrow B_S^0 \tag{8.4}$$

- UV excitation can either increase

$$N_S^+ + e^- \rightarrow N_S^0 \tag{8.5}$$

or decrease

$$N_S{}^0 + e^- \rightarrow N_S{}^- \tag{8.6}$$

$$2N_S{}^0 \overset{h\omega}{\rightarrow} N_S{}^+ + N_S{}^- \tag{8.7}$$

the concentration of neutral substitutional nitrogen and produces negatively charged substitutional nitrogen defects.

- The neutral substitutional nitrogen is a deep donor and at the temperatures studied here is not thermally ionized. However, the negatively charged substitutional nitrogen is readily thermally ionized over a temperature range which overlaps with that for thermal ionization of the neutral boron acceptor. At low temperature where there is negligible thermal ionization, charge carrier tunneling must be considered. Therefore, after UV excitation:

$$N_S{}^- \rightarrow N_S{}^0 + e^- \quad \text{(Tunneling/Thermally excited into CB)} \tag{8.8}$$

$$N_S{}^+ + N_S{}^- \rightarrow 2N_S{}^0 \quad \text{(Tunneling)} \tag{8.9}$$

$$B_S{}^0 \rightarrow B_S{}^- + h^+ \quad \text{(Tunneling/Thermally released into VB)} \tag{8.10}$$

- Charge balance:

$$[N_S{}^-] + [B_S{}^-] = [N_S{}^+] \tag{8.11}$$

8.3 "Blue-green" phosphorescence mechanism

The "blue-green" phosphorescence spectrum, lifetime, and intensity vary between growth sectors. Therefore, it is important to study individual growth sectors. The mechanism of phosphorescence in diamond varies with temperature:

- In the low temperature range, tunneling dominates and the lifetime of phosphorescence is temperature independent.

- In the high temperature range, thermal process dominates and phosphorescence is temperature dependent.
- In the intermediate temperature range, both tunnelling and thermal excitation process contribute.

B_S^0 is a relatively shallow acceptor. N_S^- is a shallow trap. They can provide an electron or a hole to enable emission from a "ready-to-emit" luminescence centre, which in this is a donor-acceptor pair with donor and acceptor both in neutral charge state (N_S^0...B_S^0). The electron can be transferred from the donor to the acceptor and give rise to phosphorescence, to produce a positively charged donor and negatively charged acceptor.

$$N_S^0 + B_S^0 \rightarrow N_S^+ + B_S^- \tag{8.12}$$

Once a neutral donor-acceptor pair has emitted, both electron and hole capture (regardless the order) are required to enable to pair the emit again as shown in figure 8.2. By resetting the charge states of the donor and the acceptor, it is possible for each luminescence centre to emit multiple times.

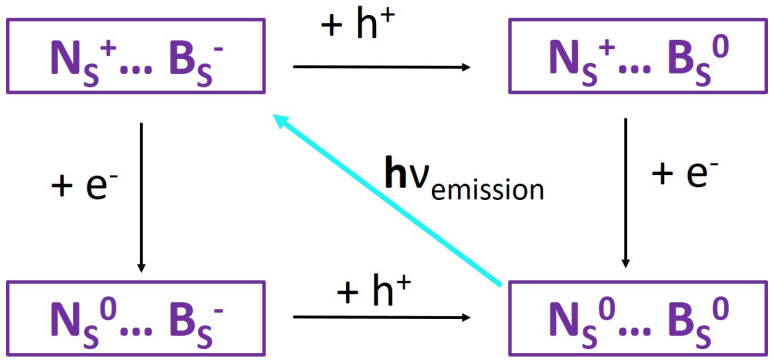

Figure 8.2: Schematic of the reset of N_S^0...B_S^0 luminescence centre.

The identification of the "blue-green" luminescence centre with N_S^0...B_S^0 DAP recombination is logical since N_S and B_S are the most abundant defects/impurities in near colourless HPHT diamond. This has been mentioned in [3]. The "blue-green" emission is observed in all the samples studied in this work and would also be expected in CVD and natural diamonds co-doped with N_S and B_S.

This assignment has previously been ruled out or overlooked because the configurational change when N_S^0 is ionized to N_S^+ was not considered. For N_S^0 this is expected to be large, and must be considered. [4]

The energy of the photon emitted from substitutional nitrogen donor and substitutional boron acceptor pair ($N_S{}^0...B_S{}^0$) in diamond is given by

$$h\nu = E_g - (E_D + E_A) - \Delta^g_{FC} + \Delta E_C \tag{8.13}$$

where $E_g = 5.47$ eV, $E_D = 1.7$ eV, $E_A = 0.37$ eV, Δ^g_{FC} is the Frank-Condon shift, and ΔE_C is the correction term. For the neutral substitutional nitrogen donor there is a strong electron-phonon coupling, which results in a Frank-Condon shift of the emission to lower energy by approximately 1.2 eV. [3] The energy at which a $N_S{}^0...B_S{}^0$ pair emits depends on the separation of the nitrogen donor and the boron acceptor, with the Coulomb correction term increasing as the separation between the donor and acceptor decreases. Statistically there will be very few close pairs. The emission probability is higher for close pairs, thus the lifetime is shorter. At low temperatures when there is no thermal activation of carriers, the emission will be dominated by distant pairs, and the majority of pairs will emit only once. Thus the peak emission will be at slightly lower energies (2.25 eV). As the temperature increases, the probability of thermal ionization increases and closer pairs can be reset by charge capture and emit multiple times. Furthermore, the long-lived distant pairs will be increasingly ionized before they can emit. Thus the emission peak will shift to higher energies (reach 2.5 eV) as the temperature is increased. The magnitude of the shift observed is 0.25 eV, which is consistent with the Coulomb correction term.

There is expected to only be a small configuration change between $N_S{}^0$ and $N_S{}^-$. The emission from a $N_S{}^-...B_S{}^0$ pair is expected to be in the UV range. If the Frank-Condon shift for this emission were $\sim$ 1.2 - 1.7 eV, we estimate the DAP peak from $N_S{}^-...B_S{}^0$ to be at $\sim$ 3.2 - 3.7 eV.

8.4 "Orange" and "red" luminescence bands

The additional luminescence bands observed in samples Sino-01 and SYN4-10 will require further study in single growth sector samples in order to identify the defect(s) responsible. It appears that for both the "orange" and "red" bands (see Chapter 6.5.4 and 7.4.5) the phosphorescence is stimulated by capture of a hole released (tunneling or via thermal excitation and VB) from the boron acceptor, such a mechanism has been seen before in cathodoluminescence and electroluminescence of NV centres. The NV^- centre captures a hole and arrives in an excited state of NV^0 and subsequently emits a photon. The vibronic structure observed at low temperature for the "red" band supports the assignment of the capture plus emission for an isolated defect. The mechanism is less clear for the "orange" emission band, and although this could arise from a different DAP (i.e. not $N_S^-...B_S^0$), a similar mechanism to that for the "red" emission is perhaps more likely. It is possible that the "orange" and "red" bands originate from nickel related defects although other impurities could be involved.

Bibliography

[1] A. T. Collins and A. W. S. Williams, Journal of Physics C: Solid State Physics **4**, 1789 (1971).

[2] R. Jones, J. P. Goss, and P. R. Briddon, Physical Review B **80**, 033205 (2009).

[3] P. Ščajev, L. Trinkler, B. Berzina, E. Ivakin, and K. Jarašiūnas, Diamond and Related Materials **36**, 35 (2013).

[4] A. Alkauskas, M. D. McCluskey, and C. G. Van de Walle, Journal of Applied Physics **119**, 181101 (2016).

Appendix A

DAP distances in diamond

Table A.1: The calculation of distances R between donor-acceptor pair in diamond lattice for both type I and type II geometry sites and the statistical abundance N_R. One atom locates at $\langle 0,0,0\rangle$ site, and the other is shown in the table. There are no atoms for shell number m equal to 28, 60, 92, 112, 124, 156, 188, 220, 240, 252, 284 when $m \leq 300$.

Shell number	**R (nm)**	**Lattice vector**	N_R
1	0.154	$\langle 1,1,1\rangle$	4
2	0.252	$\langle 2,2,0\rangle$	12
3	0.296	$\langle 3,1,1\rangle$	12
4	0.357	$\langle 4,0,0\rangle$	6
5	0.389	$\langle 3,3,1\rangle$	12
6	0.437	$\langle 4,2,2\rangle$	24
7a	0.463	$\langle 5,1,1\rangle$	12
7b	0.463	$\langle 3,3,3\rangle$	4
8	0.504	$\langle 4,4,0\rangle$	12
9	0.528	$\langle 5,3,1\rangle$	24
10	0.564	$\langle 6,2,0\rangle$	24
11	0.585	$\langle 5,3,3\rangle$	12
12	0.618	$\langle 4,4,4\rangle$	8
13a	0.637	$\langle 5,5,1\rangle$	12

13b	0.637	$\langle 7,1,1\rangle$	12
14	0.667	$\langle 6,4,2\rangle$	48
15a	0.685	$\langle 7,3,1\rangle$	24
15b	0.685	$\langle 5,5,3\rangle$	12
16	0.713	$\langle 8,0,0\rangle$	6
17	0.730	$\langle 7,3,3\rangle$	12
18a	0.757	$\langle 8,2,2\rangle$	24
18b	0.757	$\langle 6,6,0\rangle$	12
19a	0.772	$\langle 7,5,1\rangle$	24
19b	0.772	$\langle 5,5,5\rangle$	4
20	0.798	$\langle 8,4,0\rangle$	24
21a	0.812	$\langle 7,5,3\rangle$	24
21b	0.812	$\langle 9,1,1\rangle$	12
22	0.837	$\langle 6,6,4\rangle$	24
23	0.851	$\langle 9,3,1\rangle$	24
24	0.874	$\langle 8,4,4\rangle$	24
25a	0.887	$\langle 7,7,1\rangle$	12
25b	0.887	$\langle 9,3,3\rangle$	12
25c	0.887	$\langle 7,5,5\rangle$	12
26a	0.909	$\langle 10,2,0\rangle$	24
26b	0.909	$\langle 8,6,2\rangle$	48
27a	0.922	$\langle 9,5,1\rangle$	24
27b	0.922	$\langle 7,7,3\rangle$	12
28			
29	0.956	$\langle 9,5,3\rangle$	24
30	0.977	$\langle 10,4,2\rangle$	48
31a	0.989	$\langle 7,7,5\rangle$	12

31b	0.989	$\langle 11, 1, 1\rangle$	12
32	1.009	$\langle 8, 8, 0\rangle$	12
33a	1.021	$\langle 9, 7, 1\rangle$	24
33b	1.021	$\langle 9, 5, 5\rangle$	12
33c	1.021	$\langle 11, 3, 1\rangle$	24
34a	1.040	$\langle 10, 6, 0\rangle$	24
34b	1.040	$\langle 8, 6, 6\rangle$	24
35a	1.051	$\langle 9, 7, 3\rangle$	24
35b	1.051	$\langle 11, 3, 3\rangle$	12
36a	1.070	$\langle 8, 8, 4\rangle$	24
36b	1.070	$\langle 12, 0, 0\rangle$	6
37a	1.081	$\langle 11, 5, 1\rangle$	24
37b	1.081	$\langle 7, 7, 7\rangle$	4
38a	1.099	$\langle 12, 2, 2\rangle$	24
38b	1.099	$\langle 10, 6, 4\rangle$	48
39a	1.110	$\langle 11, 5, 3\rangle$	24
39b	1.110	$\langle 9, 7, 5\rangle$	24
40	1.128	$\langle 12, 4, 0\rangle$	24
41	1.139	$\langle 9, 9, 1\rangle$	12
42	1.156	$\langle 10, 8, 2\rangle$	48
43a	1.166	$\langle 11, 7, 1\rangle$	24
43b	1.166	$\langle 9, 9, 3\rangle$	12
43c	1.166	$\langle 11, 5, 5\rangle$	12
43d	1.166	$\langle 13, 1, 1\rangle$	12
44	1.183	$\langle 12, 4, 4\rangle$	24
45a	1.193	$\langle 11, 7, 3\rangle$	24
45b	1.193	$\langle 9, 7, 7\rangle$	12

45c	1.193	$\langle 13, 3, 1\rangle$	24
46	1.210	$\langle 12, 6, 2\rangle$	48
47a	1.219	$\langle 9, 9, 5\rangle$	12
47b	1.219	$\langle 13, 3, 3\rangle$	12
48	1.236	$\langle 8, 8, 8\rangle$	8
49a	1.245	$\langle 11, 7, 5\rangle$	24
49b	1.245	$\langle 13, 5, 1\rangle$	24
50a	1.261	$\langle 14, 2, 0\rangle$	24
50b	1.261	$\langle 10, 10, 0\rangle$	12
50c	1.261	$\langle 10, 8, 6\rangle$	48
51a	1.271	$\langle 11, 9, 1\rangle$	24
51b	1.271	$\langle 13, 5, 3\rangle$	24
52	1.286	$\langle 12, 8, 0\rangle$	24
53a	1.295	$\langle 11, 9, 3\rangle$	24
53b	1.295	$\langle 9, 9, 7\rangle$	12
54a	1.311	$\langle 14, 4, 2\rangle$	48
54b	1.311	$\langle 12, 6, 6\rangle$	24
54c	1.311	$\langle 10, 10, 4\rangle$	24
55a	1.320	$\langle 13, 7, 1\rangle$	24
55b	1.320	$\langle 13, 5, 5\rangle$	12
55c	1.320	$\langle 11, 7, 7\rangle$	12
56	1.335	$\langle 12, 8, 4\rangle$	48
57a	1.344	$\langle 13, 7, 3\rangle$	24
57b	1.344	$\langle 11, 9, 5\rangle$	24
57c	1.344	$\langle 15, 1, 1\rangle$	12
58	1.358	$\langle 14, 6, 0\rangle$	24
59	1.367	$\langle 15, 3, 1\rangle$	24

60			
61a	1.390	$\langle 11, 11, 1\rangle$	12
61b	1.390	$\langle 13, 7, 5\rangle$	24
61c	1.390	$\langle 9, 9, 9\rangle$	4
61d	1.390	$\langle 15, 3, 3\rangle$	12
62a	1.404	$\langle 14, 6, 4\rangle$	48
62b	1.404	$\langle 12, 10, 2\rangle$	48
63a	1.413	$\langle 15, 5, 1\rangle$	24
63b	1.413	$\langle 13, 9, 1\rangle$	24
63c	1.413	$\langle 11, 11, 3\rangle$	12
63d	1.413	$\langle 11, 9, 7\rangle$	24
64	1.427	$\langle 16, 0, 0\rangle$	6
65a	1.435	$\langle 13, 9, 3\rangle$	24
65b	1.435	$\langle 15, 5, 3\rangle$	24
66a	1.449	$\langle 16, 2, 2\rangle$	24
66b	1.449	$\langle 14, 8, 2\rangle$	48
66c	1.449	$\langle 10, 10, 8\rangle$	24
67a	1.457	$\langle 11, 11, 5\rangle$	12
67b	1.457	$\langle 13, 7, 7\rangle$	12
68a	1.471	$\langle 16, 4, 0\rangle$	24
68b	1.471	$\langle 12, 8, 8\rangle$	24
69a	1.479	$\langle 13, 9, 5\rangle$	24
69b	1.479	$\langle 15, 7, 1\rangle$	24
69c	1.479	$\langle 15, 5, 5\rangle$	12
70	1.492	$\langle 12, 10, 6\rangle$	48
71a	1.500	$\langle 15, 7, 3\rangle$	24
71b	1.500	$\langle 11, 9, 9\rangle$	12

72a	1.513	$\langle 16, 4, 4\rangle$	24
72b	1.513	$\langle 12, 12, 0\rangle$	12
73a	1.521	$\langle 13, 11, 1\rangle$	24
73b	1.521	$\langle 11, 11, 7\rangle$	12
73c	1.521	$\langle 17, 1, 1\rangle$	12
74a	1.534	$\langle 16, 6, 2\rangle$	48
74b	1.534	$\langle 14, 10, 0\rangle$	24
74c	1.534	$\langle 14, 8, 6\rangle$	48
75a	1.542	$\langle 13, 11, 3\rangle$	24
75b	1.542	$\langle 15, 7, 5\rangle$	24
75c	1.542	$\langle 13, 9, 7\rangle$	24
75d	1.542	$\langle 17, 3, 1\rangle$	24
76	1.555	$\langle 12, 12, 4\rangle$	24
77a	1.562	$\langle 15, 9, 1\rangle$	24
77b	1.562	$\langle 17, 3, 3\rangle$	12
78	1.575	$\langle 14, 10, 4\rangle$	48
79a	1.583	$\langle 15, 9, 3\rangle$	24
79b	1.583	$\langle 13, 11, 5\rangle$	24
79c	1.583	$\langle 17, 5, 1\rangle$	24
80	1.595	$\langle 16, 8, 0\rangle$	24
81a	1.603	$\langle 15, 7, 7\rangle$	12
81b	1.603	$\langle 11, 11, 9\rangle$	12
81c	1.603	$\langle 17, 5, 3\rangle$	24
82a	1.615	$\langle 18, 2, 0\rangle$	24
82b	1.615	$\langle 16, 6, 6\rangle$	24
83a	1.622	$\langle 15, 9, 5\rangle$	24
83b	1.622	$\langle 13, 9, 9\rangle$	12

84	1.635	$\langle 16, 8, 4\rangle$	48
85a	1.642	$\langle 13, 13, 1\rangle$	12
85b	1.642	$\langle 13, 11, 7\rangle$	24
85c	1.642	$\langle 17, 7, 1\rangle$	24
85d	1.642	$\langle 17, 5, 5\rangle$	12
86a	1.654	$\langle 18, 4, 2\rangle$	48
86b	1.654	$\langle 14, 12, 2\rangle$	48
86c	1.654	$\langle 12, 10, 10\rangle$	24
87a	1.661	$\langle 15, 11, 1\rangle$	24
87b	1.661	$\langle 13, 13, 3\rangle$	12
87c	1.661	$\langle 17, 7, 3\rangle$	24
88	1.673	$\langle 12, 12, 8\rangle$	24
89a	1.680	$\langle 15, 11, 3\rangle$	24
89b	1.680	$\langle 15, 9, 7\rangle$	24
90a	1.692	$\langle 18, 6, 0\rangle$	24
90b	1.692	$\langle 16, 10, 2\rangle$	48
90c	1.692	$\langle 14, 10, 8\rangle$	48
91a	1.699	$\langle 13, 13, 5\rangle$	12
91b	1.699	$\langle 17, 7, 5\rangle$	24
91c	1.699	$\langle 19, 1, 1\rangle$	12
91d	1.699	$\langle 11, 11, 11\rangle$	4
92			
93a	1.718	$\langle 15, 11, 5\rangle$	24
93b	1.718	$\langle 17, 9, 1\rangle$	24
93c	1.718	$\langle 19, 3, 1\rangle$	24
93d	1.718	$\langle 13, 11, 9\rangle$	24
94a	1.729	$\langle 18, 6, 4\rangle$	48

94b	1.729	$\langle 14, 12, 6\rangle$	48
95a	1.736	$\langle 17, 9, 3\rangle$	24
95b	1.736	$\langle 19, 3, 3\rangle$	12
96	1.747	$\langle 16, 8, 8\rangle$	24
97a	1.754	$\langle 13, 13, 7\rangle$	12
97b	1.754	$\langle 17, 7, 7\rangle$	12
97c	1.754	$\langle 19, 5, 1\rangle$	24
97d	1.754	$\langle 15, 9, 9\rangle$	12
98a	1.766	$\langle 18, 8, 2\rangle$	48
98b	1.766	$\langle 16, 10, 6\rangle$	48
98c	1.766	$\langle 14, 14, 0\rangle$	12
99a	1.772	$\langle 15, 13, 1\rangle$	24
99b	1.772	$\langle 17, 9, 5\rangle$	24
99c	1.772	$\langle 19, 5, 3\rangle$	24
99d	1.772	$\langle 15, 11, 7\rangle$	24
100a	1.784	$\langle 20, 0, 0\rangle$	6
100b	1.784	$\langle 16, 12, 0\rangle$	24
101	1.790	$\langle 15, 13, 3\rangle$	24
102a	1.801	$\langle 20, 2, 2\rangle$	24
102b	1.801	$\langle 14, 14, 4\rangle$	24
103a	1.808	$\langle 13, 11, 11\rangle$	12
103b	1.808	$\langle 19, 7, 1\rangle$	24
103c	1.808	$\langle 19, 5, 5\rangle$	12
103d	1.808	$\langle 17, 11, 1\rangle$	24
104a	1.819	$\langle 20, 4, 0\rangle$	24
104b	1.819	$\langle 16, 12, 4\rangle$	48
105a	1.825	$\langle 17, 11, 3\rangle$	24

105b	1.825	$\langle 17, 9, 7\rangle$	24
105c	1.825	$\langle 15, 13, 5\rangle$	24
105d	1.825	$\langle 17, 9, 7\rangle$	24
105e	1.825	$\langle 19, 7, 3\rangle$	24
105f	1.825	$\langle 13, 13, 9\rangle$	12
106a	1.836	$\langle 18, 10, 0\rangle$	24
106b	1.836	$\langle 18, 8, 6\rangle$	48
107	1.843	$\langle 15, 11, 9\rangle$	24
108a	1.853	$\langle 20, 4, 4\rangle$	24
108b	1.853	$\langle 12, 12, 12\rangle$	8
109a	1.860	$\langle 17, 11, 5\rangle$	24
109b	1.860	$\langle 19, 7, 5\rangle$	24
110a	1.871	$\langle 20, 6, 2\rangle$	48
110b	1.871	$\langle 18, 10, 4\rangle$	48
110c	1.871	$\langle 14, 12, 10\rangle$	48
111a	1.877	$\langle 21, 1, 1\rangle$	12
111b	1.877	$\langle 19, 9, 1\rangle$	24
111c	1.877	$\langle 15, 13, 7\rangle$	24
112			
113a	1.894	$\langle 21, 3, 1\rangle$	24
113b	1.894	$\langle 19, 9, 3\rangle$	24
113c	1.894	$\langle 17, 9, 9\rangle$	12
113d	1.894	$\langle 15, 15, 1\rangle$	12
114a	1.904	$\langle 16, 14, 2\rangle$	48
114b	1.904	$\langle 16, 10, 10\rangle$	24
114c	1.904	$\langle 14, 14, 8\rangle$	24
115a	1.911	$\langle 21, 3, 3\rangle$	12

115b	1.911	$\langle 19, 7, 7\rangle$	12
115c	1.911	$\langle 17, 13, 1\rangle$	24
115d	1.911	$\langle 17, 11, 7\rangle$	24
115e	1.911	$\langle 15, 15, 3\rangle$	12
115f	1.911	$\langle 13, 13, 11\rangle$	12
116a	1.921	$\langle 20, 8, 0\rangle$	24
116b	1.921	$\langle 16, 12, 8\rangle$	48
117a	1.927	$\langle 21, 5, 1\rangle$	24
117b	1.927	$\langle 19, 9, 5\rangle$	24
117c	1.927	$\langle 17, 13, 3\rangle$	24
117d	1.927	$\langle 15, 11, 11\rangle$	12
118a	1.937	$\langle 20, 6, 6\rangle$	24
118b	1.937	$\langle 18, 12, 2\rangle$	48
119a	1.944	$\langle 21, 5, 3\rangle$	24
119b	1.944	$\langle 15, 15, 5\rangle$	12
119c	1.944	$\langle 15, 13, 9\rangle$	24
120	1.954	$\langle 20, 8, 4\rangle$	48
121a	1.960	$\langle 17, 13, 5\rangle$	24
121b	1.960	$\langle 19, 11, 1\rangle$	24
122a	1.970	$\langle 22, 2, 0\rangle$	24
122b	1.970	$\langle 18, 10, 8\rangle$	48
122c	1.970	$\langle 16, 14, 6\rangle$	48
123a	1.976	$\langle 21, 7, 1\rangle$	24
123b	1.976	$\langle 21, 5, 5\rangle$	12
123c	1.976	$\langle 19, 11, 3\rangle$	24
123d	1.976	$\langle 19, 9, 7\rangle$	24
123e	1.976	$\langle 17, 11, 9\rangle$	24

124			
125a	1.992	$\langle 21, 7, 3\rangle$	24
125b	1.992	$\langle 15, 15, 7\rangle$	12
126a	2.002	$\langle 22, 4, 2\rangle$	48
126b	2.002	$\langle 20, 10, 2\rangle$	48
126c	2.002	$\langle 18, 12, 6\rangle$	48
127a	2.008	$\langle 19, 11, 5\rangle$	24
127b	2.008	$\langle 17, 13, 7\rangle$	24
127c	2.008	$\langle 13, 13, 13\rangle$	4
128	2.018	$\langle 16, 16, 0\rangle$	12
129a	2.024	$\langle 21, 7, 5\rangle$	24
129b	2.024	$\langle 17, 15, 1\rangle$	24
129c	2.024	$\langle 15, 13, 11\rangle$	24
130a	2.034	$\langle 22, 6, 0\rangle$	24
130b	2.034	$\langle 18, 14, 0\rangle$	24
131a	2.039	$\langle 21, 9, 1\rangle$	24
131b	2.039	$\langle 19, 9, 9\rangle$	12
131c	2.039	$\langle 17, 15, 3\rangle$	24
132a	2.049	$\langle 20, 8, 8\rangle$	24
132b	2.049	$\langle 16, 16, 4\rangle$	24
133a	2.055	$\langle 23, 1, 1\rangle$	12
133b	2.055	$\langle 21, 9, 3\rangle$	24
133c	2.055	$\langle 19, 13, 1\rangle$	24
133d	2.055	$\langle 19, 11, 7\rangle$	24
133e	2.055	$\langle 17, 11, 11\rangle$	12
133f	2.055	$\langle 15, 15, 9\rangle$	12
134a	2.065	$\langle 22, 6, 4\rangle$	48

134b	2.065	$\langle 20, 10, 6\rangle$	48
134c	2.065	$\langle 18, 14, 4\rangle$	48
134d	2.065	$\langle 14, 14, 12\rangle$	24
135a	2.070	$\langle 23, 3, 1\rangle$	24
135b	2.070	$\langle 21, 7, 7\rangle$	12
135c	2.070	$\langle 19, 13, 3\rangle$	24
135d	2.070	$\langle 17, 15, 5\rangle$	24
135e	2.070	$\langle 17, 13, 9\rangle$	24
136a	2.080	$\langle 20, 12, 0\rangle$	24
136b	2.080	$\langle 16, 12, 12\rangle$	24
137a	2.086	$\langle 23, 3, 3\rangle$	12
137b	2.086	$\langle 21, 9, 5\rangle$	24
138a	2.095	$\langle 22, 8, 2\rangle$	48
138b	2.095	$\langle 16, 14, 10\rangle$	48
139a	2.101	$\langle 23, 5, 1\rangle$	24
139b	2.101	$\langle 19, 13, 5\rangle$	24
140	2.110	$\langle 20, 12, 4\rangle$	48
141a	2.116	$\langle 23, 5, 3\rangle$	24
141b	2.116	$\langle 21, 11, 1\rangle$	24
141c	2.116	$\langle 19, 11, 9\rangle$	24
141d	2.116	$\langle 17, 15, 7\rangle$	24
141e	2.116	$\langle 15, 13, 13\rangle$	12
142	2.125	$\langle 18, 12, 10\rangle$	48
143a	2.131	$\langle 21, 11, 3\rangle$	24
143b	2.131	$\langle 21, 9, 7\rangle$	24
143c	2.131	$\langle 15, 15, 11\rangle$	12
144a	2.140	$\langle 24, 0, 0\rangle$	6

144b	2.140	$\langle 16, 16, 8\rangle$	24
145a	2.146	$\langle 23, 7, 1\rangle$	24
145b	2.146	$\langle 23, 5, 5\rangle$	12
145c	2.146	$\langle 19, 13, 7\rangle$	24
145d	2.146	$\langle 17, 17, 1\rangle$	12
145e	2.146	$\langle 17, 13, 11\rangle$	24
146a	2.155	$\langle 24, 2, 2\rangle$	24
146b	2.155	$\langle 22, 10, 0\rangle$	24
146c	2.155	$\langle 22, 8, 6\rangle$	48
146d	2.155	$\langle 18, 16, 2\rangle$	48
146e	2.155	$\langle 18, 14, 8\rangle$	48
147a	2.161	$\langle 23, 7, 3\rangle$	24
147b	2.161	$\langle 21, 11, 5\rangle$	24
147c	2.161	$\langle 19, 15, 1\rangle$	24
147d	2.161	$\langle 17, 17, 3\rangle$	12
148	2.170	$\langle 24, 4, 0\rangle$	24
149a	2.175	$\langle 19, 15, 3\rangle$	24
149b	2.175	$\langle 17, 15, 9\rangle$	24
150a	2.184	$\langle 22, 10, 4\rangle$	48
150b	2.184	$\langle 20, 14, 2\rangle$	48
150c	2.184	$\langle 20, 10, 10\rangle$	24
151a	2.190	$\langle 23, 7, 5\rangle$	24
151b	2.190	$\langle 21, 9, 9\rangle$	12
151c	2.190	$\langle 19, 11, 11\rangle$	12
151d	2.190	$\langle 17, 17, 5\rangle$	12
152a	2.199	$\langle 24, 4, 4\rangle$	24
152b	2.199	$\langle 20, 12, 8\rangle$	48

153a	2.204	$\langle 23, 9, 1\rangle$	24
153b	2.204	$\langle 21, 13, 1\rangle$	24
153c	2.204	$\langle 21, 11, 7\rangle$	24
153d	2.204	$\langle 19, 15, 5\rangle$	24
153e	2.204	$\langle 19, 13, 9\rangle$	24
154a	2.213	$\langle 24, 6, 2\rangle$	48
154b	2.213	$\langle 18, 16, 6\rangle$	48
155a	2.219	$\langle 23, 9, 3\rangle$	24
155b	2.219	$\langle 21, 13, 3\rangle$	24
155c	2.219	$\langle 15, 15, 13\rangle$	12
156			
157a	2.233	$\langle 25, 1, 1\rangle$	12
157b	2.233	$\langle 23, 7, 7\rangle$	12
157c	2.233	$\langle 17, 17, 7\rangle$	12
157d	2.233	$\langle 17, 13, 13\rangle$	12
158a	2.242	$\langle 22, 12, 2\rangle$	48
158b	2.242	$\langle 20, 14, 6\rangle$	48
159a	2.247	$\langle 25, 3, 1\rangle$	24
159b	2.247	$\langle 23, 9, 5\rangle$	24
159c	2.247	$\langle 21, 13, 5\rangle$	24
159d	2.247	$\langle 19, 15, 7\rangle$	24
159e	2.247	$\langle 17, 15, 11\rangle$	24
160	2.256	$\langle 24, 8, 0\rangle$	24
161a	2.261	$\langle 25, 3, 3\rangle$	12
161b	2.261	$\langle 21, 11, 9\rangle$	24
162a	2.270	$\langle 24, 6, 6\rangle$	24
162b	2.270	$\langle 22, 10, 8\rangle$	48

162c	2.270	$\langle 18, 18, 0\rangle$	12
162d	2.270	$\langle 16, 14, 14\rangle$	24
163a	2.275	$\langle 25, 5, 1\rangle$	24
163b	2.275	$\langle 23, 11, 1\rangle$	24
163c	2.275	$\langle 19, 17, 1\rangle$	24
163d	2.275	$\langle 19, 13, 11\rangle$	24
164a	2.284	$\langle 24, 8, 4\rangle$	48
164b	2.284	$\langle 20, 16, 0\rangle$	24
164c	2.284	$\langle 16, 16, 12\rangle$	24
165a	2.289	$\langle 25, 5, 3\rangle$	24
165b	2.289	$\langle 23, 11, 3\rangle$	24
165c	2.289	$\langle 23, 9, 7\rangle$	24
165d	2.289	$\langle 21, 13, 7\rangle$	24
165e	2.289	$\langle 19, 17, 3\rangle$	24
165f	2.289	$\langle 17, 17, 9\rangle$	12
166a	2.298	$\langle 22, 12, 6\rangle$	48
166b	2.298	$\langle 18, 18, 4\rangle$	24
166c	2.298	$\langle 18, 14, 12\rangle$	48
167a	2.303	$\langle 21, 15, 1\rangle$	24
167b	2.303	$\langle 19, 15, 9\rangle$	24
168	2.312	$\langle 20, 16, 4\rangle$	48
169a	2.317	$\langle 25, 7, 1\rangle$	24
169b	2.317	$\langle 25, 5, 5\rangle$	12
169c	2.317	$\langle 23, 11, 5\rangle$	24
169d	2.317	$\langle 21, 15, 3\rangle$	24
169e	2.317	$\langle 19, 17, 5\rangle$	24
169f	2.317	$\langle 15, 15, 15\rangle$	4

170a	2.325	$\langle 26, 2, 0\rangle$	24
170b	2.325	$\langle 24, 10, 2\rangle$	48
170c	2.325	$\langle 22, 14, 0\rangle$	24
170d	2.325	$\langle 18, 16, 10\rangle$	48
171a	2.331	$\langle 25, 7, 3\rangle$	24
171b	2.331	$\langle 21, 11, 11\rangle$	12
171c	2.331	$\langle 17, 15, 13\rangle$	24
172	2.339	$\langle 20, 12, 12\rangle$	24
173a	2.344	$\langle 23, 9, 9\rangle$	12
173b	2.344	$\langle 21, 15, 5\rangle$	24
173c	2.344	$\langle 21, 13, 9\rangle$	24
174a	2.353	$\langle 26, 4, 2\rangle$	48
174b	2.353	$\langle 22, 14, 4\rangle$	48
174c	2.353	$\langle 20, 14, 10\rangle$	48
175a	2.358	$\langle 25, 7, 5\rangle$	24
175b	2.358	$\langle 23, 13, 1\rangle$	24
175c	2.358	$\langle 23, 11, 7\rangle$	24
175d	2.358	$\langle 19, 17, 7\rangle$	24
175e	2.358	$\langle 19, 13, 13\rangle$	12
175f	2.358	$\langle 17, 17, 11\rangle$	12
176	2.366	$\langle 24, 8, 8\rangle$	24
177a	2.371	$\langle 25, 9, 1\rangle$	24
177b	2.371	$\langle 23, 13, 3\rangle$	24
177c	2.371	$\langle 19, 15, 11\rangle$	24
178a	2.379	$\langle 26, 6, 0\rangle$	24
178b	2.379	$\langle 24, 10, 6\rangle$	48
178c	2.379	$\langle 18, 18, 8\rangle$	24

179a	2.384	$\langle 25, 9, 3\rangle$	24
179b	2.384	$\langle 21, 15, 7\rangle$	24
180a	2.393	$\langle 24, 12, 0\rangle$	24
180b	2.393	$\langle 20, 16, 8\rangle$	48
181a	2.398	$\langle 19, 19, 1\rangle$	12
181b	2.398	$\langle 25, 7, 7\rangle$	12
181c	2.398	$\langle 23, 13, 5\rangle$	24
182a	2.406	$\langle 26, 6, 4\rangle$	48
182b	2.406	$\langle 22, 12, 10\rangle$	48
182c	2.406	$\langle 20, 18, 2\rangle$	48
183a	2.411	$\langle 27, 1, 1\rangle$	12
183b	2.411	$\langle 25, 9, 5\rangle$	24
183c	2.411	$\langle 23, 11, 9\rangle$	24
183d	2.411	$\langle 21, 17, 1\rangle$	24
183e	2.411	$\langle 21, 13, 11\rangle$	24
183f	2.411	$\langle 19, 19, 3\rangle$	12
183g	2.411	$\langle 19, 17, 9\rangle$	24
184	2.419	$\langle 24, 12, 4\rangle$	48
185a	2.424	$\langle 27, 3, 1\rangle$	24
185b	2.424	$\langle 21, 17, 3\rangle$	24
185c	2.424	$\langle 17, 15, 15\rangle$	12
186a	2.432	$\langle 26, 8, 2\rangle$	48
186b	2.432	$\langle 22, 16, 2\rangle$	48
186c	2.432	$\langle 22, 14, 8\rangle$	48
187a	2.437	$\langle 27, 3, 3\rangle$	12
187b	2.437	$\langle 25, 11, 1\rangle$	24
187c	2.437	$\langle 23, 13, 7\rangle$	24

187d	2.437	$\langle 21, 15, 9\rangle$	24
187e	2.437	$\langle 19, 19, 5\rangle$	12
187f	2.437	$\langle 17, 17, 13\rangle$	12
188			
189a	2.450	$\langle 27, 5, 1\rangle$	24
189b	2.450	$\langle 25, 11, 3\rangle$	24
189c	2.450	$\langle 25, 9, 7\rangle$	24
189d	2.450	$\langle 23, 15, 1\rangle$	24
189e	2.450	$\langle 21, 17, 5\rangle$	24
189f	2.450	$\langle 19, 15, 13\rangle$	24
190	2.458	$\langle 20, 18, 6\rangle$	48
191a	2.463	$\langle 27, 5, 3\rangle$	24
191b	2.463	$\langle 23, 15, 3\rangle$	24
192	2.471	$\langle 16, 16, 16\rangle$	8
193a	2.476	$\langle 25, 11, 5\rangle$	24
193b	2.476	$\langle 23, 11, 11\rangle$	12
193c	2.476	$\langle 19, 19, 7\rangle$	12
193d	2.476	$\langle 19, 17, 11\rangle$	24
194a	2.484	$\langle 26, 10, 0\rangle$	24
194b	2.484	$\langle 26, 8, 6\rangle$	48
194c	2.484	$\langle 24, 14, 2\rangle$	48
194d	2.484	$\langle 24, 10, 10\rangle$	24
194e	2.484	$\langle 22, 16, 6\rangle$	48
194f	2.484	$\langle 18, 16, 14\rangle$	48
195a	2.489	$\langle 27, 7, 1\rangle$	24
195b	2.489	$\langle 27, 5, 5\rangle$	12
195c	2.489	$\langle 23, 15, 5\rangle$	24

195d	2.489	$\langle 23, 13, 9\rangle$	24
195e	2.489	$\langle 21, 17, 7\rangle$	24
195f	2.489	$\langle 21, 13, 13\rangle$	12
196a	2.497	$\langle 28, 0, 0\rangle$	6
196b	2.497	$\langle 24, 12, 8\rangle$	48
197a	2.502	$\langle 27, 7, 3\rangle$	24
197b	2.502	$\langle 25, 9, 9\rangle$	12
197c	2.502	$\langle 21, 15, 11\rangle$	24
198a	2.510	$\langle 28, 2, 2\rangle$	24
198b	2.510	$\langle 26, 10, 4\rangle$	48
198c	2.510	$\langle 20, 14, 14\rangle$	24
198d	2.510	$\langle 18, 18, 12\rangle$	24
199a	2.514	$\langle 25, 13, 1\rangle$	24
199b	2.514	$\langle 25, 11, 7\rangle$	24
200a	2.522	$\langle 28, 4, 0\rangle$	24
200b	2.522	$\langle 20, 20, 0\rangle$	12
200c	2.522	$\langle 20, 16, 12\rangle$	48
201a	2.527	$\langle 27, 7, 5\rangle$	24
201b	2.527	$\langle 25, 13, 3\rangle$	24
201c	2.527	$\langle 23, 15, 7\rangle$	24
201d	2.527	$\langle 21, 19, 1\rangle$	24
201e	2.527	$\langle 19, 19, 9\rangle$	12
201f	2.527	$\langle 17, 17, 15\rangle$	12
202a	2.535	$\langle 24, 14, 6\rangle$	48
202b	2.535	$\langle 22, 18, 0\rangle$	24
203a	2.540	$\langle 27, 9, 1\rangle$	24
203b	2.540	$\langle 21, 19, 3\rangle$	24

203c	2.540	$\langle 21, 17, 9\rangle$	24
203d	2.540	$\langle 19, 15, 15\rangle$	12
204a	2.547	$\langle 28, 4, 4\rangle$	24
204b	2.547	$\langle 20, 20, 4\rangle$	24
205a	2.552	$\langle 27, 9, 3\rangle$	24
205b	2.552	$\langle 25, 13, 5\rangle$	24
205c	2.552	$\langle 23, 17, 1\rangle$	24
205d	2.552	$\langle 23, 13, 11\rangle$	24
205e	2.552	$\langle 19, 17, 13\rangle$	24
206a	2.560	$\langle 28, 6, 2\rangle$	48
206b	2.560	$\langle 26, 12, 2\rangle$	48
206c	2.560	$\langle 22, 18, 4\rangle$	48
206d	2.560	$\langle 22, 14, 12\rangle$	48
206e	2.560	$\langle 20, 18, 10\rangle$	48
207a	2.564	$\langle 27, 7, 7\rangle$	12
207b	2.564	$\langle 25, 11, 9\rangle$	24
207c	2.564	$\langle 23, 17, 3\rangle$	24
207d	2.564	$\langle 21, 19, 5\rangle$	24
208	2.572	$\langle 24, 16, 0\rangle$	24
209a	2.577	$\langle 27, 9, 5\rangle$	24
209b	2.577	$\langle 23, 15, 9\rangle$	24
209c	2.577	$\langle 21, 15, 13\rangle$	24
210a	2.585	$\langle 26, 10, 8\rangle$	48
210b	2.585	$\langle 22, 16, 10\rangle$	48
211a	2.589	$\langle 29, 1, 1\rangle$	12
211b	2.589	$\langle 25, 13, 7\rangle$	24
211c	2.589	$\langle 23, 17, 5\rangle$	24

211d	2.589	$\langle 19, 19, 11\rangle$	12
212a	2.597	$\langle 28, 8, 0\rangle$	24
212b	2.597	$\langle 24, 16, 4\rangle$	48
213a	2.601	$\langle 29, 3, 1\rangle$	24
213b	2.601	$\langle 27, 11, 1\rangle$	24
213c	2.601	$\langle 25, 15, 1\rangle$	24
213d	2.601	$\langle 21, 19, 7\rangle$	24
213e	2.601	$\langle 21, 17, 11\rangle$	24
214a	2.609	$\langle 28, 6, 6\rangle$	24
214b	2.609	$\langle 26, 12, 6\rangle$	48
215a	2.614	$\langle 29, 3, 3\rangle$	12
215b	2.614	$\langle 27, 11, 3\rangle$	24
215c	2.614	$\langle 27, 9, 7\rangle$	24
215d	2.614	$\langle 25, 15, 3\rangle$	24
216a	2.621	$\langle 28, 8, 4\rangle$	48
216b	2.621	$\langle 24, 12, 12\rangle$	24
216c	2.621	$\langle 20, 20, 8\rangle$	24
217a	2.626	$\langle 29, 5, 1\rangle$	24
217b	2.626	$\langle 25, 11, 11\rangle$	12
217c	2.626	$\langle 23, 17, 7\rangle$	24
217d	2.626	$\langle 23, 13, 13\rangle$	12
217e	2.626	$\langle 17, 17, 17\rangle$	4
218a	2.633	$\langle 26, 14, 0\rangle$	24
218b	2.633	$\langle 24, 14, 10\rangle$	48
218c	2.633	$\langle 22, 18, 8\rangle$	48
219a	2.638	$\langle 29, 5, 3\rangle$	24
219b	2.638	$\langle 27, 11, 5\rangle$	24

219c	2.638	$\langle 25, 15, 5\rangle$	24
219d	2.638	$\langle 25, 13, 9\rangle$	24
219e	2.638	$\langle 23, 15, 11\rangle$	24
219f	2.638	$\langle 19, 17, 15\rangle$	24
220			
221a	2.650	$\langle 21, 21, 1\rangle$	12
221b	2.650	$\langle 21, 19, 9\rangle$	24
222a	2.657	$\langle 28, 10, 2\rangle$	48
222b	2.657	$\langle 26, 14, 4\rangle$	48
222c	2.657	$\langle 22, 20, 2\rangle$	48
223a	2.662	$\langle 29, 7, 1\rangle$	24
223b	2.662	$\langle 29, 5, 5\rangle$	12
223c	2.662	$\langle 27, 9, 9\rangle$	12
223d	2.662	$\langle 23, 19, 1\rangle$	24
223e	2.662	$\langle 21, 21, 3\rangle$	12
223f	2.662	$\langle 21, 15, 15\rangle$	12
223g	2.662	$\langle 19, 19, 13\rangle$	12
224	2.669	$\langle 24, 16, 8\rangle$	48
225a	2.674	$\langle 29, 7, 3\rangle$	24
225b	2.674	$\langle 27, 13, 1\rangle$	24
225c	2.674	$\langle 27, 11, 7\rangle$	24
225d	2.674	$\langle 25, 15, 7\rangle$	24
225e	2.674	$\langle 23, 19, 3\rangle$	24
225f	2.674	$\langle 23, 17, 9\rangle$	24
225g	2.674	$\langle 21, 17, 13\rangle$	24
226a	2.681	$\langle 30, 2, 0\rangle$	24
226b	2.681	$\langle 24, 18, 2\rangle$	48

226c	2.681	$\langle 18, 18, 16\rangle$	24
227a	2.686	$\langle 27, 13, 3\rangle$	24
227b	2.686	$\langle 21, 21, 5\rangle$	12
228a	2.693	$\langle 28, 8, 8\rangle$	24
228b	2.693	$\langle 20, 16, 16\rangle$	24
229a	2.697	$\langle 29, 7, 5\rangle$	24
229b	2.697	$\langle 25, 17, 1\rangle$	24
229c	2.697	$\langle 25, 13, 11\rangle$	24
229d	2.697	$\langle 23, 19, 5\rangle$	24
230a	2.705	$\langle 30, 4, 2\rangle$	48
230b	2.705	$\langle 28, 10, 6\rangle$	48
230c	2.705	$\langle 26, 12, 10\rangle$	48
230d	2.705	$\langle 22, 20, 6\rangle$	48
230e	2.705	$\langle 20, 18, 14\rangle$	48
231a	2.709	$\langle 29, 9, 1\rangle$	24
231b	2.709	$\langle 27, 13, 5\rangle$	24
231c	2.709	$\langle 25, 17, 3\rangle$	24
231d	2.709	$\langle 23, 15, 13\rangle$	24
231e	2.709	$\langle 21, 19, 11\rangle$	24
232	2.717	$\langle 28, 12, 0\rangle$	24
233a	2.721	$\langle 29, 9, 3\rangle$	24
233b	2.721	$\langle 27, 11, 9\rangle$	24
233c	2.721	$\langle 25, 15, 9\rangle$	24
233d	2.721	$\langle 21, 21, 7\rangle$	12
234a	2.728	$\langle 30, 6, 0\rangle$	24
234b	2.728	$\langle 26, 16, 2\rangle$	48
234c	2.728	$\langle 26, 14, 8\rangle$	48

234d	2.728	$\langle 24, 18, 6\rangle$	48
234e	2.728	$\langle 22, 16, 14\rangle$	48
235a	2.733	$\langle 29, 7, 7\rangle$	12
235b	2.733	$\langle 25, 17, 5\rangle$	24
235c	2.733	$\langle 23, 19, 7\rangle$	24
235d	2.733	$\langle 23, 17, 11\rangle$	24
235e	2.733	$\langle 19, 17, 17\rangle$	12
236a	2.740	$\langle 28, 12, 4\rangle$	48
236b	2.740	$\langle 20, 20, 12\rangle$	24
237a	2.744	$\langle 29, 9, 5\rangle$	24
237b	2.744	$\langle 27, 13, 7\rangle$	24
237c	2.744	$\langle 19, 19, 15\rangle$	12
238a	2.751	$\langle 30, 6, 4\rangle$	48
238b	2.751	$\langle 22, 18, 12\rangle$	48
239a	2.756	$\langle 27, 15, 1\rangle$	24
239b	2.756	$\langle 21, 17, 15\rangle$	24
240			
241a	2.767	$\langle 31, 1, 1\rangle$	12
241b	2.767	$\langle 29, 11, 1\rangle$	24
241c	2.767	$\langle 27, 15, 3\rangle$	24
241d	2.767	$\langle 25, 17, 7\rangle$	24
241e	2.767	$\langle 25, 13, 13\rangle$	12
241f	2.767	$\langle 21, 21, 9\rangle$	12
242a	2.774	$\langle 30, 8, 2\rangle$	48
242b	2.774	$\langle 26, 16, 6\rangle$	48
242c	2.774	$\langle 24, 14, 14\rangle$	24
242d	2.774	$\langle 22, 22, 0\rangle$	12

243a	2.779	$\langle 31, 3, 1\rangle$	24
243b	2.779	$\langle 29, 11, 3\rangle$	24
243c	2.779	$\langle 29, 9, 7\rangle$	24
243d	2.779	$\langle 27, 11, 11\rangle$	12
243e	2.779	$\langle 25, 15, 11\rangle$	24
243f	2.779	$\langle 23, 21, 1\rangle$	24
243g	2.779	$\langle 23, 19, 9\rangle$	24
243h	2.779	$\langle 21, 19, 13\rangle$	24
244a	2.786	$\langle 24, 20, 0\rangle$	24
244b	2.786	$\langle 24, 16, 12\rangle$	48
245a	2.790	$\langle 31, 3, 3\rangle$	12
245b	2.790	$\langle 27, 15, 5\rangle$	24
245c	2.790	$\langle 27, 13, 9\rangle$	24
245d	2.790	$\langle 23, 21, 3\rangle$	24
245e	2.790	$\langle 23, 15, 15\rangle$	12
246a	2.797	$\langle 28, 14, 2\rangle$	48
246b	2.797	$\langle 28, 10, 10\rangle$	24
246c	2.797	$\langle 22, 22, 4\rangle$	24
246d	2.797	$\langle 22, 20, 10\rangle$	48
247a	2.802	$\langle 31, 5, 1\rangle$	24
247b	2.802	$\langle 29, 11, 5\rangle$	24
247c	2.802	$\langle 25, 19, 1\rangle$	24
247d	2.802	$\langle 23, 17, 13\rangle$	24
248a	2.809	$\langle 28, 12, 8\rangle$	48
248b	2.809	$\langle 24, 20, 4\rangle$	48
249a	2.813	$\langle 31, 5, 3\rangle$	24
249b	2.813	$\langle 25, 19, 3\rangle$	24

249c	2.813	$\langle 25, 17, 9\rangle$	24
249d	2.813	$\langle 23, 21, 5\rangle$	24
250a	2.820	$\langle 30, 10, 0\rangle$	24
250b	2.820	$\langle 30, 8, 6\rangle$	48
250c	2.820	$\langle 26, 18, 0\rangle$	24
250d	2.820	$\langle 24, 18, 10\rangle$	48
251a	2.824	$\langle 29, 9, 9\rangle$	12
251b	2.824	$\langle 27, 15, 7\rangle$	24
251c	2.824	$\langle 21, 21, 11\rangle$	12
252			
253a	2.835	$\langle 31, 7, 1\rangle$	24
253b	2.835	$\langle 31, 5, 5\rangle$	12
253c	2.835	$\langle 29, 13, 1\rangle$	24
253d	2.835	$\langle 29, 11, 7\rangle$	24
253e	2.835	$\langle 25, 19, 5\rangle$	24
253f	2.835	$\langle 23, 19, 11\rangle$	24
253g	2.835	$\langle 19, 19, 17\rangle$	12
254a	2.842	$\langle 30, 10, 4\rangle$	48
254b	2.842	$\langle 28, 14, 6\rangle$	48
254c	2.842	$\langle 26, 18, 4\rangle$	48
254d	2.842	$\langle 26, 14, 12\rangle$	48
255a	2.847	$\langle 31, 7, 3\rangle$	24
255b	2.847	$\langle 29, 13, 3\rangle$	24
255c	2.847	$\langle 27, 17, 1\rangle$	24
255d	2.847	$\langle 27, 13, 11\rangle$	24
255e	2.847	$\langle 25, 15, 13\rangle$	24
255f	2.847	$\langle 23, 21, 7\rangle$	24

255g	2.847	$\langle 21, 17, 17\rangle$	12
256	2.854	$\langle 32, 0, 0\rangle$	6
257a	2.858	$\langle 27, 17, 3\rangle$	24
257b	2.858	$\langle 21, 19, 15\rangle$	24
258a	2.865	$\langle 32, 2, 2\rangle$	24
258b	2.865	$\langle 26, 16, 10\rangle$	48
258c	2.865	$\langle 22, 22, 8\rangle$	24
259a	2.869	$\langle 31, 7, 5\rangle$	24
259b	2.869	$\langle 29, 13, 5\rangle$	24
259c	2.869	$\langle 27, 15, 9\rangle$	24
259d	2.869	$\langle 25, 19, 7\rangle$	24
259e	2.869	$\langle 25, 17, 11\rangle$	24
260a	2.876	$\langle 32, 4, 0\rangle$	24
260b	2.876	$\langle 28, 16, 0\rangle$	24
260c	2.876	$\langle 24, 20, 8\rangle$	48
261a	2.880	$\langle 31, 9, 1\rangle$	24
261b	2.880	$\langle 29, 11, 9\rangle$	24
261c	2.880	$\langle 27, 17, 5\rangle$	24
261d	2.880	$\langle 23, 17, 15\rangle$	24
262a	2.887	$\langle 30, 12, 2\rangle$	48
262b	2.887	$\langle 20, 18, 18\rangle$	24
263a	2.891	$\langle 31, 9, 3\rangle$	24
263b	2.891	$\langle 23, 21, 9\rangle$	24
263c	2.891	$\langle 21, 21, 13\rangle$	12
264a	2.898	$\langle 32, 4, 4\rangle$	24
264b	2.898	$\langle 28, 16, 4\rangle$	48
264c	2.898	$\langle 20, 20, 16\rangle$	24

265a	2.902	$\langle 29, 13, 7\rangle$	24
265b	2.902	$\langle 23, 23, 1\rangle$	12
265c	2.902	$\langle 23, 19, 13\rangle$	24
265d	2.902	$\langle 31, 7, 7\rangle$	12
266a	2.909	$\langle 32, 6, 2\rangle$	48
266b	2.909	$\langle 30, 10, 8\rangle$	48
266c	2.909	$\langle 26, 18, 8\rangle$	48
266d	2.909	$\langle 24, 22, 2\rangle$	48
266e	2.909	$\langle 22, 18, 16\rangle$	48
267a	2.913	$\langle 31, 9, 5\rangle$	24
267b	2.913	$\langle 29, 15, 1\rangle$	24
267c	2.913	$\langle 27, 17, 7\rangle$	24
267d	2.913	$\langle 27, 13, 13\rangle$	12
267e	2.913	$\langle 25, 21, 1\rangle$	24
267f	2.913	$\langle 25, 19, 9\rangle$	24
267g	2.913	$\langle 23, 23, 3\rangle$	12
268	2.920	$\langle 28, 12, 12\rangle$	24
269a	2.924	$\langle 29, 15, 3\rangle$	24
269b	2.924	$\langle 27, 15, 11\rangle$	24
269c	2.924	$\langle 25, 21, 3\rangle$	24
269d	2.924	$\langle 25, 15, 15\rangle$	12
270a	2.931	$\langle 30, 12, 6\rangle$	48
270b	2.931	$\langle 28, 14, 10\rangle$	48
270c	2.931	$\langle 26, 20, 2\rangle$	48
270d	2.931	$\langle 22, 20, 14\rangle$	48
271a	2.935	$\langle 31, 11, 1\rangle$	24
271b	2.935	$\langle 29, 11, 11\rangle$	12

271c	2.935	$\langle 25, 17, 13\rangle$	24
271d	2.935	$\langle 23, 23, 5\rangle$	12
271e	2.935	$\langle 19, 19, 19\rangle$	4
272a	2.941	$\langle 32, 8, 0\rangle$	24
272b	2.941	$\langle 24, 16, 16\rangle$	24
273a	2.945	$\langle 33, 1, 1\rangle$	12
273b	2.945	$\langle 31, 11, 3\rangle$	24
273c	2.945	$\langle 31, 9, 7\rangle$	24
273d	2.945	$\langle 29, 15, 5\rangle$	24
273e	2.945	$\langle 29, 13, 9\rangle$	24
273f	2.945	$\langle 27, 19, 1\rangle$	24
273g	2.945	$\langle 25, 21, 5\rangle$	24
273h	2.945	$\langle 23, 21, 11\rangle$	24
273i	2.945	$\langle 21, 19, 17\rangle$	24
274a	2.952	$\langle 32, 6, 6\rangle$	24
274b	2.952	$\langle 30, 14, 0\rangle$	24
274c	2.952	$\langle 24, 22, 6\rangle$	48
274d	2.952	$\langle 24, 18, 14\rangle$	48
275a	2.956	$\langle 27, 19, 3\rangle$	24
275b	2.956	$\langle 27, 17, 9\rangle$	24
275c	2.956	$\langle 33, 3, 1\rangle$	24
276a	2.963	$\langle 32, 8, 4\rangle$	48
276b	2.963	$\langle 28, 16, 8\rangle$	48
277a	2.967	$\langle 33, 3, 3\rangle$	12
277b	2.967	$\langle 31, 11, 5\rangle$	24
277c	2.967	$\langle 25, 19, 11\rangle$	24
277d	2.967	$\langle 23, 23, 7\rangle$	12

277e	2.967	$\langle 23, 17, 17\rangle$	12
277f	2.967	$\langle 21, 21, 15\rangle$	12
278a	2.974	$\langle 30, 14, 4\rangle$	48
278b	2.974	$\langle 28, 18, 2\rangle$	48
278c	2.974	$\langle 26, 20, 6\rangle$	48
278d	2.974	$\langle 22, 22, 12\rangle$	24
279a	2.978	$\langle 33, 5, 1\rangle$	24
279b	2.978	$\langle 29, 15, 7\rangle$	24
279c	2.978	$\langle 27, 19, 5\rangle$	24
279d	2.978	$\langle 25, 21, 7\rangle$	24
279e	2.978	$\langle 23, 19, 15\rangle$	24
280	2.984	$\langle 24, 20, 12\rangle$	48
281a	2.988	$\langle 33, 5, 3\rangle$	24
281b	2.988	$\langle 31, 9, 9\rangle$	12
281c	2.988	$\langle 27, 15, 13\rangle$	24
282a	2.995	$\langle 32, 10, 2\rangle$	48
282b	2.995	$\langle 26, 16, 14\rangle$	48
283a	2.999	$\langle 31, 13, 1\rangle$	24
283b	2.999	$\langle 31, 11, 7\rangle$	24
283c	2.999	$\langle 29, 17, 1\rangle$	24
283d	2.999	$\langle 29, 13, 11\rangle$	24
284			
285a	3.010	$\langle 33, 7, 1\rangle$	24
285b	3.010	$\langle 33, 5, 5\rangle$	12
285c	3.010	$\langle 31, 13, 3\rangle$	24
285d	3.010	$\langle 29, 17, 3\rangle$	24
285e	3.010	$\langle 27, 19, 7\rangle$	24

285f	3.010	$\langle 27, 17, 11\rangle$	24
285g	3.010	$\langle 25, 17, 15\rangle$	24
285h	3.010	$\langle 23, 23, 9\rangle$	12
285i	3.010	$\langle 23, 21, 13\rangle$	24
286a	3.016	$\langle 30, 12, 10\rangle$	48
286b	3.016	$\langle 28, 18, 6\rangle$	48
286c	3.016	$\langle 26, 18, 12\rangle$	48
287a	3.020	$\langle 33, 7, 3\rangle$	24
287b	3.020	$\langle 29, 15, 9\rangle$	24
287c	3.020	$\langle 25, 21, 9\rangle$	24
288a	3.027	$\langle 32, 8, 8\rangle$	24
288b	3.027	$\langle 24, 24, 0\rangle$	12
289a	3.031	$\langle 31, 13, 5\rangle$	24
289b	3.031	$\langle 29, 17, 5\rangle$	24
289c	3.031	$\langle 25, 23, 1\rangle$	24
289d	3.031	$\langle 25, 19, 13\rangle$	24
290a	3.037	$\langle 34, 2, 0\rangle$	24
290b	3.037	$\langle 32, 10, 6\rangle$	48
290c	3.037	$\langle 30, 16, 2\rangle$	48
290d	3.037	$\langle 30, 14, 8\rangle$	48
290e	3.037	$\langle 26, 22, 0\rangle$	24
290f	3.037	$\langle 24, 22, 10\rangle$	48
291a	3.041	$\langle 33, 7, 5\rangle$	24
291b	3.041	$\langle 31, 11, 9\rangle$	24
291c	3.041	$\langle 25, 23, 3\rangle$	24
291d	3.041	$\langle 21, 19, 19\rangle$	12
292a	3.048	$\langle 32, 12, 0\rangle$	24

292b	3.048	$\langle 24, 24, 4\rangle$	24
293a	3.052	$\langle 33, 9, 1\rangle$	24
293b	3.052	$\langle 27, 21, 1\rangle$	24
293c	3.052	$\langle 27, 19, 9\rangle$	24
293d	3.052	$\langle 21, 21, 17\rangle$	12
294a	3.058	$\langle 34, 4, 2\rangle$	48
294b	3.058	$\langle 28, 14, 14\rangle$	24
294c	3.058	$\langle 26, 22, 4\rangle$	48
294d	3.058	$\langle 26, 20, 10\rangle$	48
295a	3.062	$\langle 33, 9, 3\rangle$	24
295b	3.062	$\langle 31, 13, 7\rangle$	24
295c	3.062	$\langle 29, 17, 7\rangle$	24
295d	3.062	$\langle 29, 13, 13\rangle$	12
295e	3.062	$\langle 27, 21, 3\rangle$	24
295f	3.062	$\langle 27, 15, 15\rangle$	12
295g	3.062	$\langle 25, 23, 5\rangle$	24
295h	3.062	$\langle 23, 23, 11\rangle$	12
295i	3.062	$\langle 23, 19, 17\rangle$	24
296a	3.068	$\langle 32, 12, 4\rangle$	48
296b	3.068	$\langle 28, 20, 0\rangle$	24
296c	3.068	$\langle 28, 16, 12\rangle$	48
297a	3.072	$\langle 33, 7, 7\rangle$	12
297b	3.072	$\langle 31, 15, 1\rangle$	24
297c	3.072	$\langle 29, 15, 11\rangle$	24
297d	3.072	$\langle 27, 17, 13\rangle$	24
297e	3.072	$\langle 25, 21, 11\rangle$	24
298a	3.079	$\langle 34, 6, 0\rangle$	24

298b	3.079	$\langle 30, 16, 6 \rangle$	48
299a	3.083	$\langle 33, 9, 5 \rangle$	24
299b	3.083	$\langle 31, 15, 3 \rangle$	24
299c	3.083	$\langle 27, 21, 5 \rangle$	24
299d	3.083	$\langle 23, 21, 15 \rangle$	24
300	3.089	$\langle 28, 20, 4 \rangle$	48